

Structural and Optical Characterization of III-V Nanostructures Monolithically Grown on Si Substrates



Georgios Boras

A thesis submitted to University College London for the degree of
Doctor of Philosophy (PhD)

Department of Electronic and Electrical Engineering
University College London

February 2022

Declaration

I, Georgios Boras, confirm that the work presented in this thesis is my own. Where information has been derived from other sources, I confirm that it has been indicated in the thesis.

Abstract

Group III-V semiconductor nanostructures have emerged as an important material platform over the past decades for wide-range device implementation in the field of electronics and optoelectronics. Among them, nanowires (NWs) are particularly attractive owing to the elastic strain relaxation through their sidewall facets which allows for the combination of lattice mismatched materials. Hence, optically active III-V materials become compatible with the mature and prevalent Si platform. Moreover, NWs are ideal for hosting quantum dots (QDs) ensuring their deterministic positioning and uniformity. This configuration opens the route for sophisticated applications including single photon emission, a crucial function in quantum information processing. In addition, another type of nanostructures that has attracted attention is the two-dimensional nanosheets, whose principal benefit is the band structure tuning from bulk to 2D by modulation of their thickness. Consequently, they are established as promising blocks for various optoelectronic devices and applications.

In the current thesis, we reported the growth of self-catalysed AlGaAs NWs monolithically on Si (111) substrates via solid-source molecular beam epitaxy (MBE). The self-formation of an Al-rich shell is exhibited, which is thicker at the base and thins down towards the NW tip, while it demonstrates wide alloy fluctuations. The predominantly ZB structure presents twin defects and occasional WZ insertions, further increasing the intricacy of the NWs. The optical probing via photoluminescence reveals fully tuneable emission with the Al content of the alloy.

Among the morphological variations of AlGaAs NWs, the branched NWs are of unique interest. The branching events increase with Al content, while the branches are confirmed to grow on the NW trunks epitaxially. In addition, complex compositional

distribution in the branches is presented, as Ga-rich stripes along the growth direction of the branches, attributed to the different nucleation energies on different faces at the liquid/solid interface of the branch, intersect with Ga-rich stripes perpendicular to them, deriving from the rotation of the sample during growth.

Moreover, self-catalysed, single GaAs/AlGaAs dot-in-wire structures have been designed and grown by inserting a short GaAs segment in each AlGaAs NW. The exhaustive optical probing reveals centrally localized peaks, with a decently narrow linewidth of roughly 490 μeV . The QD emission is comprised of an exciton and a biexciton transition, while a high degree of polarization is noticed when compared to the AlGaAs NW-related emission. The above characteristics are important steps towards achieving single photon emission.

Finally, we optically inspect InAs nanosheets grown via MBE via photoluminescence measurements. Pristine nanosheets exhibit surface charge via carrier trapping mechanisms at the surface states, which is suggestive of the “memory effect”. The impact of sulphur passivation and core/shell configuration on the optical response of the nanosheets is evaluated. In addition, we fabricated an optoelectronic memory unit based on pristine InAs nanosheets, adopting a field-effect transistor configuration, which demonstrates negative photoresponse with good reproducibility and ultra-low power consumption.

Impact Statement

The growth and characterization of III-V semiconductor-based nanostructures has been a subject of great interest and scientific importance due to its link to a wide range of research fields. The material platforms available exhibit features which render them optically active and ideal candidates for various devices and circuit components including lasers, light-emitting diodes, transistors, solar cells, photodetectors, single photon sources, entangled photon emitters and biosensors. Hence, their successful synthesis and characterization are of high importance as they can offer new insights in the functionality and applicability of devices in the field of optoelectronics and Si photonics, energy harvesting and quantum information. Besides, the use of molecular beam epitaxy as the method for the development of the nanostructures demonstrates several advantages related to the material quality and thus the efficiency of the fabricated devices.

Furthermore, the monolithic growth of the investigated nanostructures on Si entails important benefits. This straightforward approach allows for circumvention of sophisticated techniques and equipment that have been conventionally used to avoid degradation of material quality. Ergo, the method enables a cost-effective approach for the synthesis of nanostructures of high material quality.

Importantly, the investigated ternary alloy which is AlGaAs has been reported so far to be synthesized via the Au-assisted technique. The use Au, albeit beneficial when compared to other foreign metal catalysts, can cause severe contamination and degrade the applicability of the structures. On the contrary, in this work AlGaAs nanowires (NWs) and AlGaAs/GaAs nanowire quantum dots (NWQDs) were developed via the self-catalysed approach, from Ga droplets alloyed with Al, for the

first time. Hence, the structures are compatible with a variety of applications including CMOS technologies and drive electronics. Furthermore, the investigation of 2D InAs nanosheets reveals their importance for optoelectronic memory applications, while the fabrication of such a unit in a field-effect transistor configuration demonstrates its advantageous properties including the ultralow power consumption and excellent reproducibility.

The aforementioned aspects highlight the importance of the current report in academic research. The results that were reached can be valuable in future works, such as the self-catalysed approach for the synthesis of nanostructures based on the important AlGaAs material platform. In addition, the investigation of 3D branched AlGaAs NWs can be proven significant for energy harvesting applications such as solar cells and supercapacitors, while the novel structural findings can be exploited for non-classical light sources. Eventually, the insertion of a single GaAs quantum dot in the axis of the AlGaAs NWs grown via the self-catalysed method and, which display good optical properties is highly promising for the realization of single photon sources, an essential compound for quantum information processing applications.

The experiments conducted and the results presented in the current work can also have a strong impact in the industrial sector. Specifically, the monolithic integration of III-V semiconductors with the mature and vastly explored Si platform is an important highlight as Si is the predominant material for the fabrication of compounds in the fields of electronics and optoelectronics. Hence, the above open the route for the on-chip integration of highly efficient structures without the demand of costly and intricate techniques and facilities.

Acknowledgements

First and foremost, I would like to express my gratitude to my supervisor, Professor Huiyun Liu, who offered me the opportunity to participate in this intriguing and challenging project, in the frame of which I had the privilege to work with the state-of-the-arts facilities at UCL. He offered me valuable support and guidance throughout the course of my work.

Furthermore, I would like to sincerely thank my colleagues, Dr. Xuezhe Yu, Dr. Mingchu Tang, Dr. Pamela Jurczak, Mr Haotian Zeng, Dr. Dongyoung Kim, Dr. Steve Hudziak, Dr. Yunyan Zhang, Mr Keshuang Li, Mr Junjie Yang, Mr Huiwen Deng, Mr Kevin Lee, Miss Xiao Li, Miss Manyu Dang and Miss Hui Jia for the aid they provided during my project. I consider important to specially thank Xuezhe for his guidance and supervision throughout these years and for his support in MBE growth, SEM and PL measurements, along with his valuable contributions and suggestions in the writing of our collaborative papers and the conference or meeting presentations in which I participated. Another special mention to Haotian, who helped me with useful suggestions, support and collaboration regarding my research. Steve trained me on using the scanning electron microscopy system at UCL, whilst Dongyoung and Xuezhe taught me how to use the low-wavelength PL system and Pamela tutored me in conducting high-wavelength PL measurements for the InAs nanosheet structures that we studied.

I would also like to thank Professor Ana Sanchez, Dr. Aruni Fonseka and Mr James Gott from the University of Warwick for their highly important contributions in my work with the transmission electron microscopy measurements they acquired from our grown structures. Additionally, I would like to thank Professor David Mowbray, Dr.

Anton Velychko, Dr. Tillmann Godde and Mr George Davis from the University of Sheffield for their contributions in the micro-PL measurements of the nanowire and dot-in-wire structures that we had previously grown at UCL. I would also like to express my gratitude to Prof. Jianhua Zhao and Dr. Dong Pan from the State Key Laboratory of Superlattices and Microstructures in the Chinese Academy of Sciences, for providing us with the high-quality InAs nanosheets that we characterized and inspected in our work. Besides, I would like to thank Dr. Andreas Fognini from Single Quantum in Delft, for offering me the opportunity to conduct my secondment period in their facilities in the Netherlands. In the frame of this secondment, I would like to thank my colleagues and collaborators, Mr. Antonio Guardani, Mr. Dimosthenis Toliopoulos, Mr. Leonardo Ranashinghe and Mr. Panaiot Zotev for sharing their ideas during our common training.

Finally, I would like to thank my family and friends for providing me with the moral and psychological support that was essential for me in order to focus on my research and reduce the daily stress and anxiety and without whom I could not have succeeded during my PhD.

Publications

1. **G. Boras**, X. Yu, H. Liu, III-V Ternary Nanowires on Si Substrates: Growth, Characterization and Device Applications, *J. Semicond.* **2019**, 40, 101301
2. **G. Boras**, X. Yu, H. A. Fonseka, D. Zhang, H. Zeng, A. M. Sanchez, H. Liu, Checked Patterned Elemental Distribution in AlGaAs Nanowire Branches via Vapor-Liquid-Solid Growth, *Nanoscale* **2020**, 12, 15711-15720
3. **G. Boras**, X. Yu, H. A. Fonseka, G. Davis, A. V. Velichko, J. A. Gott, H. Zeng, S. Wu, P. Parkinson, X. Xu, D. Mowbray A. M. Sanchez, H. Liu, Self-Catalyzed AlGaAs Nanowires and AlGaAs/GaAs Quantum Dots on Si Substrates, *J. Phys. Chem. C* **2021**, 125(26), 14338-14347
4. H. Zeng, X. Yu, H. A. Fonseka, J. A. Gott, M. Tang, Y. Zhang, **G. Boras**, J. Xu, A. M. Sanchez, H. Liu, Hybrid III-V/IV Nanowires: High-Quality Ge Shell Epitaxy on GaAs Cores, *Nano Lett.* **2018**, 18(10), 6397-6403
5. Y. Zhang, A. M. Sanchez, M. Aagesen, S. Huo, H. A. Fonseka, J. A. Gott, D. Kim, X. Yu, X. Chen, J. Xu, T. Li, H. Zeng, **G. Boras**, H. Liu, Growth and Fabrication of High-Quality Single Nanowire Devices with Radial p-i-n Junctions, *Small* **2019**, 15(3), 1803684
6. H. Zeng, X. Yu, H. A. Fonseka, **G. Boras**, P. Jurczak, T. Wang, A. M. Sanchez, H. Liu. Preferred growth direction of III-V nanowires on differently oriented Si substrates. *Nanotechnology* **2020**, 31(47), 475708

Conferences and Meetings

1. **Giorgos Boras**, Xuezhe Yu, H. Aruni Fonseka, Haotian Zeng, Ana M. Sanchez, Huiyun Liu, Irregular Compositional Distribution in Ternary AlGaAs Branched Nanowires, **UK Semiconductors 2019, Sheffield**

2. **Giorgos Boras**, Xuezhe Yu, Huiyun Liu, Monolithical dot-in-well and dot-in-wire growth on Si and Ge substrates, **1st 4Photon School 2018, University of Basel, Switzerland**
3. **Giorgos Boras**, Xuezhe Yu, H. Aruni Fonseka, James A. Gott, Tillmann Godde, George Davis, Yunyan Zhang, Haotian Zeng, Jia Xu, David Mowbray, Ana M. Sanchez, Huiyun Liu, Single GaAs Quantum Dots Embedded in AlGaAs Nanowires, **1st 4Photon Workshop 2018, TU Eindhoven, the Netherlands**
4. **Giorgos Boras**, Xuezhe Yu, H. Aruni Fonseka, James A. Gott, Tillmann Godde, George Davis, Yunyan Zhang, Haotian Zeng, Jia Xu, Ana M. Sanchez, David Mowbray, Huiyun Liu, Growth of AlGaAs Nanowires and AlGaAs/GaAs Nanowire Quantum Dots on Si Substrates via Molecular Beam Epitaxy, **2nd 4Photon School 2019, University of Würzburg, Germany**
5. **Giorgos Boras**, Xuezhe Yu, H. Aruni Fonseka, James A. Gott, Tillmann Godde, George Davis, Yunyan Zhang, Haotian Zeng, David Mowbray, Ana M. Sanchez, Huiyun Liu, Growth and Characterization of AlGaAs Nanowires and AlGaAs/GaAs Nanowire Quantum Dots, **2nd 4Photon Workshop 2019, Attocube Munich, Germany**
6. **Giorgos Boras**, Xuezhe Yu, H. Aruni Fonseka, Haotian Zeng, James A. Gott, Ana M. Sanchez, Huiyun Liu, Peculiar Compositional Distribution in Branched AlGaAs Nanowires, **3rd 4Photon School 2020, University of Sheffield, the UK**
7. **Giorgos Boras**, Xuezhe Yu, H. Aruni Fonseka, James A. Gott, Tillmann Godde, George Davis, Yunyan Zhang, Haotian Zeng, David Mowbray, Ana M. Sanchez, Huiyun Liu. Growth and Characterization of AlGaAs Nanowires and AlGaAs/GaAs Nanowire Quantum Dots, **3rd 4Photon Workshop 2020,**

University of Milano Bicocca, Italy (the workshop was held online due to COVID-19 restrictions)

8. **Giorgos Boras**, Xuezhe Yu, H. Aruni Fonseka, George Davis, Anton Velichko, James A. Gott, Haotian Zeng, Shiyao Wu, Patrick Parkinson, Xiulai Xu, David Mowbray, Ana M. Sanchez, Huiyun Liu. Self-Catalyzed AlGaAs Nanowires and AlGaAs/GaAs Nanowire-Quantum Dots on Si Substrates, **SIOE (Semiconductor Integrated Opto-electronics Conference) 2021, Cardiff, United Kingdom (Award for one of the two best posters)**

Secondment

Secondment in Industry, Single Quantum Delft, the Netherlands, January-March 2020

Table of Contents

<u>Declaration</u>	2
<u>Abstract</u>	3
<u>Impact Statement</u>	5
<u>Acknowledgments</u>	7
<u>Publications</u>	9
<u>Table of Contents</u>	12
<u>List of Abbreviations</u>	16
<u>List of Figures</u>	17
<u>Chapter 1: Introduction</u>	22
<u>1.1</u> Background Information on Nanoscale Structures	22
<u>1.1.1</u> Introduction to Nanowires	22
<u>1.1.2</u> Introduction to Nanowire Quantum Dots	26
<u>1.1.3</u> Crystal Structure: Zinc Blende and Wurtzite Phase	29
<u>1.1.4</u> Device Applications	33
<u>1.2</u> Growth Methods	40
<u>1.2.1</u> Top-down and Bottom-up Approaches	40
<u>1.2.2</u> Vapor-Liquid-Solid Growth Mode: Au-catalysed and Self-catalysed approaches	43
<u>1.3</u> Branched Nanowires: A Unique Type of Three-dimensional Nanowires	50
<u>1.4</u> III-V Nanosheets	53

1.5	Previous works on nanowires, nanowire quantum dots and nanosheets outside UCL	55
1.6	Previous works on nanowires and nanowire quantum dots at UCL	59
1.7	Comparison of nanostructures and material platforms	61
1.8	Organization of the Thesis	66
<u>Chapter 2: Equipment, setup and tools</u>		70
2.1	Molecular Beam Epitaxy: System and Working Principles	70
2.1.1	General Information	70
2.1.2	Molecular Beam Epitaxy system at UCL facilities	76
2.2	Measurement equipment and setups	80
2.2.1	Scanning Electron Microscopy	80
2.2.2	Transmission Electron Microscopy	84
2.2.3	Photoluminescence Measurements	89
<u>Chapter 3: AlGaAs Nanowires on Si (111) Substrates</u>		95
3.1	Background Information	95
3.2	Morphological and Structural Analysis of AlGaAs Nanowires	98
3.3	Growth Mechanism of AlGaAs Nanowires	110
3.4	Optical probing of AlGaAs Nanowires	113
3.5	Comparison of our work with previous works on AlGaAs Nanowires	121
3.6	Summary and Conclusions	123
<u>Chapter 4: Branched AlGaAs Nanowires</u>		126
4.1	Morphological and structural analysis of AlGaAs branched nanowires	126

<u>4.2</u>	Growth of AlGaAs Branches and Interpretation	133
<u>4.2.1</u>	Growth Model and First-Principles Calculations.....	133
<u>4.2.2</u>	Calculations of growth rate and volume of the trunks.....	137
<u>4.3</u>	Novel observations in AlGaAs nanowire branches.....	138
<u>4.4</u>	Comparison with previous works on III-V branched nanowires	151
<u>4.5</u>	Summary and Conclusions	154
<u>Chapter 5: AlGaAs/GaAs Nanowire Quantum Dots on Si (111) Substrates</u>		157
<u>5.1</u>	Structural Analysis of AlGaAs/GaAs Nanowire Quantum Dots	157
<u>5.2</u>	Photoluminescence of AlGaAs/GaAs Nanowire Quantum Dots.....	161
<u>5.3</u>	NextNano Simulations of the nanowire quantum dots.....	169
<u>5.4</u>	Comparison of our work with previous works on single III-V Nanowire Quantum Dots.....	173
<u>5.5</u>	Summary and Conclusions	175
<u>Chapter 6: Two-dimensional InAs nanosheets</u>		177
<u>6.1</u>	Introduction to basic principles	177
<u>6.1.1</u>	Surface Passivation Methods.....	177
<u>6.1.2</u>	Importance of InAs as a binary alloy	178
<u>6.2</u>	InAs nanosheet growth	179
<u>6.3</u>	Power-dependent photoluminescence on InAs nanosheets	184
<u>6.3.1</u>	Methods of measurements/Signs of “memory effect”	184
<u>6.3.2</u>	Pristine InAs nanosheet samples.....	185
<u>6.3.3</u>	Chemically Passivated InAs nanosheet samples	190

<u>6.3.4</u>	Physically passivated InAs nanosheet samples	193
<u>6.4</u>	Temperature-dependent photoluminescence measurements	197
<u>6.5</u>	Comparison of our work with previous works on InAs nanosheets	202
<u>6.6</u>	Optical Memory Unit Based on pristine InAs nanosheets	204
<u>6.7</u>	Summary and Conclusions	215
<u>Chapter 7: Discussion and Conclusion</u>	217
<u>7.1</u>	Summary of the presented results	217
<u>7.2</u>	Discussion of the results	221
<u>7.3</u>	Discussion of the challenges and future works	224
<u>Chapter 8: Bibliography</u>	231

List of Abbreviations

ADF	Annular dark field
CBE	Chemical Beam Epitaxy
EBL	Electron Beam Lithography
EDX	Energy Dispersive X-Ray Spectroscopy
FFT	Fast Fourier Transform
FWHM	Full width at half maximum
LED	Light Emitting Diode
MBE	Molecular Beam Epitaxy
MOVPE	Metal-Organic Vapour Phase Epitaxy
NW	Nanowire
NWQD	Nanowire Quantum Dot
PL	Photoluminescence
QD	Quantum Dot
RT	Room temperature
SAG	Selective Area Growth
SEM	Scanning Electron Microscopy
SK	Stranski-Krastanov
TBL	Three boundary line
TEM	Transmission Electron Microscopy
UHV	Ultra-High Vacuum
VLS	Vapour-Liquid-Solid
VS	Vapour-Solid
WZ	Wurtzite

List of Figures

Figure 1.1: Representative side-view scanning electron microscopy (SEM) image of a GaAs NW sample

Figure 1.2: Schematic representation of GaAsP/GaAs nanowire quantum dots (NWQDs)

Figure 1.3: Schematics of WZ and ZB crystal phase, as well as polytypism.

Figure 1.4: Schematics of top-down fabricated nanowires (NWs) with tapering at the tip.

Figure 1.5: Schematics of Au-assisted vapor-liquid-solid growth of nanowires.

Figure 1.6: Schematics of nanowire bending caused by strain in the core/shell interface.

Figure 1.7: SEM images of branched nanowires, forming tree-like structures.

Figure 1.8: Schematic representations of the nanostructures employed for the current thesis

Table 1: Basic features of the material platforms employed.

Figure 2.1: Basic schematic representations of MOCVD and MBE reactors.

Figure 2.2: Schematic representation of the growth chamber of a Molecular Beam Epitaxy reactor.

Figure 2.3: Picture of the Molecular Beam Epitaxy system at UCL facilities.

Figure 2.4: Schematic diagram of a typical SEM system.

Figure 2.5: Picture of the JEOL IT-100 SEM system at UCL Nanotechnology Laboratory.

Figure 2.6: Schematic diagram of a typical TEM system.

Figure 2.7: Schematics of the function of a typical PL set-up.

Figure 2.8: Macro-photoluminescence (PL) setup at UCL, with a green 532 nm laser as the light source.

Figure 3.1: SEM images of the AlGaAs NWs with 10%, 20%, 30% and 40% nominal Al content.

Figure 3.2: Statistical analysis of the diameter and length of the AlGaAs NWs as a function of the Al composition.

Figure 3.3: Energy dispersive x-ray spectroscopy (EDX) mapping of the NW tip for Al, Ga, As and O and EDX scanning along the NW axis.

Figure 3.4: Annular Dark Field (ADF) imaging showing the thickness of the shell at the bottom, middle and top of the AlGaAs NWs with 20% Al, numerical data on the composition at different regions of the shell revealing alloy fluctuations and transmission electron microscopy (TEM) image showing the crystallinity of the NWs.

Figure 3.5: EDX mapping for Al and Ga of the self-formed AlGaAs shell.

Figure 3.6: EDX scanning across and along the AlGaAs NW, showing the inhomogeneous elemental distribution and the self-formation of the shell.

Figure 3.7: Schematic representation of the AlGaAs NW growth mechanism.

Figure 3.8: Room temperature (RT) PL measurements for the nanowires with different Al contents and position-dependent micro-PL measurements for individual structures with varying Al compositions.

Table 2: Effective Al content based on EDX and PL calculations.

Table 3: Al content based on PL calculations for ZB and WZ AlGaAs.

Figure 3.9: TEM image showing the various WZ insertions and twins within the AlGaAs crystal.

Figure 4.1: Representative SEM of an AlGaAs NW with 10% Al content, showing two frequent variations; kinked and branched NWs.

Figure 4.2: SEM images of individual branched NWs for samples with 10%, 20%, 30% and 40% Al compositions.

Figure 4.3: Statistical analysis of the branching events percentage as a function of Al content.

Figure 4.4: TEM images showing (a) the vertical orientation of the branch with respect to the trunk and (b) the identical crystallinity between the branch and the trunk. FFT patterns in (c) and (d) confirm the epitaxial nature of the growth.

Figure 4.5: SEM images of an AlGaAs NW with three branches. The top view image shows the 6-fold symmetry of the branches.

Figure 4.6: Modelling of the AlGaAs NW branches and ab-initio computations using VASP.

Figure 4.7: Schematic representation of the growth mechanism for the branched AlGaAs NWs.

Figure 4.8: ADF images of the branches showing the formation of a checked pattern of compositional distribution and intensity profile revealing the periodicity of the perpendicular Ga-rich stripes.

Figure 4.9: EDX mapping for Ga and Al of the intersection of axial and perpendicular Ga-rich stripes, showing the formation of Ga-rich elemental boxes.

Figure 4.10: Schematic representation and interpretation of the formation of the perpendicular Ga-rich stripes; rotation of the sample during growth.

Figure 4.11: High-resolution TEM and schematics showing the segregation of Ga in one type of ZB facets and interpreting the formation of axial Ga-rich stripes.

Figure 5.1: Typical SEM image and TEM data from the NW tip.

Figure 5.2: TEM data, including ADF imaging and EDX, showing the formation of the GaAs QD in the AlGaAs NW.

Figure 5.3: Position-dependent micro-PL data from the GaAs/AlGaAs dot-in-wire structures.

Figure 5.4: Power- and temperature-dependent micro-PL results from the AlGaAs/GaAs NWQDs.

Figure 5.5: Optical image and polar plot from the AlGaAs/GaAs NWQDs.

Figure 5.6: Nextnano simulation results.

Figure 6.1: SEM images of InAs nanosheets.

Figure 6.2: Intensity profiles for the dimensions of the nanosheets.

Figure 6.3: Typical TEM images of the nanosheets, as previously reported in ref.[200].

Figure 6.4: Power-dependent spectra from pristine InAs nanosheets.

Figure 6.5: Schematics of the nanosheets showing the “memory effect” interpretation.

Figure 6.6: Plot of intensity vs excitation power and Gaussian fitting of the peak from pristine InAs nanosheets.

Figure 6.7: Power-dependent PL measurements from chemically passivated InAs nanosheets.

Figure 6.8: Plot of intensity vs excitation power and Gaussian fitting of the peak from chemically passivated InAs nanosheets.

Figure 6.9: Power-dependent PL measurements from physically passivated InAs nanosheets.

Figure 6.10: Plot of intensity vs excitation power and Gaussian fitting of the peak from physically passivated InAs nanosheets.

Figure 6.11 Temperature-dependent PL measurements on all of the realized InAs nanosheet samples.

Table 4: Basic PL features of the different InAs nanosheets measured.

Figure 6.12: Schematics of the InAs nanosheet-based device, NPR mechanism of the nanosheet and electrical characteristics of the fabricated FETs.

Figure 6.13: Graphs of V_g and I_{DS} of FETs with programming and/or erasing pulses being applied.

Figure 6.14: Channel current stability tests, binary NPR loops under different drain-source voltages and the power of each binary NPR.

Chapter 1: Introduction

1.1) Background Information on Nanoscale Structures

1.1.1) Introduction to Nanowires

The synthesis and development of nanostructures with at least one dimension in the nanoscale have resulted in breakthroughs for novel device implementation in the field of electronics, optoelectronics and bio-applications. Among the different nanostructures that have been realized, nanowires (NWs) are particularly intriguing owing to their unique morphological properties. Their origin is dated back in 1964, when Ellis and Wagner first developed a novel structure which was named “silicon nanowhiskers”.^[1] Since then, NW growth and fabrication has presented immense progress and evolution. Particularly, NW realization has been massively increased over the past two decades by the vast amount of scientific research, focusing on improved material quality, optimum physical and chemical properties and novel applicability in functional devices.^[2-4]

NWs are 1D columnar shape structures, the radial dimensions of which are typically in the range of 100 nm or below, whilst the axial length can reach several tens of micrometres. This characteristic leads to a 2D quantum confinement of the carriers over the radial dimensions, while they are rendered free to propagate along the NW axis. One of the most important features is the small footprint of the structures, caused by the small radial dimensions, which results in elastic strain relaxation along the NW sidewall surfaces, thus enabling accommodation of materials with large lattice mismatch.^[5-6] The generation of threading dislocations within nanowire structures is circumvented. Consequently, the range of materials that can be combined is significantly broadened for applications in various fields, without the need of any

sophisticated techniques or equipment.^[7] The peculiarity in the columnar shape and one-dimensionality of NWs also leads to a high light extraction efficiency and waveguiding properties,^[6] rendering them ideal candidates for light-emitting applications.

On the other hand, among the available platforms for NW fabrication, group III-V semiconductors are optically active and present several advantageous features, including direct bandgap and high carrier mobility, making them beneficial for optoelectronic applications. The past years have seen important progress in III-V NW synthesis, such as structures with high phase purity^[8-10] and hybrid group III-V/IV core/shell NWs.^[11-12] In addition, III-V NWs have been investigated as a platform for the fabrication of various devices, most notably lasers,^[13-17] light-emitting diodes (LEDs),^[18-22] solar cells,^[23-27] photodetectors^[28-32] and field-effect transistors (FETs).^[33-37] For example, the first report on NW-based lasers from an array of ZnO NWs, suggested that the 1D nature of the structures leads them to act as Fabry-Perot cavities.^[38] This was further supported by the fact that lasing peaks were observed in individual, single NW structures, which interestingly were dependent on the diameter of the NW, as below a certain critical value laser function was impeded.^[39] The amplification occurs via light reflection at the NW end facets which propagates through the gain medium. The reflection occurs as a result of the 2D carrier confinement along with the diameter of the NWs being in the same order of magnitude as the wavelength of light, causing reflection at the NW/air interface due to scattering.^[40] NWs have strong waveguide properties deriving from their morphological uniqueness which renders them ideal for such applications. Taking into consideration the high refractive index of III-V semiconductors, NWs based on these material platforms are good candidates for lasing applications among others. Simultaneously, indirect-bandgap Si

has been the mainstream platform in information technologies, on which the majority of electrical and optical circuits are founded, as a result of its cost-efficiency, thermal conductivity and abundance.^[41] Ergo, the combination of direct bandgap III-V semiconductors with the mature Si platform has been considered vital for the realization of on-chip light sources and other devices as well as for the fabrication of state-of-the-arts photonic circuits. Nevertheless, until recently the large lattice mismatch of group III-V semiconductors with Si impeded their efficient on-chip integration. This is because the large amount of strain that is formed causes issues including the formation of threading dislocations that penetrate the III-V material and jeopardize the device performance.^[5] The aforementioned challenge, however, can be effectively addressed by adopting the NW geometry, which allows for the monolithic integration of III-V semiconductors on Si substrates.^[42] A characteristic example of a NW array monolithically grown on Si is depicted in the SEM images of Fig. 1.1.^[43]

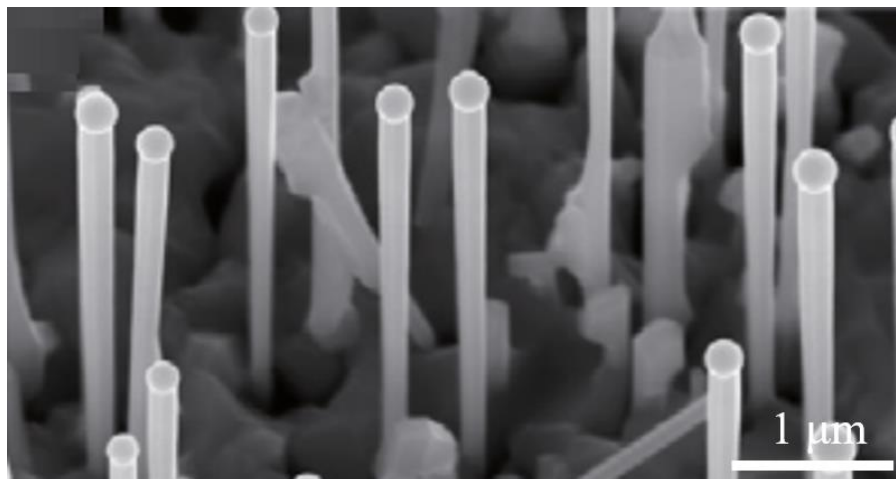


Figure 1.1: SEM image with 30° tilting of a GaAs NW array monolithically grown on Si, where the majority of the structures are grown perpendicularly on the substrate wafer.^[43]

A peculiar category of NWs that presents a wide interest over the potential they have in future applications is ternary structures, which are composed of an alloy of two group III and one group V or two group V and one group III elements. The basic benefit of adopting such an intriguing material combination is the fully tuneable bandgap that can be controlled via modifying the elemental content within the alloy. Thus, an additional degree of freedom in the structural design of NWs is enabled, whilst the implementation of such nanostructures in device applications is accelerated.^[44]

The main factor to control the composition of a ternary alloy is the growth parameters. It is already well-known that parameters such as the temperature, elemental flux and V/III ratio are fundamental to the properties of the resulting NWs. The flexibility in determining the growth parameters has led to tremendous accomplishments in the realization of ternary NWs with fully tuneable bandgap, which have been applied in energy harvesting devices such as solar cells^[45-46] and even the more challenging water-splitting devices.^[47] Furthermore, ternary NWs have been effectively used for the fabrication of light-emitting devices, namely lasers^[48-49] and LEDs^[50-51] with emission that can be tuned over a broad range of the spectrum depending on the composition of the alloy. The tunability of the bandgap has also been important for the development of ternary III-V NW-based photodetectors with good performance.^[52-53] Finally, the high carrier mobility that is observed in ternary III-V alloys is regarded as ideal for the realization of well-functioning high-speed FETs.^[54-55]

Additionally, a significant advantage of ternary NWs is the improved material quality that they can achieve. The enhanced material quality is an important factor to be taken into account in nanoscale structures, as formed defects can have a severe impact on the optoelectronic properties of the NWs, hence jeopardizing the functionality or

efficiency of the fabricated devices. For instance, it has been proven that defects or the presence of mixed zinc blende (ZB)/wurtzite (WZ) structural phase can influence the band structure of NWs and alter their electronic properties.^[56-57] Moreover, defects can act as non-radiative recombination centres, which drastically reduce the intensity of the emission deriving from the NWs.^[58-59] On the contrary, the introduction of specific elements in binary alloys can stabilize the phase and improve the material quality of the crystal. A characteristic example is Sb, the presence of which promotes pure ZB formation due to its surfactant properties.^[60]

Furthermore, due to the advanced growth and fabrication techniques, several novel ternary III-V alloys have been exploited as material platforms with the assist of NW formation. The structures exhibited good properties. Additionally, because of the effective strain relaxation, the material quality of these NWs is higher when compared to conventional structures. Characteristic examples of these novel, ternary III-V alloys are InGaSb,^[61] InPSb,^[62] GaPSb^[63] and AlInP,^[64] that demonstrate promising features for various devices, such as efficient LEDs and lasers. It is important to mention that most of these structures has been grown only on III-V substrates, while reports on these platforms have been extremely limited, rendering the aforementioned alloys rare in the existing literature, potentially due to the difficulties associated with their growth. However, if future works achieve effective transfer of these NWs on Si substrates, it would be a significant accomplishment towards their efficient implementation in on-chip applications.

1.1.2) Introduction to Nanowire Quantum Dots

One of the most widely employed nanoscale structures for various applications is the 0D quantum dot (QD), where the carriers are confined in all three dimensions. Due

to the low dimensions of QDs, the quantum confinement effect is pronounced enabling the use of these structures for novel applications, including telecommunications, quantum information processing^[65-66] and quantum key distribution.^[67-68] The most common growth mode for QD growth has been the Stranski-Krastanov (SK) method. SK growth is a powerful tool for the realization of QDs of high quality and good properties. The procedure is driven by strain, stemming from the lattice mismatch in materials forming matrix and QDs. During the initial steps of the growth, a 2D layer is formed. This is similar to the Frank-Van der Merwe growth mode, where a layer-by-layer formation is presented. Nevertheless, there are stark contrasts, since in Frank-Van der Merwe growth, the adatoms attach to surface sites in order to form layer-by-layer sequence. On the contrary, in SK growth mode after the layer reaches a critical thickness, it becomes energetically favourable for 3D islands to nucleate rather than the layer growth. This step allows for effective release of the strain energy.^[69-70] The accomplishments regarding SK growth mode have been astonishing and QDs grown via this method are the basis for applications such as solar cells,^[71-72] lasers,^[73] photon emitters^[74] and planar LEDs.^[75]

However, the advances of SK QDs have been marred by two major disadvantages that hinder their applicability in a wide scale. These are the relatively weak control over the position and over the uniformity of the dots stemming from the roughness of the surface. Notably, the fact that the procedure is strain-driven renders control of the position and size of the dot particularly challenging. Hence, new alternative routes regarding QD fabrication are imperative. A novel and promising method regarding this subject is the embedment of QDs inside NWs, forming the so-called nanowire quantum dots (NWQDs). The resulting structures lead to extended freedom in the choice of materials combined. The strain relaxes elastically, thus no severe

dislocations are introduced, signifying those materials can be combined ideally with no restrictions in terms of their lattice mismatch or their thickness. The basic requirement for the QD to be formed is to stack a narrower bandgap material axially during NW elongation, most frequently via controlling the elemental supply in the growth reactor, thus controlling the position and composition of the dots.^[76] The colossal achievements of SK QDs and the advantages of NWQDs such as the deterministic dot position, controllable dot size, large strain tolerance and high light extraction efficiency induced by the NW geometry, have triggered great interest over NWQDs which have been employed for numerous devices, such as single photon emitters,^[77-81] LEDs^[82-84] and single electron transistors.^[85-86] Recently, the first optically pumped NWQD laser, fully functioning at room temperature, has been presented.^[87] An example of a NWQD schematics is provided in Fig. 1.2 below, based on the work by Wu et al., who developed GaAs QDs embedded in ternary GaAsP NWs.^[88]

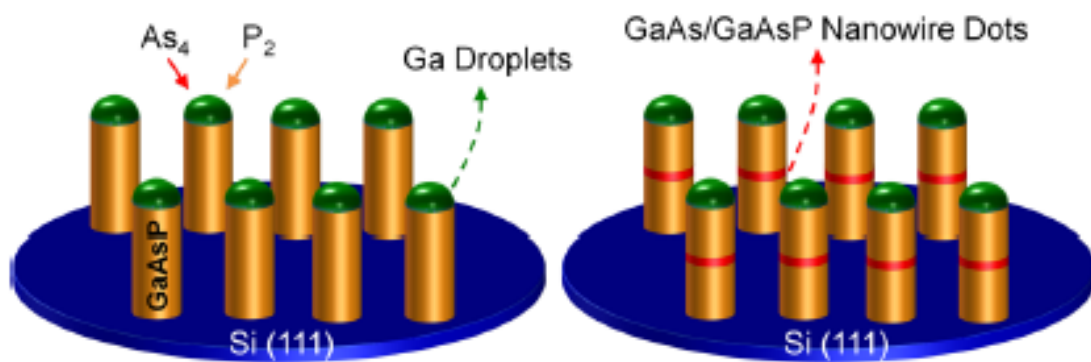


Figure 1.2: Schematic representation of the GaAsP/GaAs NWQDs. The red wafer in the middle illustrates the QD region, which induces 3D confinement of the carriers.^[88]

After having described the basic information and background research on the NWs and NWQDs it is important to separately discuss a significant difference between

these structures and bulk materials, which is the crystal phase. This topic will be the focal point of the following section.

1.1.3) Crystal structure: Zinc Blende and Wurtzite Phase

It is known that, whilst group III-V materials are merely crystallized into the ZB phase, this is not the case for NW structures, which can adopt either the ZB or the WZ crystal structure. The former is characterized by a cubic shaped atomic arrangement within the unit cell. On the contrary, WZ crystallization entails the formation of a hexagonally shaped atomic arrangement of the unit cell. This differentiation leads to fundamental changes in the electronic properties and optical behaviour of the structures, which open the route for novel functionalities. It has been suggested that there is a critical value of diameter for the NW structure, below which it is substantially more likely for WZ crystallization to occur.^[89] In order to interpret this NW peculiarity, one of the growth mechanisms of such structures has been employed. As will be described later in the current thesis, one of the methods of NW growth is based on nucleation of a monolayer occurring at the interface between a liquid catalyst droplet and the solid material, which comprise the NW. Based on the above, if the nucleus is formed fully surrounded by the liquid droplet and laterally expanding from there, ZB formation is favoured.^[104] However, nucleation often occurs at the edge of the liquid droplet, signifying that the nucleus is partly in contact with the vapor. This is nucleation at the triple line and in some of these cases WZ formation is favoured.^[104] For this to be the case, one condition to be met is a high level of supersaturation while the second condition is that the interface energy for the WZ layer is smaller than the corresponding for ZB layer. This has been found to be related to the elemental supply.^[104] Consequently, as a result of their growth mechanism NWs can adopt either ZB or WZ phase, while in several cases the two phases can coexist in the same crystal since the

NW is comprised after the formation of multiple monolayers at the liquid/solid interface, each of which could adopt an orientation leading to one of the two different crystal structures.

Schematic illustrations presenting models of ZB and WZ crystal phases are shown in Figs. 1.3a-b, respectively.^[90] As mentioned above, NWs can frequently be crystallized into a mixed ZB/WZ phase, where the two structures coexist within the crystal. This is called polytypism and the schematics of such a crystallization is presented in Fig. 1.3c.^[91] As a result, scientific research has also focused on the controllable tuning of the crystal phase in a single NW structure.^[90-92] Characteristically, it has been inferred that at small diameters, the NWs are more likely to adopt a WZ phase, whilst a gradual transition to ZB crystallization is noticed with increasing NW diameter.^[92] It should also be noted that the NW tip is frequently tailored to adopt a tapered shape. The angle that this tapering forms at the NW tip has a direct relation with the crystal phase that will be adopted. Specifically, it has been proposed that, as the WZ segment facets are vertical to the substrate and the ZB facets can form an angle, the tilting contributes to the irregular, tapered NW shape.^[90] Hence, the ratio of the WZ/ZB segments of a polytypic structure can be indicative of the tapering angle at the NW tip.^[90]

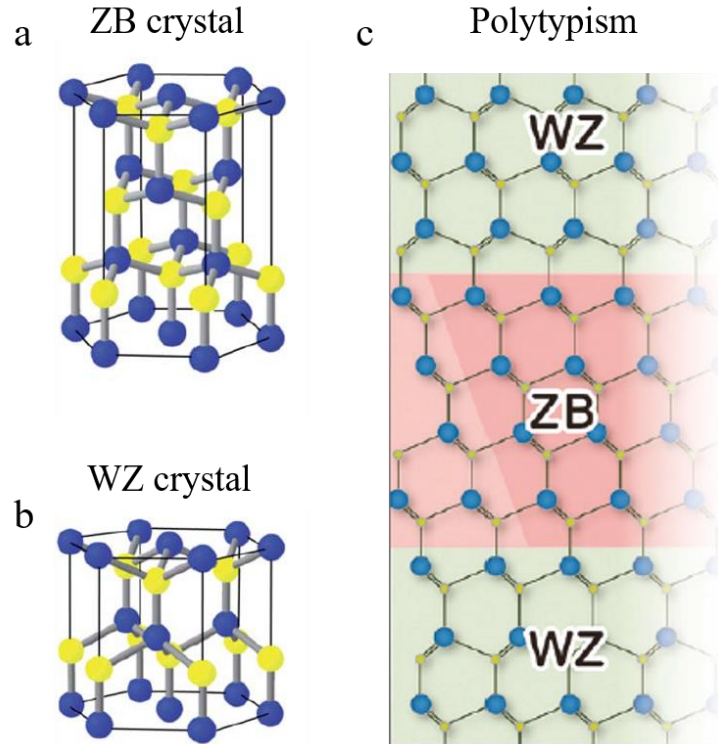


Figure 1.3: a-b) 3D schematic models of a ZB and a WZ crystal, respectively.^[90] c) Schematic representation of the atomic arrangement in a polytypic crystal with mixed WZ/ZB phases being shown.^[91]

The most profound influence of the crystal phase is the impact it has on the NW electronic properties.^[92-94] The origin of this impact has not been exhaustively proven yet but different mechanisms have been suggested. The most dominant interpretation is the differences that appear in the bandgap of the semiconductors under different crystal phase. For instance, variations of the band alignment lead to alterations in the electronic properties and the emission wavelength of the NWs.^[95-97] Especially in the case of polytypic NWs, the most frequently observed case is the formation of a type II (staggered) band alignment, with the electrons in the ZB segments and the holes in the WZ segments. It is noted that this phenomenon can be uplifted when the NW diameter becomes very narrow.^[98] That is because the stronger quantum confinement effect makes the energy level of the valence band minimum in the WZ segments drop

faster than that of the ZB segments, placing both electrons and holes in the ZB regions.^[98] It is also important to point out that in the majority of the cases the bandgap energy of WZ crystals is effectively larger than the one observed in ZB structures, hence directly influencing the conductivity and functionality of the NWs.^[99-100]

Besides, other differentiations can be presented as a function of the crystal phase. For example, it has been concluded that elements adopt different segregation energies for ZB and WZ phase surfaces.^[101-108] Hence, different compositions can be potentially presented in WZ and ZB phase sections despite the identical conditions of the nucleation during the growth of nanostructures.^[105] The crystal phase and the nucleation are also strongly linked,^[105-108] as different compositions can be adopted.

The connection between composition, nucleation and crystal phase has led to important advances in synthesis of novel nanostructures. For instance, segregation of Al at the vertices of the hexagonal AlGaAs shell of 1D NWs caused the formation of self-assembled quantum dot-like emitters, without the need of further processing steps, rendering the procedure cost-effective.^[109] Furthermore, in our work Ga segregation was noticed in ZB regions of AlGaAs NW branches. This phase segregation is driven by the nucleation energy and may provide an alternative route for obtaining non-classical light-emitters.^[110]

It is significant to underline that, while threading dislocations are not formed due to the elastic strain relaxation in NW structures, there are other types of crystal defects that are frequently observed. The most typically noticed defects are stacking faults and twins. Stacking faults are planar defects which derive from an error occurring in the pattern of the sequence of atoms. They are most usually formed during crystal growth. Taking the cubic crystal structures as an example, there are three types of

layers that are formed, labelled A, B and C. The atoms in the fourth, fifth and sixth layer are directly above the first, second and third layer, respectively. Hence, the stacking sequence in a defect-free crystal in this example would be ABCABCABC. Nevertheless, a stacking fault causes a misplacement of one of the layers that alter this sequence. The characteristic of stacking faults is that they only extend from one to three-layer deviations. For instance, the sequence could take the form of ABCAB**AB**CA, where the highlighted part is the stacking fault. The second type of frequently observed defects are twins, occurring when two crystals share some lattice points. The twinning is extended leading to an alteration of the entire layer sequence after the appearance of the original error. For instance, the sequence ABCABCABC would take the form ABC**ACBACB**, where the twinning occurs at the highlighted part. The defects are not stationary but present a dynamic nature with their movement usually being thermally activated.^[111]

The above information on the polytypic nature and defects in a NW crystal play an important role in the structural characterization of NWs, NWQDs and nanosheets and have been an investigated subject in the experimental part of the current thesis.

1.1.4) Device Applications

As described in the previous sections, the unique properties and morphology of NWs and NWQDs enable their implementation in a wide range of functional optoelectronic devices, such as lasers, solar cells, photodetectors, and FETs. NWQDs are also good candidates for single photon emission, a function that is crucial for quantum information processing applications.

Regarding the implementation of III-V nanostructures for laser fabrication, the key factor is the morphology of the NW, which has a 1D nature, low radial dimensions,

small footprint and allows for the carriers to propagate along its axis. The above indicate that generated light can be guided to one of the ending facets of the NW from where it can be collected for further measurements or processing after its coupling with one of the fundamental modes of free space. Light amplification is achieved via the light being reflected from the ending facets and passing through the gain medium. From the above, it can be seen that the necessary optical cavity that is required to obtain stimulated emission is intrinsically formed as a result of the NW geometry. Group III-V semiconductors are ideal candidates for lasers. One of the advantages of NWs regarding device performance is the circumvention of threading dislocations that renders growth and device fabrication highly straightforward, as thoroughly explained earlier. Furthermore, the refractive index of III-V semiconductor NWs is intrinsically high, which is an important aspect for laser fabrication. It is also beneficial that the cavity is obtained without the need for any costly or sophisticated technique, thus greatly simplifying the fabrication procedure.

The combination of GaAs/AlGaAs core/shell architecture and its implementation in nanowire laser fabrication has been systematically reported in literature due to the interest caused by the negligible lattice mismatch of the two materials. GaAs/AlGaAs NW lasers have demonstrated good performance at RT.^[18] Such lasers have shown characteristic temperatures of 109 K.^[112] GaAs/AlGaAs core/shell NWs containing InGaAs QDs have also been employed for lasing applications.^[87,113] These structures have exhibited lasing at the near-infrared region, with a threshold of 179 $\mu\text{J}/\text{cm}^2$ having been reported.^[87] It is noted that tuning the size of the dots, which can be easily controlled, directly modulates the wavelength of lasing emission. Moreover, GaAsSb and InGaAs have been utilized for laser realization.^[114-115] The exploitation of ternary

alloys presents the benefit of efficient tunability of the emission wavelength by controlling their composition.

Another important application is the realization of solar cells. Solar energy is one of the most promising and attractive renewable energy sources as it is abundant and environmentally friendly. Hence, its conversion into electric energy is one of the fields at the frontier of scientific research. Solar cells are units that conduct this conversion, where light is absorbed by the active material that is employed and as a result electron-hole pairs are generated. These pairs are separated as a result of the built-in electric field. Eventually, current is generated inside the p-n junction, which is essential in such applications.

Thin film-based solar cells have already been employed for high-efficiency solar cells, while NWs seem an intriguing architecture for such a function. It is important to clarify that even though thin film-based solar cells have achieved a high efficiency, the efficiency of NW-based devices has been significantly lower, reaching 18%.^[116] This is a direct result of the enhanced recombination rate that is inherent in NWs. Nevertheless, significant progress is being made by ongoing research. This increased interest is based on the advantageous properties of III-V semiconductor NWs which make them attractive for solar cell fabrication and render imperative the need to overcome challenges related to the growth and properties of NWs.

Among the properties that are promising for solar cells, the 1D NW nature along with the high surface-to-volume ratio can significantly increase light absorption. Another significant advantage is that while light absorption occurs along the axial direction of the NW, which is typically in the microscale, carrier separation occurs at the radial dimensions, typically in the nanoscale.^[117] As a result, the range of the

materials that can be employed is significantly widened, while demands in terms of material quality are less stringent, although high-quality materials are anticipated to exhibit a better performance. The high surface-to-volume ratio ensures the large surface area that is needed in solar cell fabrication, while the pathway for the carriers is long, considering that the NW axis is much longer compared to the radial dimensions. It is interesting to mention that 3D branched NWs demonstrate an increased surface area and longer pathways for the carriers, which are strongly suggesting that their implementation in energy harvesting applications is effective. More details on this vibrant topic will be discussed later in the current chapter.

Particularly, ternary NWs, with a high level of bandgap tunability, are crucial as the bandgap needs to be small enough to absorb a broad range of the solar spectrum.^[47] Usually, the radial p-i-n junction that is required for the energy conversion is achieved by opposite doping of the NW core and shell.^[118] For instance, solar cells based on GaAsP NWs have been effectively fabricated with an efficiency exceeding 10% due to successful InGaAs surface passivation.^[119] On the other hand, InGaAs NWs have also been used for solar cell realization, where a most interesting report shows that after the growth of an InAlAs shell, the short circuit current increases from 4.3 to 10 $\mu\text{A}/\text{cm}^2$, while the I-V curves show a lack of S-shape behaviour that highlights the lack of losses and accentuates their device performance.^[45]

Besides, NW-based photodetectors have been reported in the recent past. Photodetectors are light sensing devices that perform the conversion of the incident light into current. III-V NWs have excellent potential for such devices due to their advanced optoelectronic properties. Among the different III-V alloys that have been employed for photodetector fabrication, the most important are antimonides, as they enable detection of near-infrared or mid-infrared light. Ternary III-V antimonides are

particularly attractive due to the easy bandgap modulation. For instance, GaAsSb NWs have been frequently employed for near-infrared light detection, presenting rectifying behaviour of the I-V curve.^[52,120] The asymmetric Schottky contacts are formed as a result of the inhomogeneous Sb distribution and the Sb-related defects.^[120] Good results have also been reported for InAsSb NW-based photodetectors with a remarkably low dark current and facilitated fabrication and on-chip integration.^[121] Finally, the development of an AlGaAs shell for surface passivation also led to realization of ensemble NW photodetectors.^[53]

Moreover, another important contribution of NWs in device implementation is the fabrication of FETs. This topic has gained vast attention due to the high carrier mobility of III-V semiconductors combined with the prevalent role of FETs in electronics. Most notably, the aforementioned monolithic integration of III-V materials with the mature Si platform that is the basis for electronic circuits has been a focal point of research. Among the III-V semiconductors, InGaAs is an attractive ternary alloy for FET fabrication, owing to the high carrier mobility. Hence, FETs has been fabricated based on InGaAs NWs after the appropriate metal contact realization,^[55,122-123] demonstrating n-type conductivity. Moreover, InAsSb NWs have been investigated for FET applicability.^[60] These devices display remarkably low resistivity due to the enhanced electron mobility upon Sb incorporation,^[60] much higher when compared to pure InAs NWs.

Eventually, a prominent role of NWQD structures is their use for single photon emission, which is a vital requirement for quantum computing applications. Specifically, quantum information processing is a concept in which the superposition states of photons are employed in order to transmit the information with enhanced security. The vital difference between classical computing applications and quantum

information processing is that while bits can take discrete values, quantum information bits (qubits) exploit any superposition state. This technology is very promising for a variety of practical applications, with quantum cryptography being the most notable example. The main issues that arise with respect to the wide-scale implementation of quantum computing are technical and relate to the qubit properties. For instance, qubits should be high in number, easy to read once the information reaches the terminal, while the cost and maintenance of the devices should be kept low. NWQDs could address some of the aforementioned challenges, as a result of their potential for single photon emission, where the polarization of the photon will be the quantum information that is transmitted.

Single photon emission is the ability of the NWQDs to emit a single photon per excitation unit. The importance of single photon sources lies in the high brightness and interconnectivity of the emitted photons.^[124] What is more, the photons need to be highly indistinguishable, which means that they must have the same wavelength, polarization, space and time. Photons emitted by NWQDs can meet the aforementioned criteria. In order to ascertain single photon generation, the second order correlation function at zero-time delay ($g^2(0)$) is typically measured. This value gives the possibility of a second photon being emitted simultaneously. In principle, it should be kept at low levels, ideally around 0.^[125] In real-time applications and experiments the criterion to characterize a nanostructure as single photon source is for $g^2(0)$ to be lower than 50%. Although this method provides confirmation of single photon generation, there are strong indications in PL spectra that can be acquired, such as the sharp and narrow peak, as single photon sources are more likely to exhibit linewidths in the low microscale, or polarization measurements. All of the above are properties that have been exhibited in QDs in the past, with excellent results having

been reported.^[126-129] For example, GaN QDs have led to $g^2(0)$ of 2%, thus exhibiting excellent antibunching behaviour.^[127] It is important to point out that NWs do not inherently act as single photon sources as their emission is frequently characterized by broadening usually stemming from alloy fluctuations. On the other hand, stacking single QDs axially in the NWs leads to 3D carrier confinement in the dot region and the potential of obtaining single photon emission is vastly increased, especially considering the natural photon antibunching behaviour of QD structures.

Single photon sources have been accomplished in the past via III-V NWQDs. For example, single crystal phase GaAs QDs embedded in GaAs/AlGaAs core/shell NWs have presented a second order correlation function of 51%.^[130] Even though this value is marginally higher than the 50% limit for single photon characterization, it shows the trend of these NWQDs to exhibit antibunching behaviour, which means that potential improvements on the crystal quality could lead to further reduction of $g^2(0)$. Single GaAs QDs embedded in Au-catalysed AlGaAs NWs have shown excellent characteristics with a narrow linewidth of 30 μeV and $g^2(0)$ of 19%.^[131] Moreover, GaAsP/GaAs NWQDs have been studied with respect to this function. The results show a value of $g^2(0)$ below 50%, which were further improved upon surface passivation.^[88]

The above practical applications reveal the importance of the examined III-V structures and explain the excessive research that has been devoted to their growth, development and characterization. Different growth techniques have been adopted in the past years. This topic will be thoroughly described and analysed in the following section of the thesis.

1.2) Growth Methods

1.2.1) Top-down and bottom-up approaches

NWs and NWQDs can be realized via the top-down approach. During this technique, the 1D NWs are etched down from bulk materials after they are coated with a mask.^[132] The main peculiarity of top-down method is the extensive use of lithography techniques and the employment of either a liquid solution or dry etching. The problem that arises is related to the quality of the structures, which can be significantly degraded due to surface roughening during the etching steps. Moreover, the top-down etched NWs usually exhibit a high proportion of crystal defects owing to the standard epitaxial growth, including threading dislocations on Si, as the fabrication is conducted in already-grown bulk material. Nevertheless, this method is still under investigation and can be considered beneficial as it is compatible with the current thin film fabrication technique.

Despite the issues related to the high cost of this method and the potential introduction of threading dislocations, top-down approach is still considered a powerful tool for NW development, as novel methods can be formulated and adopted aiming to its improvement. A prototypical example of such a technique is the top-down fabrication of tapered NWs.^[133] The tapering angle at the NW tip allows for significantly enhanced light collection efficiency, as it improves the coupling of the transmitted emission to one of the modes of the space surrounding the NW.^[134-135] In the work cited here, the top-down tapered NWs were obtained via sacrificial gradual etching of a mask that is composed of Ti and Cr.^[133] This sacrificial etching leads to the NW surface being exposed in steps, creating a tapered profile on the NW tip. The procedure is elucidated in the following figure (Fig. 1.4).

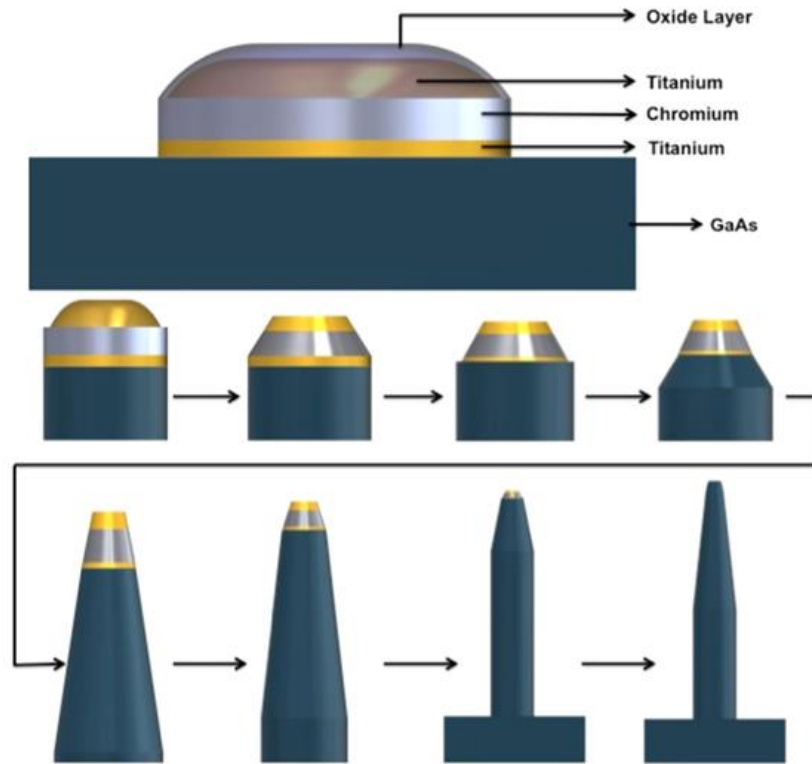


Figure 1.4: Top-down fabricated tapered NWs via sacrificial etching of a Ti- and Cr-based mask. This procedure leads to the realization of a tapering angle in the NW tip.^[133]

Regarding dot-in-wire structures, successful growth has been accomplished in the past by the top-down approach. The disadvantages that were mentioned earlier render it less favourable when compared to other fabrication techniques. Nevertheless, NWQDs that display good properties have been reported via this method over the past years.^[78,136-137]

The second approach that is widely used is the bottom-up approach that exploits epitaxial methods such as Metal-Organic Vapor Phase Epitaxy (MOVPE) or Metal-Organic Chemical Vapor Deposition (MOCVD), Chemical Vapor Deposition (CVD), Chemical Beam Epitaxy (CBE) and Molecular Beam Epitaxy (MBE). It is noted that for our experiments we used MBE, while due to the popularity and significance of CVD

and MOCVD a comparison is provided in chapter 2 of the current thesis, where MBE growth and facilities are described. The NWs are grown monolithically on the substrate. The first method belong to this category is selective area growth (SAG). The NW growth occurs through holes that are patterned on the substrate via the use of a mask and lithography techniques.^[138] The most profound advantage of this technique is the high level of uniformity with respect to the NW position and the size distribution, leading to the formation of highly homogeneous NW arrays.^[139] The basic underlying principles for SAG are similar to the ones for thin film epitaxy. Nevertheless, the patterned pitch that is used suppresses growth in the lateral dimensions, allowing only for perpendicular elongation of the NWs, even though parasitic growth may occur. It is significant to mention that one of the greatest issues related to the wide-scale implementation of this technique is the limited understanding to the processes and parameters that affect the selectivity during material growth. This has been a topic of scientific interest over the past years.^[140] Despite this challenge, the high level of uniformity acquired via SAG has led to the successful growth of NW arrays, exploited for devices such as the surround-gated FETs^[141] and LEDs.^[142-143]

Regarding bottom-up approach of NWs via the SAG method, several examples of successful NW realization can be found. For instance, InGaAs nanopillars have been grown on silicon-on-insulator (SOI) substrates with good potential for nanolaser fabrication.^[144-146] Moreover, highly homogeneous arrays of AlInP,^[64] InGaP,^[147] and InGaAs.^[148] have been successfully realized. Despite the advantage of the good uniformity, which as stated earlier can be advantageous for device implementation, literature on SAG is substantially less when compared to VLS growth. This is mainly attributed to the limited comprehension of the processes that regulate the growth

mechanism.^[140] This issue has been researched in order to broaden the understanding of this valuable technique.

One of the most popular methods that is used for the realization of NWs and NWQDs is the vapor-liquid-solid (VLS) growth. The growth is induced by a catalyst seed, which can be either a foreign metal (most usually Au) or an element that is also a NW component. Due to the importance of this method, it will be separately discussed in the following section.

1.2.2) Vapor-Liquid-Solid Growth Mode: Au-catalysed and Self-catalysed approaches

The potential material quality-related issues of the top-down fabrication method and the issues associated with SAG create the need for another alternative in NW growth. This can be addressed by the second subcategory of bottom-up approach which is the catalysed growth, where the NW elongation is achieved via catalyst droplets. The droplets can be either a foreign metal or an element that is already a NW component. The latter case is called self-catalysed growth mode. This globally accepted growth mechanism is called vapor-liquid-solid (VLS) growth mode. In VLS method, prior to the growth, nanoparticles are deposited on the surface of the substrate wafer. These particles are used as catalyst droplets for the growth process. The most common foreign metal that is used to compose the nanoparticles is Au. Next, thermal annealing where the temperature exceeds the melting point of the particles, ensures they transit into nanodroplets.^[5] Then the feeding material is supplied and the liquid metal droplet acts as the material collector. The gas phase molecules are absorbed by the catalyst, which becomes supersaturated and in order for the chemical balance to be restored, a layer of solid crystal is nucleated and grows in the liquid/solid interface.^[5] Nucleation

usually occurs in the triple-boundary line (TBL) followed by a lateral expansion of the nucleated island to form a monolayer covering the entire NW/droplet interface. Usually, that expanded area is predetermined by the size of the droplet and the interface between the liquid and the solid phases. It is interesting to mention that whilst nucleation at TBL is assumed, there are cases where nucleation occurs at different positions, owing to various parameters such as the contact angle between the liquid and the solid.^[5] This topic has also been a subject of great interest. The nucleation and expansion procedure continue until no more precursors are supplied in the system. The main reason for the choice of Au than other metals is its resistance to oxidation and its reproducible ability to grow various NWs. On the drawback, the use of Au often involves severe contamination of the system and NW materials. For instance, Au diffusion, which is commonly observed, can lead to the formation of deep-trap levels in the NW material, while Au clusters can be formed on the substrate.^[6] The above render the structures incompatible with CMOS technology applications.^[149] Despite these issues, the Au-catalysed approach is widely adopted, for the growth of NWs.

It is interesting to mention that even though Au is the chosen material for the metal seed in the overwhelming majority of the cases, other materials can also be used. For instance, an interesting case is the use of Ag as catalysts for the growth of InGaAs NWs on Si substrates with good results having been reported.^[150] Other examples of metals that have been used in the past include Sn for the growth of GaSb NWs^[151] and Ni for InAs NWs.^[152] However, the use of metals other than Au for this type of growth are far from being fully comprehended. As mentioned earlier, the use of Au can cause problems related to contamination of the nanostructures that renders them incompatible with CMOS electronics. Nevertheless, the use of Au as catalyst has led

to triumphs over the realization of NW structures^[153-158] with excellent progress having been achieved.

The case of self-catalysed growth is fundamentally similar to the metal-assisted growth. However, the element of which the liquid droplet consists of a component of the NW itself. For instance, in III-V NW growth the droplet is a group III element with Ga and In as the most usual cases.^[159-162] The choice of these elements is based on their low melting points, which allows them to easily promote VLS growth under the appropriate conditions. That way contamination is avoided. The nucleation of the monolayer covering the liquid/solid interface occurs in the same manner as in the case of Au-catalysed growth.^[163] A characteristic schematic representation of the VLS growth mechanism for the growth of 1D NW structures is presented in Fig. 1.5 below.^[6] In addition, numerous reports have been published on the exploitation of self-catalysed approach as the method for ternary NW realization.^[2,47,160,164-166] The growth of III-III-V alloys is far more demanding when compared to III-V-V alloys, owing to the high solubility of group III atoms in the droplet, in both VLS approaches. This leads to any alterations between group III elements having a strong impact on the chemical consistency of the droplet. This is the reason why the reports on III-III-V alloys in literature remains considerably more limited when compared to III-V-V alloys.

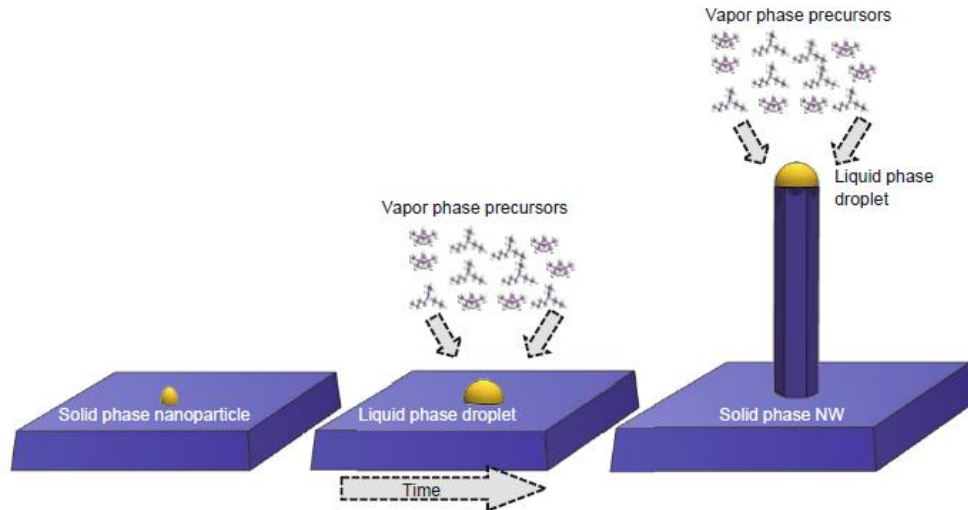


Figure 1.5: Schematic representation of the VLS growth mechanism for NW formation.^[6]

In comparison, embedding the QDs in NWs via the bottom-up approach can be achieved regardless of the growth mode, by merely stacking a narrower bandgap material axially within the NW. This can be done by carefully controlling the supply of the feeding materials during the NW elongation. The interfaces between the dot and the NW should be kept as abrupt as possible. The carriers are confined in the narrower bandgap region that acts as a QD, which results in radiative recombination usually occurring in that particular segment.^[167] The emission is later guided by the NW, which acts as a waveguide, to one of its ending facets. From there it can be collected for further measurements or processing, after being coupled with one of the fundamental modes of free space.^[168] Taking III-V NWs as an example, the change from material A to material B can be conducted either by altering a group III element^[169-170] or a group V element.^[171]

III-V NWQD structures have been obtained by the use of Au as a catalyst, with satisfying results.^[172-173] However, as mentioned in the previous section, the contamination induced by the Au nanoparticles acting as catalyst seeds along with the

major difficulties in post-growth removal of the droplets are the main hazards for the successful applicability and functionality of the structures developed by this method. On the other hand, self-catalysed growth mode has been performed in numerous cases to embed 0D dots in 1D NWs.^[88,174-175] The procedure of NWQD growth is similar to the growth of a pure NW ensemble. More specifically, the group III droplet acts as a collector for the precursors, and in order for a narrower bandgap material to be embedded, the supply of elements in the reactor needs to be modified either by stopping or by introducing an element. In some cases, the lack of an element causes a chemical imbalance. Thus, for compensation, the supply of other elements is appropriately tuned as well. This does not require any growth interruption, as this could lead to roughening of the QD/NW interfaces, that in principle need to be maintained as sharp as possible. For example, when growing GaAs QDs in the axis of GaAsP NWs, the QD is formed by stopping the supply of phosphorus. Meanwhile, in order to compensate for the lack of phosphorus during the QD growth, the pressure of arsenic is correspondingly adjusted.^[88] That way the chemical balance is sustained at a suitable level throughout the entire growth. It is highlighted that since the catalyst droplet is a group III element acting as both collector and supplier, altering group III fluxes while ensuring the stability of the growth procedure is far more challenging in self-catalysed growth. This is attributed to the fact that the component that forms the droplet needs to be replaced.^[76] On the contrary, group V elements are expected to leave the droplet almost unaffected due to their low solubility in the group III droplet.^[76]

A special mention should be paid to the reservoir effect, a phenomenon that is observed during the VLS growth of NWs and NWQDs and can degrade the abruptness of the interface between the different NW regions in NW heterostructures or the NW and the QD in NWQDs. Ideally, these heterointerfaces need to be maintained sharp

in the atomic level. However, because some elements from the NW are not entirely consumed in the droplet, there may be contamination and element intermixing, which causes shallow interfaces. Moreover, the same phenomenon can be exhibited since a portion of the adatom contribution may derive from diffusion over the substrate on the NW sidewalls and not from the direct impingement on the droplet.^[176] The reservoir effect is presented in both Au-catalysed and self-catalysed approaches of VLS growth mode. It is noted however that the intrinsic properties of group V adatoms allow for sharper interfaces and circumvention of the reservoir effect, due to the low group V solubility in Au or in the group III droplet.^[76] So a potential alternative to avoid this issue would be to alter only group V elements instead of group III.^[177]

After having described the aforementioned growth methods and cited relevant literature works, it is significant to pay special attention to the strain that can be developed in NW structures. It was explicitly mentioned in the previous sections of the thesis that one of the most dominant peculiarities of NW structures is the lack of strain due to the elastic relaxation occurring along the sidewall facets.^[5-6] Some misfit dislocations may appear at the NW/substrate interface,^[178-180] but the small footprint of the structure does not leave room for the development of the destructive threading dislocations that are a main issue in growth that involves buffer layers (i.e. GaAs on Si).

An architecture regularly employed in ternary NWs is the core/shell configuration. The growth of a shell surrounding the NW core exhibits significant advantages, the most prominent of which is surface passivation which reduces non-radiative recombination traps. Moreover, it protects the core from oxidation.^[181-182] Additionally, alloy fluctuations in the shell have been exploited as a novel tool for the formation of self-assembled QDs in this part of the structure that opens new routes in NWQD

fabrication.^[109] However, the strain that is induced by the lattice mismatch between the core and the shell leads to the formation of dislocations and defects at the core/shell interface, as it is inelastically relaxed.^[183-184] This can have a serious influence on the morphology of the NWs, causing occasional bending or kinking. Two types of strain may be developed this way: tensile strain and compressive strain. It is noted that examples of lopsided shells causing severe NW bending to have been reported for tensile-strained NWs.^[185-186] This is well-illustrated in Figures 1.6a-b. The reports on compressively strained NWs are more limited and mostly focus on binary alloys.^[187]

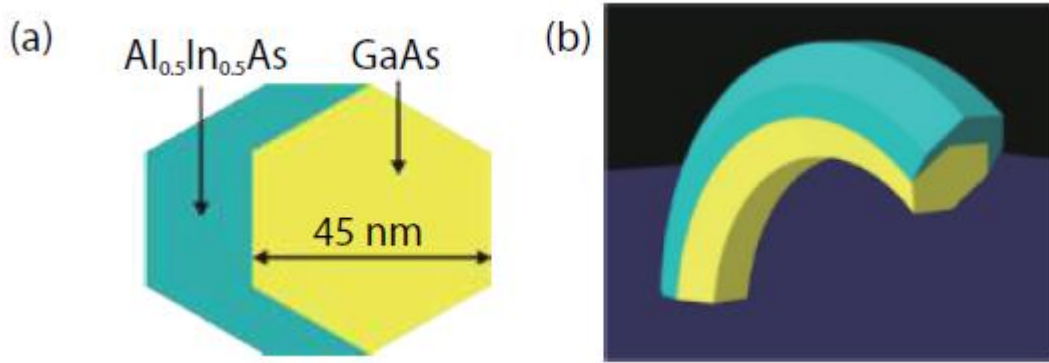


Figure 1.6: a-b) Top-view and front-view, respectively, of schematic representations for a GaAs NW cladded with an AlInAs shell. The strain between the core and the shell causes significant NW bending.^[186]

Following the description of the basic properties and growth methods of NWs and NWQDs, we will focus on a peculiar type of 3D NWs that has arisen as a popular candidate for energy-related applications, called the branched NWs. This will be analysed in the next section.

1.3) Branched Nanowires: A Unique Type of Three-Dimensional Nanowires

Based on the information analysed in the previous sections of the current thesis, it is conspicuously concluded that NWs and NWQDs are rendered particularly attractive and promising for large scale fabrication of on-chip, financially accessible devices in a wide range of scientific fields. However, the increasing demand for excellence in crystal quality and pioneering design of intricate structures with ameliorated performance poses an accelerating speed in the necessity for growth optimization and versatile nanostructures. Following these demands, a significant amount of efforts has been devoted to the growth of 3D NWs, composed of one standing part called backbone or ‘trunk’, which is decorated with single or multiple ‘branches’, forming tree-like structures. The resulting NWs are referred to as branched NWs and exhibit increased complexity and versatility in straightforwardly grown nanostructures.

The first report on branches nucleating on a NW trunk was created almost a decade ago.^[188] The ZnO NWs of that work presented three-dimensional expansion with stringent hierarchical features. Since then, research focused on the growth of such structures by adopting different techniques for the branch nucleation, including electrodeposition,^[189] sequential seeding,^[190] manipulation of strain^[191] or droplet confinement.^[192] The advantages of the branched NWs are the large surface area, elongated optical path and direct transport pathway for the carriers.^[193] These features render branched NWs ideal for energy harvesting application such as solar cells, supercapacitors and Li ion batteries.^[193] Furthermore, the reduced reflectivity that they exhibit causes a radical increase in light absorption.^[193] Branched NWs also have the potential of exhibiting enhanced luminescence.^[194]

Among the applications that can be realized via branched NWs, energy harvesting is one of the most prominent. As mentioned earlier, 1D standing NWs hold promise for implementation in solar energy conversion, due to light absorption occurring along the axial direction of the NW, while carrier separation occurs across the axis. Hence, there is flexibility as to the materials that can be employed.^[117] On this regard, 3D branched NWs pose a more versatile alternative due to several factors. First and foremost, the increased surface area increases light absorption as there is higher amount of the semiconductor material to absorb incident light. In addition, the path for the absorbed light is longer owing to the increased scattering.^[117,193]

Besides, the pathway for the carriers remains direct, which means that the branches can act as “terminals” to the NW backbone or trunk. Since the branches and the trunk are interconnected, carriers can be easily transported from one branch to another or to the trunk. The factors of the increased light absorption and collected carrier transport is vital for energy harvesting applications including solar cells and water splitting devices.^[117,195] Nevertheless, it is important to point out that a necessary condition for the facilitation of carrier transport is the high quality of the material and especially the branch/trunk interfaces, which ensures that the structure remains coherent and branches and trunk are interlinked.

The potential of 3D branched NWs for solar cell fabrication is pronounced considering the effect of the density of the NW array and the volume of the structure in the reduction of the reflectance and increase of the light absorption. For instance, even in Si NWs, the increase of the surface area owing to the forest-like morphology of the structures led to a reduced light reflectance within the range of 300-1100 nm and a broad external quantum efficiency of 12% at 690 nm.^[196] In addition, a report of InAs branches on InP NW trunks on black Si showed a reduced reflectance and

increased scattering which was dependent on the NW density.^[197] The reflectance was even lower after the addition of the InAs branches indicating that branched NWs can be effective in their use for solar cells.

The branches are grown on the backbone of the NWs epitaxially, signifying that the former fully adopt the crystal structure and orientation of the sidewall facets of the NW trunk. This property has been exploited to realize novel morphologies and configuration, with a prototypical example being the growth of antimonides in the WZ phase.^[198] It is noted that this has been a challenge due to the surfactant effect of Sb, which vastly promotes ZB crystal phase. Besides, QDs have been embedded in branched NWs, with intriguing results having been reported. Specifically, in the work by Ying Yu et al, QDs were inserted in the branch/trunk junction of GaAs/AlGaAs core/shell NWs. After optical probing, the structures exhibited narrow peaks, enhanced intensity of luminescence and exquisitely low second order correlation function, features that made them ideal for single photon emitting applications.^[199]

Representative paradigms of branched NWs are presented in Figures 1.7a-b. The NWs present multiple branching events adopting a versatile and highly intricate morphology. The specific structures were GaP NWs grown via MOVPE with the Au-assisted technique.^[190]

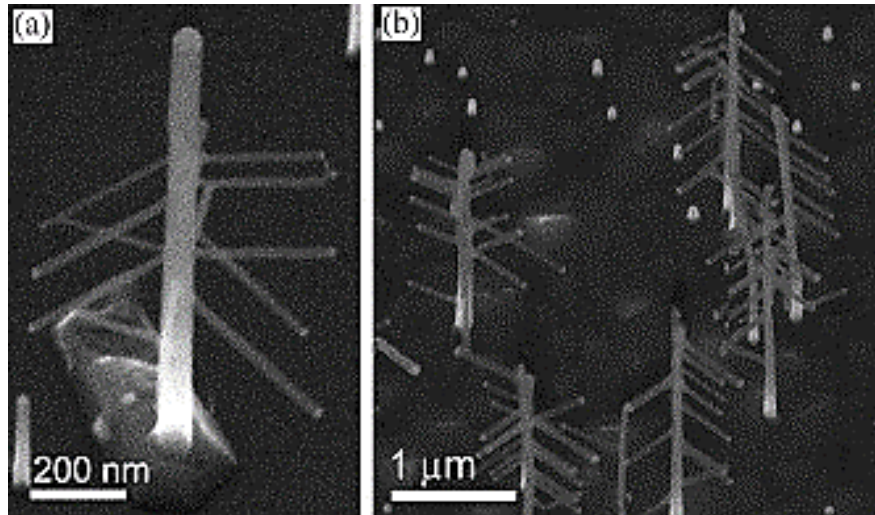


Figure 1.7: SEM of a) one branched NW and b) several NWs of the same sample. The number of branches that nucleated on the NW trunk exceeded 10 forming nanotrees.^[190]

1.4) III-V Nanosheets

Apart from the progress that has been made in the subject of NW structures, other types of nanostructures have also been investigated and inspected. One of the finest examples is the development of 2D materials in the nanoscale, which exhibit advantages because of the band gap tuning from bulk to 2D by adequate modulation of their thickness.^[200] Those materials are called nanosheets. An advantageous aspect of 2D materials is the lower contact resistance and channel resistances, which allows for photogenerated hole-pair separation and is favoured for FET fabrication. Another application for which these structures have been employed is optoelectronic memory units.^[201-202]

III-V nanosheets have been demonstrated in previous works by employing widely used binary alloys such as GaAs,^[203-205] InSb^[206-207] and InAs.^[200,208-209] The most popular method for the fabrication of high quality III-V nanosheets is SAG.^[203-205] Despite the importance of this technique, there are disadvantages involved that

require for a more straightforward and versatile alternative. One alternative that has been applied is the formation of III-V nanosheets directly from 1D NWs. For instance, a recent report describes the elemental segregation of an Ag-In alloy which was exploited for the realization of nanosheets of high structural quality and potential for light emission.^[200] The 2D nanosheets can be developed from 1D NW growth via adequately adjusting the growth parameters.

A crucial parameter that needs to be considered while realizing this type of nanostructures is the high density of surface states. This is a direct consequence of the large surface-to-volume ratio, as is the case for NWs. Surface states can have a powerful impact on the optical properties of the nanosheet-based devices as they act as carrier traps, which can potentially cause the appearance of the “memory effect”. One of the reasons that induce the “memory effect”, on which we will focus in chapter 6 of the current thesis, is the charging and discharging of the surface states, as photogenerated carriers are initially trapped (charging) and later recombine after subsequent excitations (discharging). It is significant to underline that the “memory effect” is not necessarily a negative phenomenon. On the contrary, it is crucial in order to achieve optoelectronic memory applications based on III-V nanosheet structures.^[210-211] However, under its influence, suppression of the light emission is easy to occur as non-radiative recombination processes take place at the surface states. Resultingly, the removal of surface states via surface passivation depends on the application for which the structures are intended and is another factor that needs to be taken into consideration while designing the III-V nanosheets.

After having introduced and described all the structures that were synthesised and studied within the frame of the current project, it is important to refer to beneficial and scientifically valuable previous works that were conducted both outside and in our

facilities at UCL, related to the subject of NWs and NWQDs. This discussion will be carried out in the next two sections of this chapter, respectively.

1.5) Previous works on nanowires, nanowire quantum dots and nanosheets outside UCL

The rich topic of nanoscale structure growth on Si substrates has been a focal point of extensive research over the past decades. As mentioned earlier, the issue of monolithic integration of III-V semiconductors on Si can be addressed via the employment of NW or nanosheet configuration. Hence, several works have been reported regarding the successful growth of such structures. Regarding NW structures, the most popular binary alloy that has been employed is GaAs owing to its ability to emit in the near infrared region of the spectrum rendering it ideal for light-emitting and detecting applications. The above have led to the successful realization of GaAs NWs based on several growth techniques, including self-catalysed VLS growth,^[212-214] metal-assisted VLS growth,^[156-157] and SAG.^[215] For instance, SAG has been employed for the fabrication of a GaAs array with varying thicknesses, where it has been established that thicker NWs tend to adopt WZ phase and thinner NWs are mostly ZB, which is in stark contrast with the experimental trends and observations. They attributed this phenomenon to unexpected surface diffusion of Ga which alters the contact angles of Ga atoms with the NWs.^[215] Moreover, study of self-catalysed GaAs NWs has shown that modification in V/III ratio during growth can alter the size of the droplet, hence the morphology and orientation of the NWs, which is useful for the formation of kinked or branched NWs that can be used in interconnected networks.^[214] Besides, contact angle between the droplet and the NW or substrate is also linked to the crystal phase, as very small or very large angles tend to cause ZB

crystallization.^[212] Recently, high-quality structures have been achieved with few if any crystal defects and controllable crystal phase via Be-doping.^[216]

On the other hand, the importance of ternary NWs has been underlined earlier in the current chapter, mostly owing to the bandgap tunability as a result of the alloy composition. As a result, numerous III-V ternary NWs have been synthesized using various growth methods. Among the most important alloys employed is GaAsP due to its large bandgap tunability between 1.43 eV and 2.24 eV at room temperature. The realization of such structures has been achieved via MOVPE^[217] and MBE.^[2,44] It has been shown that V/III ratio is the most vital factor for homogeneous NW growth.^[2] while the content of P is also important since for P percentages over 44% the bandgap becomes indirect.^[217] Moreover, via controlling the V/III ratio and the growth temperature, high-quality GaAsP NWs have been obtained, as reduced V/III ratio promotes ZB formation as opposed to polytypism for elevated values.^[218] This is particularly important, as twin defects have been established to modify the bandgap and alter the optical properties of the NWs.^[217] Another significant ternary alloy has been AlGaAs, which is also one of the material platforms we used for our experiments described in chapters 3-5. AlGaAs has a bandgap between 1.42 eV and 2.16 eV at room temperature. This means that its emission can be tuned in the red and near infrared regions of the spectrum, thus rendering it a good candidate for optoelectronic applications. AlGaAs NWs have been fabricated in the past via Au-catalysed VLS growth.^[219-223] It is underlined that the catalyst is the major difference with our self-catalysed VLS approach, as will be discussed extensively in chapter 3 of the thesis. Besides, AlGaAs has been used as shell surrounding GaAs core NWs, with these heterostructures exhibiting improved and high quality PL properties, with strong polarization and much enhanced intensity.^[224-226] Other high-quality NWs that have

been fabricated include InGaAs NWs, where surface passivation strongly enhances PL emission and their high carrier mobility renders them ideal for surround-gated FETs.^[54]

As described earlier, apart from the optimum properties of NWs, they are also ideal as hosts for QDs. It is reminded that among the advantages of NWQDs, deterministic position and controllable dimensions are the most prominent. Embedding binary III-V QDs in ternary III-V NWs has been thoroughly explored via various material platforms. Among the materials combined, particular interest is presented in GaAs QDs embedded in GaAsP NWs.^[88, 227] Specifically, QD emission with very narrow linewidth of 130 μeV at 1.66 eV have been observed.^[88] This is promising for non-classical light-emitting applications and quantum information processing applications. Besides, AlGaAs NWs are considered very good candidates for hosting GaAs QDs, owing to the lattice matching of the two platforms, thus minimizing induced strain.^[228] The QD emission can be tuned via altering the size of the dot, while peaks with a narrow linewidth of 458 μeV have been reported in the past.^[228] Further details and comparison with our grown structures will be provided later in the current thesis.

It has already been analysed that branched NWs offer a versatile alternative route in NW synthesis, with increased surface area and longer carrier path. Among the high-quality branched NW structures that have been synthesized particular interest is presented for InAs branched NWs with a GaAs QD embedded in the trunk/branch junction, which is intriguing for single photon generation,^[199] High quality branched NWs have been fabricated in the past decade based on different approaches including InAs branched NWs via droplet confinement,^[192] and InSb branched NWs via electrodeposition.^[189] It is also interesting to notice that the important property of branches to be epitaxial with respect to the trunk allows for the realization of antimony-

containing samples crystallized in the WZ phase, which had not been achieved before under other configurations due to the surfactant property of Sb.^[198] For instance high-quality InAsSb branched on WZ InAs NW trunks have been reported.^[198]

Eventually, III-V 2D nanosheets are structures that have gained interest owing to the combination of the optically active III-V properties and 2D, free-standing nature of nanosheets, which allow for high-quality, low-defect structures to be fabricated and facilitate device implementation without the need for sophisticated techniques. Several alloys have been used for such a purpose including GaAs,^[203-205] InAs,^[200,208-209] and InSb.^[206-207] The structural analysis of InAs nanosheets grown via metal-assisted VLS growth, similar to the ones that we used for our experiments, reveals very low amount of defects that are effectively suppressed at higher growth temperatures. For example, while growth at 475°C leads to nanosheets with severe twinning, increase to 505°C causes a drastic reduction of these twins and drastically leads to high-quality materials.^[200] Apart from VLS growth, SAG has also been employed regularly for the fabrication of III-V nanosheets. Impressively, SAG of GaAs nanosheets has led to defect-free structures with no twinning or stacking faults. The mechanisms behind this are still being investigated but the explanation has been twofold; one related to the effect of temperature and its role in the dynamic nature of the defects and the second in the selected orientation of patterning which could increase surface energy and render twin formation less favorable.^[203-204]

In the next section, we will focus on the work in our group at UCL and its contributions to this vibrant scientific field.

1.6) Previous works on nanowires and nanowire quantum dots at UCL

In the MBE group at UCL, we have achieved the growth of high-quality NWs and NWQDs with intriguing properties that have been explored. For the growth procedure, we use the self-catalysed growth via Ga seeds acting as catalyst droplets. Hence, we avoid contamination that is induced by external metal nanoparticles. Furthermore, after the termination of the growth, the droplet can be easily consumed under high group V flux, which is challenging to achieve at foreign metal-catalysed structures. So far, we have been able to grow several samples with satisfactory results. First, we reported on the growth of GaAsP NWs that were monolithically developed on Si substrates. PL measurements revealed narrow peaks located at 710 nm, even at room temperature, which suggests good crystal quality of the structures. It is noted that this was achieved even without the use of surface passivation.^[2,44,229] Besides, the significance of surface passivation was highlighted by reports on the effect of GaAsP shell layers surrounding GaAs NWs, which has led to a threefold enhancement of the PL intensity.^[230] Another material combination that has been explored regarded the growth of InAs NWs, which were optically probed in a high-wavelength setup slightly different than the one described above. It has been proven that a record-high 10-fold enhancement of the PL intensity can be exhibited after the growth of a shell which provides adequate surface passivation.^[231] Finally, novel hybrid group III-V/IV core/shell NWs have been realized, with Ge shells surrounding GaAs NW cores, via exploiting the twin chamber architecture of our MBE system.^[14]

Regarding NWQDs, single GaAs dots have been embedded in GaAsP NWs grown via the self-catalysed VLS growth mode. The emission deriving from the QD segment

is confirmed to have a much narrower FWHM and enhanced intensity when compared to pure NW samples.^[88] Additionally, good thermal stability has been acquired, demonstrating the good structural purity of the structures, with remarkably sharp interfaces, which is a necessary requirement to achieve good optical response and higher possibilities for single photon emission.

In the current thesis, we investigated AlGaAs NWs and AlGaAs/GaAs NWQDs grown via our MBE system. SEM and TEM on the samples enabled us to assess the morphological and structural properties of the NWs and NWQDs and led to very interesting findings, exhibiting the good potential of the structures. PL spectra were obtained by both structures to evaluate how the presence of the dot affects the optical properties of the NWs and investigate their potential for device implementation. Besides, a regular variation, AlGaAs branched NWs, was studied as well. By SEM and TEM techniques, branches were observed to nucleate on the NW sidewalls and grow epitaxially, as corroborated via theoretical calculations. The structural features of the branched NWs were acquired and a growth mechanism was proposed for the formation of branches, based on our results and literature. Finally, a brief section will refer to optical measurements of novel InAs nanosheets, that are a highly promising type of nanostructures, offering vast potential for light-emitting, energy harvesting and memory applications. Prior to proceeding to the description of the organization of the current thesis, we consider it important to provide a brief comparison of the material platforms that are employed for our experiments, including GaAs which has not been used in the current research project but is considered one of the most popular binary alloys among III-V semiconductors. This comparison will be conducted in the following section of the introduction.

1.7) Comparison of nanostructures and material platforms

The increased demands in terms of the structural and optical properties of III-V semiconductor-based nanostructures has led to the exploration of numerous material combinations, each of which presents its own properties. In the current work, we used AlGaAs, AlGaAs/GaAs and InAs in the experimental section, employing them for NWs (some of which are branched), NWQDs and nanosheets, the peculiarities and previous research of which is described individually in the beginning of the corresponding chapter. However, it is also significant to provide a brief comparison of the morphological differences of the nanostructures, as well as to examine the properties of the employed alloys in comparison with the widely used GaAs to establish the properties associated with each platform.

As a first step, the structures that we used for our research were NWs and NWQDs, synthesized at UCL and nanosheets synthesized by collaborators, which we thoroughly inspected optically. Based on the descriptions in the previous sections, NWs are 1D, columnar shape nanostructures with a high surface-to-volume ratio and can be synthesized via either the bottom-up or the top-down approach and the corresponding subcategories that were analysed earlier. On the other hand, 3D branched NWs can be synthesized via different methods, either deliberately or spontaneously (as is the case in our experiments and will be discussed in chapter 4). The structures exhibit a tree-like configuration where the standing NW part is the trunk and the extensions are the branches, which have a hierarchical nature. In addition, a QD insertion axially in the NW leads to the realization of NWQDs, which present a highly controllable method of QD realization, while harvesting the benefits of the NW unique features. The QD can also be formed spontaneously but in the deliberate NWQD synthesis it is realized via the adequate modifications in the elemental supply.

For instance, in our case we introduced the GaAs QD segment via stopping the supply of Al for 7 seconds in order to enable the deposition of binary GaAs. As the dot needs to be embedded in the NW, the initial configuration of elemental supply is restored to grow the top part of the NW. Finally, nanosheets that are also examined have a 2D nature and can also be fabricated by similar epitaxial methods. Although one of the most common and useful approaches is SAG, VLS growth of nanosheets has also been achieved. For instance, in the samples we optically inspect in chapter 6 of the thesis, the growth was achieved directly from 1D InAs NWs via increasing In flux which led to morphological alterations and tuned the change of the structures from 1D to 2D.^[200]

The above are schematically depicted in Fig. 1.8, where we illustrate characteristic examples of a single NW, branched NW, NWQD and nanosheet, in Figs. 1.8a-d, respectively. It is noted that the spherical droplet at the tip of the NWs and the branches is present in VLS growth mode of such structures, hence it is not always demonstrated if a different approach is followed. However, considering that we adopted the VLS growth mode, we thought it is important to include them in the schematic representations. It is interesting to mention that in the case of nanosheets, the droplet was unstable and did not maintain its spherical shape covering the tip of the structure as the growth occurred from 1D NWs via modifying the In flux. This will be examined in chapter 6 of the thesis.

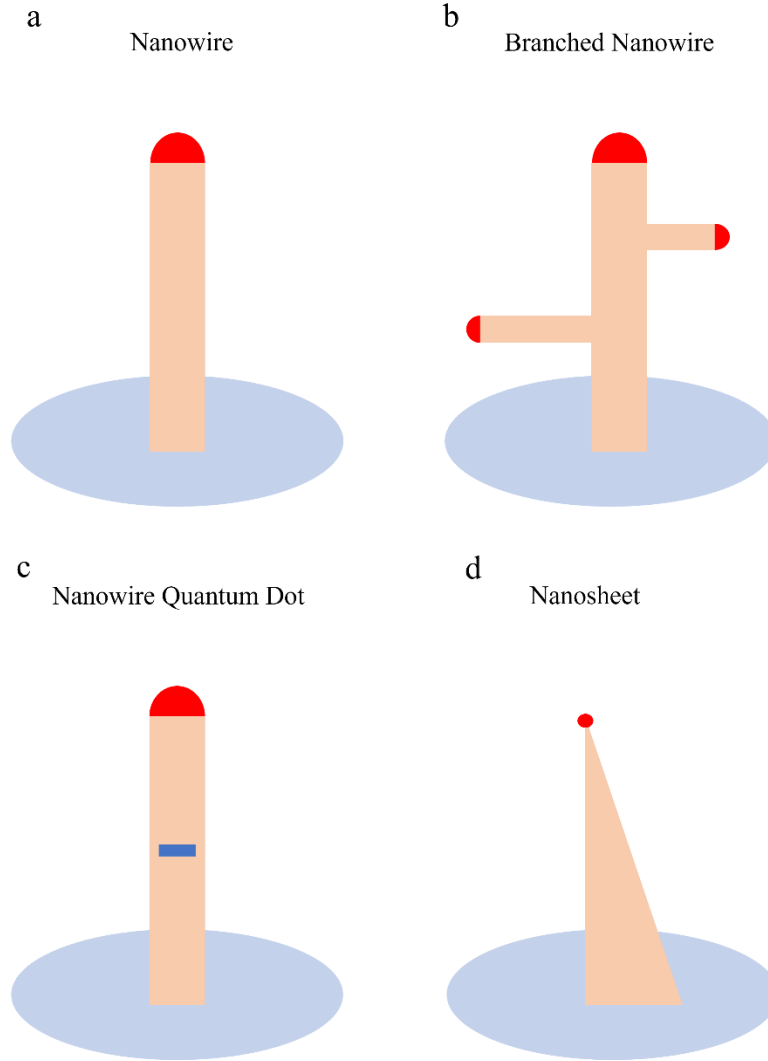


Figure 1.8: a-d) Schematic representations of a NW, branched NW, NWQD and nanosheet, respectively. The catalyst droplet for the VLS growth is depicted in red, while the QD segment is depicted in dark blue colour.

Besides, a comparison of the alloys that are used and the popular GaAs is also elucidating. GaAs is a binary III-V alloy with a bandgap which at room temperature has an energy of roughly 1.42 eV, corresponding to a wavelength of 873.13 nm. One important property is the direct nature of the bandgap, allowing GaAs to emit and detect near-infrared light. Moreover, it is crystallized into the ZB structure, in typical conditions, even though the realization of WZ GaAs has been reported.^[232-233] The

refractive index of GaAs is 3.3 at room temperature and the electron mobility is $8500 \text{ cm}^2/(\text{V}\cdot\text{s})$.

GaAs has been regularly combined with AlGaAs, mostly in core/shell NWs,^[18, 224-226] while the topic of AlGaAs/GaAs NWQDs has attracted attention over the past decade.^[234-236] This interest is mainly based on the lattice match between the two compounds, allowing for minimal strain, hence facilitating superior quality nanostructures. On the other hand, AlGaAs is a ternary alloy with a bandgap that remains direct at room temperature for Al contents no higher than 40%. After this value it becomes indirect and therefore is not practical for optoelectronic applications. The refractive index of AlGaAs lies between 2.86 and 3.3, while its use as shell combined with GaAs in NWs has a threefold role; confining the carriers in the core, protecting the core from oxidation and passivating surface states, which are usually high in NWs and nanosheets owing to the large surface-to-volume ratio.^[171] Due to the tunability of the bandgap as a function of the Al composition, this ternary alloy has the ability to emit red to near-infrared light usually within the range of 700-850 nm. It is also important to remind that while AlGaAs is usually crystallized into ZB phase, the works on AlGaAs NWs have revealed a polytypic nature with frequent WZ insertions, while the formation of WZ AlGaAs shell layers has also been reported, as a result of the epitaxial nature of the growth, where the shell adopts the crystal structure of the core.^[170] Finally, the electron mobility is given by the equation $8 \cdot 10^3 - 2.2 \cdot 10^4 x + 10^4 x^2 \text{ cm}^2/(\text{V}\cdot\text{s})$ for x between 0 and 0.45, while for x above 0.45 it is given by the equation $-255 + 1160x - 720x^2 \text{ cm}^2/(\text{V}\cdot\text{s})$. Hence, the values range between roughly 215 and $8000 \text{ cm}^2/(\text{V}\cdot\text{s})$ at room temperature.

Regarding the combination of AlGaAs and GaAs in NWQDs, the frequently adopted architecture includes one GaAs QD inserted axially in an AlGaAs NW. In this design,

carriers are confined in the 0D QD region, while the AlGaAs layers surrounding the dot minimize carrier escape especially at low temperatures where carrier mobility is lower. The emission of such structures is typically consisted of a sharp peak in the near-infrared region attributed to GaAs emission and a comparably broader peak located at lower wavelengths, in the red or near-infrared region, which is originating from AlGaAs NW emission. The above are fundamental aspects for several optoelectronic applications. For instance, the importance of NWQDs for single photon generation and quantum information processing has been described earlier in the current chapter.

Finally, it is important to describe some basic parameters of InAs, which is another popular binary alloy for implementation in optoelectronics. InAs is a direct-bandgap III-V semiconductor, whose narrow bandgap of 0.354 eV at room temperature is one of its most prominent feature. In combination with the direct nature of the bandgap, infrared emission and detection are enabled in nanostructures based on this material platform. Another distinguished characteristic of InAs is its high electron mobility which reaches $40000 \text{ cm}^2/(\text{V}\cdot\text{s})$, rendering it ideal for high-speed electronics. Its refractive index is 3.51 at room temperature, while its crystal structure is predominantly ZB. Nevertheless, it is noted that the realization of WZ InAs has been regularly reported, quite more frequently in comparison with AlGaAs.^[89-90, 237]

Based on the information provided above, a table encapsulating the properties stated in the current section of the thesis is depicted below (Table 1).

III-V alloy	Bandgap Nature	Bandgap Energy (at RT)	Crystal Structure	Refractive Index (at RT)	Electron Mobility (at RT)
GaAs	Direct	1.42 eV	ZB (occasional WZ)	3.3	8500 cm ² /(V*s)
Al _x Ga _{1-x} As	Direct for x<0.4	1.42 eV- 2.16 eV	Polytypic	2.86-3.3 (depends on x)	215-8000 cm ² /(V*s) (depends on x)
InAs	Direct	0.354	ZB (frequently reported WZ)	3.51	40000 cm ² /(V*s)

Table 1: Summary of the basic features of GaAs, AlGaAs and InAs alloys.

In the next and final section of the introduction, we will describe the aim of the project along with the detailed organization of the thesis.

1.8) Organization of the Thesis

As a result of the benefits of the nanoscale structures that were analysed above and the important role they can play in device applications of low volume and cost, their growth and investigation has been a significant task in scientific research over the past years. The objective of the current thesis is the synthesis of advantageous nanostructures, including NWs, NWQDs and 2D nanosheets, based on prominent and beneficial material platforms, monolithically on Si substrates, which is an important feature considering the role of Si in optoelectronics and photonic circuits. The choice of material platforms that are scrutinised (AlGaAs, AlGaAs/GaAs and InAs) is based on the advantages of each one of them for practical applications, also considering their impact on our research field and their interesting characteristics. The realized structures should be of good material quality, which is a key factor for their wide-scale implementation in applications. Moreover, a thorough study of the structural and morphological properties of the grown nanostructures is imperative in order to

characterize them in depth and potentially unravel the mechanisms lying beneath some interesting or irregular findings. In addition to the above, another aim of the current work is to examine the optical response of the grown nanostructures and to assess the results as well as interpreting observations that will be manifested. The optical address of the samples occurs in our case via photoluminescence (PL) excitation using a laser source, as will be described in the following chapter of the thesis. The structures are synthesised via state-of-the-arts MBE facilities, an epitaxial method which will be thoroughly analysed further on in the current thesis.

The inspected structures in our work include 1D AlGaAs NWs, a peculiar type of self-assembled 3D, branched AlGaAs NWs and single AlGaAs/GaAs NWQDs grown in our facilities via the advantageous self-catalysed VLS growth mode that was described above and thoroughly characterized by means of microscopy and optical techniques. In addition to this, we characterise InAs nanosheets, which are structures based on a prominent and highly explored material platform with advantageous features, which were grown by our collaborators. The optical analysis was conducted in our facilities at UCL using PL measurements that allowed us to reach an uncommon and very interesting observation that indicates the role these structures can play in their implementation for optoelectronic memory units of ultra-low power consumption.

Based on the above, our experimental work, results and publications led to the synthesis of a thesis comprised of 7 chapters with an additional 8th chapter being the rich bibliography that is cited. The content and brief description of the chapters is included below. Specifically, in Chapter 1, we initiated the thesis by presenting a thorough background and recent developments in the growth of high-quality III-V nanostructures on Si, commenting on their suitability for a wide number of applications. Specifically, we began by describing the basic properties and achievements in the

growth of NWs and NWQDs, respectively. We continued by introducing some basic information on the ZB or WZ crystal phase and we introduced device applications that were developed based on III-V NWs and NWQDs. Besides, we analysed the growth methods that have been employed for the NWs and the NWQDs that have been achieved and comment on the strain in NWs. Then, we introduced a variant of NWs which is the 3D branched NWs and described the highly promising III-V nanosheets, that are useful for a variety of applications. Finally, we briefly referred to previous relevant works conducted in our facilities at UCL.

Chapter 2 includes the components and functions of an MBE system, along with its basic working principles and a brief comparison with the popular CVD and MOVPE methods. Additionally, we introduce the state-of-the-arts MBE system at UCL facilities that was used for the conduction of our work. Moreover, we present the tools, setups and equipment that have been used for the microscopical and optical analysis, located either at UCL or in collaborating institutions.

In Chapter 3, we demonstrate the results of our investigation on standing 1D AlGaAs NWs, after having analysed and specified the scope for the use of this particular ternary alloy. The self-formed, Al-rich shell is shown to have two distinct characteristics that are observed and interpreted. The optical analysis reveals efficient emission, tuneable in the range of 700-850 nm.

In Chapter 4, we exhibit the studies on branched AlGaAs NWs, where a thorough transmission electron microscopy investigation is shown. The branched NWs were observed to display uncommon compositional distribution, with stripes of Ga segregation being formed both along the branch axis and perpendicular to it, leading

to the realization of a complex checked pattern. This phenomenon is interpreted and its significance is clarified.

Chapter 5 includes a systematic study of single GaAs/AlGaAs dot-in-wire structures. The presence of the dot is established via transmission electron microscopy and energy dispersive x-ray spectroscopy, while the thorough optical investigation via PL and micro-PL measurements reveals GaAs-related peaks that are centrally localized and relatively narrow in linewidth. The above strongly indicate the quantum confinement occurring in the axially embedded GaAs segment and are promising for non-classical light-emitting applications.

Moreover, in Chapter 6, we introduce another type of nanostructures; InAs nanosheets grown via MBE, which were subject to systematic optical study. We analyse the memory effect that was observed for pristine nanosheets and compare and evaluate the impact of the different types of surface passivation on the optical behaviour of the structures. Furthermore, we display the promising potential of the structures as fundamental units for optoelectronic memory devices, operating with ultra-low power consumption.

Finally, in Chapter 7, we summarize the results that were acquired from the experiments and describe the challenges that were met and the plan for future works related to this research topic.

Chapter 2: Equipment, setup and tools

The samples that we develop in our lab are grown via a solid-source MBE system with twin growth chambers; one for group III-V semiconductors and the other one for group IV semiconductors. The second will focus on the description and analysis of the system, its components and the operating principles. Additional information will also be provided on the various setups and pieces of equipment that were used to conduct the structural, morphological, and optical analysis of the grown samples.

2.1) Molecular Beam Epitaxy

2.1.1) General Information

MBE is a powerful epitaxial method for thin film deposition of single crystal, which was invented in the late 1960s.^[238] Its working principles are founded on a physical evaporation procedure, where the beam flux is transferred onto the substrate wafers. Upon arrival of the elemental adatoms on these wafers very intricate physical interactions take place. The entire procedure is performed under high vacuum or ultra-high vacuum (UHV). The basic feature of MBE is the very slow deposition rate which allows for the structural epitaxial growth. To fulfil this purpose, an essential prerequisite is the high quality of the UHV, which ensures negligible or low level of unwanted dopants, thus maintaining the purity of the grown crystals, while it ensures that the adatoms adopt a long enough mean free path in order to reach the surface of the wafer.^[238] MBE exhibits some major beneficial characteristics in comparison to other epitaxial systems such as MOVPE or CBE. First and foremost, it is a physical evaporation procedure without involvement of interaction between beam fluxes prior to the arrival of the adatoms at the wafer. The slow growth rate of the layers of atoms enables to control the procedure with a remarkably high level of accuracy. On top of

that, the aforementioned UHV conditions ensure that the mean free path of a molecule is larger than the one recorded in other systems. Ergo, the transport of the molecules occurs in a ballistic manner, meaning that minimal or no scattering occurs.^[239] MBE systems are mainly comprised of the growth chamber, the buffer chamber (or preparation chamber) and the load-lock module. The growth chamber, which is considered the heart of the MBE reactor, is pumped by a cryopump and an ion pump, maintaining a base pressure of 10^{-10} mbar. The chamber also includes a manipulator of the sample holder, capable of continuous rotation at some set value (i.e., 10 revolutions per minute (rpm)), which can be heated up to 1000°C and a cryopanel that is cooled down to -140°C via the use of liquid nitrogen prior to the growth. This cryopanel surrounds the walls of the growth chamber internally and its basic aim is to maintain the background pressure at a sufficiently low level. Furthermore, the low temperature eradicates the 'memory effect' that is usually displayed in other systems such as MOVPE. The memory effect is a phenomenon according to which elements are desorbed from the inner walls of the system. Thus, it can cause uncontrolled incorporation of source materials in the growing crystal, which can hinder structural purity and jeopardize the stability of the device performance based on these samples.^[240]

In solid-source MBE systems, the elements that are intended to be used (such as Ga, As, In, Al etc.) are heated in separate quasi-Knudsen effusion cells, until they slowly begin to sublime. Next, the gas phase elements condense into the substrate wafer, where they begin chemically interacting with each other, thus triggering material growth. The elements that impinge on the surface can be adsorbed or desorbed. All of these processes are controlled by a careful determination of the temperature of the

source and the substrate, respectively. It is reminded that no interaction among the gaseous elements takes place before they reach the substrate wafer.

A special mention should be paid to the UHV inside an MBE system, which provides the adequate environment for incorporation of many different systems that can operate under such conditions. Another fundamental benefit of UHV is the capability to incorporate electron diffraction probes, such as Reflective High Energy Electron Diffraction (RHEED) into the system. RHEED is a supplementary system that provides valuable in-situ information on the wafer surface during the growth and is rendered vital for the realization of thin films.

To underline the importance of MBE and its main differences compared to other significant growth techniques and facilities, a brief comparison between MBE as a physical evaporation procedure and CVD is required. CVD is a method of material deposition where similar to our system the procedure is conducted under vacuum conditions on substrate wafers. In the case of CVD the substrate receives elemental precursors which chemically react in order to form the wanted material layers. It is a popular method especially regarding thin film fabrication. CVD can be subcategorised depending on the pressure, the physical form of the vapor precursors and the substrate temperature, which are the main parameters regulating its realization. One feature of CVD is the multiple directions that the deposition can adopt.^[241] The precursors are deposited via a carrier gas, such as argon or nitrogen. Based on the fact that the formation of the material layers is realized via chemical reactions, it is a chemical procedure. A schematic representation of its fundamental mechanism in the reactor is presented in Fig. 2.1a. It is noted that MOCVD or MOVPE is a variant of CVD, where, like CVD and unlike our method (MBE), deposition occurs following chemical reactions rather than physical evaporation and the precursors in their vapor

form are transferred on the substrate wafer for the chemical reaction to be realized. Also in this case, the reaction does not occur in vacuum but at intermediate pressures reaching roughly 760 Torr. The gas in this case is inserted in the reactor via relevant devices and can usually be hydrogen or nitrogen. Due to their chemical nature, such methods require a waste system, where hazardous waste is converted into solid for easier disposal.

Based on the above, it can be seen that the differences between CVD (and MOCVD) and MBE are mainly originating from their different nature, the former being chemical while the latter being physical. CVD is done at higher pressures when compared to MBE, as it can also be conducted at atmospheric pressure. Hence, UHV is possible but not necessary. This also means that the cost related to this aspect is lower in CVD processes. The main parameters in CVD that control the quality of the materials are temperature, pressure and flow rate of the vapor phase precursors. The growth temperatures usually range from 500 to 1200 °C. The growth rates in the case of CVD procedures are significantly higher, as they can reach 5 μm per hour, thus facilitating mass production. On the contrary, MBE is a physical procedure, where the heating of effusion cells leads to sublimation of the gaseous elements, which are ballistically deposited on a substrate. UHV is necessary in this process, which increases the cost but on the positive side it impedes chemical reactions taking place before the adatoms reach the substrate, due to the increased mean free path. Another important difference is the possibility of in-situ characterization (for instance using RHEED) which is enabled due to the UHV in MBE while it is not the case for CVD. The growth rates are much slower typically barely reaching 1 μm per hour, which renders mass production challenging but facilitates high-quality crystal fabrication. It is noted that based on the above, MBE allows for a better control over the dimensions of the

nanostructures that are synthesized. For facilitation, a schematic representation of an MBE system is given in Fig. 2.1b. It is noted that a more detailed schematic of the growth chamber, which is the core of the entire procedure, is provided separately below.

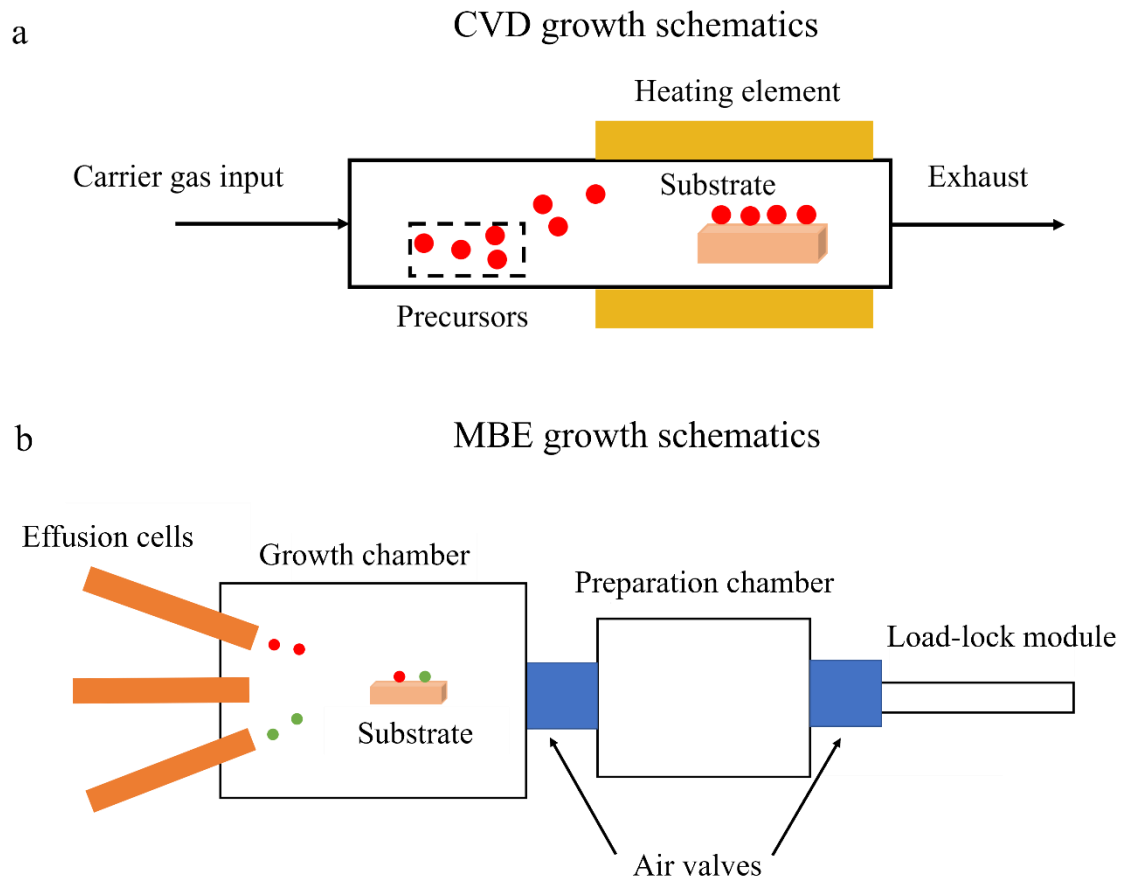


Figure 2.1: Basic schematics of a) CVD and b) MBE growth reactors. The additional components of the MBE, which is the method we used, are going to be depicted in a separate schematic later in the current chapter.

As mentioned above, the key parameters in CVD growth are the temperature, the pressure and the gas flow rate. In MBE, there are important growth parameters to be considered as well, which can profoundly affect the grown crystals. One of the most important growth parameters is growth temperature, which can affect the structure and optical properties of the resulting nanostructures. For instance, it has been shown that

the composition and elemental distribution of ternary alloys is linked to the growth temperature as higher temperatures can show better compositional stability.^[242] On the other hand, temperature has been related to the crystal quality. For example, in a work of InAlAs layers grown on InP substrates, it has been found that increased growth temperature causes defects on the surface of the crystal, while at low temperatures there is increased surface roughness.^[243] This means that careful study of the impact of temperature should be carried out while designing the nanostructures, based on the wanted features and potential for specific device applications.

A second key parameter is the elemental beam flux ratio. In binary III-V alloys, this is defined as the V/III ratio, while in ternary alloys apart from the aforementioned factor, a III(1)/III(2) or V(1)/V(2) ratios are also defined. The ratio can have an impact as it can determine the composition of an alloy, which in turn regulates the optical transitions, wavelength of emission, additional peaks etc. For instance, in our case, a lower V/III ratio has led to increased Al presence in the alloy, which in turns shifts the emission towards lower wavelengths, while branching events are much more pronounced at these values, as will be thoroughly examined in chapters 3-4. The growth of nanosheets is also affected, as we will establish based on the growth mechanism of our investigated InAs nanosheets, where higher In flux resulted in transition of 1D InAs NWs to a 2D InAs nanosheet morphology, while increase of In beyond a value suppressed growth.^[200] Moreover, the duration of growth is crucial, as shorter times potentially do not allow for fully-formed nanostructures to be developed and distort their morphology.^[228]

Besides, the UHV conditions are also important mainly due to their role in the ballistic deposition of adatoms. In addition, UHV ensures that there is limited contaminations due to impurities present. The pumping of the pressure in the

chambers of an MBE system is conducted via cryopumps or ion pumps and will be thoroughly described later in the current chapter. In the case of our MBE system the background pressure could reach the ultra-low values of 7.5×10^{-10} Torr (10^{-10} mbar) which ensures the required high-purity UHV that is vital.

The aforementioned general information helps us understand the basic functionalities and working principles of an MBE system. Nonetheless, each type of reactor used presents slight variations in the function and the potential for nanostructure growth. In the following section we will thoroughly describe the system we use in our lab at UCL, which enabled us to realize the nanostructures that are studied in the current thesis.

2.1.2) Molecular Beam Epitaxy system at UCL facilities

The solid-source III-V MBE system at UCL consists of four chambers: a load-lock module, a preparation chamber, a growth chamber and a phosphorus recovery system. All of these chambers are separated from each other via the use of an UHV gate valve.

The load-lock chamber is an essential part of the growth system, as it is the means of introducing the substrate into the system, whilst prohibiting contamination of the rest of the chambers with components of the atmospheric air. The chamber is pumped by a turbo pump during unloading and reloading samples and is vacuumed into UHV. After reloading, a cryopump that is connected to the chamber replaces the turbo pump to maintain the vacuum in the load-lock chamber. Usually, reloading is followed by an outgas procedure of the substrates by thermal annealing at 200°C. During this stage, majority of contaminants are eliminated from the wafers. Before introducing the substrate in the MBE system, the substrate is degassed for approximately 12 hours

under these UHV conditions. After this step, the substrate is ready to be loaded into the buffer chamber of the main MBE system.

The buffer or preparation chamber is responsible for isolating the growth chamber from the external environment to further prevent contamination by air that derives from the load-lock chamber. Apart from this role, it is also a space where the substrates can be thermally prepared prior to the growth. A heating stage on the sidewalls lifts the temperature up to 600°C for a second degassing procedure, which is necessary to ensure that more contaminants are removed from the wafer. The heater is separated from the growth chamber, signifying that the thermal treatment of the substrate can occur even during growth. Moreover, the buffer chamber acts as a storage space for substrates before or after the growth. It is merely connected to an ion pump that is able to function only in the UHV environment.

The growth chamber is the most important part of the MBE system, as it is the space where the main growth of the samples is being carried out. It includes a variety of other supplementary systems and components that help monitor, control and alter the growth parameters, as required. It includes a substrate manipulator, a substrate heater, a thermocouple, effusion cells, cryopanel, beam flux monitors and vacuum facilities. The substrate manipulator is the holder of the substrate. It can move along two axes. The first one is used to position the substrate for growth, transfer and flux measurements, respectively. The second axis allows the substrate to rotate around itself, thus enabling homogeneous growth around the entire wafer. The substrate heater can lift the temperature up to 1000°C, which is much larger than the average range of temperature that a typical MBE system can reach. The thermocouple, on the other hand, along with the pyrometer are used to measure the temperature of the substrate. The former is located behind the substrate and the latter is situated facing

the surface of the substrate at growth position. Finally, the effusion cells are components possessing a port which is designed in such a fashion that is directed to the position of the sample during growth. The effusion cells are attached to the growth chamber. It is important to point out that beam flux monitors are widely used to determine flux ratios and growth rates at the position of the sample (or at its vicinity). The high purity of UHV is maintained via the collaborative function of a cryogenic pump and an ion pump. The III-V elements we have in our disposal at UCL are Gallium, Indium, Aluminium (Group III) and Arsenic, Phosphorus and Antimony (Group V). For clarity, a schematic diagram of the basic components of an MBE growth chamber is depicted in Fig. 2.2.

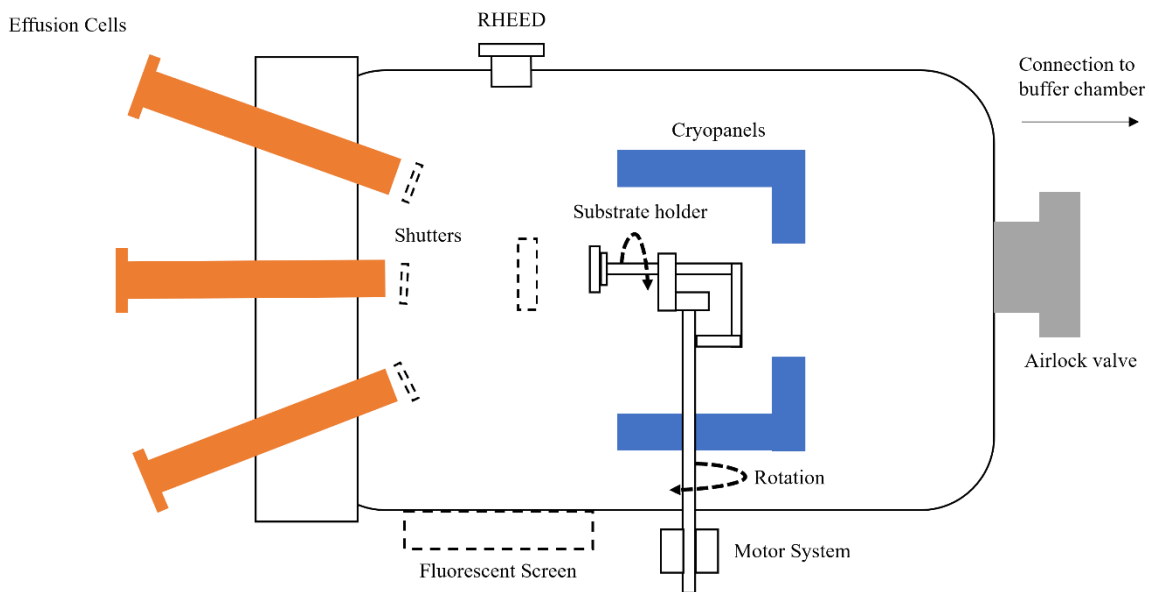


Figure 2.2: Schematic diagram of the growth chamber of our MBE system, including the effusion cells, RHEED gun and fluorescent screen, rotating sample holder, cryopanel and connection to the buffer chamber via an airlock valve.

One of the peculiarities of our growth system is the use of phosphorus for some of our samples. This required an additional component in the MBE facility. This component is called Phosphorus Recovery System, which is responsible for rapidly

removing P that exists in the growth chamber. Phosphoric content can be hazardous to the safety of the system and the researchers. Hence, special attention and careful handling are required to employ it in an efficient and safe manner.

One of the most important supplementary systems of an MBE system is RHEED. This is a technique during which an electron gun emits an electron beam generated by a tungsten filament and the beam is focused on the sample. It is noted that the UHV in the growth chamber of the MBE is a necessary requirement for RHEED systems to function. The characteristic of RHEED is that the beam reaches only the surface of the sample to produce a diffraction pattern of the electrons that can provide significant information regarding the crystallinity of the grown structure. RHEED is particularly common and useful in thin film growth and in QD growth. However, it can also be used to inspect NW synthesis. Based on RHEED observations, the consumption of Ga droplets after the termination of the elemental supply has been reported,^[244] while the impact of fluxes on the structural properties have also been scrutinised.^[245] The patterns that are produced by RHEED are also used in the case of heterostructure growth such as heterostructure NWs or NWQDs, where the change of the pattern as a result of the different crystal phase or structural properties of the various material platforms can confirm the realization of the heteroepitaxy.

Although in our experiments, RHEED analysis was not carried out in-depth, the system was employed to confirm that NWs are grown adequately. Monitoring the diffraction pattern of the RHEED system allows us to evaluate whether NWs are successfully elongated or whether the growth conditions were not appropriate causing parasitic growth or thin film growth. A picture of the MBE system that is used in our lab for the realization of the structures that will be described in the next chapters of the current thesis is presented in Fig. 2.3.

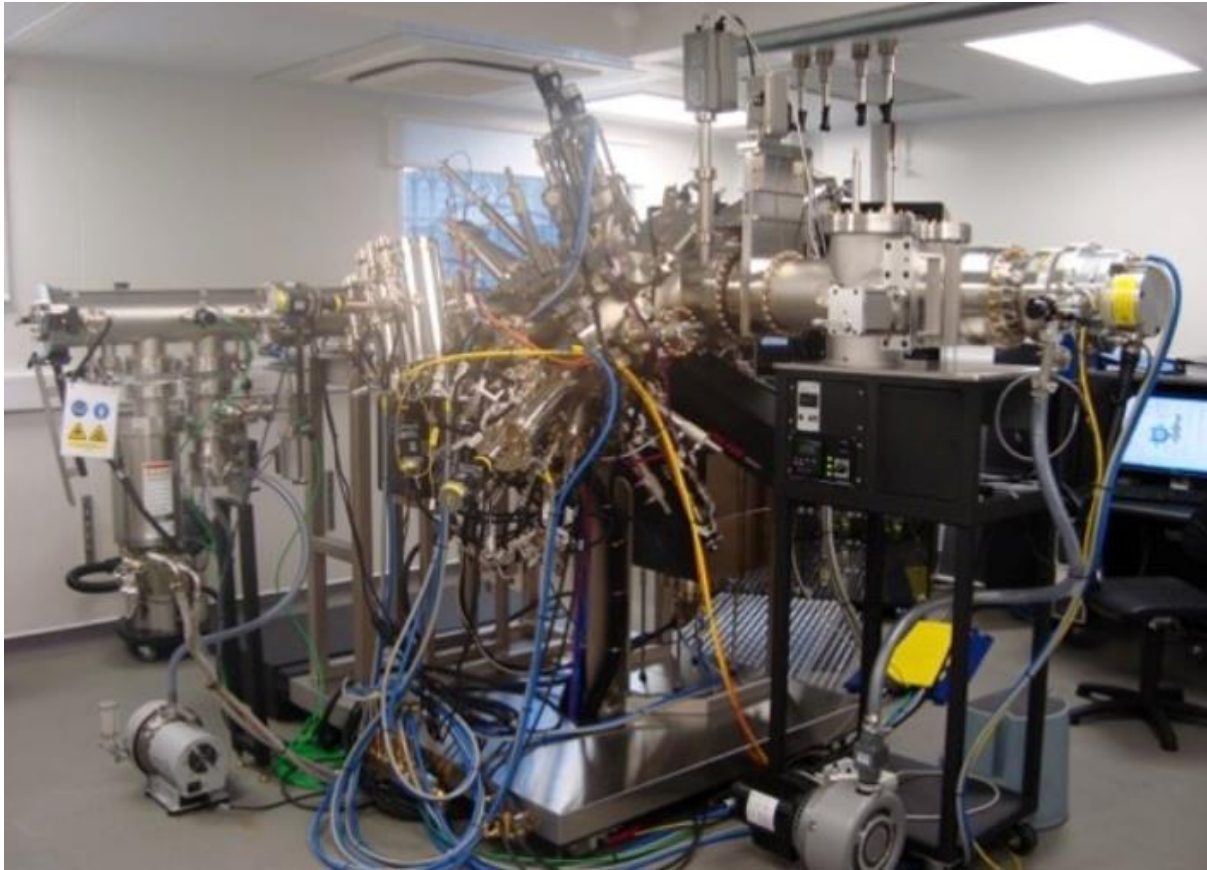


Figure 2.3: MBE system used for the growth of our structures in our lab.

2.2) Measurement equipment and setups

2.2.1) Scanning Electron Microscopy

Scanning Electron Microscopy (SEM) is a technique allowing the user to inspect the morphology of the samples. The system is comprised of a scanning electron microscope whose function is to acquire an image of the sample, driven by the scan of the surface via a beam of electrons. The electron beam is produced by a filament, most commonly a loop of tungsten acting as the cathode. The heating of the filament leads to the generation of an electron beam. The beam passes vertically through the microscope components. Initially, it passes through the anode and reaches the lenses of the microscope, which direct the beam on the sample. Following this step, the beam reaches the scanning coils, which are used to deflect the beam in both X and Y axis.

This way it ensures that a rectangular area of the sample will be scanned. Finally, the beam scans the surface of the sample. Some of the electrons in the beam interact with the atoms of the material and are scattered forming secondary electrons and back-scattered electrons, which are collected by the corresponding detectors and produce a signal which is projected on the screen. The above are illustrated in the schematic diagram of Fig. 2.4.

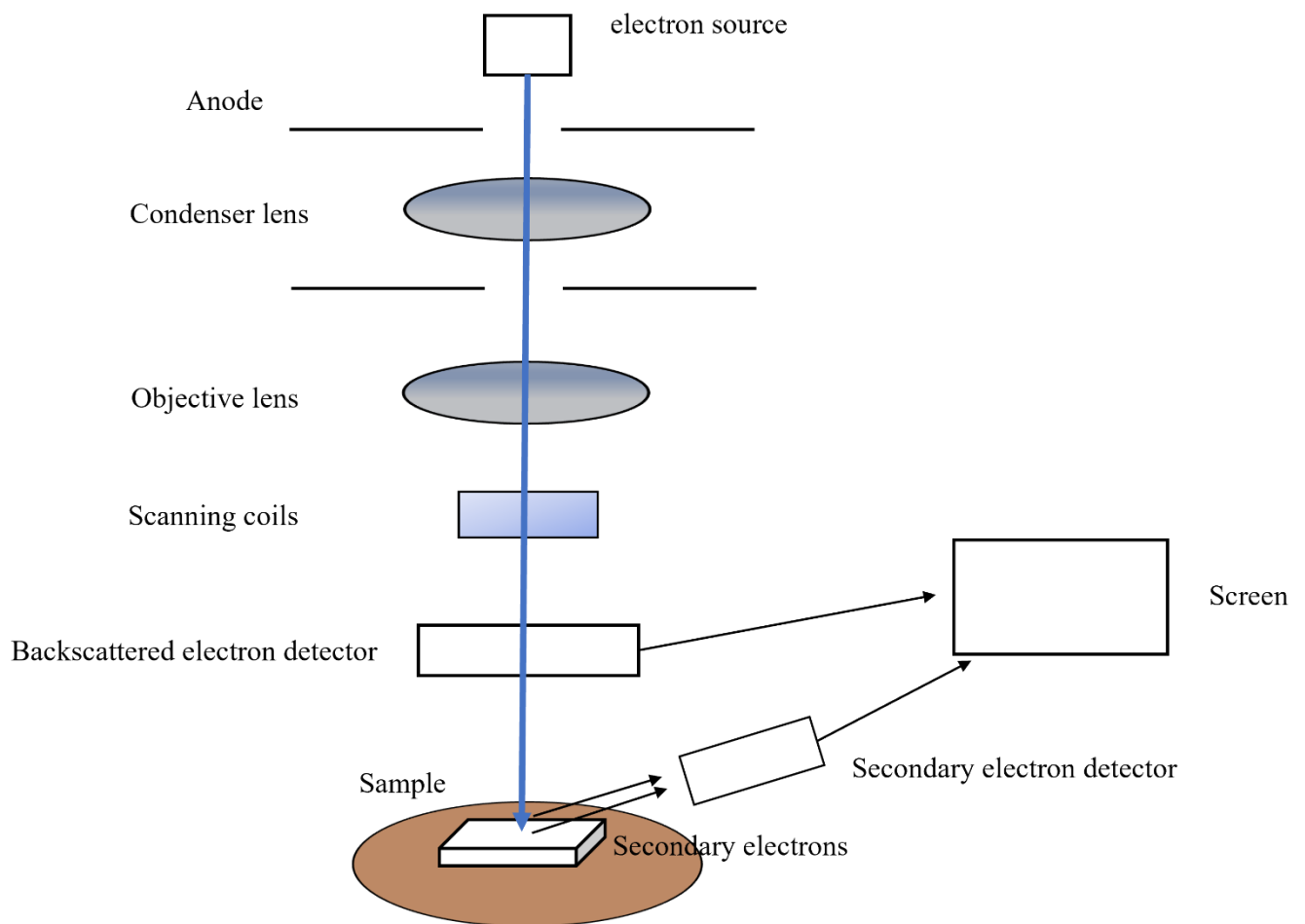


Figure 2.4: Schematic diagram of the basic functions and components of an SEM system.

It is noted that the signals that are detected and lead to the production of the high-quality image can be secondary electrons, back-scattered electrons, cathodoluminescence or transmitted electrons. The most common approach,

however, is secondary electron imaging. This approach is also adopted by the SEM in our facilities. Via this method, the low-energy electrons that are emitted from conduction or valence bands of the sample are collected after their interaction with the beam of electrons of the microscope. These secondary electrons derive from the vicinity of the surface of the examined sample and are accelerated towards a positively biased phosphor. This acceleration provides them with the adequate amount of energy that is required for the phosphor to exhibit cathodoluminescence, which is then driven to a photomultiplier via a light pipe and a window in the wall of the chamber of the system. This signal at the output of the photomultiplier can be illustrated and photographed either in analogue or digital form. It is important to notice that in order to increase the mean free path of the electrons the chamber where the sample is placed is evacuated to low pressures. This reduces the frequency of the collisions of the electrons with gas atoms, thus increasing the mean free path. Depending on the instrument and the facilities the lowest resolution of an SEM tool can range between 1 nm and 20 nm. The best resolution achieved so far globally from such a facility has been as low as 0.4 nm.

Apart from the above it should be mentioned that back-scattered electron imaging is also beneficial for SEM characterization. Back-scattered electrons are high-energy electrons that are reflected back due to elastic scattering of the electrons comprising the incident beam with the material. Unlike secondary electrons, which are the result of inelastic interactions between the beam and the surface of the sample and have lower energy, back-scattered electrons derive from deeper regions of the specimen. Hence, they contain different types of information, with the most characteristic being the sensitivity to the atomic number of the material, with heavier elements appearing brighter as they are more likely to scatter the electrons. This type of imaging can also

offer information on the crystallography of the material. Nevertheless, it is noted that secondary electron imaging is ideal for inspection of the morphology of the surface of the structures. It is reminded that in our facilities secondary electron imaging was used.

Besides, it is underlined that for our experiments SEM could not be used to confirm the QD-in-NW formation, as the dot is embedded in the NW axis. Moreover, the resolution of the equipment that we possess cannot reach the low level that is required to acquire information on the QD. Nevertheless, this technique was ideal to provide important morphological data on the NW samples, including their dimensionality, orientation and potential parasitic growth.

Our SEM measurements were conducted in a JEOL IT-100 system, which is presented below in Fig. 2.5. The NW samples are first cut and stick to the sample holder by the use of conductive tape. The chamber where the sample is positioned is pumped down. Next, an electron gun generates electrons with energy ranging from 500 eV to 30 keV. The NW atoms interact with the emitted electrons and generate secondary electron signals, which map the sample morphology. It is important to mention that parameters such as the height of the holder and the tilting angle can be controlled to obtain more accurate images of remarkably high resolution. In our case, the voltage of the electron beam was set at 20 kV and the samples were tilted by 30°. The tilting of the sample is considered crucial as a vertically guided electron beam leads to the escape of a number of electrons deriving from the sample as the activated region is homogeneous with respect to the axis of the beam. On the contrary, as the tilting increased, the area of electron interaction is increased. Hence, more secondary electrons are emitted from the sample and collected via the aforementioned procedures. In our case, experimental observation has shown that the used

configurations are the ones under which the resolution of the acquired images was the most satisfying.



Figure 2.5: JEOL IT-100 Scanning Electron Microscopy system at UCL facilities

2.2.2) Transmission Electron Microscopy

Another tool we have in our disposal for the morphological and structural analysis of the grown samples is Transmission Electron Microscopy (TEM), which is a technique where an electron beam is transmitted through the sample to generate an image. The main difference between SEM and TEM is that the former uses a line-by-line scanning over the surface of the samples, while the latter exploits a beam that passes through the sample. This function is rather challenging and thus demands for careful preparation of the specimen prior to its conduction. The sample needs to be ultrathin, in a scale of less than 100 nm and is placed on a grid.

In Fig. 2.6, the basic schematic representation of a typical TEM system is provided. Each TEM facility is comprised of an electron source or cathode, such as tungsten filament among other options. This source emits electrons under the application of appropriate voltage (usually within the frame of 100 kV) into the vacuum. It is noted that the control of the electron beam can be conducted via electromagnets, using the influence of a generated magnetic field. Following this, the electron beam is accelerated until it obtains its voltage and reaches the optical part of the system, which is mainly comprised of different types of lenses. A typical TEM system is comprised of condenser lenses, objective lenses and projector lenses. The first level that is reached by the electron beam is condenser lenses which focus the beam on the sample. The beam passes through the sample (unlike SEM, where the sample is scanned) and the output beam is directed to the objective lenses, whose role is to focus furthermore the exit beam. As a next step, the beam reaches the projector lenses, whose importance lies in the expansion of the beam onto the imaging device, typically a screen. Moreover, apertures which are metallic plates represented by thick black lines in the schematic representation of Fig. 2.6, are the components that exclude specific electron types whose distance from the optical axis is larger than a specified value. Hence, apertures contribute to the decrease of the intensity of the signal, effectively acting as a filter which removes high-angle scattered electrons. Finally, it is worth mentioning that an additional type of lenses, frequently used, is intermediate lenses which are located between the projector lens and the objective lens and their role is to change the focus of the image before the signal reaches the projector lens.

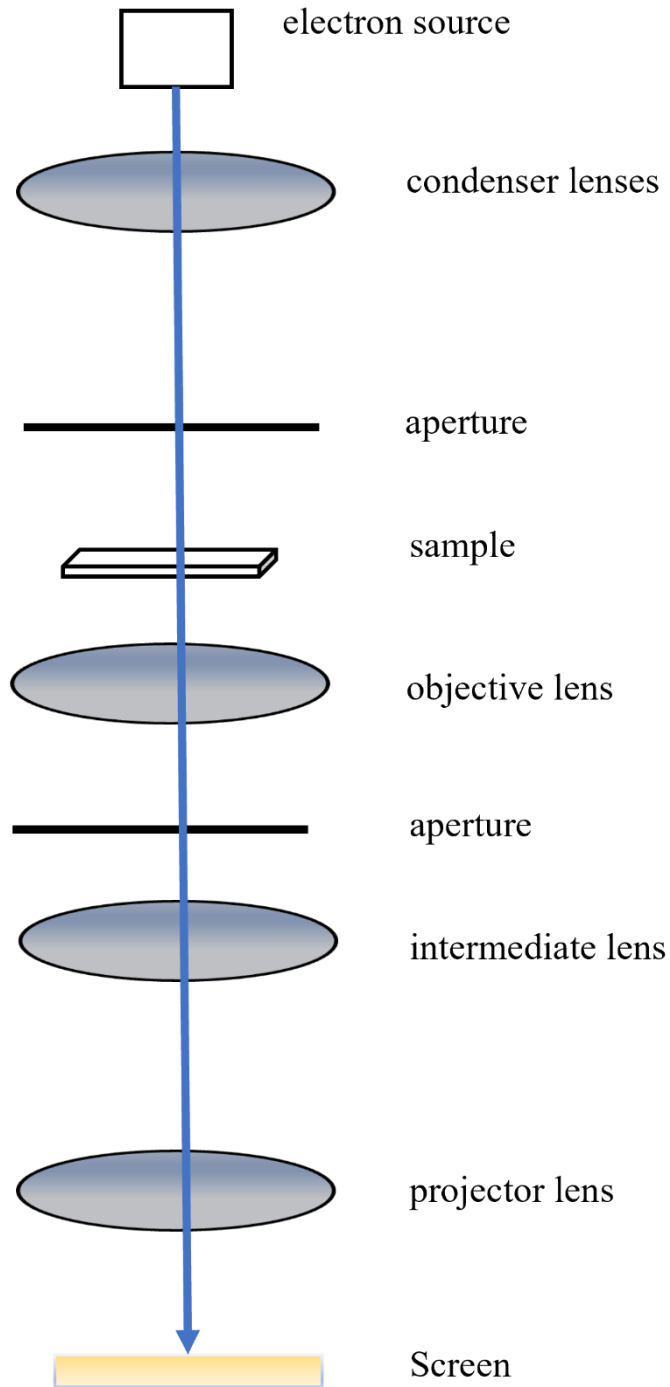


Figure 2.6: Schematic representation of the typical operation and components of a TEM system.

It is significant to underline that there are two basic operating modes of TEM systems, the imaging mode and the diffraction mode.^[246] Following electron-sample interaction, two types of electrons are generated, namely scattered and unscattered

electrons, with the latter being the ones that comprise the central beam and the former changing their path after their interaction with the material. The objective aperture, within the objective lens, can be programmed to filter the scattered electrons and allow only the central beam to pass through. This is the way a bright field (BF) image is acquired. The opposite is the case for the dark field (DF) image, where the central beam is filtered out and only the diffracted electrons are used to obtain the image. The signal reaches the projector lens which focuses it on a screen or another optical medium. The aforementioned procedure is conducted in imaging mode. In diffraction mode, the operating principles are the same but the basic difference is that in this case an addition aperture (selected area aperture) focuses the beam more precisely in the area of the sample which needs to be closely inspected, thus rendering this function important for highly accurate characterization.

It is noted that vacuum system is of vital importance for the functionality of a TEM facility. The vacuum (typically 7.5×10^{-7} Torr) allows for the mean free path of electrons to be increased, as mentioned earlier for other high-vacuum facilities such as our MBE system. This is important because it significantly reduces the collision of electrons with gas atoms, which could jeopardize the validity of the experiments. Moreover, it is reminded that the preparation of the sample is a definite requirement in TEM measurements. The sample needs to be sectioned and the measured portion should not exceed 100 μm in thickness. It is placed on a grid, which is inserted into the holder.

In a TEM system, the resolution of the generated images is much higher when compared to SEM because of the small de Broglie wavelength of the transmitted electrons. This is beneficial for a more detailed monitoring of the structural features of the specimen. In addition, it is a powerful method for obtaining information on the compositional distribution of the sample, which is helpful for its design and the

interpretation of the subsequent optoelectronic analysis. The details that can be obtained via a TEM system can be as small as a single column of atoms, which enables the user to determine the crystal phase of the structures and other important characteristics regarding their crystallinity, such as orientation and crystal defects. The operating modes of TEM tools are various and include scanning TEM (STEM), diffraction, spectroscopy etc. For instance, an important mode in the investigation of the crystal structure is high-resolution TEM, according to which the images are formed because of phase contrast of electron waves, when the specimen is uniform in the thickness. This is a difference when compared to conventional TEM imaging, which exploits amplitude contrast instead of phase contrast to produce the image. The advantage of high-resolution TEM is that it can provide a variety of structural information about the sample and can be manipulated. On the drawback, the challenge is that since the image is not only dependent on the electrons hitting the screen but also on the phase contrast, the direct elucidation of the images is demanding. Furthermore, Energy Dispersive X-Ray Spectroscopy (EDX) can be conducted via TEM analysis, where vital data describing the exact compositional distribution of the samples are provided.

One particularly useful operating mode is annular dark field (ADF) imaging. ADF is a method where the images are constructed via collecting scattered electrons with the use of an ADF detector. This is a difference between conventional TEM, where scattered electrons are collected by an objective aperture. As the collected electrons in an ADF mode are not required to pass through an aperture, the number of scattered electrons collected is higher when compared to conventional dark field TEM. A specific type of ADF that is worth mentioning is high-angle annular dark field (HAADF), which uses high-angle electrons to produce an ADF image. This method is highly sensitive

to the atomic number Z of the elements of the scrutinised samples. More specifically, elements with higher Z produce a greater number of high-angle scattered electrons because the interactions between the nuclei and the electron beam is more pronounced. Hence, the signal from elements with higher Z leads to their brighter appearance in the images. This will be used for the analysis of the elemental distribution of our samples, in Chapter 4 of the current thesis, where increased presence of Ga as the heaviest elements leads to higher brightness on the ADF images.

TEM measurements were regularly employed in our work and played a key role in the thorough characterization of our samples, whilst they helped in elucidating their behaviour at optical probing. The measurements were performed by our collaborators in the University of Warwick. Via EDX and TEM analysis, we evaluated the compositional distribution of our structures and highlighted the interesting, irregular findings, which will be analysed further on in the current thesis. TEM measurements were conducted via a JEOL 2100 facility and doubly corrected ARM200F microscopes, all operating at 200 kV. It is important to point out that, as a necessary step in sample preparation prior to the measurements, NWs were transferred onto porous carbon grids. Our images include BF, DF and ADF images along with subsequent EDX measurements such as scans and mappings. These will be discussed thoroughly in chapters 3-5 of the thesis.

2.2.3) Photoluminescence measurements

Apart from the structural characterization, an important step is the optical performance of the nanostructures and the investigation of the emission spectra deriving from them. This is particularly beneficial for determining the potential that

these structures exhibit for future device implementation but also for detecting imperfections and adjust the growth conditions to optimize the sample performance. The above can be achieved via PL measurements. The phenomenon of PL is essentially emission of light stemming from the absorption of photons by the material. It derives as a result of excitation, by photons that excite electrons to a higher energy level. The typical case involves excitation of a semiconductor via a light source (most frequently a laser source), which provides photons with an energy that is higher than the bandgap energy of the material. The aforementioned photons are absorbed, leading to the formation of electrons in the conduction band and holes in the valence band of the semiconductor. More specifically, the electrons in the valence band absorb the energy of the incident photons and pass to the conduction band, leaving holes at the valence band behind them. These photoinduced electron-hole pairs recombine radiatively, which leads to photon emission.

In the vast majority of the experimental procedures related to PL measurements, the excitation is non-resonant, signifying that the semiconductor structure is excited with excess energy. The excitation energy is usually discriminated by using an optical filter. In the first moments after excitation, the distribution of carriers is regulated by the width of the excitation spectrum and is usually similar to Gaussian distribution. Following this, carrier scattering occurs most frequently via phonon-related scattering. This leads to a partial relaxation of the system. Eventually, the carrier system is cooled down via emission of phonons.

Despite the ideal scenario described above, in real-time experiments each system will induce imbalances. The most typical example is structural defects that always exist at least in small densities, even at carefully grown material systems. These defects lead to carrier localization via trapping mechanisms which increase the emission

lifetime. Additionally, defects can act as scattering centres that can be hazardous towards the intensity of the emission. Additional peaks may appear as well, the overlapping of which frequently results in inhomogeneous broadening of the emission peaks in the spectra. Another source of disorder is the non-uniform elemental distribution, which is the case in ternary NWs and poses a significant obstacle for the efficient optical behaviour of the structures. Another frequent feature that causes deviations from the theoretical models is surface states in the case of structures with a large surface-to-volume ratio, such as NWs, NWQDs and nanosheets. The surface states can act as non-radiative recombination centres that lead to a radical decrease in the PL signal and can potentially harm the functionality and applicability of the nanostructures as light sources.

For a more representative depiction of a PL setup, a basic schematic diagram with the key components is illustrated in Fig. 2.7. The laser source emits light of a specific wavelength that is reflected via the use of a mirror and reaches the sample after being transmitted through a neutral density filter. The role of the latter is to reduce the intensity of the incident light, which is achieved via absorbing a part of it. It is noted that in some cases, instead of absorption neutral density filters can reduce the intensity of the emitted light via reflection. Following this step, the light is focused on the sample via the use of lenses. It is significant to mention that the sample is mounted on a cryostat which allows for the control of temperature and allows the user to acquire PL spectra at low temperatures. After the light is emitted from the sample via the mechanisms described above, it is focused on a detector via the use of the focus lenses. The light reaches the detector and then reaches a monochromator, whose role is to transmit a band of selected wavelengths among the ones available. The importance of this component will be analysed later in the current chapter. After the

procedure described above, the data that are being transmitted are projected on a screen.

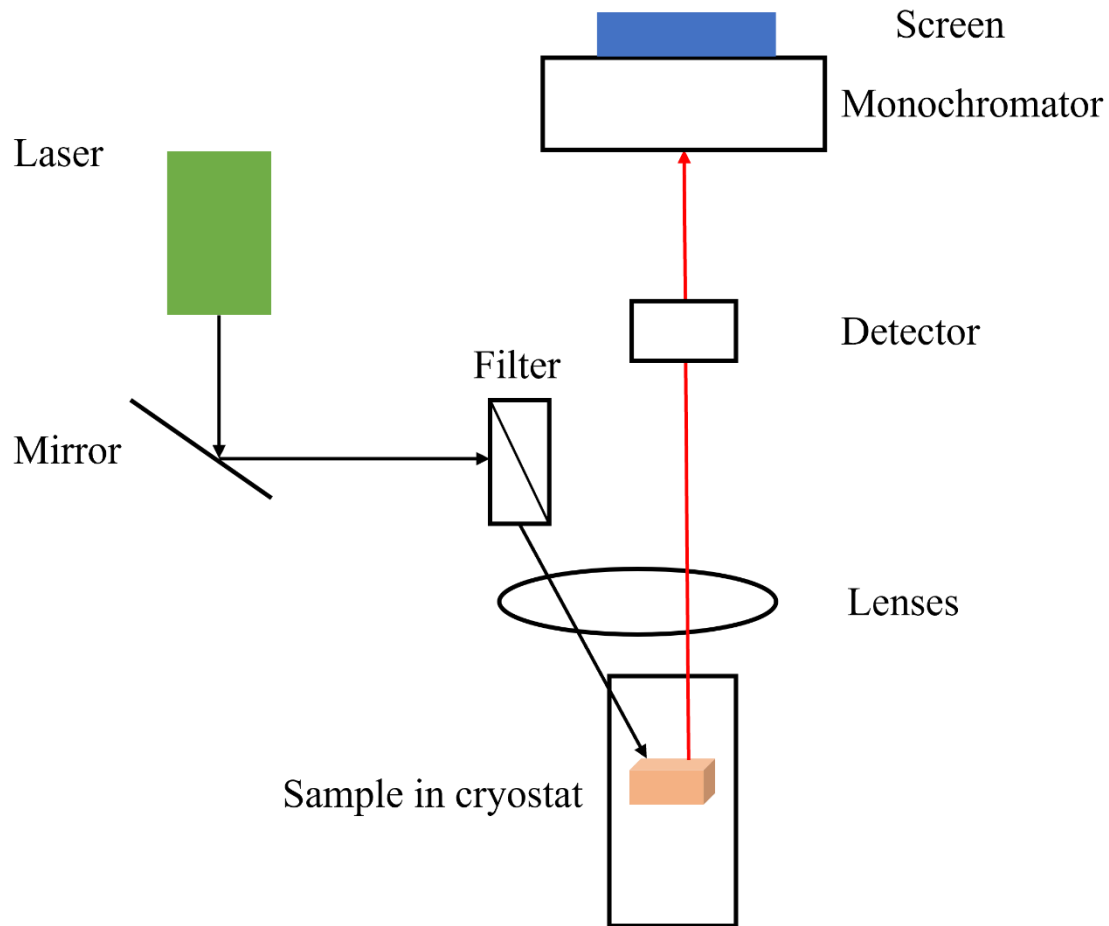


Figure 2.7: Schematic representation of a PL setup including its key components. The incident beam is depicted in black, while the emitted beam is depicted in red colour.

The exhaustive use of PL systems in the characterization of nanostructures have led to valuable results having been acquired. It is noted that the profound impact of deviations caused by crystal imperfections and the subsequent evaluation of the results can be frequently addressed phenomenologically. Nevertheless, their value in material evaluation and inferences on the optical properties of semiconductor nanostructures is of vital importance.

PL measurements can stem from the entire ensemble (macro-PL) or from individual NWs of the sample (micro-PL (μ PL)). The macro-PL setup we used in our lab to obtain the spectra is depicted in Fig. 2.8. In μ PL the laser beam is focused on a much narrower area of the wafer in order to address individual structures of the NW ensemble.

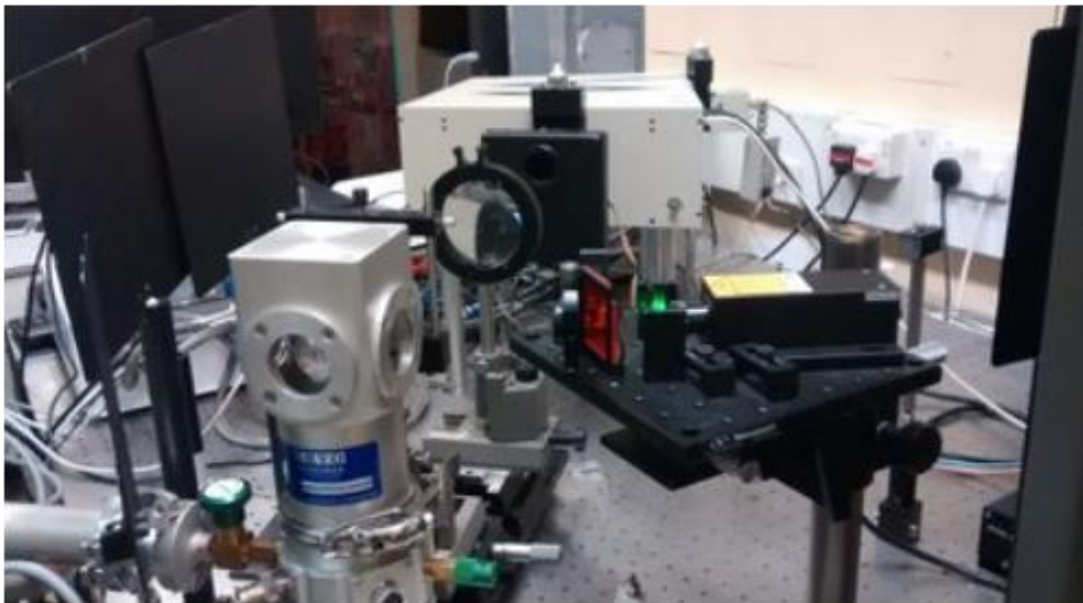


Figure 2.8: Macro PL setup at UCL facilities, using a green laser as the excitation source.

In our lab, we have used a macro-PL self-setup comprised of a 532 nm, green laser as the excitation source and Si or Ge detectors for light detection, each of which covers different regions of the wavelength. Another vital component of the system is the monochromator. The function of this optical device is to transmit a narrow band of selected wavelengths from a wide range of available wavelengths of the emitted light. In order to accomplish this objective, the monochromator employs the phenomenon of optical dispersion in a prism to spatially separate colours of light. The selected

colour, which is the light of a specific wavelength range, is guided to an exit slit and is subsequently directed towards the sample. It is important to note that the dispersion is controllable if the light is collimated, which means that all the rays of light are parallel. That can be achieved only in sources that are placed away from the monochromator. In this practical application, however, the laser source is positioned in the vicinity of the monochromator. Hence, it is necessary to include an optical system in the monochromator that converts the diverging light of the laser source to collimated light. This can be frequently achieved via the use of collimating mirrors.

The setup allows for measurements at low temperatures (down to 10 K) via the combination of a vacuum pump and a liquid helium compressor. This way, temperature-dependent measurements from 10 K to room temperature (RT) can be performed. On the other hand, μ PL measurements were conducted in the University of Sheffield. Prior to these measurements, individual NWs were dispersed onto Si substrates. The laser beam is focused on a small area of the wafer to excite single NWs and inspect their behaviour. The samples were first mounted into a cryostat supplied with liquid helium, in order to reach low temperatures of 5 K or below.

After having described the different systems and setups that were used for the realization of our project, we will proceed to the analysis of the results that were obtained from the experimental work that we conducted in our lab and will be thoroughly discussed in the following four chapters of the thesis.

Chapter 3: AlGaAs Nanowires on Si (111) Substrates

3.1) Background Information

Among the various semiconductor alloys available, group III-V semiconductors are particularly vibrant for scientific research in optoelectronic applications and silicon photonics. Their optically attractive characteristics include the direct bandgap, which renders them good candidates for light-emitting applications such as lasers and LEDs, whilst the high carrier mobility widens their potential for implementation in devices such as high-speed transistors. Furthermore, the realization of ternary III-V alloys allows for a broadly tuneable emission from visual to mid-infrared range depending on the composition of the alloy, which in turn can be regulated to a great extent by the choice of the suitable growth parameters, as thoroughly described in Chapter 1. The growth mechanism in MBE systems along with the efficient tolerance of large amounts of strain in NWs facilitated to grow III-V NWs monolithically on Si substrates, regardless of their lattice mismatch. It is noted that despite the benefit of elastic strain relaxation, there are challenges that could render the combination of compositing elements demanding. Additionally, the core/shell architecture regularly employed in NWs can significantly widens the range of materials that can be combined although it leads to crystal defects being formed due to inelastic strain relaxation at the core/shell interface.

Based on the above, an important quality exhibited in NW structures is their capability to be monolithically integrated on the mature and easily accessible Si platform. Thus, on-chip integration of NWs can be achieved to exploit them in fabrication of electronic and optical circuits. In the past, lots of materials have been

combined and their growth conditions have been carefully optimized to be adjusted to specific expectations and aims.

The importance of the ternary III-V alloys that was described earlier generated the need for exploration of their properties as active materials of optoelectronic structures. Among the various material combinations, AlGaAs has been particularly attractive as a result of its combination with the mature GaAs platform and its ability to emit at red and near-infrared regions depending on its composition. More specifically, AlGaAs is a ternary alloy with a bandgap varying between 1.42 eV (GaAs) and 2.16 eV (AlAs) depending on the composition of Al. The near-infrared emission that can be acquired renders AlGaAs intriguing for applications in the field of electronics and optoelectronics. For these reasons, the growth of AlGaAs NWs has already been reported in the past via the bottom-up approach.^[219-223] It is noted, however, that in all of the existing works, this has been obtained via the Au-assisted approach, which can lead to metal-related contamination, as described in the introduction. On the contrary, in our work, we achieved successful growth of AlGaAs NWs via the self-catalysed technique.

On top of that, the material combination of GaAs/AlGaAs has been frequently employed for core/shell NW heterostructures where the role of the AlGaAs shell is threefold; first it acts as passivation for the surface states of GaAs core, second it protects the core from oxidation and third it confines the carriers in the core region.^[171] Such heterostructures presented enhanced PL features and strong polarization of the emission when compared to conventional GaAs NWs.^[224-225] The GaAs/AlGaAs core/shell architecture has also been adopted for lasers, which have more stringent requirements regarding the NW optical properties.^[18, 226]

For the growth of the AlGaAs NW samples, we used epi-ready p-type Si (111) substrates, covered with native oxide with a diameter of 3 inches and a thickness of 380 μm . The substrates were initially inserted in the system via the load-lock module and were degassed in the buffer chamber by thermal annealing at 600°C for 60 mins to remove contaminants. The thermally prepared substrates were then moved to the growth chamber to initiate the procedure. Initially, as the aim was to obtain self-catalysed AlGaAs NWs due to the aforementioned foreign metal-related issues, Ga was deposited on the Si substrate. It has already been shown that deposition of Ga under UHV conditions in an MBE reactor leads to the formation of Ga droplets acting as catalysts for the remaining growth process.^[247] It is noted that during Ga deposition the substrate was rotating at 10 rpm in order for Ga to be distributed as homogeneously as possible. Due to the temperature in the reactor exceeding the melting point of Ga (which is merely 29.76°C) the transition into Ga nanodroplets is ensured. The growth procedure is initiated via the formation of bare GaAs stems for 10 mins at 610°C, which is achieved by introducing As flux. The As flux that is used is 2.75×10^{-6} Torr while Ga flux matches to thin film growth rate of 0.6 ML/s, as established by earlier GaAs thin film calibrations on GaAs (100) substrates. The length of the GaAs stems was 600 nm. It is noted that even though the crystal phase of the GaAs stems was not scrutinized, based on previous report from our group the GaAs stems are expected to adopt a ZB crystal phase, while the subsequent introduction of Al is expected to cause formation of defects at the bottom region until the ternary growth is stabilized.^[218] Following this stage, Al was supplied to the reactor in order for the AlGaAs NWs to start growing. The Ga and Al flux that were used in the growth were anticipated to produce $\text{Al}_x\text{Ga}_{1-x}\text{As}$ thin films of the corresponding composition on GaAs (001) substrates. The flux of As was stable at 2.75×10^{-6} Torr for all of the grown

samples, resulting in an As/Ga beam flux ratio of 15. Based on the above, the V/III beam flux ratio varied depending on the Al content, as Al beam flux was the only variable that was modified. Specifically, for the samples with 10%, 20%, 30% and 40% nominal, atomic Al concentration, the beam flux ratios are 14.05, 13.12, 12.13 and 11.07, respectively. The nominal Al content was kept at a maximum of 40%, as further increase would cause a direct-to-indirect transition of the bandgap, rendering the samples optically inactive. It is noted that for the rest of the current thesis, by nominal composition we are referring to atomic compositions. It is also significant to mention that AlGaAs is expected to exhibit indirect bandgap in higher Al compositions. For this reason, the selected range of Al contents was chosen in order to inspect the impact of the elemental composition on the properties of the structures, while ensuring direct bandgap, hence optically active nanostructures. The samples were rotated during growth with a speed of 10 rpm. The total duration of the AlGaAs NW growth was 100 mins.

3.2) Morphological and Structural Analysis of AlGaAs Nanowires

The first step towards a thorough characterization of the grown structures is the performance of SEM measurements. SEM images were acquired for samples with varying Al content of 10%, 20%, 30% and 40%. The results are presented in Figs. 3.1a-d, respectively. The tilting angle that is used is 30°. From these figures it can be conspicuously viewed that the NWs were grown perpendicularly oriented on the Si substrates, signifying their elongation along the (111) direction. Another interesting observation is the well-defined spherical droplets at the NW tips, which indicate the successful VLS growth mode. This can be elucidated in Figs. 3.1a-d. What is also interesting to notice is that the samples containing 10%, 20% and 30% Al present a much higher NW density. This can be attributed to the modifications in the NW

morphology induced by the increased Al presence. Two morphological variations that are found are kinked and branched NWs. More information on this interesting phenomenon will be provided in chapter 4 of the current thesis.

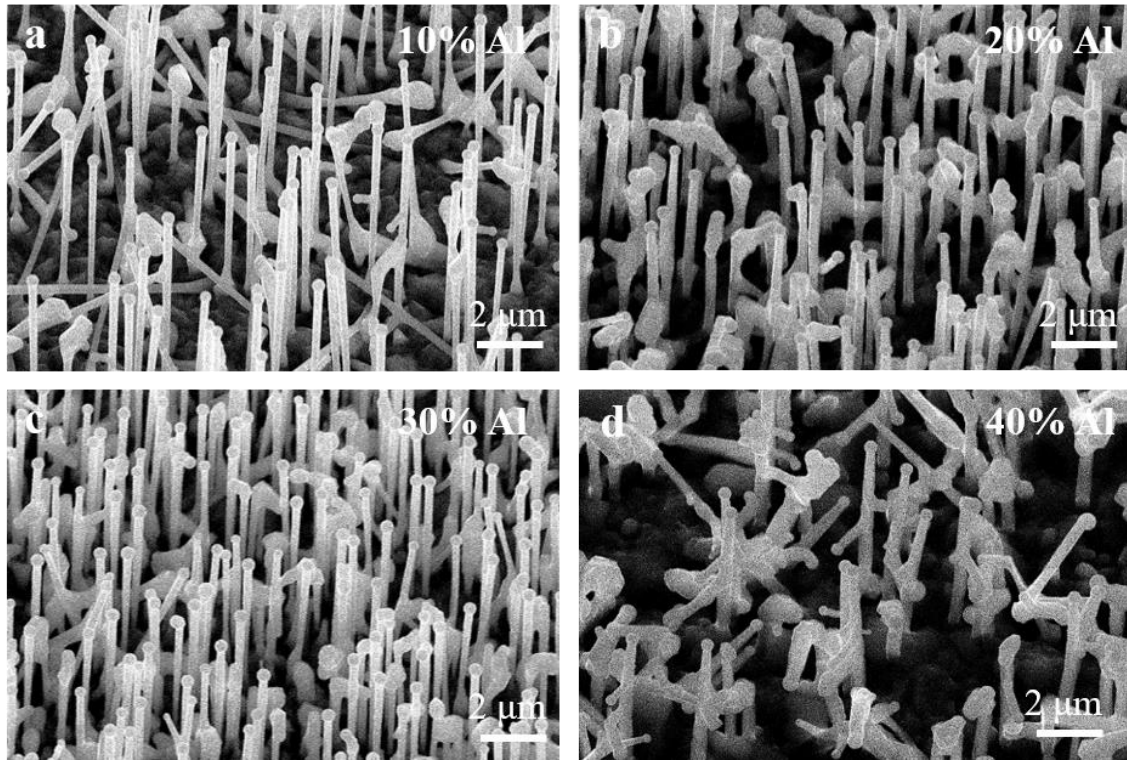


Figure 3.1: SEM images of the AlGaAs NW samples with atomic, nominal compositions of Al at: a) 10%, b) 20%, c) 30% and d) 40%. At 40% Al, several NWs are bent or not fully grown, rapidly decreasing the density of the standing NWs via lowering the vertical NW yield. The tilting angle in all of the measurements was 30°.

Increase in Al content has a significant effect in the dimensions of the NWs. To illustrate this influence, a brief statistical analysis was conducted on 100 individual NWs. The results are shown in Fig. 3.2. Al-deficient structures, where nominal Al content reached 10%, are thinner with a diameter of averagely 200 nm. It is clarified that this value corresponds to the diameter measured in the middle of the structure. In practical terms, the inverse tapered shape of the structures renders the diameter

distribution slightly inhomogeneous along the NW axis. For the measurement of the length of the NW, we were based on trigonometry and considering the scale bar we measured the length and the images and multiplied it with $1/\sin 30^\circ$, which was the tilting angle. The $\text{Al}_{0.1}\text{Ga}_{0.9}\text{As}$ NWs are rather long at 8 μm in length. What is observed with increasing Al composition is the shortening of the structures. At 40% Al, the length of the NWs is merely 4 μm . Meanwhile, their diameter is radically increased at 400 nm. These phenomena are correlated and are attributed to the lower diffusion length of Al atoms, leading to their preferential incorporation at the external facets of NW sidewalls, which leads to an increase in diameter. At the same time, increasing Al content causes a reduction in the length of the NWs because Al suppresses the diffusivity of Ga adatoms on the surface of the sidewalls. Hence, a smaller number of elements is incorporated in the axial growth and the majority contributes to the lateral expansion of the structures.^[223]

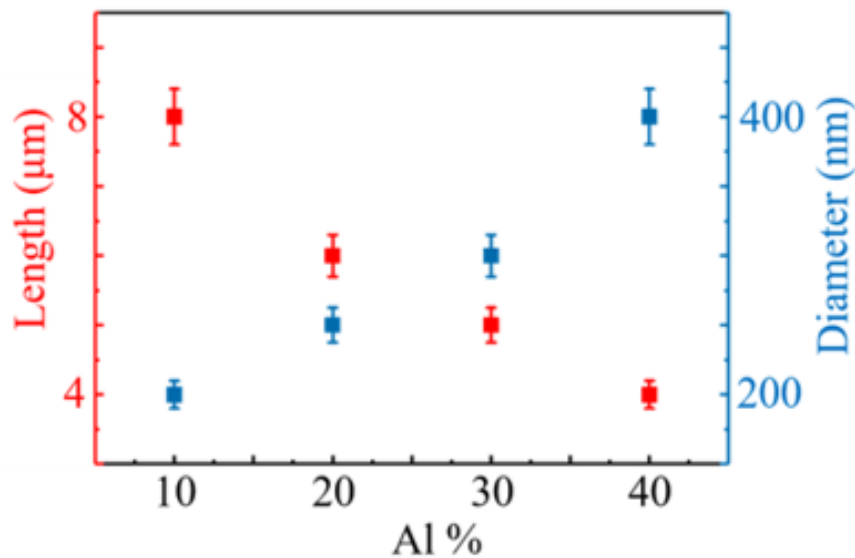


Figure 3.2: Statistical analysis of the length (red) and diameter (blue) of the NWs as a function of their Al content.

Besides, TEM analysis was conducted to assess the structural and compositional characteristics of the structures. It is clarified that even though all the samples were subject to the measurements, the results presented refer to NWs with 20% nominal Al content to show the typical structural characteristics. Initially, in order to corroborate the growth mechanism, EDX mapping was performed in the vicinity of the NW tip. These results are shown in Fig. 3.3a and confirm that the droplet is composed of a binary Al-Ga alloy, whilst As is not traced within the droplet. This signifies that Al is absorbed by the Ga droplet during the elemental supply in the reactor, which drives the VLS growth mechanism of ternary AlGaAs NWs. The absence of As is expected due to the low solubility of group V adatoms in the Ga droplet. Nevertheless, it is noted that there are some occasional NWs that deviate from this model. In these cases, the droplet is composed merely of Ga and no Al is detected possibly because of the high speed with which Al leaves the droplet after group III supply is terminated.^[219] This phenomenon is clearly illustrated while inspecting another NW with the same nominal Al content. Specifically, the TEM of the structure in Fig. 3.3b marks the direction of the scanning via the black arrow. EDX line scan of Fig. 3.3c reveal the Al signal at the NW tip rapidly drops and is reaching zero. Meanwhile, this scan exposes the highly inhomogeneous NW elemental distribution, with Ga increasing from the NW base to its tip and Al following the opposite trend. This will be further discussed and more scans will be presented further on in the current chapter.

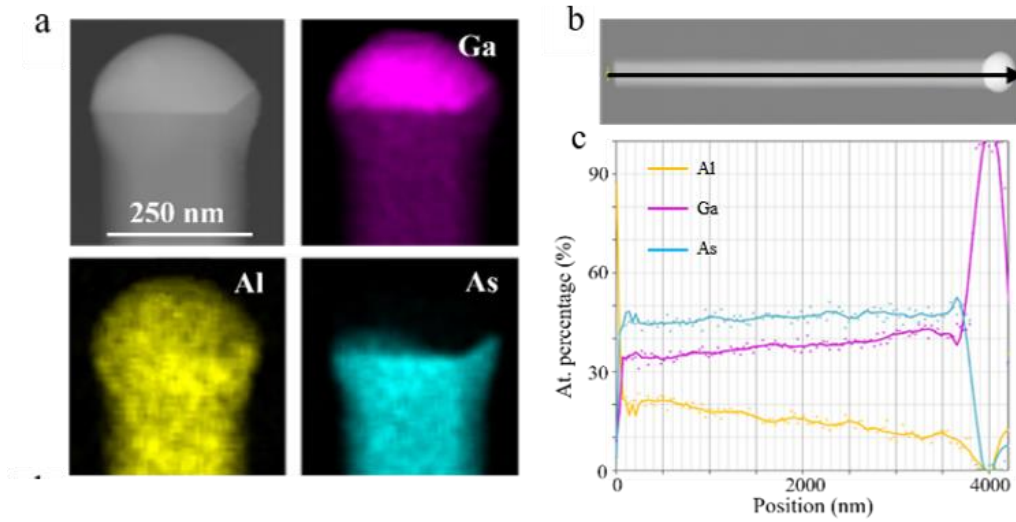


Figure 3.3: a) EDX maps of the droplet region in an AlGaAs NW with 20% nominal Al content exposing the formation of an Al-Ga alloy in the droplet. b) TEM image of an individual AlGaAs NW with the same nominal content, with the black arrow showing the direction of the scan. c) EDX line-scans along the direction of the black arrow in Fig. 3.3b. The droplet in this case is Ga-only as opposed to other cases.

Moreover, TEM study included a thorough investigation of the NW cross section. For this purpose, NWs were sectioned perpendicular to the growth direction by the use of an ultramicrotome. This way, ADF images were acquired for structures with 20% nominal Al content. The ADF of the bottom NW region, close to the base (Fig. 3.4a) reveals darker contrast layers surrounding the brighter inner part of the NW, which signifies the formation of an AlGaAs shell. The shell is self-formed and exhibits a significantly higher Al content than the NW core, since bright regions in ADF correspond to higher content of the heavier element, which in this case is Ga. Vice versa, darker contrast corresponds to deficiency of the heavier element, marking regions with higher Al content. The self-formation of an AlGaAs shell has been reported for AlGaAs NW growth in the past^[219-223] and is stemming from the low

diffusion length of Al, which promotes its preferential adhesion to the external facets of the NW sidewalls.

The self-formed shell presents two features: namely the variations in its thickness along the NW axis and the inhomogeneous elemental distribution. The former characteristic is distinguished by inspecting ADF images at different heights of the axis (Figs. 3.4b-c), where it can be seen that the thickness of the shell decreases towards the NW tip. More specifically, the thickness at the base is roughly 35 nm, thinning down in the middle at 18 nm and eventually vanishing close to the tip, where core-only NWs are viewed. As expected, the opposite trend is noticed for the core. The increasing thickness of the core is attributed to the reduction of the V/III ratio after the introduction of the Al material in the reactor, which causes an expansion in the volume of the droplet.^[226] The thinning of the shell, on the other hand, can stem from the short diffusion length of Al, as more Al adatoms are adhered to the NW sidewalls, whilst less Al is available to reach the top facets. This mechanism has been reported in the past for InGaAs, with a similar explanation having been formulated.^[248] Besides, the top part is formed later during the growth stages, meaning that it is less prone to develop a shell, opposite to the NW base which has been exposed to material supply for a longer period of time.

Regarding the second conspicuous feature of the inhomogeneous distribution in the shell, the same NW was examined as a representative example. An indicator is revealed in the ADF of the bottom region (Fig. 3.4a) where contrast variations are observed in the AlGaAs shell. This observation indicates the formation of intricate nanostructures with varying Al content, which in turn forms a sequence of quantum wells (QWs) and barrier layers. This can also be inferred by a higher-magnification ADF of the area within the red square of Fig. 3.4a, which is presented in Fig. 3.4d. The

variations are much more noticeable, while 5 positions at regions with different brightness were numerically investigated. The results are shown in the table of Fig. 3.4e, which reveals that Al contents in the shell range widely from 65% to almost 89%. Once again it is noted that the Al composition of the brighter regions is lower when compared to the darker regions. This phase separation, which manifests itself as alloy fluctuations, have been presented in the past and have been a focal point of scientific analysis, as non-uniformity in the composition can profoundly affect the properties of the structure in ambiguous ways. For instance, on the one hand it can lead to the appearance of multiple peaks in the optical spectrum, whose overlapping can cause inhomogeneous broadening of the emission, which could impede the applicability of the structures in light-emitting devices. However, on the other hand, it opens new routes and possibilities to be explored for novel, functioning nanostructures. A prototypical example is the self-assembly of GaAs QDs driven by Al fluctuations in GaAs/AlGaAs core/shell NWs that has been reported in the past.^[109]

It is noted that the extracted values in Fig. 3.4e were obtained via the use of point-EDX measurements. The quantification of the data in such experiments has been proven to be highly accurate but there are some factors that need to be considered. For instance, the impact of probe size and current in the X-ray related experiments is known. The standard deviation is given by the equation $\sigma = N^{1/2}$ where N is the number of X-ray counts in the examined peak after the subtraction of background. The total error is given by the equation: $\text{Error}(\%) = \pm 3 \cdot N^{-1/2} \cdot 100$,^[249] signifying that more counts lead to more accurate results. A typical acceptable error ranges between $\pm 1\%$ and $\pm 5\%$. In our particular experiments the error is roughly $\pm 2\%$, which renders the related experiments accurate.

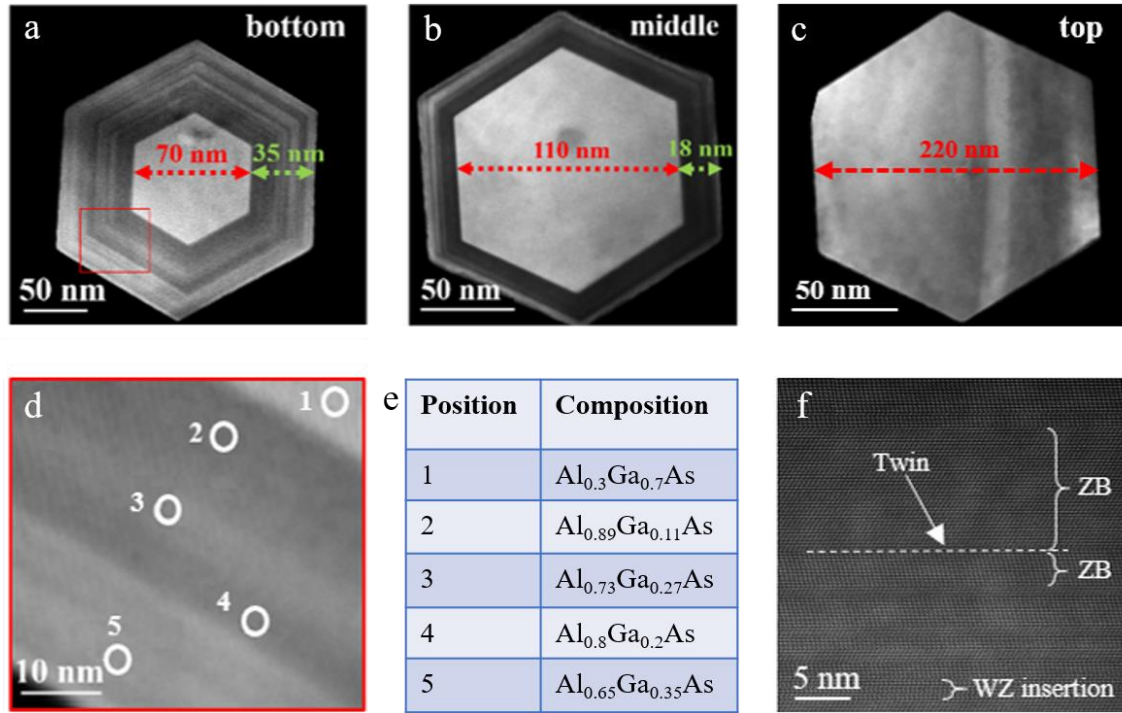


Figure 3.4: a-c) ADF images of the bottom, middle and top regions of an AlGaAs NW with 20% Al content, respectively showing the thinning down and final vanishing of the AlGaAs shell. The red box in Fig. 3.4a marks the area of focus for Fig. 3.4d. d) Higher magnification ADF image of the red square of Fig. 3.4a, where the elemental composition was extracted at the different contrast regions marked with the white circles. e) Numerical data from the extracted values in Fig. 3.4d, quantitatively displaying the alloy fluctuations. f) High-resolution TEM image of the AlGaAs NW, showing a WZ insertions and twin defects in the predominantly ZB crystal. One representative twin defect is marked by the dashed white line along its length.

Next, further TEM probing was required to obtain valuable information that would allow us to optimize NW design and growth conditions. For this reason, high-resolution TEM images were recorded to address the AlGaAs NW crystal phase. A typical image is presented in Fig. 3.4f. The crystal phase is predominantly ZB. It is noted that AlGaAs is inherently crystallized into the ZB phase, predominantly, due to its nature. Besides,

the diameter of the nanowires is relatively large, which promotes ZB over WZ crystallization. However, it can be conspicuously shown that severe twinning and occasional thin WZ insertions appear in the ZB crystal. The WZ insertions are thin up to 6 monolayers and they can be attributed to sequential ZB twinning.

The spontaneously formed AlGaAs shell has also been studied via using EDX mapping. In the following Fig. 3.5a, an AlGaAs NW with nominal 20% Al composition is investigated via ADF imaging. It is conspicuously shown that contrast variations are wide in the entirety of the shell region, indicating alloy fluctuations manifesting themselves as phase separation features. In order to thoroughly examine the aforementioned phenomenon, EDX mapping of this structures was conducted for Ga and Al. It is noted that As is assumed to be homogeneously distributed in the NW shell. Fig. 3.5b illustrated an image where the individual maps of Ga (Fig. 3.5c) and Al (Fig. 3.5d) are overlapping, with purple sections signifying Ga-richness and yellow sections Al-richness. The maps confirm the varying Al and Ga compositions in the shell, forming a complex compositional distribution in the NW shell.

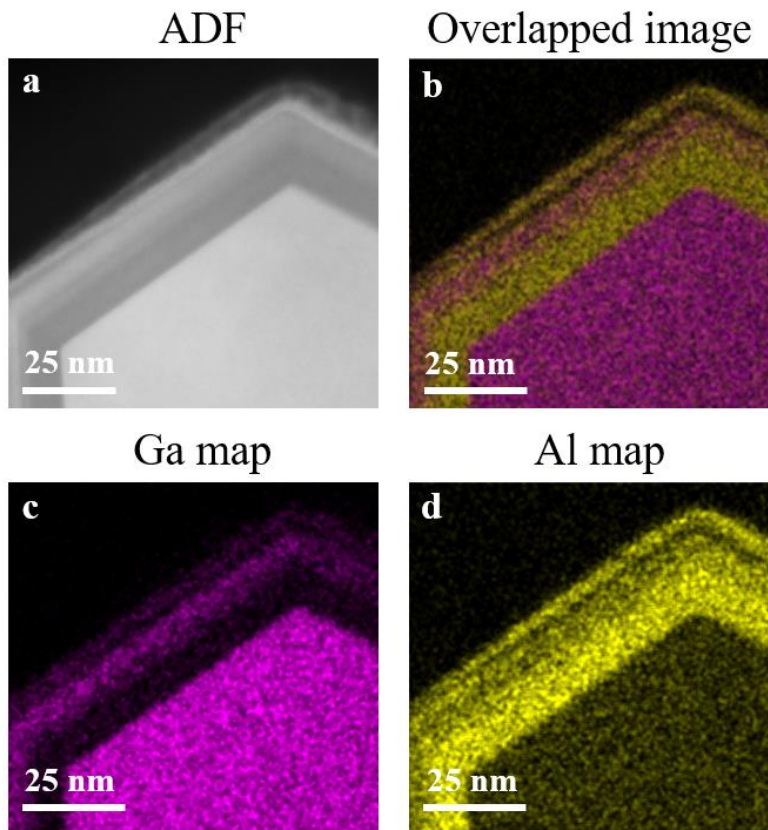


Figure 3.5: a) High magnification ADF image of the shell, depicting the contrast variation. b) Elemental map of the same image as that in (a), where purple and yellow regions indicate Ga -rich and Al -rich regions, respectively. c-d) Individual EDX maps of Ga and Al, respectively, exhibiting both Al and Ga-rich regions in the NW shell.

After having described the peculiarities in the compositional distribution and morphology of the self-formed shell, the elemental distribution of Al, Ga and As along the entire length and diameter of the structures will be discussed. This has been determined by EDX measurements conducted on individual AlGaAs NWs with 40% nominal Al composition. The results are presented in Figs. 3.6. First, we focus on the radial scanning of the NW (Fig. 3.6a), where it can be inferred that the effective Al composition varies widely at the NW cross section. As mentioned earlier, Al tends to

be incorporated at the external facets of the NW, which leads to the spontaneous formation of an Al-rich shell (Fig. 3.6b).^[250] This is attributed to the intrinsically low diffusion length of Al, which renders it preferential for Al adatoms to adhere to the side facets rather than propagate towards the droplet seed. Furthermore, highly complex and non-uniform distribution is noticed along the NW axis (Fig. 3.6c), where Al is observed to be much more concentrated on the NW base, due to its low diffusivity, whilst the top regions in the vicinity of the tip are Ga-rich.^[250] It is interesting to notice that oxygen distribution follows the same trend as Al, being more pronounced close to the NW base. This is a direct result of the easy oxidation of Al. The intricacy of the compositional distribution could be possibly arising from the different diffusivity of Al and Ga. Specifically, the shorter diffusion length of Al leads to its preferential incorporation in the external facets and in the bottom region of the NWs, while the vicinity of the NW top exhibits a significantly higher Ga percentage when compared to the NW base.

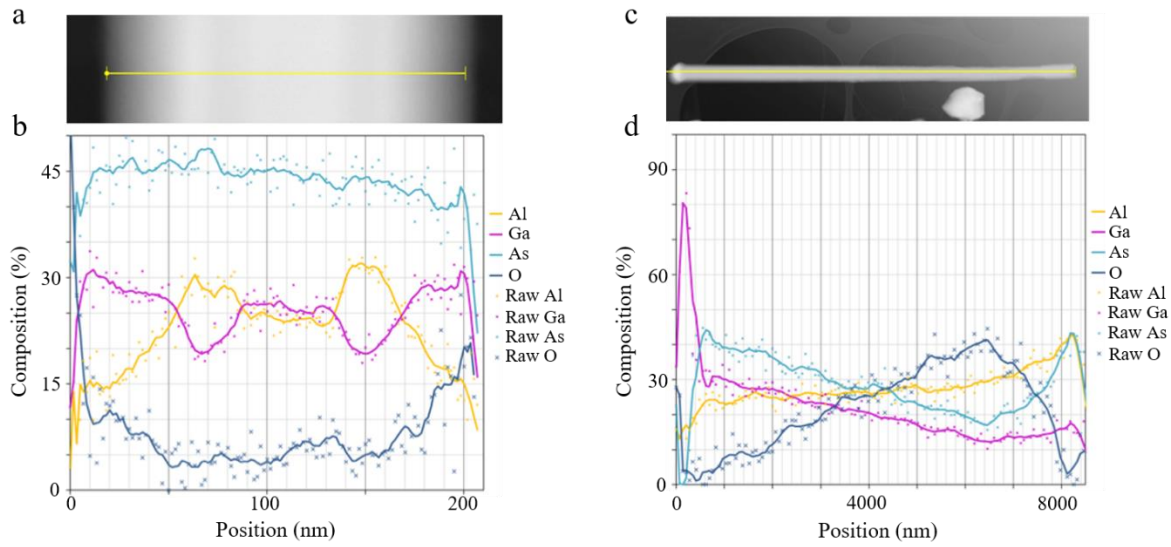


Figure 3.6: a) Direction of the EDX scanning at the cross section of the NW. b) Graph of percentage of each element along the direction of the scanning. The peak in Ga and dip in O and Al at the center of the wire which is the higher brightness segment of the upper image, confirms our speculations about the Ga-rich core of the structure. Al is concentrated in the external facets spontaneously forming a shell-like structure. c) Direction of the EDX scanning along the axis of the NW. d) Graph of percentage of each element with the distance from the NW tip. In the image below we see the graph of the percentage of each element with the distance from the tip. The percentages refer to the center of the NW.

It is significant to mention that the widely inhomogeneous elemental distribution along the NW axis that has been established from Fig. 3.6b has been frequently observed in III-III-V NWs and is attributed to the fact that group III elements have a high solubility in the droplets, which means that the stability and balance are sensitive to the conditions. Nevertheless, there have been efforts to study the impact of growth parameter alterations on the elemental distribution of III-III-V NW structures. For instance, InGaP NWs grown via MOCVD have demonstrated widely inhomogeneous

axial elemental distribution, which has been suppressed by linearly increasing the supply of In.^[251] This led to increased homogeneity along the NW axis. It is noted, however, that the application of this technique could be limited in the case of AlGaAs as the bandgap of the alloy becomes indirect at 40% Al content which hinders their applicability in optoelectronic devices. Hence, increase in the Al composition should be carefully designed in order to ensure the direct nature of the AlGaAs bandgap.

It is also known that temperature has a profound impact on the elemental ratio, hence the composition of the NWs. A paradigm is the study of the effect of parameter alterations on the composition of InGaSb NWs,^[242] where it has been shown that increasing temperatures affect the ratio of In and Ga, thus allowing for changes on the elemental distribution of ternary NWs. It is interesting to mention that the frame for change of temperature in the case of AlGaAs is relatively narrow as high temperatures lead to reduced supersaturation, hence slower axial growth rate.^[228] However, increasing Al content improves thermal stability due to the enhanced AlGaAs barrier layers and the self-formed Al-rich shell. This could allow for a wider window for the optimization of the growth temperatures. Nevertheless, due to the challenges related to the sensitive nature of the growth and the indirect nature of the AlGaAs bandgap for Al content above 40%, there are no extensive reports regarding the study of the parameter change on the elemental uniformity of AlGaAs NWs. Hence, further works on this particular topic are important.

3.3) Growth Mechanism of AlGaAs Nanowires

Following the structural measurements and interpretation of the obtained results and prior to conducting optical experiments on the AlGaAs NWs, it is important to establish the growth mechanism. The formation of the AlGaAs NWs is regulated, in

principle, by the diffusivity of Al and Ga adatoms. As already explained in the introduction, the incoming elemental fluxes can lead to either atoms being incorporated via direct impingement on the droplet seed or atoms adhering to the structure by diffusing along the NW sidewalls. In the second case, the diffusion length of Al and Ga are important for the spontaneous formation of the AlGaAs shell and its morphology of varying thickness.

The much longer diffusivity of Ga renders it preferential for the Ga adatoms to reach the group III droplet and hence participate in the axial elongation of the NWs via the VLS growth mode. This is the source of the higher percentage of Ga that is exhibited in the core, which is even more pronounced in the vicinity of the tip. Opposite to this, the short diffusion length of Al makes it challenging for Al adatoms to reach the group III droplet as they are most likely adhered to the sidewall facets via the VS growth mechanism occurring during lateral NW growth. The above procedure is illustrated in the schematic representation of Fig. 3.7. It is noted that the core is presented in light blue, while the Al-rich, AlGaAs shell is illustrated in dark blue in the corresponding figure. Specifically, in Fig. 3.7a, the Ga droplet is formed via deposition of Ga atoms on the Si substrate. In Fig. 3.7b, As is introduced and the first 600 nm of bare GaAs stems are formed. Furthermore, Al is introduced in the reactor and the ternary NW growth begins. The elongation of the NW at the first stages is originating from direct impingement of Al and Ga on the droplet or to diffusion on the Si substrate. As the length increases (Fig. 3.7c), the lower diffusivity of Al leads to less Al adatoms reaching the droplet. Hence, the core is Ga-rich. On the contrary, Al preferentially adheres to the sidewalls leading to the self-formation of the Al-rich shell. It is also noted that the shorter diffusion length of Al explains two observations. First the higher concentration of Al in the bottom region of the NW core, when

compared to the NW tip and second the decreasing thickness of the shell from bottom to top. Finally, the elemental supply is terminated and the NW growth stops. At this stage it is clear that the NW tip is comprised of a core-only structure which contains a higher Ga percentage than Al (Fig. 3.7d). This mechanism is in accordance with all the aforementioned findings of the TEM analysis.

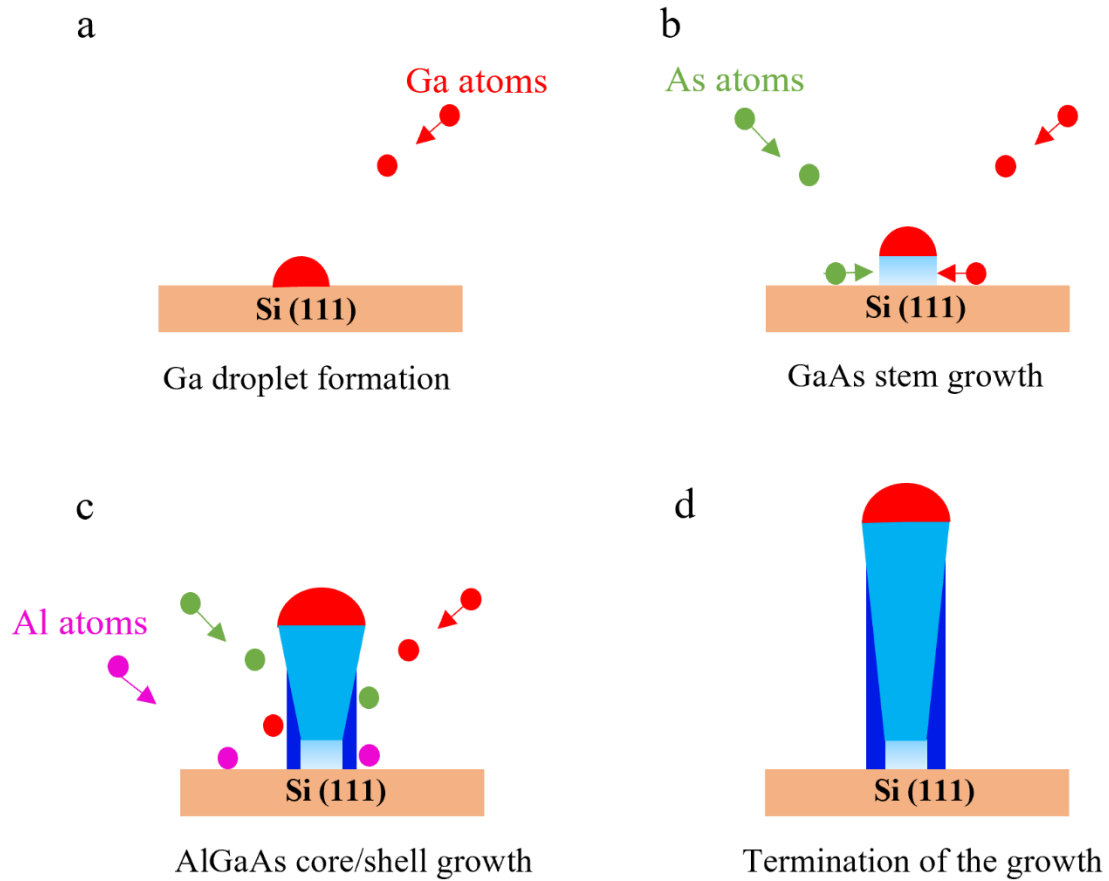


Figure 3.7: a-d) Schematics of the growth mechanism of the AlGaAs NWs, revealing the realization of the spontaneously formed Al-rich AlGaAs shell, with decreasing thickness from bottom to top, depicted in dark blue. Ga, As and Al atoms are depicted in red, green and purple colors, respectively.

3.4) Optical probing of AlGaAs Nanowires

As mentioned earlier, ternary AlGaAs NWs have the potential for ameliorated optical properties in terms of the intensity of the emission, the linewidth and the tunability of the emission wavelength. It is noted however that NWs were not tailored and spontaneously adopted an inversely tapered shape that was described in the previous sections. For the optical probing of the NW samples, we measured NWs with nominal composition of Al varying between 10% and 30%. It is highlighted that Al-richer NWs of 40% nominal content were also probed but no optical signal could be detected.

Specifically, low temperature μ PL was carried out on individual NWs with nominal content within this range. Three representative spectra, each corresponding to a single NW from each sample, are presented in the inset of Fig. 3.8a, Increasing Al content leads to a non-negligible blueshift of the emission, due to the increasing bandgap energy. The outset of Fig. 3.8a demonstrated room temperature macro-L measurements on the NW ensemble. The first, important conspicuous feature is the robust room temperature emission, which renders the structures promising for device implementation. Besides, PL measurements can provide us with valuable data to estimate and assess the real composition of the structures, which is important for their future design and functionality. The real composition of the NWs was calculated via employing the empirical equation $E_g(x) = 1.422 + 1.2475x$, where x is the Al fraction and E_g is the bandgap energy at room temperature.^[252] Based on the emission wavelengths of the RT ensemble (Fig. 3.8a outset) and corresponding them to bandgap energy, the effective Al composition of the samples with 10%, 20% and 30% nominal Al content is $7 \pm 2\%$, $13 \pm 3\%$ and $22 \pm 4\%$, respectively. It is noted that these estimated contents correspond to an optically average value that was determined by PL measurements. The actual compositional distribution may exhibit wide variations

along the NW axis and cannot be determined with high precision. The fact that room temperature emission is strong exhibits the potential of these structures as on-chip light sources, taking into consideration their relatively easy integration on the mature Si platform. Nevertheless, two factors should be considered, namely the lack of emission from samples with 40% Al and the high complexity of compositional distribution and structural features that could deteriorate the optical performance. These two factors indicate that further optimization of the growth is required.

Meanwhile, μ PL spectra were obtained at low temperature (roughly 6 K) at different positions along the NW axis. The laser spot was about 1 μm and the excitation wavelength was 515 nm. This enabled us to evaluate the spatial variation of the Al content. For each NW, spectra were acquired at equidistant positions along its axis. The results are presented in Fig. 3.8b, the top axis of which is calibrated to indicate Al composition using the AlGaAs bandgap vs composition relationship at 6 K. The length of each NW is also indicated in the corresponding figure. The first, distinct feature of the spectra is the multiple, sharp emission lines of varying intensity and position along the NW axis. This phenomenon is stemming from the fluctuations in the distribution of AlGaAs composition. Specifically, due to the very low incident laser power, which was roughly 6 μW , a low density of localized states generated by the aforementioned alloy fluctuations are excited and recombine producing the sharp emission lines. The peaks are weaker in the vicinity of the NW ends and are much more robust in the middle region of the structures. Due to the necessary NW preparation for μ PL measurements, which included their transfer onto different substrates, it is impossible to distinguish the bottom and top facets with certainty. It is interesting to observe that increasing laser power led to the replacement of the series of sharp peaks by a broad, continuous emission, more reflective of the average Al content. A representative spectrum

depicting this broadening of the peak due to coalescence of the sharp series of peaks is shown in Fig. 3.8c, for an individual NW with 20% nominal Al content. The Al compositions estimated from the high-power spectra are 6%, 13% and 22% for NWs with 10%, 20% and 30% Al content, respectively. These values are in reasonable agreement with the ones based on macro-PL measurements.

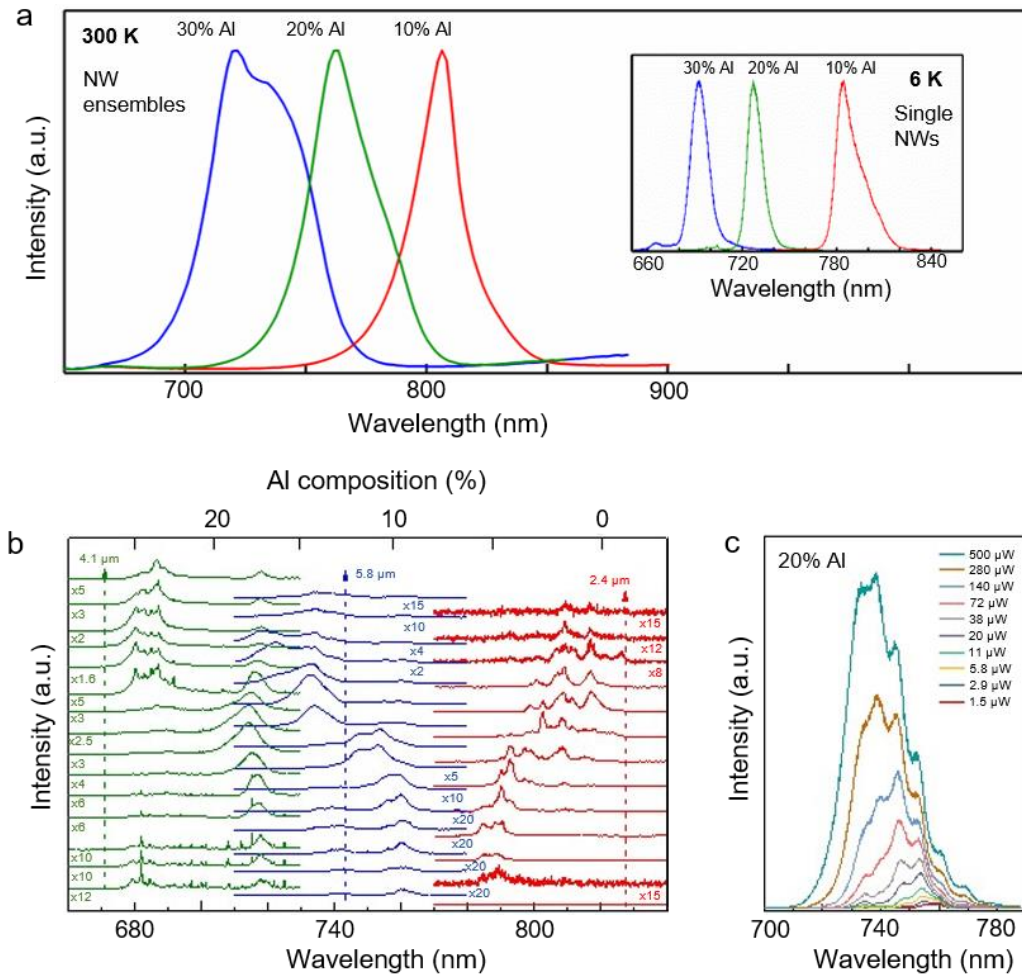


Figure 3.8: a) Outset: Room temperature PL measurements of the AlGaAs NW ensemble with different Al contents. Inset: Single AlGaAs NW μ PL spectra are depicted. b) Position-dependent μ PL spectra for samples with 10% (red), 20% (blue) and 30% (green) Al content. Based on the peaks, the spatial variations of Al content are marked at the top axis. c) Power-dependent spectra from an individual NW with 20% nominal Al composition, where the broader peaks at higher powers are viewed.

It is interesting to clarify that the optical response as determined by the PL analysis of the AlGaAs NWs that we acquired has been substantially different from the well-studied PL response of binary GaAs NWs. First and foremost, the location of the PL peak is different as a result of the bandgap change of the alloy with the introduction of Al. In the reported works the GaAs NW peak is located at a range of 1.45-1.52 eV, corresponding to wavelengths between 816 nm and 855 nm, depending on the structure,^[253] doping^[254] or substrate used for the growth.^[255] On the contrary, in our case the peaks were located at essentially lower wavelengths ranging from 720 nm to 805 nm, depending on the Al content. That is anticipated as the inclusion of Al in the alloy leads to a higher bandgap energy. This has been examined in the past via comparing bare GaAs NWs with multilayer GaAs/AlGaAs NWs, observing that the peak of the AlGaAs-containing samples is located at higher energies (lower wavelengths) when compared to the peak of bare GaAs samples.^[219] It renders AlGaAs NWs attractive for tunable red and near-infrared light emission and other applications in this range of the spectrum.

The growth conditions are crucial in terms of the optical properties of AlGaAs NW structures. First and foremost, Al content regulated the emission wavelength, as increased Al presence causes a blueshift of the emission peak, as observed above. Considering that the Al content is controlled by the Al/Ga and V/III ratio, these parameters are linked directly to the optical properties of the structure. For instance, in our experiments we see that increasing Al/Ga ratio and decreasing V/III ratio leads to higher Al content in the samples, while it is mentioned that 40% Al samples did not emit light. Moreover, the duration of the growth is important, as reduced growth time does not allow for axial structures to be fully developed and impacts their morphology and crystallinity, which can have an impact on the optical properties of the NWs.^[228]

For this reason the duration of growth in our work was chosen to be 100 mins, which was enough for the realization of fully-formed, axial NWs. Importantly, temperature is also a key factor, as increased temperatures could cause reduction of the PL signal,^[228] while on the other hand reduced temperatures render inhomogeneous elemental distribution easier, which can lead to suppression or significant broadening of PL peaks. Ergo, it is important to carefully optimize the growth parameters while designing and fabricating the structures. In our case, the moderate growth temperature allowed for robust PL peaks being presented, while the non-uniform distribution did not significantly distort optical features.

It is also mentioned that bare GaAs without the additional growth of a shell are rendered sensitive to surface-related processes in terms of their optical properties. It has been shown that unpassivated GaAs NWs can exhibit a surface charge density of roughly 10^{12} cm^{-2} which leads to carrier depletion in the surface, while in GaAs/AlGaAs core/shell NWs grown via the same method carriers recombine through surface states mainly.^[256] On the contrary, in the case of AlGaAs NWs, the AlGaAs shell is spontaneously formed, providing surface passivation which can eliminate carrier trapping at surface states. The spontaneous formation of the shell ensures surface passivation without having to modify the growth conditions. Based on the above, it can be inferred that the importance of the AlGaAs NW optical properties is based on the tuning range of the emission depending on the composition of the ternary alloy and their suitability for red and near-infrared light emission, along with the inherent surface passivation via the spontaneous core/shell configuration.

It is interesting to point out that there is a spotted inconsistency between the TEM data and the calculated compositional values based on the PL experiments. Whilst TEM reveals effective Al compositions higher than the nominal values, calculations of

the bandgap based on the PL emission peaks correspond to largely lower Al contents. This can be clearly deduced by the values demonstrated in Table 2 below, where the PL-based content is significantly lower than the EDX measured values or the nominal composition. In order to interpret this situation, three potential reasons were reflected.

Nominal Al %	EDX Al %		PL RT Al %	μ PL 6 K Al %
	Range	Mean Value and Standard Deviation		
10	11-18	13.5 \pm 2.3	7 \pm 2	5 \pm 1.2
20	17-48	29 \pm 5	13 \pm 3	13 \pm 2.2
30	32-49	39 \pm 5	22 \pm 4	22 \pm 1.4

Table 2: *Effective Al contents based on EDX measurements and PL-based calculations, respectively.*

Initially it is significant to mention that the higher Al content deduced by the TEM data is anticipated for the NW growth. The reason for this is that under the temperature conditions that prevailed during growth (640°C), the formation of Al-rich clusters and unintentional superlattices is promoted.^[256] On the contrary, the nominal values are based on earlier calibrations for thin film growth at lower temperature. Hence, the effective Al content is expected to be higher than the nominal. A potential factor that participates in the lower Al content inferred by the PL spectra is that there is a thick epilayer between the NW root and the Si substrate that is formed during AlGaAs growth, which could shift the peaks to lower wavelengths and affect the calculations. Nevertheless, this phenomenon is rapidly excluded as the actual cause of the discrepancy for two main reasons. First, similar results of lower Al content than the nominal were deduced via the μ PL measurements as well, where the samples were transferred onto SiO₂ substrates and the epilayer was absent. Second, if the epilayer

was optically active, we would expect a second peak at the lower wavelength range, which is not the case. As a result, the impact of the AlGaAs epilayer on the optical measurements can be considered negligible.

Next, a second factor that needed to be taken into consideration is the polytypic nature of the NWs, that was mentioned earlier. This can be observed in the TEM image of Fig. 3.9, where the ZB phase is interrupted often by twinning segments, whilst there is a conspicuous WZ insertion at the bottom of the image, as marked in the figure. It is already known that the bandgap of WZ AlGaAs is effectively higher than the one of ZB AlGaAs, which signifies that carriers could diffuse into the WZ sections prior to recombination, leading to emission peaks shifted at lower wavelengths, which correspond to lower Al contents.^[257] This can be further supported by the results of the calculations for the Al content based on PL measurements if we consider ZB or WZ phases, respectively (Table 3). It can be inferred that the values for WZ phase AlGaAs match the nominal contents and the effective contents measured by EDX much better. This theory can have an impact on the inconsistencies observed between the two types of measurements used to define the bandgap of the alloys.

Last, it is considered that the compositional distribution exhibits significant variations along the axis of the NW (as easily distinguished in Fig. 3.6d). Under these circumstances, most contribution of PL emission may derive from the lower energy bandgap of the AlGaAs NWs, which presents a lower percentage of Al, when compared to the average value. On the contrary, EDX data better reflect the average value of the non-uniformly distributed elements along the NW axis. It is also possible, if we reflect on the wide range of the compositional variations that were described earlier in the text. For this reason, the calculated values are lower than the ones observed in the EDX analysis earlier.

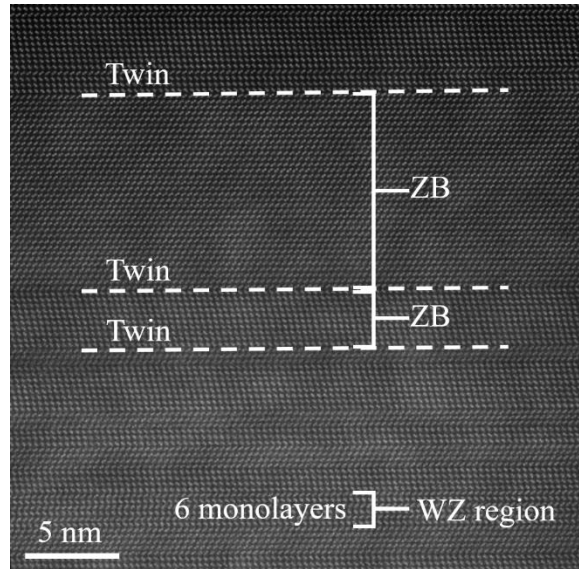


Figure 3.9: TEM image showing a WZ insertion of 6 monolayers in the predominantly ZB crystal of AlGaAs NWs. Three typical twin defects that alter the polarity of the ZB planes are also marked.

Nominal Al %	ZB Al % (μ PL-based)	WZ Al % (μ PL-based)
10	5 ± 1.2	9.65 ± 0.05
20	13 ± 2.2	20.2 ± 2.3
30	22 ± 1.4	35.8 ± 0.8

Table 3: Comparison between PL-based calculated Al contents for ZB and WZ crystal phases of AlGaAs, respectively.

3.5) Comparison of our work with previous works on AlGaAs Nanowires

After having analysed our experimental results on the topic of AlGaAs NWs, we consider it important to briefly compare our work with the cited literature of the same field, in order to underline the major findings and contributions of our research.

The interest on AlGaAs NWs is mainly based on its potential to be combined with the popular and vastly explored GaAs due to their lattice match. With respect to GaAs NWs, self-catalysed approach has been used in the past regularly with important contributions having been reported. For example, a thorough scrutiny of the structural properties of GaAs NWs allowed for the study of the crystal phase and its dependence on NW features such as the diameter or the contact angle of the solid with the liquid droplet.^[212] GaAs NWs have been found to be crystallized predominantly in the ZB phase, however regular polytypic features with WZ insertions have been observed.^[212-214] In addition, tuning to predominantly WZ GaAs NWs has been accomplished.^[215] Be-doping has also been found to improve material quality in GaAs NWs.^[216] Regarding their optical properties, GaAs NWs typically emit in the vicinity of 870 nm, signifying that they are ideal as near-infrared light-emitters. The peaks present a narrow linewidth provided that the material quality is high which ensures that crystal defects do not act as scattering centres. Moreover, the combination of GaAs/AlGaAs NWs in core/shell architecture has been thoroughly researched.^[18,224-226] As a result of the lattice match, there is no significant strain in the core/shell interface, hence no major dislocations are anticipated. The AlGaAs shell allows for enhancement of the PL by confining the carriers in the core region, while acting as a means of surface passivation reducing surface recombination.^[171] The main emission derives from the

NW core which means that it is expected to be located in the near-infrared region of the spectrum. This is in stark contrast to our material platform, which can also emit in the red region depending on the Al composition of the alloy. Besides, this is one of the most important advantages of employing ternary alloys for nanoscale structure realization.^[44]

On the other hand, AlGaAs NWs have not been realized before via the self-catalysed VLS growth method.^[226,228] Prior to the current research, the successful growth of Au-assisted AlGaAs structures has been reported. The results revealed the self-formation of a rough AlGaAs shell similar to our case, with inhomogeneous elemental distribution along the NW axis and comparatively more uniform distribution at the cross section. Higher Al percentages have caused tapered morphology in the past.^[228] The growth temperature is also important for the morphology of the NWs, with higher temperatures leading to slow axial growth rates affecting the dimensions of the structures.^[226] Tuning of the emission has also been noticed in previous works with distinct peaks having been traced.^[228] It is noted that despite the interest in AlGaAs, literature on this topic has been substantially less compared to GaAs, owing to the challenges of the III-III-V ternary alloy implementation in nanostructure synthesis, which was commented in chapter 1.

Compared to the aforementioned works and despite the common results, the vital difference in our research is the use of Ga droplets as catalysts, which eliminates Au-induced contamination and renders the NWs compatible with CMOS technology applications. Importantly, the growth parameters that we used, most notably the high Ga flux, allowed for the shell to adopt an increasingly rough surface, which formed concavities. This is key for the spontaneous formation of AlGaAs branches that will be examined in the following chapter and present intriguing structural characteristics. The

peaks were robust demonstrating the suitability of the structures for light-emitting applications, while such NWs are ideal for hosting GaAs QDs with promising potential in novel functions such as quantum computing, as will be discussed in chapter 5 of the current thesis.

3.6) Summary and Conclusions

To summarize, we demonstrated the successful growth of AlGaAs NWs via the self-catalysed approach for the first time. It is reminded that this growth method eliminated Au-related contaminations that render the structures incompatible with CMOS applications and drive electronics. Specifically, AlGaAs NWs with varying Al content of 10%, 20%, 30% and 40% were synthesised. The structures were predominantly vertically oriented with respect to the Si substrates, which signifies that they elongate along the energetically favoured (111) direction. Nevertheless, deviations can be conspicuously observed, especially at higher Al contents, with morphological variations being developed. This phenomenon along with the analysis of one peculiar type of variants will be described in detail in the following chapter of the thesis.

The NWs were thoroughly scrutinized via TEM measurements. Their growth was initiated by droplets comprised of an Al and Ga alloy, with some cases of Ga-only droplets being distinguished. As previously observed in existing literature, the self-formation of an Al-rich shell was exhibited, attributed to the shorter diffusion length of Al adatoms that tend to adhere to the NW sidewalls closer to the base. The shell presented two distinguishable features, as it was thicker close to the base and grew thinner towards the top, leading to the vicinity of the NW tip being core-only structure. Second, the shell presented wide alloy fluctuations manifesting themselves as phase separation, forming intricate nanostructures comprised of sequential QWs and

barriers. The crystal structure was also investigated and it was confirmed that the crystal phase is predominantly ZB. This can be attributed to the relatively large NW diameter, which inherently promotes ZB crystallization,^[88] as mentioned earlier in the current thesis. Nevertheless, it can be seen that a high density of twin defects and occasional WZ insertions, a few monolayers thick, are presented in the structures.

The AlGaAs NWs were optically probed via PL measurements. The emission was fully tuneable with Al content. Specifically, increasing Al concentration caused a shift of the peak towards lower wavelengths due to the widening of the bandgap energy. Furthermore, position-dependent μ PL revealed robust peaks in the middle of the NWs, while sharp transitions were observed in the vicinity of the NW ends, stemming from the highly inhomogeneous Al distribution. Eventually, increasing power of excitation caused the initially sharp peaks to be replaced by broad emission, more reflective of the average Al composition.

Interestingly, the calculated compositions based on PL measurements were lower than the nominal, while the values measured via EDX measurements were higher. This disagreement is potentially attributed to the fact that PL addressed parts that have a lower energy bandgap, thus reflect a lower Al content. The above appear as a result of the highly inhomogeneous Al distribution that was exhibited in all the grown samples. Nevertheless, more works are necessary in order to conclusively interpret this phenomenon.

In conclusion, the self-catalysed AlGaAs NWs presented interesting morphological and structural characteristics, with the major phenomena being linked to the self-formation of the AlGaAs shell. The PL measurements showed good tunability features

of the emission peak, while the robustness of the peaks even at RT displays the suitability of the NWs for on-chip light-emitting applications.

After having examined the morphological, structural and optical features of AlGaAs NWs, we will proceed with describing a morphological variation frequently encountered in our samples, namely the branched AlGaAs NWs. The next chapter will unveil the peculiarities of this 3D form of NWs and inspect their origin and their potential in device applications.

Chapter 4: Branched AlGaAs Nanowires

4.1) Morphological and structural analysis of AlGaAs branched nanowires

As described in the previous chapter, SEM analysis on AlGaAs NWs allowed us to visualise and comprehend their morphology before proceeding to TEM analysis in order to conduct their structural evaluation. For clarity, a typical SEM image of NWs with 10% Al content, which includes these variations is exhibited in Fig. 4.1a. Whilst the majority of the individual NWs are perpendicularly oriented on the Si substrate, there is a percentage that adopts different configurations. It is significant to underline that the variations were noticed on the AlGaAs NW samples that were grown via the same procedure and parameters as described in the initial section of chapter 3. The two common variations that were frequently encountered in all the samples are the kinked NWs and the branched NWs. Typical examples of a kinked and a branched AlGaAs NW are presented in Fig. 4.1b and 4.1c. Kinked NWs are attributed to the supply of Al that reaches the Ga droplet, which has an impact on the favourable nucleation and induces growth along directions other than $\langle 111 \rangle$. NW kinking reduces the yield of vertically oriented structures and affects the NW density on the Si substrate. Nevertheless, even more intriguing is the second type of variant, the branched NWs (Fig. 4.1c). In this case, AlGaAs NW branches are grown on the sidewall facets of the backbone of standing NW that is called the trunk. It is clarified that the angles that branches form with the NW trunks is 60° , thus adopting a 6-fold symmetry. These features will be described and inspected by means of top-view SEM images and will be discussed in more details later in the current chapter.

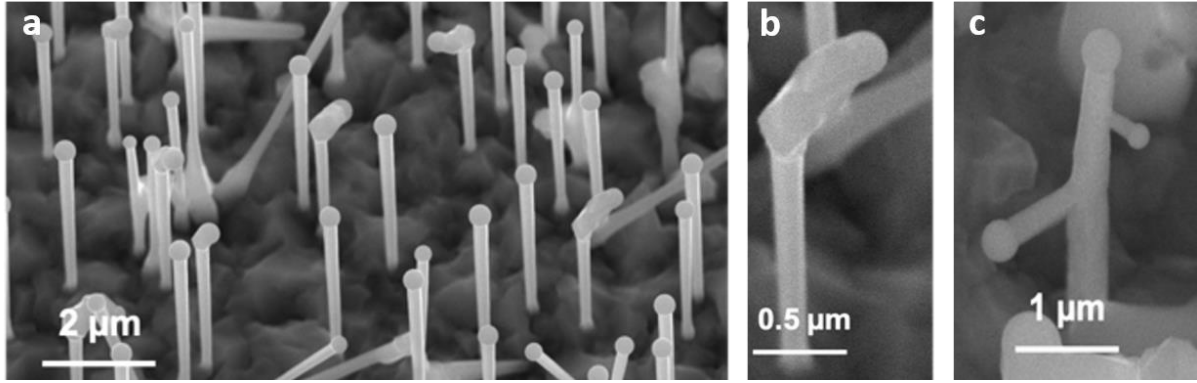


Figure 4.1: a) Typical, representative SEM of an AlGaAs NWs sample with 10% nominal Al content. b-c) The two typical variations, namely the kinked NW and the branched NW, respectively. In all of the figures the tilting angle was 30°.

NW branching events lead to a 3D, hierarchical geometry of the structures. This morphological peculiarity has vast potential for devices, such as solar cells as described in Chapter 1 of the current thesis. Owing to the increased scientific interest that they present and the findings associated with their morphology, we concluded that it was important to inspect this type of NW structures more thoroughly. Ergo, higher-magnification SEM images of the samples with 10%-40% nominal Al content were obtained. This enabled us to focus on a single branched structure from each sample. The results of the SEM imaging are illustrated in Figs. 4.2a-d. The presence of the branches is confirmed in all of the grown NW samples. It is reminded that the NW trunks are elongated along $\langle 111 \rangle$ direction and are perpendicularly oriented to the Si (111) substrate. As mentioned in Chapter 3, Al-richer samples are wider and shorter, whilst more pronounced branches are conspicuously viewed. It is noted that the angle of tilting is again 30°.

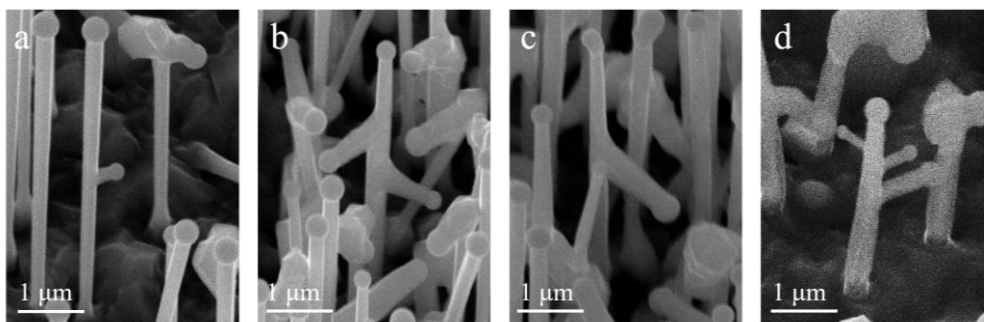


Figure 4.2: a-d) SEM images with 30° tilting angle of individual AlGaAs branched NWs with 10%, 20%, 30% and 40% nominal Al content, respectively.

A brief statistical analysis was conducted on 100 individual NWs, to assess the number of branching events as a function of the nominal Al composition. The results are presented in Fig. 4.3, where it can be inferred that at low Al content of 10%, 20% and 30% the percentage of standing NWs that developed branches on their sidewall facets was limited to roughly 10-15% of the studied NW sum. However, for 40% nominal Al composition, this percentage is rapidly enhanced at 60%. This phenomenon is originating from the direct impact that increasing Al has on the number of the branches via altering the morphological features of the NW trunk, which will be analysed further on in the current thesis. It is noted that another possible contributing factor could be the expansion in the volume of the droplet caused by the increased group III flux,^[248] which could lead to the droplet sliding along the NW sidewalls, thus provoking the VLS growth of more branches. This method has been applied in the past for branched NW growth via the so-called “droplet confinement”.^[192] Nevertheless, we do not anticipate droplet sliding to be the stem of the increased branching events for two reasons. First, the branches that are realized are multiple in several cases and exhibit principal hierarchical characteristics, as observed by the longer branches that are grown in the vicinity of the NW base. This would be unlikely in the event of droplet sliding. Second, in the overwhelming majority of the cases the droplet in the tip of the

trunks is well formed, as observed in the SEM images that are demonstrated in Figs. 4.2, where the spherical seeds are conspicuously shown. Ergo, the most possible explanation of the increased branching events with increasing Al composition is the roughening of the surface of the shell. More details of this phenomenon will be provided further on in the current thesis along with theoretical calculations in order to formulate the growth mechanism of the branched NWs and interpret their presence at Al-rich structures.

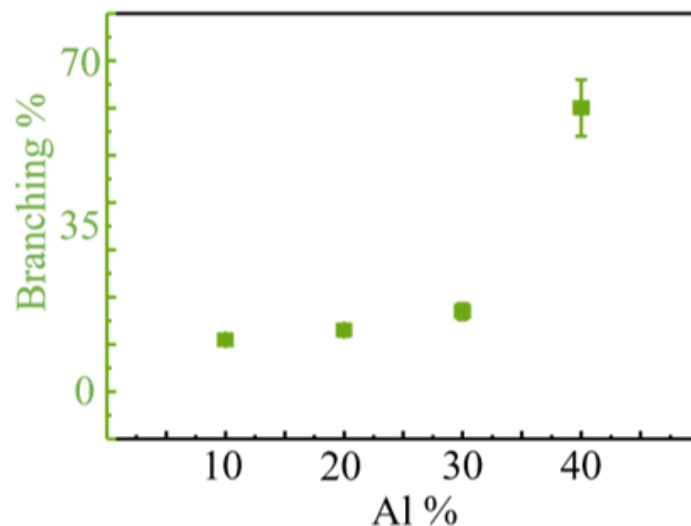


Figure 4.3: Graph of the branching percentage of the samples, as a function of the nominal Al composition. The branching events are highly pronounced at the highest Al content used.

After the interesting observations regarding the branched NW morphology, it is crucial to separately investigate the structural properties of the trunks and the branches. For this purpose, STEM analysis was performed via acquiring bright field (BF) images, which are depicted in Fig. 4.4a. The low magnification BF image in the inset of Fig. 4.4a confirms the 90° angle formed between the NW trunk and the branch,

signifying that in principle the branches are orthogonal with respect to the NW backbone. Based on the crystallographic orientations, the elongation of the branches is inferred to be $\langle 112 \rangle$. This can be further supported by top-view SEM that will be presented later in the current chapter. A higher magnification image of the orange square is presented in the outset of Fig. 4.4a and gives us a more detailed perspective of the branch/trunk junction. Further high magnification BF images along the interface in areas similar to the one marked with the green square in Fig. 4.4a expose the crystal structure which is identical for both the branch and the trunk (Fig. 4.4b). It is also important to point out that WZ insertions and extensive twinning coexist in the crystal and extend from the NW trunk to the branches. This phenomenon confirms the continuity of the branch growth. Despite the twin defects, no dislocations or grain boundaries are noticed. In addition, the FFT patterns from BF images at different areas (marked by blue and red squares in Fig. 4.4b) from both the branch (Fig. 4.4c) and the trunk (Fig. 4.4d) have identical orientations, which corroborates the epitaxial nature of the growth. It is also interesting to observe that the FFT patterns exhibit streaky features, which signify phase impurity and specifically, crystal defects and WZ phase insertions in both the branch (Fig. 4.4c) and the trunk (Fig. 4.4d). This is in accordance with the polytypism and the complex crystallinity of AlGaAs NWs that was described in Chapter 3 of the current thesis.

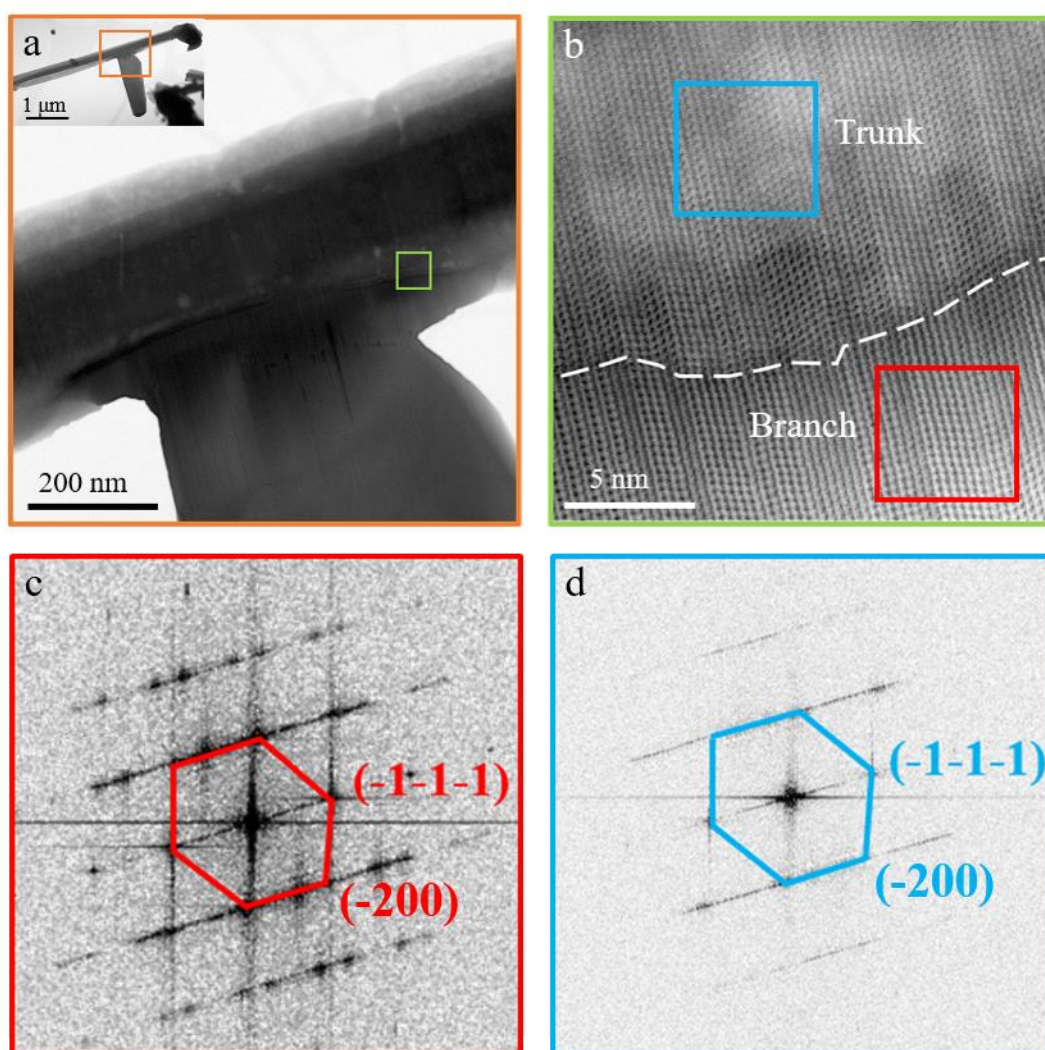


Figure 4.4: a) Inset: BF image of an individual branched NW, demonstrating the perpendicular orientation of the branch with respect to the trunk. Outset: High magnification of the orange square of the inset, focusing on the trunk/branch junction. The green square marks the area of focus for Fig. 4.4b. b) High-Resolution ADF of the trunk/branch junction, revealing the identical crystal phase between the two parts. The blue and red square mark the area for the FFT of the trunk and the branch, respectively. c-d) FFT patterns of the branch (4.4c) and the trunk (4.4d), which are identical, corroborating the epitaxial nature of the growth.

Further inspection of the directionality of the branches can be conducted by more in-depth SEM measurements that were carried out. In Fig. 4.5a, we present a typical branched NW with 40% Al content, that was already displayed in Fig. 4.2d, for clarity. It is distinctly noticed that three branches with stringent hierarchical features are nucleated on the NW backbone. Fig. 4.5b illustrates the top-view SEM of such a structure. It can be seen that the branches form a six-fold symmetry if we consider the extensions of each branch on the other side of the trunk. This can be further established by measuring the angle between two consecutive branches, which is 60° . This unambiguously verifies the symmetric configuration. In addition, the branches are vertical on the NW trunk, which is known to elongate along (111) direction. Furthermore, if the trunk is imaged in the (110) zone axis, the branches are again vertical to the NW trunk. In addition, it is important to remember that since the nature of the growth is epitaxial the branches and the trunk are located in the same zone axis. Based on the above and considering the basic schematic representation for the crystallographic orientation that is presented in Fig. 4.5c, the direction that is perpendicular to both (111) and (110) is (112). From the above it can be convincingly concluded that the branches are elongating along (112) direction.

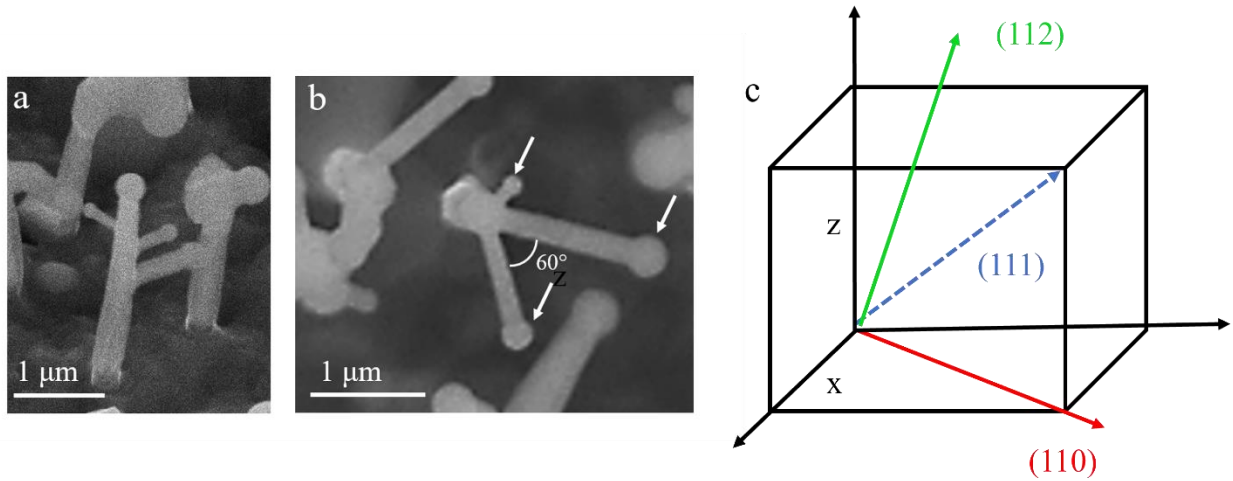


Figure 4.5: a) Representative SEM image of a NW with three branches and a nominal Al content of 40%. The tilting angle is 30°. b) Top-view SEM of the NW with the three branches, revealing a six-fold symmetric geometrical configuration. c) Schematic of the investigated crystallographic orientations.

4.2) Growth of AlGaAs Branches and Interpretation

4.2.1) Growth Model and First-Principles Calculations

Following the microscopy scrutiny of the branched AlGaAs NW structures, theoretical calculations via the Vienna ab-initio software package (VASP) were conducted in order to establish the growth mechanism and the principles lying beneath it. It is important to mention that for the modelling, GaAs NW trunks were assumed instead of AlGaAs, to focus on the mere behaviour of Al adatoms adjacent to the branch/trunk interface. The calculations were performed using the Perdiew-Burke-Ernzerhof (PBE) functional and the generalized gradient approximation (GGA) within the density functional theory for the exchange-correlation energy. The projected augmented wave (PAW) pseudopotentials were adopted while the kinetic cutoff energy was set at 560 eV. The Monkhorst Pack reciprocal k-points grid was sampled by sums over 1x1x13.

The models are depicted in Figs. 4.6a-b, with Ga and As depicted as brown and cyan spheres, respectively. The ternary NWs are modelled by introducing Al adatoms in the branched GaAs NWs, where Al replaces Ga atoms at various positions either at the branch/trunk interface (Fig. 4.6c) or to exemplary positions away from it (Figs. 4.6d-g). In these designs, the number of atoms is fixed at 180. In Figs. 4.6c-g, Al atoms are depicted as yellow clusters. For these figures, the Al content ranges at 1.1%, 2.2%, 3.3%, 4.4% and 5.5%, respectively. Despite the fact that the aforementioned numbers are much smaller than the nominal values, which was chosen due to computational limitations, the basic interpretations and conclusions that will be drawn from the VASP modelling are valid for the experimentally realized structures. The modelling was conducted with few Al atoms, whilst considering that the remaining Al atoms in the branched NWs are distributed randomly and their contribution will be eliminated after the comparison of the total energy of the different configurations.

Based on the above, the variation of the formation energies ($\delta\Delta$) for the depicted models was computed. It is noted that the selected configurations are realized with the aim of maintaining stoichiometry. In order to imitate the grown samples, the models have the same geometric designs, as only the Al content and the Al adatom location is considered for the comparison. Using these, the calculations were performed via the following equations:

$$\delta\Delta = E_n - E_0 - xE_{\Delta},$$

$$E_n = (90-x)E_{\text{Ga}} + xE_{\text{Al}} + 90E_{\text{As}} + \Delta_n$$

where, E_{Ga} , E_{Al} and E_{As} are the total energies of single Ga, Al and As atoms, respectively. Δ_n is the formation energy of the “n” branched NW model, x is the number of Al atoms and E_0 is the total energy of pristine GaAs. $E_{\Delta}=E_{\text{Al}}-E_{\text{Ga}}$ is a term representing the total energy difference in vacuum, which was introduced to eliminate energy differences which might arise from the unequal number of Al adatoms in the models. Hence, $\delta\Delta$ is solely determined by the various positions taken by Ga and Al atoms in the model, regardless of the number of atoms that are doped.

The results are shown in Fig. 4.6h where the trend of variations in $\delta\Delta$ exposes that Al atoms preferentially accumulate away from the branch/trunk interface. This can be inferred by the energetically favoured states that they occupy, while Ga is preferentially positioned at the interface. From these, the growth mechanism can be deduced, which is attributed to preferential Ga accumulation at the rough surface of the Al-rich shell. The high density of twins leads to the increase of the roughness of the shell, forming concavities where Ga accumulates.^[258-259] The accumulated Ga atoms amalgamate as droplets and cause the branch elongation. It is noted that higher Al composition leads to thicker shell with more pronounced concavities for Ga accumulation, which could potentially explain the enhanced branching events with increasing Al content. Unlike other works that induced deliberate branch growth on the NW sidewalls,^[189-192] the growth of branches in these samples took place spontaneously. For clarity, a schematic representation of the growth mechanism is provided in Fig. 4.7. The liquid Ga droplet acts as a collector (Fig. 4.7a) which causes the nucleation of a solid monolayer and eventually leads to the NW elongation according to the VLS growth mode (Fig. 4.7b). The shell presents concavities due to its rough surface. Ga accumulates in the concavities (Fig. 4.7c), which leads to the nucleation and subsequent growth of the AlGaAs branches (Fig. 4.7d). Adatom accumulation on the

NW sidewalls has been reported in the past as the source of NW branching events, for GaAs/GaAsBi core/shell NWs^[260] and GaSb NWs.^[261] However, growth of branches in AlGaAs NWs has not been observed before, even though the self-formed shell was present in all cases. The fact that this is the first time that spontaneous AlGaAs branches are formed can be attributed to two reasons. First and foremost, the growth duration in this work is long, resulting in the shell surface being excessively rough. Second, Ga flux that is chosen in this work is adequately large, which assists in two ways. Initially, it further enhances the roughness of the shell and additionally it promotes the Ga adatom amalgamation as droplets.

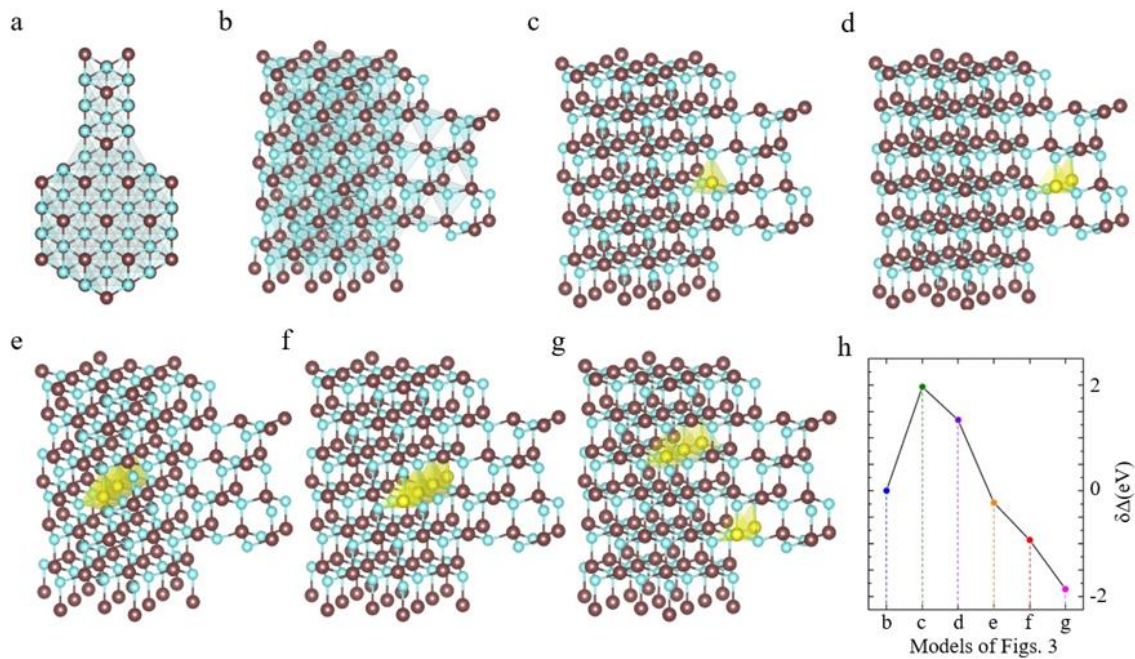


Figure 4.6: a-b) Top view and side view of a GaAs branched NW, where Ga and As atoms are depicted as brown and cyan spheres, respectively. c-g) Al atoms (depicted in yellow) replace Ga atoms at different positions at the interface (Fig. 4.6c) and away from the interface (Figs. 4.6d-g). h) The continuous reduction of the formation energies for the different configurations in Figs. 4.6c-g.

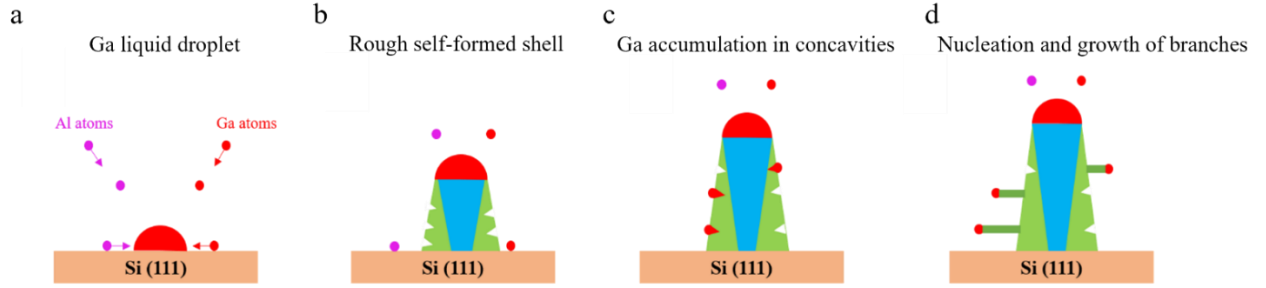


Figure 4.7: a-d) Schematics of the growth mechanism of the 3D branched AlGaAs NWs. a) Ga droplet acts as a collector for the adatoms, which leads to the nucleation of a monolayer. b) NW elongates following VLS growth mode, with a rough self-formed shell being present. c) The concavities of the shell cause Ga accumulation, which act as droplet for the branches. d) Nucleation and growth of the branches perpendicularly to the NW trunk.

4.2.2) Calculations of growth rate and volume of the trunks

Based on all of the above, one conclusion that could be drawn is the calculation of the branched AlGaAs NW growth rate. In order for this to happen, it should be taken into consideration that the growth duration was 100 mins for all the samples, no matter what their nominal composition was. Additionally, it should be considered that As flux was kept stable at 2.7×10^{-6} Torr, while Ga flux was fixed at a value so that As/Ga beam flux ratio was 15. This means that Al supply was the only contributing factor to the morphological alterations of the branched AlGaAs NWs. From the statistical analysis of the NW trunks (Fig. 3.2), the average values of the NW trunk length are 8 μm , 6 μm , 5 μm and 4 μm for 10%, 20%, 30% and 40% nominal Al composition, respectively. The first 600 nm of the NW trunks corresponded to bare GaAs stems that were grown for 10 mins before Al was introduced in the MBE system. From these details, the values of the axial growth rate for Al contents 10%-40% are 1.23 nm/s, 0.9 nm/s, 0.73 nm/s and 0.57 nm/s, respectively. The noticed decrease of the axial growth rate with

increasing Al contents is anticipated because of the trend of Al to be adhered to the side facets rather than incorporate in the droplet and participate in the axial VLS growth, as a result of its low diffusivity, that was described earlier. Besides, Ga diffusivity is suppressed by the increased Al supply.^[223] It is important to clarify that in real experimental conditions the structures cannot be growing by the same amount in each unit of time. Nevertheless, the approximation of linear growth rate that was used above leads to values that are considered valid as they are corroborated by the experimental findings. The volume of the NW trunks can also be calculated. It is noted that precise computations are rendered intricate due to the asymmetric and irregular NW shape. However, it can be assumed that NWs are perfectly cylindrical which is a sufficient approximation. The average volume is thus calculated by the formula $V=\pi r^2 h$, where r is the radius of the NW end and h is the NW height. The average diameter of the samples with 10%-40% Al content derive from the statistical analysis of Fig. 3.2 and are 100 nm, 125 nm, 150 nm and 200 nm, respectively. Based on the above, the volumes of the four samples with increasing Al compositions are $0.25\ \mu\text{m}^3$, $0.29\ \mu\text{m}^3$, $0.35\ \mu\text{m}^3$ and $0.5\ \mu\text{m}^3$.

4.3) Novel observations in AlGaAs nanowire branches

Further STEM measurements were carried out on the AlGaAs NW branches in order to explore their compositional distribution. This procedure was considered necessary, not only for the comprehension of the branched NW behaviour, but also due to the novelty that self-catalysed AlGaAs branched NWs present. It is important to mention that the previous, reports on AlGaAs NWs are describing Au-catalysed growth mode, whilst branched AlGaAs NWs have not been reported so far.

As a first step towards their compositional characterization, ADF images were obtained, which reveal conspicuous bright stripes along the growth axis of the branches. This is distinctly viewed in Fig. 4.8a. It is reminded that bright regions in ADF images indicate increased presence of the heavier element, which in this case is Ga. For clarity, five of these stripes are shown by blue arrows in the aforementioned figure. More importantly, via inspection of a higher magnification ADF image of the NW branch (Fig. 4.8b), an additional set of bright stripes, perpendicular to its growth direction, can be noticed. The two types of stripes will be referred to as axial and perpendicular stripes, respectively, for the rest of the thesis. The axial and perpendicular stripes intersect, a phenomenon that leads to the self-formation of a “checked pattern” of the compositional distribution. However, the two types exhibit a particularly interesting differentiation. The axial stripes are not equally spaced to each other, while on the contrary, perpendicular stripes are highly periodic in their positioning. To confirm this observation, the integrated intensity of the region surrounded by the red rectangle in Fig. 4.8b was recorded. The peaks presented in the spectra correspond to the perpendicular bright stripes and are established to be highly periodic, presenting a period of roughly 3.6 nm (Fig. 4.8c).

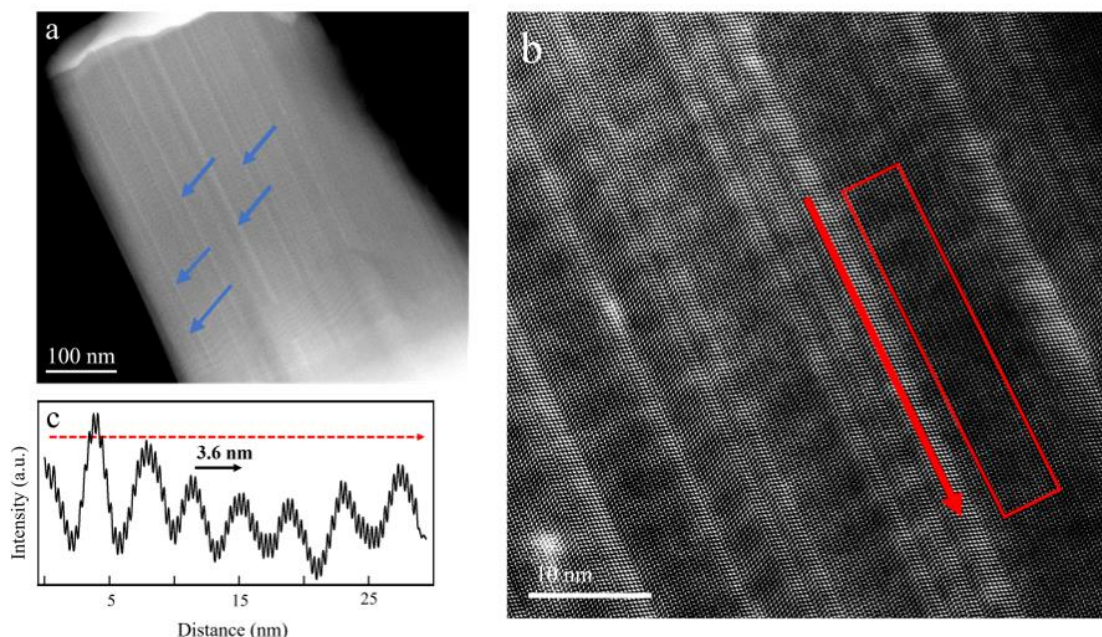


Figure 4.8: a) ADF image of a NW branch, with the five blue arrows marking five examples of bright stripes along the growth direction of the branch. b) Higher magnification ADF image of the branch in Fig. 4.8a, exposing bright stripes both parallel and perpendicular to the branch growth direction. The red arrow and rectangle indicate the direction and area of the integrated profile that was acquired. c) Intensity profile from the corresponding region in Fig. 4.8b. The high degree of periodicity of the perpendicular bright stripes is defined as roughly 3.6 nm.

Besides, axial EDX scanning of a single NW branch is conducted. The results are presented in Figs. 4.9a-b. Initially, in Fig. 4.9a, a TEM image of the region of the scanning is presented. It is visible that there are lines of high brightness perpendicularly to the scan direction. The latter is marked by the white arrow. In the graph of Fig. 4.9b, it can be seen that the high brightness stripes correspond to peaks in Ga and dips in Al, as marked by the black, dashed arrows, which further confirms their origin as Ga segregation. It is important to clarify that the branches grow for considerably smaller time when compared to the NW trunk. This could be the potential

reason why the distribution of Al does not present the inhomogeneity that was exhibited in the case of the trunks, as examined in chapter 3. Furthermore, due to the small dimensions of the branches, the area is not representatively large so it could not be used on its own to interpret the findings as Ga segregation. However, the similar observations between EDX and ADF images confirm the intriguing stem of these lines as accumulation of Ga atoms. Besides, the diameter of the NW branches, which is considerably small does not allow for representative EDX scanning to be conducted. Nevertheless, considering that the nanowire length is smaller and that the growth direction is different than (111), it is anticipated that the elemental distribution would be less inhomogeneous when compared to the trunk, as shown in Fig.4.9b. It is also reminded that the distribution of Ga and As is uniform across the diameter of the NWs, while Al accumulation is presented at the sidewall facets causing the formation of the core/shell architecture. However, considering that the branches are exposed to the elemental supply for considerably smaller time as shown earlier, this phenomenon is expected to be highly reduced or eliminated in these parts of the structure.

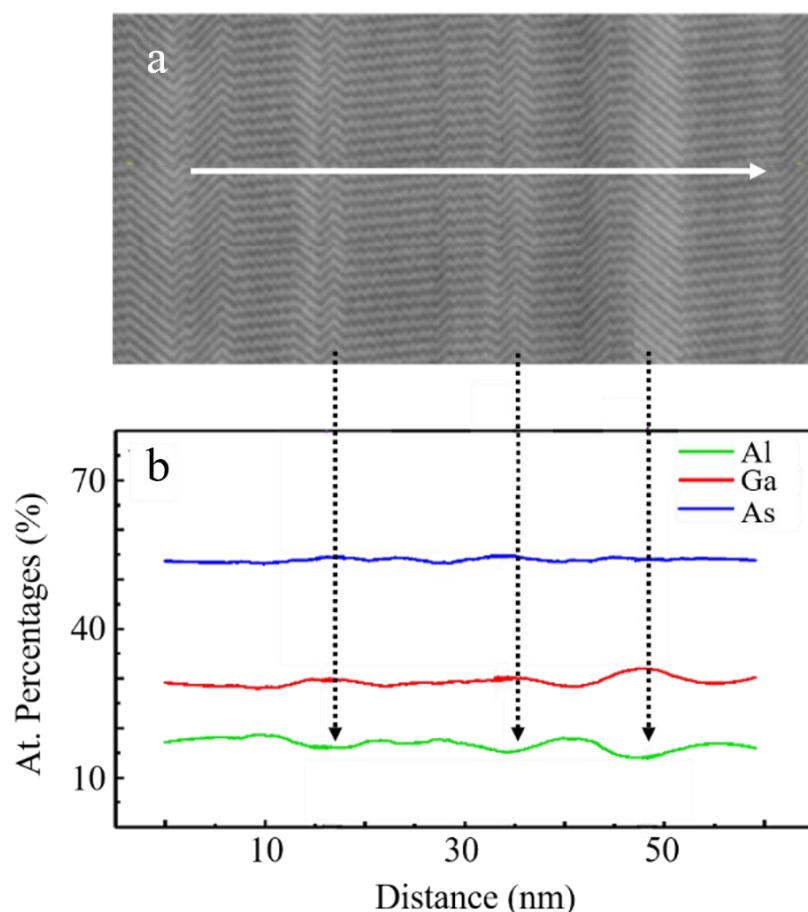


Figure 4.9: a) TEM image of a region of the NW branch. b) Axial EDX scanning in the direction marked by the white arrow in Fig. 4.9a. The bright stripes of Fig. 4.9a correspond to peaks in Ga and dips in Al, as marked by the black, dashed arrows, further confirming the origin of the high brightness stripes to be segregation of Ga.

This highly uncommon phenomenon is intriguing for further analysis and interpretation. A higher magnification ADF image of the region of the intersection is presented in Fig. 4.10a. The formation of the checked pattern can be confirmed, with the axial and perpendicular stripes both marked by dashed, white lines. A representative area of intersection is pointed out by the white square in Fig. 4.10a. Another interesting observation derives from the EDX maps for Ga and Al of the region of the intersection (Figs. 4.10b-c, respectively). In both maps, bright and dark regions expose enrichment or deficiency, respectively, of the mapped element. The images

indicate higher Ga composition in the bright stripes. What is more, the intersection of the axial and perpendicular stripes leads to the formation of Ga-rich (and, thus, Al-deficient) “boxes” at these regions, as pronounced by the dashed lines in Figs. 4.10b-c. This property is very promising, as such phase separation at this low dimensionality can be potentially exploited in the future for the self-assembly of QDs, that represent novel types of spontaneously formed light emitters. However, it is noted that in order for this function to be achieved in a tuneable and controlled manner, further understanding of the intricate compositional distribution is imperative.

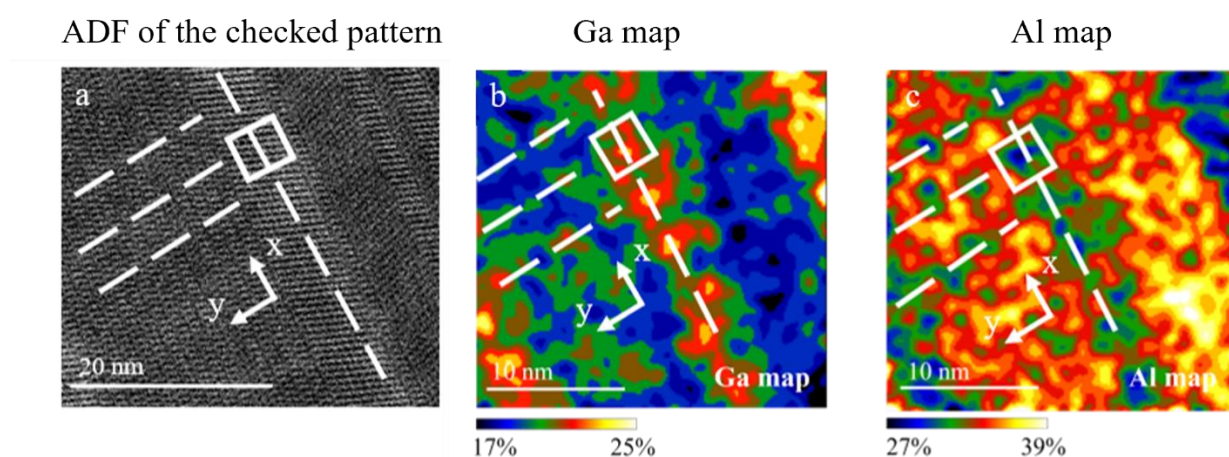


Figure 4.10: a) ADF image indicating the area of the subsequent elemental mapping. b-c) Elemental mapping of the “checked pattern” in the area in Fig. 4.10a for Ga and Al where the bright orange areas signify Ga-rich regions and Al-rich regions, respectively. Both the periodic and the axial Ga-rich (Al-deficient) stripes are marked by the dashed, white lines in Fig. 4.10b (Fig. 4.10c). Ga-rich and Al-deficient “boxes” are formed in the intersection of the two types of bright stripes.

After having established the validity of the Ga and Al-rich stripes formation, it is necessary to formulate an interpretation for this intricate, vibrant and highly uncommon behaviour. With some further consideration on the growth and characterization of the

samples, the dual nature of the stripes can be safely assumed to untangle in a twofold mechanism. First, regarding the formation of the perpendicular, periodic stripes are attributed to the rotation of the samples during growth in the MBE reactor, which in our case was 10 rpm. It is known that this rotation is widely employed as a technique of maintaining the morphological uniformity of the samples during their synthesis. Via the NW rotation around their axis, all of the facets receive the same proportion of elemental beam fluxes, regardless of their position, after taking into consideration the stability of the elemental sources. However, due to the 3D nature of the branched NWs, some differentiations occur in the case of these interesting structures and the situation deviates from this design significantly. Specifically, the non-vertical components, which in this case are the NW branches, are exposed to inhomogeneous elemental beam fluxes as a result of the aforementioned rotation. It is noted that this is not valid for the standing NW trunks but merely for the branch region of the samples. More specifically, as the rotation occurs with respect to the growth direction of the trunks, which are vertically aligned on the substrate, each NW trunk facet receives the same proportion of elemental fluxes. In stark contrast, the branches grow perpendicularly to the NW trunks, hence the angle between the branch grown direction and the elemental sources is constantly changing during the rotation. Furthermore, the aforementioned rotation causes a shadowing effect on the branches by the NW trunk.^[262] Consequently, when a NW branch is in the vicinity of one elemental source, the shadowing effect will lead to less adatoms of the rest of the elemental beam fluxes being incorporated to this region of the structures. This leads to the compositional inhomogeneity perpendicular to the growth direction of the branch that was described earlier.

The above information is schematically represented in the illustrations of the branched NWs that are exhibited in Figs. 4.11a-d. The branches are labelled as '1' and '2'. It is important to note that the position of the Ga and Al sources is similar to their physical position in the reactor. Due to the stability of the elemental sources, when branch '1' is facing the Ga source, it is shadowed from the Al source by the trunk. Hence, a higher amount of Ga is adhered to branch '1' whilst a deficiency in Al is also demonstrated (Fig. 4.11a). Based on our growth mechanism, the adatoms are collected by the Ga droplet at the tip of each branch and the nucleation of a monolayer occurs following the VLS growth mechanism. This is similar to the case of the NW trunk growth, as described earlier in chapter 3. As more Ga adatoms are incorporated at this stage in the droplet, a monolayer that is Ga-rich will nucleate at the liquid/solid interface in the vicinity of the branch tip. This is the origin of the Ga-rich stripe (Fig. 4.11b). Analogously, due to the rotation of the sample, branch '1' leaves the vicinity of the Ga source and approaches the Al source (Fig. 4.11c). This causes the opposite phenomenon of more Al adatoms being absorbed by the Ga droplet at the branch tip, thus a monolayer that is Ga-deficient will nucleate at the liquid/solid interface. That way, the Al-rich stripes are formed (Fig. 4.11d). It is also important to note that, in the illustrated structure, branch '2' is located on the other side of the trunk, so the aforementioned procedure occurs in the opposite order for this branch. The repetition of the mechanism described above, ultimately results in the AlGaAs NW superlattice in the branch with alternating Ga-rich and Al-rich stripes perpendicularly to the growth direction of the branch. This is a striking difference to the standing NW trunks or 1D NWs, which are vertically aligned on the Si substrate, the angles between the elemental sources and their growth direction is stable and consequently no shadowing

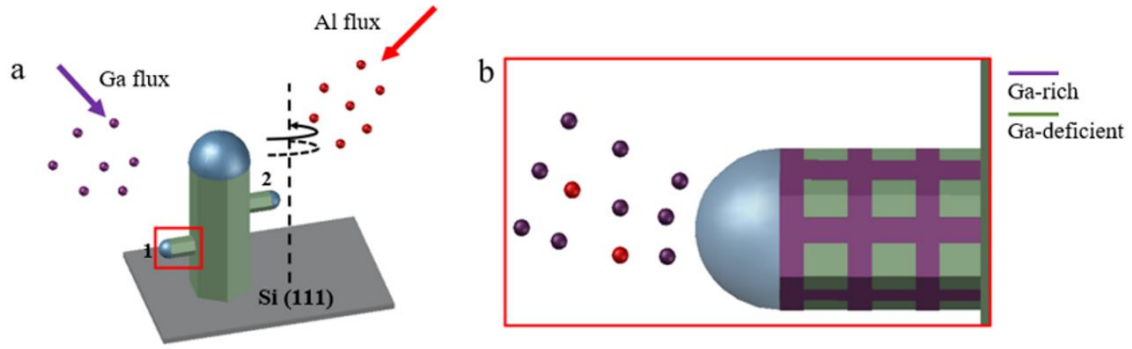
effect on the droplet in the trunk NW tip is presented. This is the reason why the perpendicular stripes of Ga distribution are absent in 1D NWs or the NW trunks.

It is interesting to mention that considering the impact of the rotation speed on the formation of the perpendicular stripes, altering the value of the rotation speed could also influence this finding. For instance, changing the speed would directly affect the time during which each branch would be located in the vicinity of the respective source. Even though the quantification of the Al/Ga ratio in this case cannot be obtained, it is safe to assume that lower rotation speed would leave to more time of the branch in the vicinity of each source, hence increasing the thickness of the perpendicular stripes. The opposite could be the case if the rotation speed was increased.

The above self-consistent explanation based on literature and experimental observation also accounts for the high level of periodicity in the branches, which was established earlier. It is reasonable to believe that increasing the rotation speed would alter the periodicity as well, since the amount of time that the NW branches would be located in proximity of Ga or Al source, respectively, would change.

Branch '1' in the vicinity of Ga source

Focus on branch '1'



Branch '1' in the vicinity of Al source

Focus on branch '1'

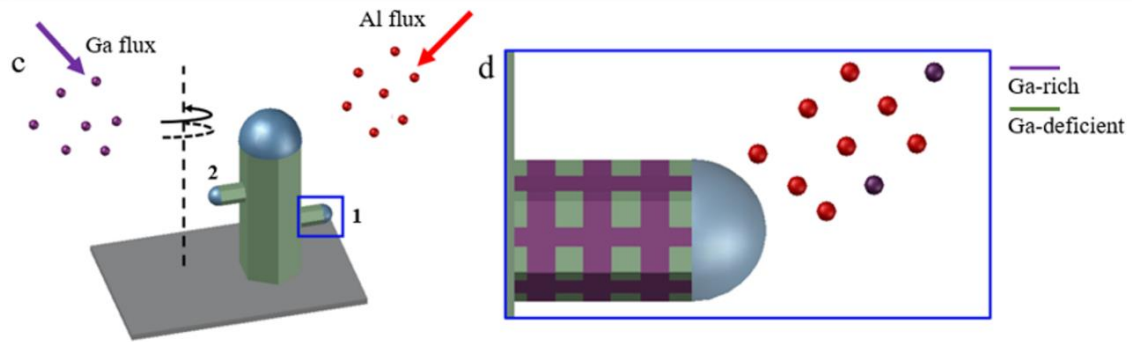


Figure 4.11: a) Schematic representation of a branched NW, rotating as indicated by the black arrows. b) Focus on the red square of (a) for a closer view of the branch. The Ga-rich stripes are depicted in purple color in the figure. Al adatoms are shown in red. c) Schematic representation of the same sample after its rotation by 180° . d) Focus on the blue square of (c) on branch '1' after its rotation. Much less Ga and more Al are incorporated, forming Al-rich regions depicted with green.

On the other hand, the formulation of the second interpretation to explain the axial stripes is even more challenging. The compositional distribution along the growth direction of the branches does not present periodic nature. However, a detailed analysis via ADF imaging leads to a complementary yet vital observation that facilitates the comprehension of the axial stripes' growth mechanism. High-resolution ADF images are shown in Fig. 4.12a, where seven bright stripes are visible along the

branch growth direction in four different regions. These regions are defined by white, dashed squares, for clarity. From a more focused inspection of these squares, we can clearly observe that axial Ga accumulation occurs merely on ZB segments. Such preferential segregation has been already reported that different elements exhibit different segregation energies between ZB and WZ regions of polytypic NWs.^[101-104,263] Moreover, it is already known that the type of the nucleation and the crystal phase can be safely correlated.^[105-108] A characteristic example is stating that in ternary NWs it is possible for different compositions to be observed in WZ and ZB segments, even if their nucleation takes place under identical conditions.^[108] It is noted that the latter paradigm is based on nucleation theory, which is in line with experimental observation.

Even more interestingly, the preferential Ga segregation can be further differentiated. From Fig. 4.12b, it is conspicuously shown that Ga-rich regions are formed only on one type of ZB segments, which from now on we will refer to as type II, whilst the ZB segments of the opposite polarity, which we will refer to as type I, do not accumulate Ga. This can be corroborated by the brightness contrast between the regions, which is most clearly depicted in square 4 of Fig. 4.12b. It is important to clarify that some bright regions that can be occasionally distinguished in regions of the opposite crystal phase and polarity are attributed to the perpendicular, periodic stripes and have already been explained by the sample rotation mechanism earlier. As a result, our observations confirm that only type II ZB segments demonstrate Ga segregation, indicating the important role of polarity in the compositional distribution of the branched NW structures. The prominent role of the polarity of ZB segments can also be confirmed by the reduced Ga incorporation in WZ segments. This is not the first report of polarity-driven mechanisms inducing elemental segregation along (112) direction. Specifically, similar phenomena have been reported in the past for GaAsP

shell layers, exhibiting an enriched P incorporation in (112)A ZB facets, when compared to (112)B ZB facets, a phenomenon that has been attributed to the higher incorporation coefficient of group V adatoms in facets with B-polarity.^[264] Due to the stronger group III bonds, the adatoms of group III have a larger incorporation coefficient at (112)A facets, causing weaker phase segregation when compared to facets with the opposite polarity. Additionally, in the case of GaAs/AlGaAs core/shell NWs, thicker (112)B polar bands have been deriving from the increased growth rate of the facets with the opposite polarity, that incorporated less amount of group III elements.^[265] In the case of AlGaAs branched NWs that is inspected in the current chapter, the peculiarity in the compositional distribution can be attributed to the stronger bonds among group III adatoms in (112)A facets, due to the coordination numbers of the unit cells.^[266] It is clarified that in all of the reported cases, the observations were carried out on shells that were grown via the vapor-solid (VS) growth mode, due to lateral expansion of the crystal. Nevertheless, it is reminded that in the case of branches, (112) oriented surfaces are located at the growth front, signifying that the same principles could be valid for the VLS growth mode that was adopted here. In order to depict the correlation between the crystal phase and the segregation of Ga, we present the atomic arrangement, as modelled via the VESTA software, in the paradigm illustrated in Fig. 4.12c. For our representation, we chose to include a twinning region and a WZ insertion in the same crystal, with the twin defect marked by black lines, for clarity. The stacking sequence can also be provided for facilitation. It is viewed that the crystal twinning modifies the crystal phase and polarity of the NW from ZB type II to ZB type I. Due to the epitaxial nature of the growth, the front presents alternating polarity as well, which causes Ga adatoms to adhere preferentially to ZB type II regions. Despite the fact that it was not possible to

distinguish if type II facets are A-polar or B-polar, it is safe and rational to assume that the aforementioned explanation for the VS mechanism is valid in our case, as well. Finally, the entire growth mechanism based on the multinucleations model is elucidated in Fig. 4.12d, where the formation of the Ga-rich stripes at the liquid/solid interface is illustrated.

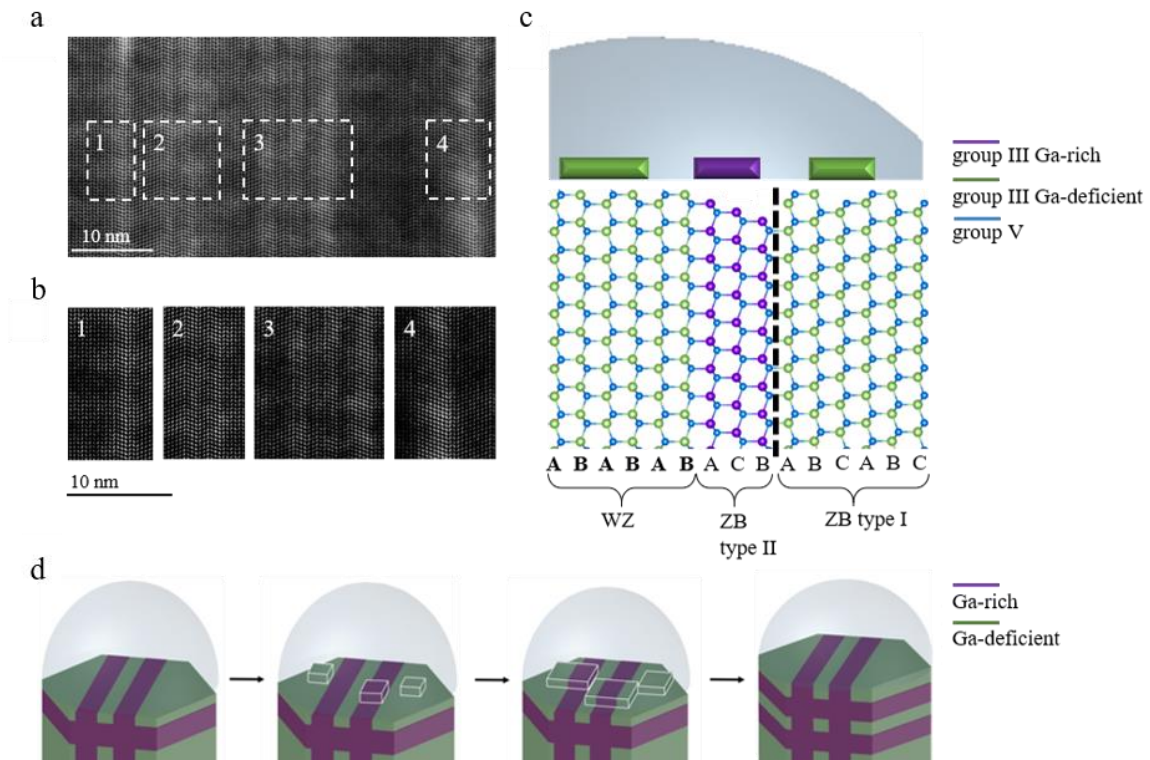


Figure 4.12: a) High-resolution TEM image of an AlGaAs NW branch which includes seven axial bright stripes, enclosed in the four dashed, white rectangles numbered 1-4. b) Focus on each of the squares of Fig. 4.12a, labelled by the corresponding numbers. It can be seen that only one type of ZB twins is brighter. c) Representative model of a NW branch via VESTA. Group III Ga-rich, group III Ga-deficient and group V atoms are illustrated as purple, green and blue spheres, respectively. The twin that is included is marked by the black, dashed line. d) Schematic representation of the growth mechanism based on the multinucleations model, with the nuclei being surrounded by white lines for clarity.

4.4) Comparison with previous works on III-V branched nanowires

After having presented the results on our experiments in the interesting topic of branched AlGaAs NWs and having described the uncommon findings of the compositional distribution, it is interesting to provide a comparison of our work with previous reports on the same topic of III-V branched structures.

As mentioned earlier in the current thesis, the topic of hierarchical, 3D branched NWs has attracted attention mainly owing to the longer optical pathway and the increased surface area that could be useful for device applications. In addition, these morphologically unique structures are versatile and entail a high level of complexity that can contribute to the realization of several practical applications. Based on the above, several works have tried to explore different types of III-V branched NW structures.

The methods that were employed for the growth of such structures vary. One of the explored methods include the manipulation of strain which has been used for the synthesis of GaAs branched NWs.^[191] Specifically, in this case the nucleation of branches occurred on the facets or at the vertex of neighbouring facets and form an angle of 109.5° with the NW trunk. The amount of GaAs leads to increase branching events, while the driving mechanism was the strain that led to the formation of stacking faults at the external facets of the NW. As the NW elongates, those sites accumulate under Ga-rich conditions at these sites and act as droplets for the branch growth.^[191] The amalgamation of Ga adatoms as droplets is similar to the mechanism that we described above, with the important difference that we emphasized on intricate ternary AlGaAs NWs and the driving mechanism was the rough, self-formed shell that includes

concavities rather than strain. In addition, the ternary nature of the alloy led to the novel findings of Ga segregation that were described.

Moreover, InAs branched NWs have been fabricated via droplet confinement, where As supply was stopped and In supply continued for roughly 10 mins. This led to the droplet expanding and sliding along the NW sidewalls, while atoms comprising the droplet migrated and were confined by deliberately induced ZB segments in the predominantly WZ crystal. Continuation of the growth under regular conditions led to these confined droplets causing the nucleation of branches.^[192] The main challenge of this very useful and interesting approach is the complexity in the growth requirements including the ZB segment formation which can have a nature challenging to control. Nevertheless, it remains an insightful method for deliberate NW branching. The structural characterization confirmed the polytypic nature with WZ predominant crystal and ZB inclusions for the droplet confinement. Furthermore, GaP nanotrees have been grown via sequential seeding,^[190] where Au aerosol nanoparticles were deposited on the sidewalls of GaP NWs to initiate the branch growth. This technique allowed for the growth of multiple branches, in some cases 15 on a single NW backbone thus the structures are characterized as nanotrees.^[190] Similar to our case, the length of the branches depended on their number and the growth was hierarchical. It is also interesting to notice that via ex-situ seeding of Au nanoparticles InP/InAs branched NWs were grown on black Si.^[197] Nevertheless, some of the challenges are related to the use of Au and the Au-induced contamination that was described in the introduction and the additional processing steps, as two rounds of seedings were required.

Moreover, InSb branched NWs have been acquired via electrodeposition of InSb.^[189] The highlight of this method is the high-crystallinity structures as thin as sub-10 nm and reaching 150 nm in thickness after a post-annealing argon treatment. Their

structures also showed antireflection properties which render them good candidates for solar cell applications. This method is a different approach compared to our epitaxial method.

Apart from the growth methods and the morphological interest that branched structures provide, interesting results have been reported in such NWs. For instance, it has been shown that the emission intensity via PL measurements of branched, “brush-like” GaN NWs is significantly enhanced when compared to pristine GaN NWs grown via similar steps.^[194] In this case this enhancement could be attributed to quantum confinement of excitons, which is not usually anticipated in NWs, but in this particular case the diameter of the branches was lower than 11 nm, which is the Bohr radius of excitons for GaN. Hence, quantum effects were expected and caused the radical increase of the PL signal.^[194] Moreover, NWQDs have been acquired via inserting the dot section (InAs) in the branch/trunk junction of GaAs branched NWs grown via MBE.^[199] The results revealed a narrow linewidth of 101 μeV and second order correlation function measurements showed a value as low as 3.1%, far lower than the threshold value for single photon emission which is 50%.^[199]

It is noted that in our case, the optical results of the branched NWs are essentially identical to the 1D AlGaAs NWs described in Chapter 3. This is because, the branched NWs were spontaneously formed via the analysed mechanism signifying that they were morphological variations in the same samples as the ones examined in Chapter 3. This is indicated in Figs. 4.1 and is attributed to the fact that the branched NWs occurred via the accumulation of Ga at the concavities of the rough AlGaAs shell. Therefore, the spectra we obtained for the 1D AlGaAs NWs were the same as in the case of 3D branched AlGaAs NWs. It is noted that in Al-deficient samples, the presence of the branching events is limited, while it is far more pronounced in Al-rich

samples. Nevertheless, increase beyond our designated values is challenging in the optical address of the samples as the bandgap of the alloy becomes indirect for Al contents higher than 40%. The stripes of Ga segregation could exhibit signs of quantum confinement and act as non-classical light emitters, especially if we consider that similar results of segregation has led to such phenomena in the case of Al segregation in AlGaAs shells acting as self-assembled QDs.^[109] Although no such observations were made in the case of the branched AlGaAs NWs, further works aim to address this phenomenon and explore the possibility of harvesting the novel phase separation observed in our samples as quantum light emitters.

To sum up, despite the interest and the important results reported in the past regarding the topic of III-V branched NWs, the focus on the formed 3D branched structures in terms of their structural and compositional analysis indicates that our method provides a straightforward approach for obtaining branched NWs monolithically grown on the dominant Si platform, while the structural analysis revealed the interesting formation of the Ga-rich and Ga-deficient stripes of compositional distribution, which could be examined in the future as novel types of quantum emitters. Furthermore, the self-catalysed approach that we adopted allowed for elimination of Au-induced contamination, while to the best of our knowledge there are no other reports on the growth of versatile, ternary NWs, which have the ability of bandgap tuning as a result of their composition. The above underline the importance of this contribution in the III-V branched NW research field.

4.5) Summary and Conclusions

In conclusion, this chapter investigated a highly promising AlGaAs NW variant that was frequently presented in the realized samples, which is the 3D branched NWs. This

type of nanostructures is particularly interesting for energy harvesting applications and novel light emitters. Even though branched structures were presented in all of the samples, the branching events were observed to increase with elevating Al content, reaching 60% of the total number of structures at the highest nominal Al composition of 40% that was used. TEM imaging was employed and revealed that the branches grown on the sidewalls of the trunks epitaxially, which means that they adopt the crystal structure and defects that are exhibited in the NW backbones.

Moreover, *ab initio* calculations and investigation of the existing literature allowed us to formulate the growth mechanism of the AlGaAs branched NWs, which is founded on the self-formation of the AlGaAs shell. The roughness of the shell leads to the formation of concavities where Ga atoms preferentially accumulate. These accumulated atoms amalgamate as droplets that initiate the elongation of the branches. This is supported by the calculations which show that Ga is most likely to be found at the vicinity of the base of the branches. More analytical TEM inspection showed that there are bright stripes of Ga segregation along the growth direction of the branches and perpendicular to it. The intersection of these stripes causes the appearance of a unique checked pattern of elemental distribution, with Ga-rich boxes being formed at the area of the intersection. The perpendicular stripes exhibit a high level of periodicity of roughly 3.6 nm. Based on the above, these periodic stripes are attributed to the rotation of the sample within the growth chamber, where the shadowing of the branches by the NW trunks leads to this peculiarity in the compositional distribution. On the contrary, the bright stripes along the growth direction, which are observed to be formed only on ZB facets of one particular polarity, are driven by the formation of Ga-rich nuclei at the tip of the branches in the aforementioned facets.

The thorough investigation conducted is beneficial in comprehending the mechanisms that promote this peculiar, novel elemental distribution and can be an important source of material for the realization of more self-catalysed, ternary III-V NWs. Furthermore, the Ga-rich elemental boxes formed by the intersection of the bright stripes can be exploited in the future as a novel type of quantum light emitters.

After having thoroughly analysed the morphological and structural findings of the branches, we will subsequently focus on another very important scientific domain, which is the embedding of single GaAs QDs within the AlGaAs NWs that were investigated. This inspection will be the topic of the following chapter.

Chapter 5: AlGaAs/GaAs Nanowire Quantum Dots on Si (111) Substrates

5.1) Structural analysis of AlGaAs /GaAs Nanowire Quantum Dots

The importance of nanostructures being embedded standing NWs lies in the combination of the advantageous optical properties of the latter, such as the distinct waveguide effect, with the high level of confinement offered in the lower scale stacked nanostructures. As described in Chapter 1, the majority of the emission ideally derives from the QD or QD segment, whilst it can be guided to the ending facets of the NW, maximizing light extraction. It is interesting to observe that NW tapering can drastically improve optical properties of such structures, as it promotes adiabatic transmission of the light modes. That way highly bright emission from NWQD structures has been achieved.^[167]

In the current chapter, we will analyse the synthesis of single GaAs/AlGaAs dot-in-wire structures. This signifies that there is one GaAs QD segment axially embedded in each of the AlGaAs NWs comprising the sample. For the realization of the samples, we employed epi-ready, native oxide-covered p-doped Si (111) substrates, degassed in the buffer chamber by thermal annealing at 600°C for 10 mins, exactly as in the case of AlGaAs NWs that was described in chapter 3. The AlGaAs/GaAs NWQD samples were synthesized using our MBE system that has been described in chapter 2 of the current thesis. Exactly as in the case of bare AlGaAs NWs, 600 nm of bare GaAs stems were formed for 10 mins at 610°C. Next, Al flux was introduced for the NW growth. It is noted that the atomic nominal Al composition varied between 10% and 40%. In order for the QD segment to be formed, the supply of Al was interrupted for 7 s. This allowed for the deposition of merely Ga and As during this time which led to

the realization of a nanoscale-thick GaAs segment, acting as QD, as is the typical case in single, axial NWQDs. Following this stage, Al was re-introduced for the top NW part to be developed. The total duration of the procedure was roughly 100 mins. Ga flux was corresponding to a thin film growth rate of 0.6 ML/s, as determined by earlier GaAs film calibrations on GaAs (100) substrates. The flux of As was kept stable at 2.75×10^{-6} Torr, leading to an As/Ga ratio of 15. The V/III beam flux ratio for the samples with 10%, 20%, 30% and 40% atomic nominal Al content is 14.053, 13.119, 12.134 and 11.075, respectively.

The SEM inspection of the NWQD samples did not present differences when compared to the corresponding images of bare NWs, as anticipated since the QD could not be verified via this technique. As a representative example, we present one typical SEM image of a sample with 20% nominal Al content in Fig. 5.1a, which is similar to the results obtained for AlGaAs NWs with the same composition. An initial TEM inspection was conducted in the vicinity of the NW tip. The BF image of Fig. 5.1b illustrates the spherical droplet at the NW tip, whose existence after growth confirms the VLS growth mechanism and its success in acquiring the structures. Further focus on the red square of Fig. 5.1b is presented in Fig. 5.1c, where we can see that the crystal structure is predominantly ZB. It is noted that there is the conspicuous appearance of defects, which are pronounced at this part of the structure due to the growth conditions during the final stages of the nanostructure synthesis, such as the increased group V flux, as observed in previous NW structures.□

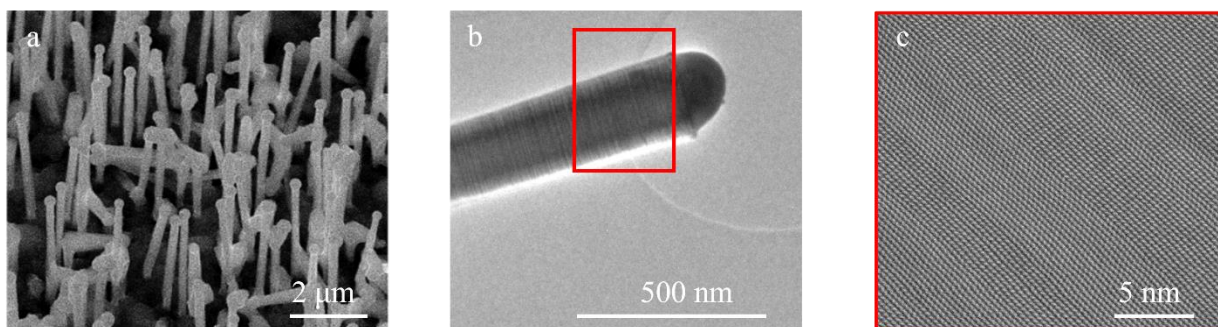


Figure 5.1: a) Typical SEM of a sample with 20% nominal Al content. b) BF image of the NWQD tip, with the spherical droplet maintained. c) Focus on the red square of Fig. 5.1b. The crystal structure is predominantly ZB with twin defects being observed.

The NW/QD interfaces should be kept as sharp as possible, even though Al tracing could not be fully avoided, due to the Al-rich shell formation, leading to increased Al presence in the EDX measurements. In order to corroborate the GaAs segment formation, it was required to conduct TEM analysis on the structures, via following the same procedure as described earlier for bare AlGaAs NWs. The results are shown in Fig. 5.2. Initially, the ADF image of Fig. 5.2a indicates the presence of the QD. The bright contrast in TEM images signifies the increased presence of the heavier element, which in this case is Ga. Due to the lack of Al, Ga content is enhanced in the dot region, leading to darker NW and brighter dot segment. For clarity, the GaAs region is marked by a white arrow in the corresponding figure. The width of the dot is approximately 5 nm. An additional, high-magnification TEM image of the QD region is presented that demonstrates the high brightness region corresponding to the dot segment. This is presented in Fig. 5.2b, where the red rectangle and white arrow show the region of the intensity profile and the direction of the EDX radial scanning for the following figures, Fig. 5.2c and 5.2d, respectively. The intensity profile of Fig. 5.2c exhibits a clear peak which corresponds to the QD and reveals a 5 nm thickness. Furthermore, EDX radial scanning was conducted at the height of the dot insertion

along the direction of the white arrow in Fig. 5.2b and is presented in Fig. 5.2d. The QD is marked by a peak in Ga and a corresponding dip in Al line. It is noted that the counts of Al are not dropped to zero in the GaAs QD region, as expected, due to the spontaneous formation of the core/shell structure. However, the clear dip in Al confirms the presence of the QD and exhibits the interfaces that demonstrate minimal intermixing.

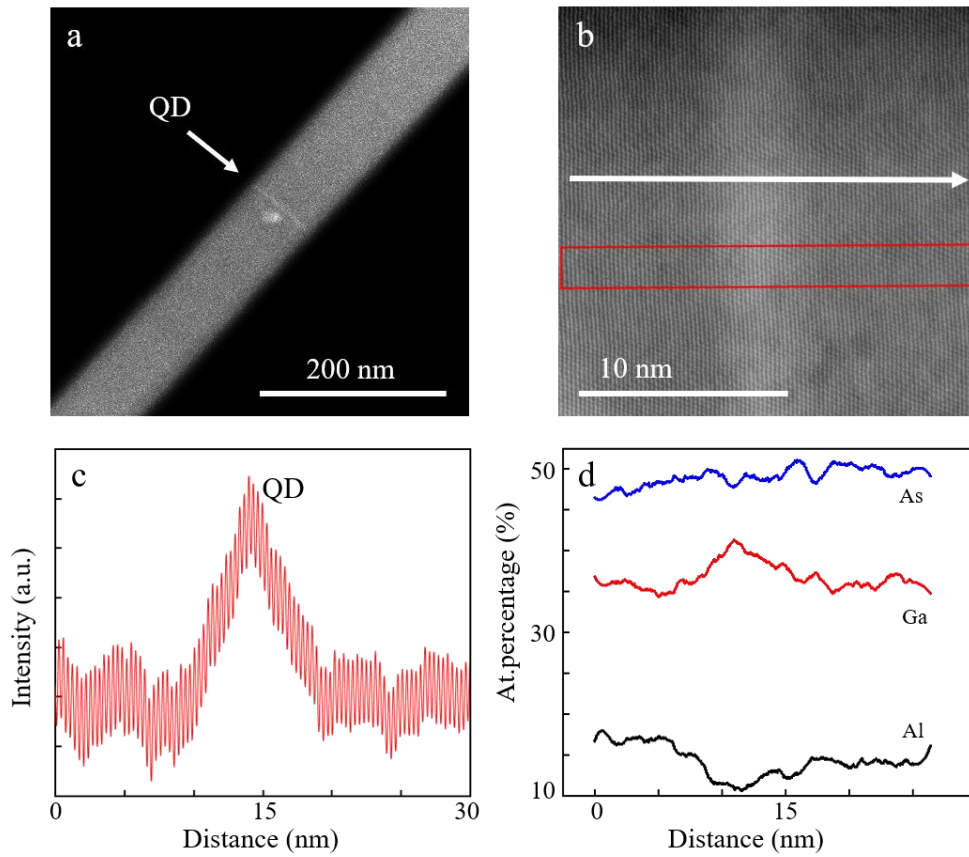


Figure 5.2: a) ADF of the AlGaAs/GaAs NWQD. The brighter region in the midpart of the NW corresponds to the GaAs QD. b) Higher-magnification ADF of the QD (presented vertically). The red rectangle shows the area of the intensity profile (Fig.5.1c) and the white arrow marks the direction of the EDX (Fig. 5.2d). c) Intensity profile along the direction of the white arrow in Fig. 5.2b. The peak corresponds to the QD, which is 5 nm thick. d) EDX scans along the NW axis. The dip in Al (peak in Ga) signifies the GaAs QD.

The structural characteristics of the remaining part of the NWQD samples were identical to the case of bare AlGaAs NWs, with increased presence of rotational twins and polytypism being demonstrated. The major differences between the two types of nanostructures, however, were presented in their optical properties. This intriguing topic will be fully explored via macro-PL and μ PL measurements in the following section of the thesis.

5.2) Photoluminescence of AlGaAs/GaAs Nanowire Quantum Dots

Despite the promising optical properties that were exhibited by AlGaAs NWs, with the most prominent being the room temperature emission, the intensity was kept at a relatively low level and the linewidth was fairly large. Hence, these structures are not ideal for achieving single photon emission, which is key for quantum computing applications. Additionally, the anticipated degree of polarization for the emitted light is small due to the intrinsic nature of the 1D NW structures. All of these points could be addressed via the development of NWQDs, the realization of which has already been described in previous chapters. Even though the structural and morphological features between NWs and NWQDs were similar, significant alterations are observed in the optical spectra that were acquired via macro-PL and μ PL measurements.

Via employing the PL setup that was described in Chapter 2, we recorded the optical spectra from NWQDs with nominal Al content varying between 10% and 30%. It is important to mention that structures with 40% Al composition were also investigated but no optical signal could be traced, as in the case of bare AlGaAs NWs. Fig. 5.3a presents low power μ PL spectra recorded as a function of the laser position along the NW axis. The relevant positions are ascribed at the right hand side of the graph. The lowest energy emission is observed at 791 nm and is comprised of a single peak,

whilst the linewidth is relatively narrow as it reaches as low as 2.53 nm at low temperature of 6 K, which corresponds to 490 μeV . We attributed this peak to the GaAs dot insertion, as revealed by its strongly spatially localized character. It is noted that narrow emission from QDs embedded in NWs has already been reported in the past and is considered very promising for light-emitting applications.^[167-168, 267] In Fig. 5.3b we present the plot of the emission against laser position, where we can clearly deduce that the behaviour of the peak is consistent with the size of the focused laser spot, being much larger than the height of the dot. Higher energy emission is comprised of two groups of lines, a small number at 778 nm and a larger number at 750 nm, as seen in Fig. 5.3a. Both groups are sustained over a wide range of laser positions, which signifies that their origin is the AlGaAs barrier layers. These two emission wavelengths correspond to Al contents of 6% and 11%, respectively. Although we notice that both emission line groups are robust in both sides of the dot, a different set is dominant for each side. Although the inhomogeneity in the composition of the AlGaAs NW core was anticipated due to the aforementioned peculiarities in the elemental distribution that was analysed in chapters 3 and 4 of the current thesis, the fact that a different set of peaks is dominant before and after the location of the GaAs QD could be indicating towards an impact of the insertions of the dot in the compositional characteristics of the NW, due to the termination and re-introduction of the Al supply. Nevertheless, more works are necessary in order to corroborate the existence of this impact.

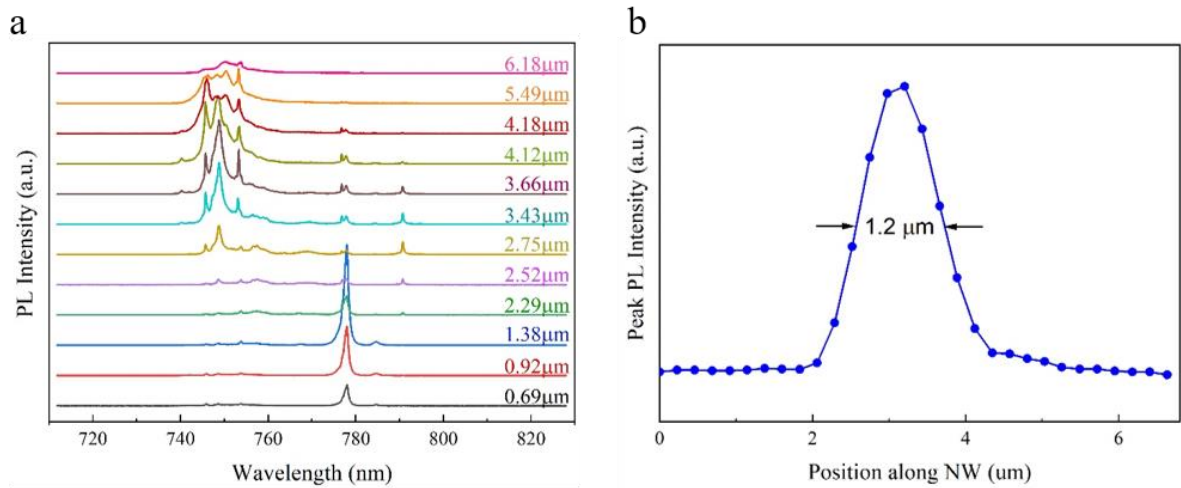


Figure 5.3: a) Position-dependent μ PL spectra from samples with 20% nominal Al content, that confirm the strong, central localization of the peak at 789.7 nm. b) Plot of the dot-related emission against laser position, where we show that the spatial profile is consistent with the size of the focused laser spot.

Apart from the position-dependent spectra that were studied and confirm the spatial localization of the GaAs QD peaks, we recorded additional measurements as a function of laser power. For this procedure, the laser was positioned at the maximum of the QD emission. It is clear that at low powers, the dot emission is a single line representing single exciton recombination. Nevertheless, with increasing power, more lines emerge due to multi-exciton recombination. The above are well-illustrated in Fig. 5.4a. On the other hand, Fig. 5.4b presents the plot of the power dependence of the two most resolved lines, which indicate an increase with power, followed by saturation and eventually exhibiting a decrease at the higher powers. This is a typical paradigmatic behaviour of a zero-dimensional system with increasing carrier occupancy. The gradients of the two lines unambiguously suggest exciton and biexciton transitions for values of 1 and 2.2, respectively. Their energy separation is

roughly 2 meV, which is in line with a calculated value of the biexciton energy in GaAs/AlGaAs QDs, that is 1.5 meV.^[268]

Besides, Fig. 5.4c depicts temperature-dependent spectra, where it can be inferred that the dot emission is quenching very rapidly with raising temperature. In fact, the emission is entirely suppressed above 60 K showing a small potential barrier for carrier escape from the GaAs section. It is noted that thermal stability could be potentially improved in future works via further optimization of the growth. For instance, elimination of defects of the AlGaAs barriers surrounding the dot could positively influence the optoelectronic response of the structures. Nonetheless, the existence of a QD-related emission that was grown via the self-catalysed approach is an important step in harvesting the benefits of the aforementioned structures. Moreover, the integrated intensity of the dot emission and its ratio to the barrier emission are plotted in the upper panel of Fig. 5.4d. It is noted that presenting the results in terms of the ratio can correct any potential misalignment of the samples as a result of the increasing temperature. It is not possible to extract a reliable value for the activation energy of the quenching of the QD emission but taking into account that the lowest energy AlGaAs emission takes place at 778 nm, which is only 24 meV above the GaAs peak, it is expected that there would be a rapid decrease in the emission intensity. Higher Al percentage on both sides of the dot could possibly lead to a higher stability in the optical behaviour of the structures. On the other hand, the lower panel of Fig. 5.3d illustrates the plot of the temperature dependence of the QD single exciton emission linewidth. At low temperatures, the linewidth is as low as 490 μeV , as mentioned earlier. However, it is quickly increased with raising temperature. This trend is described well by a model in which carriers are scattered out of the ground state of the QD by acoustic phonons.^[269] The energy related to this model is the separation energy

between the ground state and the first excited state of the QD. The value that was extracted from the fit to the experimental data is roughly 3 meV. Both the power-dependent measurements and the temperature-dependent measurements indicate that the GaAs segment displays properties of a 0D system, confirming its nature as a single QD. This can be seen because on one hand there are different orders of exciton processes in the power-dependent spectra and on the other hand the emission linewidth is strongly dependent on the temperature. The above optical experiments demonstrate the suitability of the AlGaAs NWs as hosts of QDs with good optical characteristics.

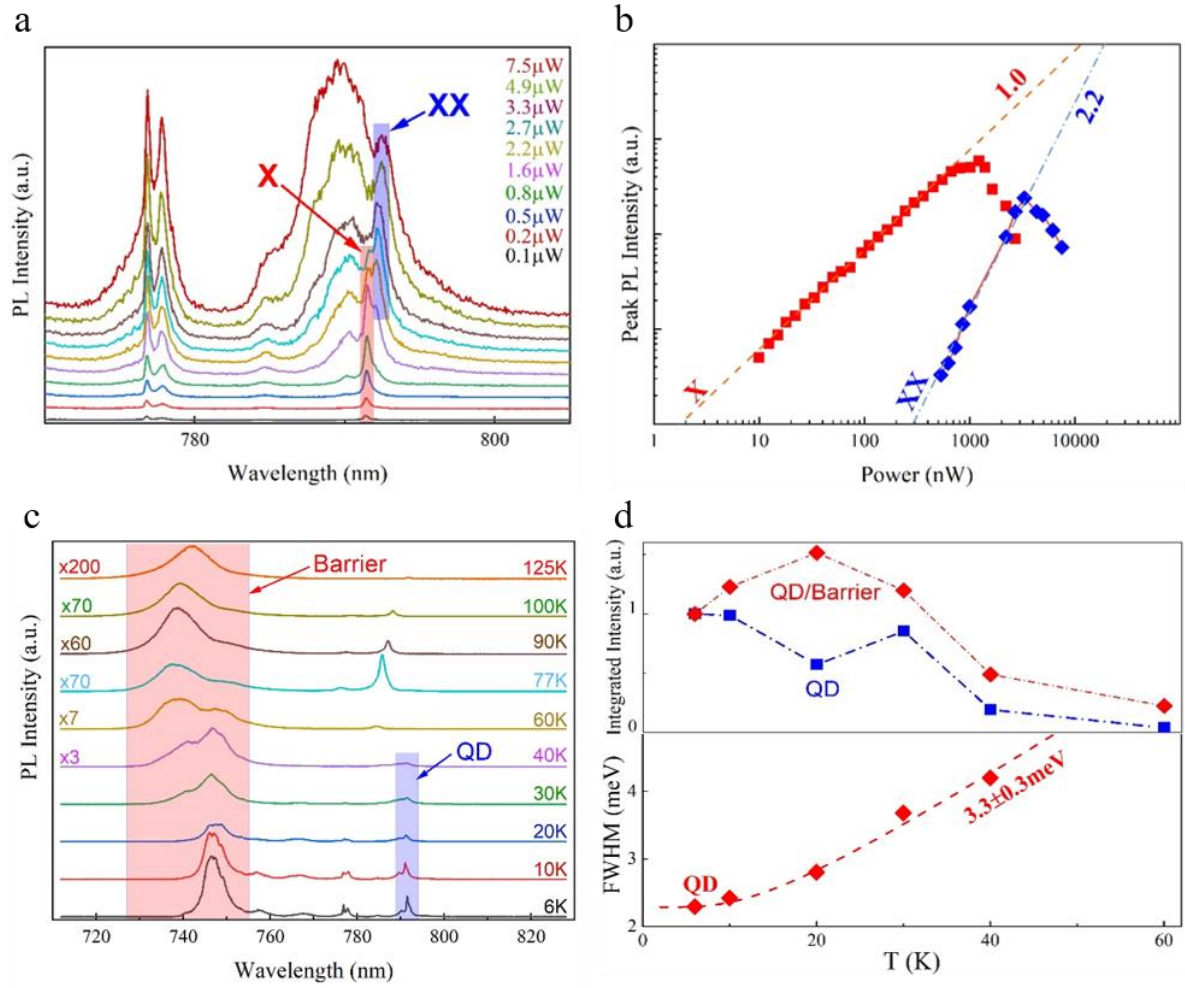


Figure 5.4: a) Power-dependent μ PL from samples with 20% nominal Al content. The dot-related peak at 789.7 nm is comprised of one exciton transition dominant at low powers and a biexciton transition prevailing at high powers. b) Plot of the peak PL intensity as a function of the power, showing the linear dependence and quadratic dependence for the two peaks, confirming their origin as exciton and biexciton transitions, respectively. c) Temperature-dependent μ PL spectra from the same sample, where we demonstrate that the dot-related peak is rapidly quenching and is unnoticeable above 60 K. d) Upper panel: Plots of the integrated intensity of the QD emission and its ratio to the barrier emission. Lower panel: Plot of the temperature dependence of the QD single exciton emission linewidth.

Besides, polarization of the emission was evaluated in the same NWQDs, by conducting measurements with the excitation power set at roughly 1 μW , whilst the laser spot was fixed on the position that produced the most intense QD-related peak. A linear polarizer and a half-wave plate were inserted in the beam path, prior to the spectrometer in order to acquire the results. In Fig. 5.5a, we observe the NW image, clearly illustrating the orientation of the structure. The polar plot of the three main peaks at 748.8 nm, 787.6 nm and 789.7 nm are demonstrated in Fig. 5.5b. It is important to note that the polar plot orientations are such that 0° on the plot correspond to the x-direction of Fig. 5.5a and 90° correspond to the y-direction. Consequently, by overlaying the NW image on the polar plot, it is possible to define the orientation of the NW in the latter, which is indicated by the black arrow (Fig. 5.5b). The AlGaAs NW-related peak at 748.8 nm is very slightly polarizer, which is anticipated due to the non-polarized nature of the bare NW emission. On the contrary, the two QD peaks at the high-wavelength side of the spectrum are more strongly polarizer, when compared to the AlGaAs band. For the peaks at 787.6 nm and 789.7 nm, the maximum light intensity is presented at 62° and 70° clockwise off the NW axis, respectively, whilst the minimum light intensity is exhibited at 26° anticlockwise for both peaks. It is reminded that the former is attributed to AlGaAs barrier emission, while the latter is deriving from the GaAs QD segment. At this point, we should highlight that the recording of the measurements was carried out by rotating the half-wave plate and keeping the linear polarizer at a fixed position to circumvent the challenges of the polarization dependence on the reflectance of the spectrometer grating. Considering that a full rotation of the half-wave plate corresponds to two full rotations of the linear polarizer, each set of measurements produced two plots of similar shape corresponding to each peak (Fig. 5.5b), with only some slight deviations in the exact

value of the light intensity. Besides, in order to quantitatively estimate the degree of polarization (DOP), we used the equation $(I_{\max}-I_{\min})/(I_{\max}+I_{\min})$ to calculate the exact value. For the AlGaAs NW-related peak, the light was very slightly polarized with the DOP being roughly 20%. On the other hand, the value of DOP was increased at 70% for the AlGaAs barrier-related emission and obtained the maximum value of 72% for the QD peak at 789.7 nm. The enhanced polarization exhibited in the dot-related emission, when compared to NW emission and barrier emission, is promising for their implementation in entangled photon sources.^[270] Nevertheless, it should be mentioned that the high density of impurities, such as twin defects and polytypes of the crystal, is considered a degrading factor. Consequently, optimization of the structural purity of the NWs is a vital requirement for their broader applicability, which should be investigated in future works.

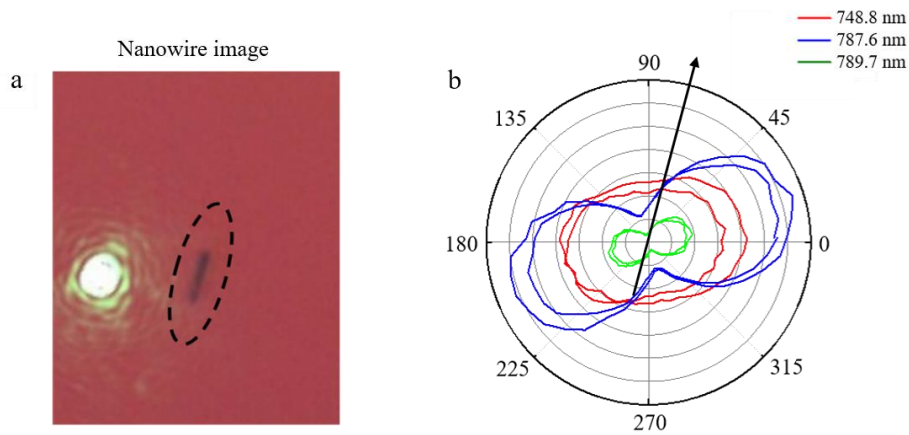


Figure 5.5: a) Image of the NW with an embedded QD, showing its orientation. The NW is marked by the dashed ellipse, for clarity. b) Polar plot of the peaks of the disk-in-wire structures. The AlGaAs-related peak (748.8 nm) is very slightly polarized. On the contrary, the dot-related peaks show a remarkably higher level of polarization with the peak at 789.7 nm reaching a DOP of 72%. The black arrow marks the direction of the NW.

5.3) NextNano Simulations of the nanowire quantum dots

In order to corroborate the experimental observations regarding the optical response of the GaAs/AlGaAs dot-in-wire structures, simulations were run using NextNano, which is a versatile software allowing for the simulation of nanoscale structures and devices.^[271] As a package that focuses on structures where quantum mechanics play a dominant role, it allows the users to identify features such as electronic band structures and magnetic field effects among others. The input is a file specifying the material platforms that are used along with geometrical information.

As NextNano is beneficial for simulating the quantum mechanical properties of systems, its role in the analysis of quantum dots where such phenomena prevail is useful. For instance, it is highly significant in order to conduct computations on the electronic band structure and the optical properties of III-V quantum structures.^[272] A paradigm is the use of NextNano to determine the electron activation energy in single GaAs QDs embedded in GaAsP NWs along with the separation energy.^[227] The aim of employing these simulations in our structures was to simulate the electronic band structure in order to extract the simulated values of the ground hole and electron separation energy. After subtracting the known exciton binding energy for the current material system,^[230] we can acquire the anticipated exciton emission energy for the given material platform and specific geometrical features. If the exciton emission energy matches the PL emission that was measured and described in Fig. 5.4, the system is confirmed to be a dot-in-wire structure.

In our case, the input file was comprised of the geometrical information on the AlGaAs/GaAs NWQDs. This is presented in Figs. 5.6a-b. Specifically, in Fig. 5.6a, the cross-sectional geometry of the simulated NWQD above and below the QD segment

is presented. In addition, the same geometry through the QD region is illustrated in Fig. 5.6b. It is noted that for the NW core, the effective Al composition that was modelled was 20%. This is because this sample is more representative as shown during the TEM inspection that was analysed earlier. The Al content of the shell was regarded as 70%.

For our simulations, we employed the minimised strain model, where the substrate strain is set to zero. The width of the hexagonal QD that we simulated was assumed to be 110 nm, normal to the NW axis, while the height of the dot was 5 nm along the axis. These values are chosen in accordance with the TEM data of the NWQDs that were presented earlier in the current chapter. Fig. 5.6c depicts the calculated conduction and valence band edges along the NW axis. The energies of the lowest QD electron and hole confined states for non-interacting particles are also presented. The energy separation of the ground hole and electron state is 1.599 eV. It is noted that in order to see if the anticipated energy separation corresponds to the PL emission that was experimentally observed, the exciton binding energy needs to be subtracted from the aforementioned value. The exciton binding energy is 25 meV for this material system (AlGaAs/GaAs).^[230] The eventual value of the exciton emission energy is 1.574 eV, which corresponds to a wavelength of 787 nm. This is in reasonable agreement with the experimentally observed value of the PL peak, which is 789.7 nm for samples with 20% atomic nominal Al content. The negligible discrepancy in the values can be attributed to computation limitations and the high complexity in terms of structure and composition of the grown NWQDs. Nevertheless, the matching of the simulated and experimentally extracted values is considered acceptable and accurate. Q

The separations of the ground and first excited QD states are calculated to be 1 meV for electrons and 0.6 meV for holes. It is noted that the activation energy extracted

from fitting the temperature-dependent spectra with a model based on exciton scattering by acoustic photons has been reported in the past as 3 meV.^[269] Despite the difference in our calculations, the values of 1 meV and 0.6 meV mentioned above are considered within the frame of acceptable error with the previously reported value.

It is interesting to mention that even though the QD thickness was as low as 5 nm along the NW axis, its lateral dimensions that were simulated as well as observed in the TEM inspection of the previous sections were relatively large (110 nm in the case of the NextNano simulations). Despite this fact, the QD nature of the peak, as revealed by the localized peaks, the narrow linewidth and importantly the exciton and biexciton transition confirm that the GaAs segment is a QD, as the linewidth would be expected to be larger in the case of quantum wells. Optical activity in larger QDs has been observed in the past, as it has been calculated that QDs with lateral dimensions as high as $80a$, where a is the lattice constant, can present over 6000 discrete energy states for QD-related emission to occur.^[273]

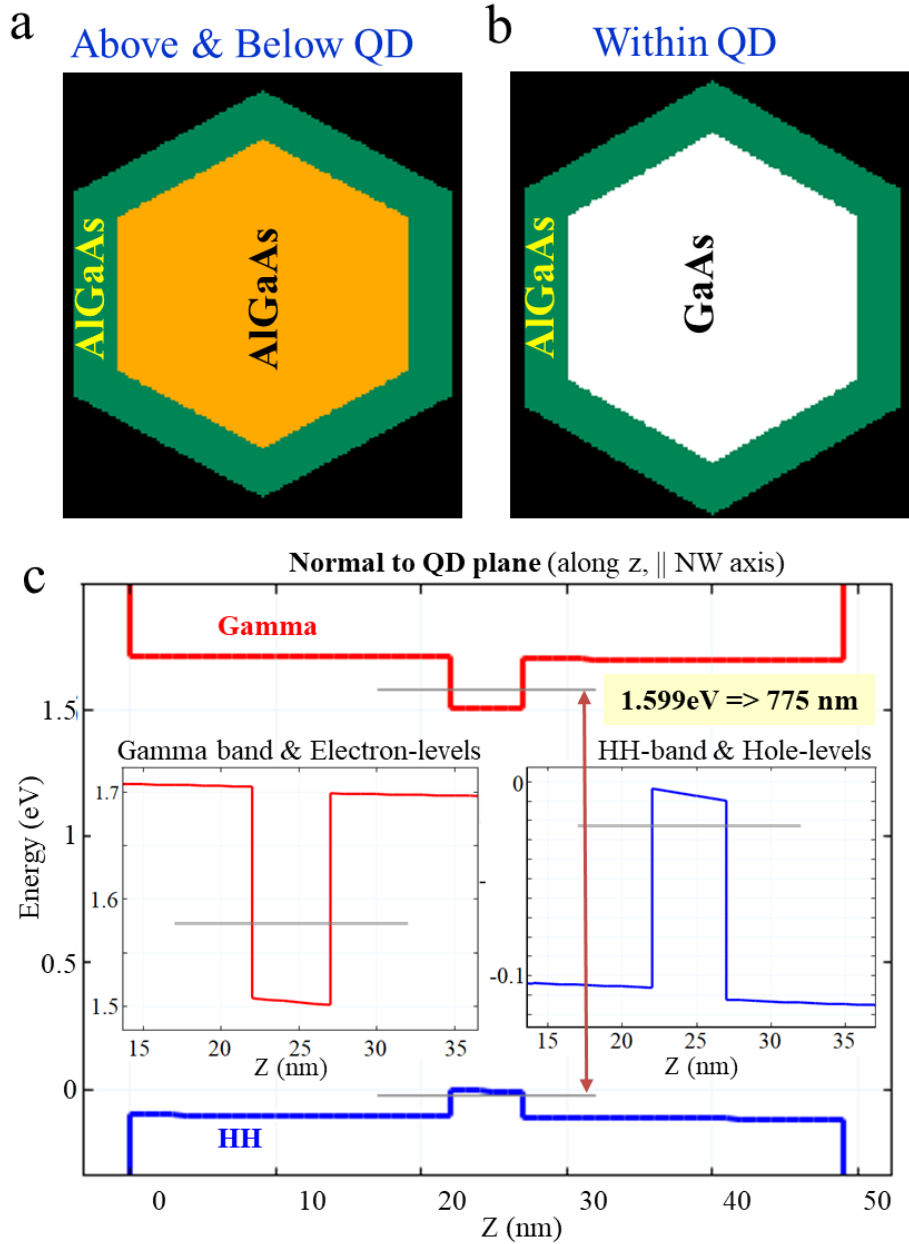


Figure 5.6: a-b) Geometry of the simulated AlGaAs/GaAs NWQD structure. Slices of the structure above and below the dot (Fig. 5.5a) and through the QD (Fig. 5.6b) are depicted. b) Band edge profiles along the central axis of the NW and energies of the lowest electron and hole confined GaAs QD states. The insets depict the ground state electron and hole levels on an expanded scale.

5.4) Comparison of our work with previous works on single III-V Nanowire Quantum Dots

Before proceeding to the summary and conclusions of the current chapter, it is interesting to compare our work with similar NWQD structures that have been obtained in the past especially considering the wide impact of these nanoscale structures in novel applications such as quantum information processing. Initially, works have been reported on the particular material platform that we have employed (AlGaAs/GaAs NWQDs). The optical emission typically occurs within the spatial range of 600 nm to 800 nm.^[131, 228, 274-276] The existence of the dot region in the NWs manifests itself as an additional peak, similar to what was observed in the PL measurements that we presented in the current chapter. Moreover, In addition, resonant excitation of an exciton and a biexciton transition has been observed in Au-catalysed AlGaAs/GaAs NWQDs.^[277] The growth parameters are considered highly important for the emission properties, as increase in the growth temperature after a critical value could reduce or suppress emission.^[228] Moreover, the compositional distribution of Al affects, as we noticed in our experiments. Specifically, higher Al composition can cause a blueshift of the AlGaAs NW emission, although its impact on the QD emission which is comprised of GaAs is not directly linked to this phenomenon. Nevertheless, increased presence of Al could lead to unintentional intermixing in the QD region especially considering the self-formed Al-rich shell surrounding the dot-containing NW segment. This is something that was observed in our case were despite the clearly formed GaAs QD some Al counts were traced in that region, which however did not affect the measurements. Besides, the QD size has also been found to affect in previous reports, in terms of the wavelength of the QD emission as longer growth times beyond the ones we used could increase the width of the dot and reduce the impact of quantum

confinement effect.^[131] We underline at this point that the most prominent differentiation in our research is the use of self-catalysed AlGaAs NW structures instead of Au-catalysed growth, which up to our knowledge has not been exhibited before. This reduces Au-related contamination and allows for the easy consumption of the Ga droplet under high As flux without further processing steps.

Apart from AlGaAs core NWs, GaAs QDs have been embedded in the shell of GaAs/AlGaAs core/shell NWs.^[219-220, 267, 274] Via adequate control of the growth parameters ultralow emission peaks have been recorded.^[274] The emission is attributed to an exciton and biexciton transition, with the later showing a narrow linewidth of 458 μeV , comparable to our 490 μeV -wide emission that we achieved in AlGaAs core NWs. These values can be compared to popularly grown SKQDs.^[70] The difference in this case is the embedding of NWs in the shells instead of axially in the core, which albeit effective, could pose challenges related to the careful control of the growth parameters, as it is highly important to maintain Al in the dot region to the lowest possible level (some Al counts in real conditions are to be anticipated).

Importantly, other III-V material platforms have been used for the realization of single dot-in-wire structures. The most important results have been achieved for InP/InAsP NWQDs with very low linewidth of 120 μeV at roughly 1.4 μm .^[168] Nevertheless, these structures were grown on InP (111)B substrates and their formation monolithically on Si, with all the advantages that have been discussed in the current thesis, has not been achieved so far. Another useful material platform is GaAsP/GaAs NWQDs with sharp emission deriving from the QD region at 1.66 eV while the linewidth is narrow at 130 μeV , developed in our group at UCL.^[88,227,278] Similar to our case, the peaks quench after 60 K as a result of carrier escape from the QD segment.^[88] These types of NWQDs have exhibited good photon antibunching

behaviour and a degree of polarization of 82.5%.^[227] It is noted that among the challenges in this material platform is the indirect nature of the bandgap for P contents above 44%, rendering the study of further increase of P content impractical.

Based on the results described above and on the importance of AlGaAs ternary alloy for red and near-infrared emitting applications, we believe that the importance of our research is accentuated, while the monolithic growth on Si and the self-catalysed, Au-free growth technique along with the good optical results and narrow linewidth comparable to SKQDs displays that NWQDs based on this material platform hold promise for future implementation in device applications.

5.5) Summary and Conclusions

The current chapter examined the growth of single GaAs/AlGaAs dot-in-wire structures and investigated on their structural features and mostly their optical response via PL inspection. The formation of the GaAs QD segment was confirmed via TEM imaging, where the high brightness of a region close to the centre of the NW signified Ga richness and corresponded to the QD insertion. This was further corroborated via the extraction of the intensity profile and EDX scanning. It is reminded that Al was significantly reduced within the GaAs QD, but the counts could not reach zero, which is the ideal scenario, due to the formation of the self-grown AlGaAs shell.

The optical investigation of the samples revealed that the QD-related peaks were spatially localized and exhibited a narrower linewidth of roughly 490 μeV , as opposed to the AlGaAs barrier-related peaks that were broad and presented several transitions. Moreover, it could be seen that QD emission was comprised of an exciton and a biexciton transition, which was confirmed by the plot of the intensity of the peak as a function of the excitation power, where the gradients of the lines were indicative of

exciton and biexciton transitions for values of 1 and 2.2, respectively. The QD emission was rapidly suppressed with increasing temperature and was eventually quenched after 40 K. However, further optimization of the crystal structure could lead to the emission being sustained at higher temperatures. In addition, the QD peak at roughly 789.7 nm was shown to be highly polarized, with a DOP of 70%, while the AlGaAs NW emission was unpolarized as the DOP did not surpass 30%. Finally, NextNano simulations via the minimised strain model indicated that the energy separation of the ground hole and electron states was roughly 1.599 eV, which after subtracting the exciton binding energy, led to a value of 1.574 eV, corresponding to 787 nm. This value confirmed the QD nature of the peak located at 789.7 nm.

The results presented in the current chapter demonstrate the good optical properties of the self-catalysed AlGaAs/GaAs NWQDs, while eliminating Au-related issues. The QD nature of the GaAs-related peak was established via the analysis of the PL measurements, while the simulations confirmed the experimentally observed conclusions. The above indicate the importance of these structures in light-emitting applications, including single photon sources and entangled photon pair sources that are vital for novel, quantum information processing applications.

Following the description of the morphological and optical behaviour of the GaAs/AlGaAs single dot-in-wire structures that we realized, the analysis of the AlGaAs-based nanostructures grown via self-catalysed MBE is finished. In the next chapter, we will introduce a different type of nanostructures that have re-attracted attention over the past years due to their vast potential in device applications; 2D nanosheets. We will also present the thorough and systematic optical study of the PL behaviour of the structures that render them promising for ultralow power consumption optoelectronic memory units.

Chapter 6: Two-dimensional InAs nanosheets

6.1) Introduction

6.1.1) Surface Passivation Methods

As described in the introduction, the large surface-to-volume ratio of nanosheets causes a high density of surface states that act as carrier traps. This opens the route for interesting applications. For instance, InAs nanosheets exhibit the “memory effect” which renders them good candidates for optoelectronic memory applications but in the drawback, it suppresses the intensity of the emitted light due to the introduction of non-radiative recombination paths at the surface states. As a result, surface passivation is important in order to apply these techniques whenever necessary and depending on the application that is aimed.

Surface passivation leads to neutralization of the surface states, which are then inactive and stop carrier trapping procedures. As NWs are also nanostructures with a potentially high density of surface states, some practices of surface passivation have been applied to them as well. For instance, one of the most widely employed methods, frequently encountered in works related to 1D NWs is the realization of a core/shell architecture.^[170-171] This technique is direct and most importantly financially effective as it does not involve any additional processing steps that would require a higher cost. The shell covering the surface of the structure’s core impedes carrier trapping processes at the surface states and allows for an enhancement of the PL intensity. Nevertheless, the lattice mismatch at the core/shell interface, which occurs when incompatible materials are combined, leads to the formation of dislocations, that can be potentially detrimental to PL peaks.^[172-173] Another alternative is passivation via applying a chemical solution. This is a post-growth technique, where a solution is used

to deactivate surface states. A characteristic example of a passivation method for III-V nanostructures is the employment of a sulphur solution that leads to the formation of bonds between sulphur atoms and surface atoms. This way, the surface dangling bonds are eliminated, while the formation of oxide layers is prohibited. This is also a method that has been systematically applied for passivation of NW surface states.^[279-283] A characteristic example is the use of organic sulphide for passivation of InGaP NW-based LEDs which has increased the device efficiency.^[279-283] Inorganic sulphide (NH₄)₂S solution has also been applied for the passivation of InAs NWs, leading to a 17-fold enhancement of their PL intensity.^[281] Despite the high interest of 2D nanosheets and the successful analysis of their growth and crystallinity, the passivation of their surface is a subject that is far from being fully unravelled.

6.1.2) Importance of InAs as a binary alloy

Despite the advantages of ternary alloys (including AlGaAs that has been studied in the current work) and the maturity of GaAs, there are several other binary alloys that are of equal importance. Among the various III-V alloys, InAs is a significant material platform in the field of optoelectronics, owing to the high electron mobility that facilitates carrier transport.^[284] Another advantage of InAs nanostructures is the electrical conductivity, reached without any need for doping due to the Fermi level pinning at the conduction band, rendering them ideal for electronic applications.^[285]

Implementation of InAs in nanoscale systems has been reported in the past for QDs^[286-287] and NWs,^[288-290] with good results. Due to the advantageous features of 2D materials and InAs nanosheets have regained scientific interest over the past years. Consequently, structures with high material purity have been accomplished.^[200,208-209] Apart from the SAG method for nanosheet development,

another alternative that has been adopted is the growth of InAs nanosheets directly from 1D InAs NWs. For instance, Pan et al. suggested that elemental segregation of an Ag-In alloy could be the stem of the transition from NW to nanosheet form in InAs structures.^[200] The nanosheets produced that way are of optimum quality and present vast potential for light-emitting functions and applications.^[200]

After having introduced and accentuated the importance of InAs nanosheets along with the surface passivation methods available, in the following sections we will focus on the systematic optical study of InAs nanosheets grown directly from 1D NWs via MBE. The optical study will shed light on the clear signs of “memory effect” of pristine structures and the effect that different passivation methods applied have on the nanosheet response.

6.2) InAs nanosheet growth

The importance of InAs nanosheets owing to their two-dimensionality and free-standing nature ensuring minimised strain has led to these structures regaining interest over the past years. Growth of III-V nanosheets with good results has been achieved in the past via SAG, regularly.^[203-205] In the case of the samples that we optically addressed later, the growth occurred straightforwardly from 1D InAs NWs. The growth method is identical to the one described in ref.[200]. The growth occurred via MBE on epi-ready, p-type Si (111) substrates which were immersed in a diluted hydrogen fluoride (HF) 2% solution for 1 min to eliminate surface contaminants. The growth time was 40 mins, while the growth temperature was 505°C. The flux of In was initially 1.5×10^{-7} Torr while As flux was 4.42×10^{-6} Torr, signifying that the V/III ratio was 29.5. With this configuration, the sample is comprised of 1D NWs and some parasitic 2D growth. However, with increase of the In flux to 7×10^{-7} Torr, while keeping As flux

stable, the growth of fully formed nanosheets is observed.^[200] The growth was terminated in all cases by stopping the supply of In, while the supply of As was kept for a few more minutes until the temperature of the substrate drops to 300°C.

We acquired SEM images of the InAs nanosheets that we examined in our facilities. One representative example of an SEM image grown at a V/III ratio of 6.3 is presented in Fig. 6.1a. Considering the structural study that was conducted on the samples by the group that fabricated them, a typical SEM image that they acquired is presented for comparison in Fig. 6.1b. Despite the different focus and slightly different tilting, as we used 30° while in ref.[200] they used 25°, the similar morphological results are evident and show that 2D InAs nanostructures were successfully grown via the aforementioned technique. It is noted that reduction of the V/III ratio by increasing In flux beyond a critical value is anticipated to impede the successful growth of a continuous InAs 2D nanosheet, due to the In-induced modification in the consistency of the droplet.^[200]

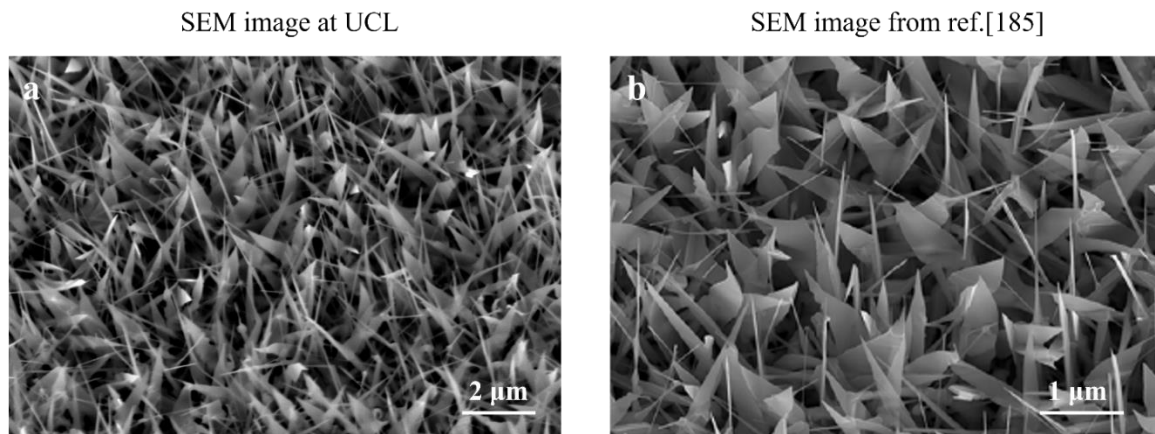


Figure 6.1: a) SEM image with 30 degree tilting that we acquired at UCL facilities. b) Comparison with SEM image from ref.[200] on the same samples. The results are very much alike indicating that 2D InAs nanosheets were successfully grown directly from 1D NWs.

It is interesting to mention that the dimensions of the nanosheets were also measured. The axial and radial dimensions on the p-doped Si (111) were $4 \times 1 \mu\text{m}$ and the thickness of the nanosheets was roughly 40 nm. These values were obtained via intensity profiles that were conducted on atomic force microscopy (AFM) images. It is noted that AFM was conducted on FETs that were fabricated based on the InAs nanosheets. This will be further analysed later in the current chapter. Initially, in Fig. 6.2a, we present an additional SEM of the InAs nanosheet samples. In Fig. 6.2b, a typical AFM image of the fabricated FET is presented. The blue and red arrows correspond to the axial and radial directions of the sample and illustrate the directions of the intensity profiles. The results are presented in Figs. 6.2c and d for the radial and axial dimensions, respectively. The dimensions depicted by the spacing between the peaks of Fig. 6.2c and the linewidth of the peak in Fig. 6.2d are $4 \times 1 \mu\text{m}$, while the thickness represented by the amplitude of the peak is 40 nm.

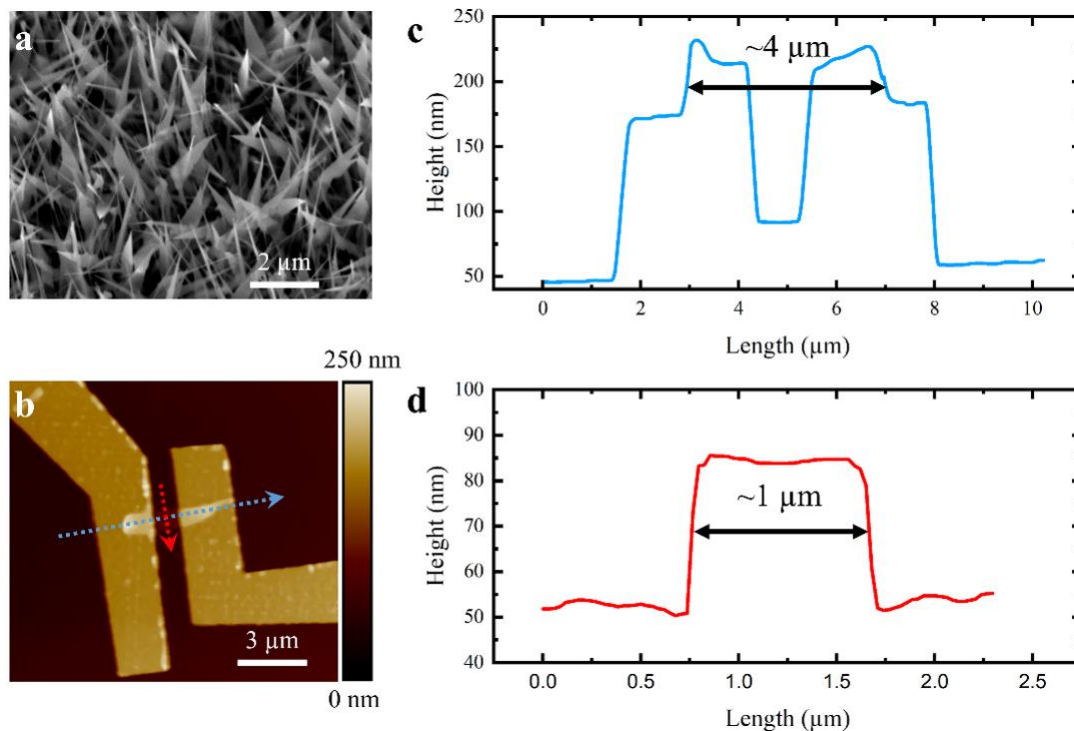


Figure 6.2: a) SEM image of the InAs nanosheets. The formation of dense structures is confirmed. b) AFM image of the fabricated FET, where the blue and red arrow mark the nanosheet axial and radial dimensions. c-d) Intensity profiles for the blue and red arrows, respectively, revealing dimensions of 4 μm in length and 1 μm in width for the sample. The height is revealed to be roughly 40 nm.

The crystal structure of the nanosheets was polytypic with WZ/ZB mixed formation. As described earlier, this is typical in nanostructures grown via VLS growth mode as is the case for the samples used in our experiments. A characteristic TEM image of a nanosheet structure is presented in Fig. 6.3a.^[200] The red square is the area of focus for the subsequent high-resolution TEM image (Fig. 6.3b), where it is also clearly viewed that the catalyst droplet did not maintain its spherical shape, indicating polycrystalline growth.^[200] Further focus on the blue and green squares of this figure, corresponding to the top and side regions of the nanosheet, are presented in Figs. 6.3c-d. In these detailed images it can be seen that there are twin defects and stacking

faults, while the polytypic nature is confirmed. It is interesting to notice that in ref.[200], which examines the structural aspects of the current samples, increasing the temperature at 525°C leads to a further reduced density of crystal defects. The same was the case after increase of the In flux to 8.5×10^{-7} Torr.^[200] The improvement of crystal quality with increasing growth temperature is an observation that has been made before in 1D InAs NWs^[8] and is consistent with previous reports stating that defects are not static and their movement is thermally activated.^[111] The above indicate the high material quality of the samples and the potential for further improvement in the future via the aforementioned adjustments in the growth conditions. It is noted that the high brightness region surrounding the darker nanosheet core in Fig. 6.3, which could correspond to the shell formation due to the addition of Ga, has a thickness of roughly 20 nm.

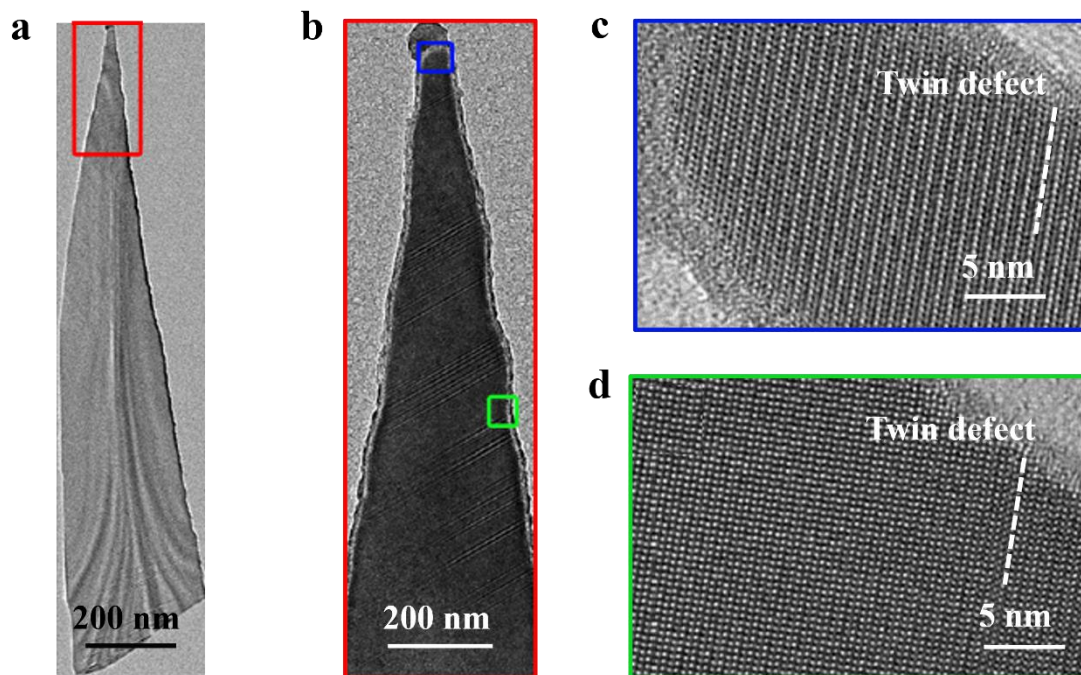


Figure 6.3: a) TEM image of a nanosheet structure. b) Focus on the red square of Fig. 6.3a. c-d) Further focus on the blue and green squares of Fig. 6.3b representing regions of the tip and side of the InAs nanosheet, respectively.^[200]

After having referred to the structure and morphology of the nanosheets, we will proceed with the optical analysis, which has been the main focus of our research due to the interesting optical response of the samples. The above are described in detail in the following sections of chapter 6.

6.3) Power-dependent photoluminescence on InAs nanosheets

6.3.1) Methods of measurements/Signs of “memory effect”

As previously mentioned in the current chapter, the high density of surface states in 2D nanosheets causes significant differentiations in the PL spectra that are acquired due to charging of the material via electron trapping at these states. The results are indicative of the arising of the “memory effect”. It is pointed out that optoelectronic memory units typically function by carrier trapping in states.^[291] For instance, carrier depletion in the active channel occurring due to carrier trapping at the surface of the material can lead to robust PL signal after light irradiation.^[292-293] This is indicative of the ability of the structure to acquire “memory” of its previous state via a charging and discharging procedure of the surface. In order to evaluate whether this phenomenon is presented in the different samples that we measured, we performed two sets of measurements. In the initial approach, the power of excitation was increased from 0 mW to 1000 mW, whilst in the second approach it was reduced from 1000 mW to 0 mW. For the rest of the current chapter, the two techniques will be referred to as the “power-up” and “power-down” approach, respectively. It is important to mention that for all the power-dependent measurements in both approaches, the temperature was stable at 10 K, after cooling down the system with liquid helium. For the temperature-dependent measurements, the power of excitation was set at the value that resulted in the maximum signal for each sample, in order to trace it at higher temperatures. The

temperature was increased from 10 K to RT, in order to inspect the maximum temperature where robust emission was exhibited.

6.3.2) Pristine InAs nanosheet samples

Initially, the measurements were carried out on pristine InAs nanosheets, where an intriguing phenomenon was observed. The “power-up” measurements showed no strong emission throughout the entire range of scanning. This can be viewed via the solid lines of Fig. 6.4. It is demonstrated that from 50 mW until 1000 mW the peak is very weak and exhibits severe broadening and wide fluctuations. It is noted that the lack of peak at 0 mW signifies that the emission derives from the InAs nanosheet samples and that the noise contributions are negligible if any. However, after the termination of the “power-up” approach, a second scan at 1000 mW was immediately recorded. Following that, the “power-down” approach was conducted, where strong emission was evident in the entire range of measurements acquired. This can be viewed via the dashed lines in Fig. 6.4.

From the results of Fig. 6.4, it is clearly depicted that there is a radical increase in the PL intensity of the “power-down” approach, when compared to the “power-up” approach. This is indicative of the presence of a mechanism that instantly weakens the PL response during the latter approach. On the contrary, this mechanism is significantly weakened after the scanning at the maximum power of 1000 mW. The function of this mechanism is possibly based on carrier depletion in the channel due to trapping by the surface states leading to reduced recombination rate. Hence, the optical response is radically reduced, as the trapped carriers at the surface states do not recombine. Nevertheless, after the first scan at 1000 mW, the large number of photogenerated carriers occupies the majority of surface states, eventually saturating

this mechanism. Ergo, strong peaks appear during the subsequent “power-down” approach. Considering the high density of surface states and the known impact they have regarding optoelectronic “memory effect” via electron trapping and de-trapping,^[292,294] it can be interpreted that the peculiar observations originate from electron trapping at the surface of the InAs nanosheet samples during the initial “power-up” approach, which is saturated after scanning at high excitation powers leading to the appearance of strong PL peaks during the “power-down approach”. The above are suggestive of the “memory effect”.

It is noted that the role of electrons at the surface states is prominent in InAs-based materials that typically form an electron accumulation layer, causing modifications in the band diagram. This is depicted in the schematics of Fig. 6.5. Specifically, at the initial stages the photoexcited carriers are filling surface states and start forming the accumulation layer (Fig. 6.5a). Next, after the termination of the “power-up” approach, the surface states are occupied and the accumulation layer at the clean InAs surface has formed (Fig. 6.5b). Finally, the “power-down” approach begins and since the surface states are occupied the newly photoexcited carriers will recombine radiatively leading to the generation of strong PL peaks (Fig. 6.5c).

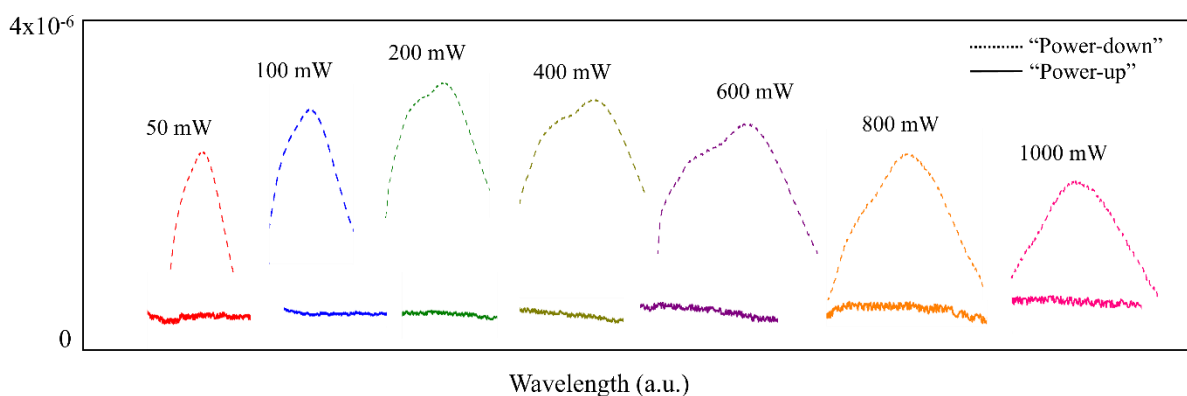


Figure 6.4: Plot of the signal as a function of the excitation power, for “power-up” (solid lines) and “power-down” (dashed lines) approaches for pristine InAs nanosheets.

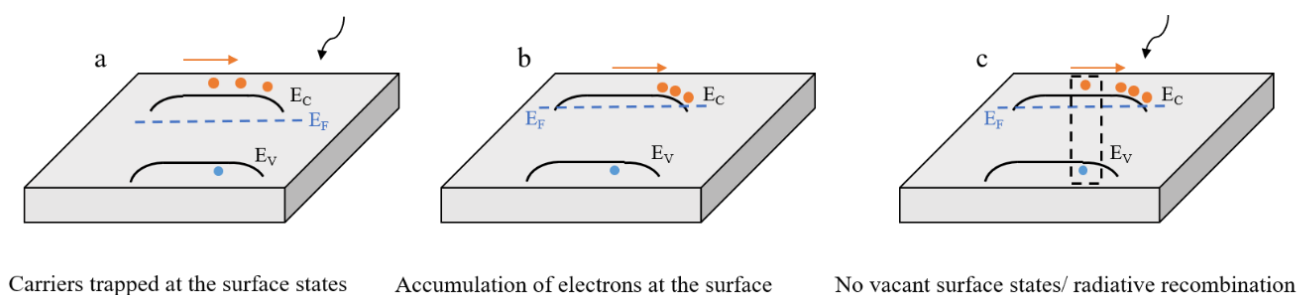


Figure 6.5: a-d) Schematic representation of electron trapping based on the band diagram schematics. Initially the photogenerated carriers due to laser excitation (black arrow) leads to occupation of surface states that leads to the formation of an electron accumulation layer at the surface (Fig. 6.5a). Then after the “power-up” approach is terminated, the surface states are filled and the electrons have accumulated at the InAs clean surface (Fig. 6.5b). Hence, subsequent further excitation will lead to the new carriers recombining as depicted with the dashed rectangle of an electron-hole pair (Fig. 6.5c).

For a more representative inspection of the PL intensity trends, the values for both “power-up” and “power-down” approaches for pristine InAs nanosheets were plotted

as a function of the excitation power. The results are presented in Fig. 6.6a. The curve for the “power-up” approach shows weak intensity of the emission peaks, which is almost stable at low excitation powers and slightly increases at the highest powers used. Opposite to this, the “power-down” measurements indicate the intensity increases. Interestingly, two regimes are clearly illustrated. Regime II includes the surprising observation of increasing PL intensity with declining excitation power from 1000 mW until 200 mW. Regime I extends from 200 mW to 0 mW, where this behaviour is reversed and the intensity of the peak is decreasing with declining excitation power. The latter is presenting the anticipated behaviour in power-dependent optical experiments. The origin of the two regimes is suspected to be the modifications in the ambient temperature caused by laser heating. Specifically, at the initial stages of the “power-down” measurements the surface states are fully occupied, so the carriers provided by the excitation beam recombine radiatively, but it is possible that the intensity is reduced due to the impact of laser heating in the temperature. While reducing the power of excitation, laser heating becomes less pronounced, the temperature is reduced and the intensity of the PL signal increases.

Besides, Gaussian fitting was performed on the peak with the maximum intensity (200 mW excitation power). This peak is centred at 2870 nm and exhibits broad linewidth. The results are displayed in Fig. 6.6b, where it is conspicuously presented that the broad peak (spectrum A) is centred around 2870 nm is comprised of three individual transitions, located at 2649 nm, 2838 nm and 3040 nm (labelled as spectra B, C and D, respectively). These values of the wavelength correspond to 468 meV, 437 meV and 408 meV, respectively. Spectrum C has the highest intensity, while spectrum D is very broad and exhibits the smallest contribution to the overall emission. Similar results have been reported for InAs in the past.^[295] It can be suspected that the

peak at 2838 nm which is the most pronounced is related with ZB InAs band-edge emission.^[295] On the other hand spectrum D can be deriving from previously observed donor-acceptor pair recombination, as reported by Lacroix et al.^[296] Finally, spectrum B could be linked to surface state emission.^[296] This can be further supported by the fact that this peak is suppressed upon employment of surface passivation, as will be described further on in the current chapter. It is noted that surface-state related above-band-edge emission is not uncommon in InAs nanostructures. This is attributed to the electron accumulation layer that is formed on clean InAs surfaces.^[297-298] Some of the surface states lead to Fermi level pinning above the conduction band minimum which in turn leads to surface excitation at energies higher than the bandgap and above the conduction band minimum.^[298] As this is the case on clean InAs surfaces, this phenomenon is uplifted upon surface passivation, as will be discussed later on.

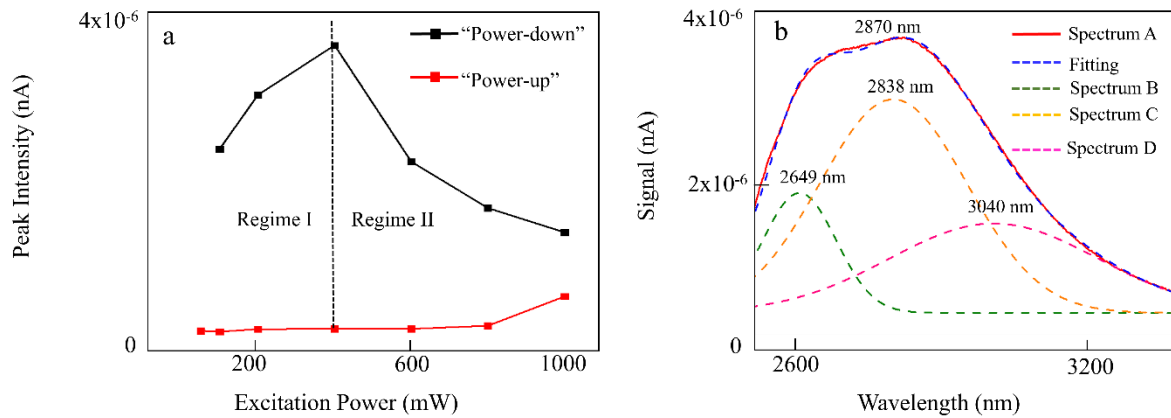


Figure 6.6: a) Plot of the intensity of the emission as a function of the excitation power for “power-up” (red) and “power-down” (black) approaches in pristine samples. b) Gaussian fitting of the peak with the maximum intensity at 200 mW excitation power. Three transitions are contributing to the formation of the total emission.

6.3.3) Chemically Passivated InAs nanosheet samples

In the beginning of this chapter, an introduction on the passivation methods applied for NWs which also have a high density of surface states was made. Here, we will describe the first passivation technique that we performed in the InAs nanosheet samples that we inspected, which is chemical passivation. Specifically, we exploited $(\text{NH}_4)_2\text{S}_x$ solution to remove surface dangling bonds, by the trend of sulphur atoms to be bonded with both In and As.^[297] The passivation was achieved via placing the InAs nanosheets samples in 40 mL of $(\text{NH}_4)_2\text{S}_x$ with 5% concentration. This corresponds to 50 grammars of sulphur. The samples in the solution was heated at 40 °C for 10 mins. The proceeding measurements recorded were the same as in the case of pristine structures. “Power-up” PL experiments on chemically passivated samples revealed the presence of a distinct peak, which is strong even at low excitation power of 50 mW. The peaks related to the “power-up” approach are illustrated as solid lines in Fig. 6.7, which demonstrates the graph of the signal as a function of the excitation power. The peak intensity is continuously increasing until 400 mW. Opposite to the case of pristine samples, the results of the “power-down” approach are almost identical to the ones of the “power-up” approach in terms of general trend and are presented with the dashed lines in the same figure. The above indicate that surface passivation was effective in neutralizing the vast majority of surface states and enhancing the optical response of the nanosheets.

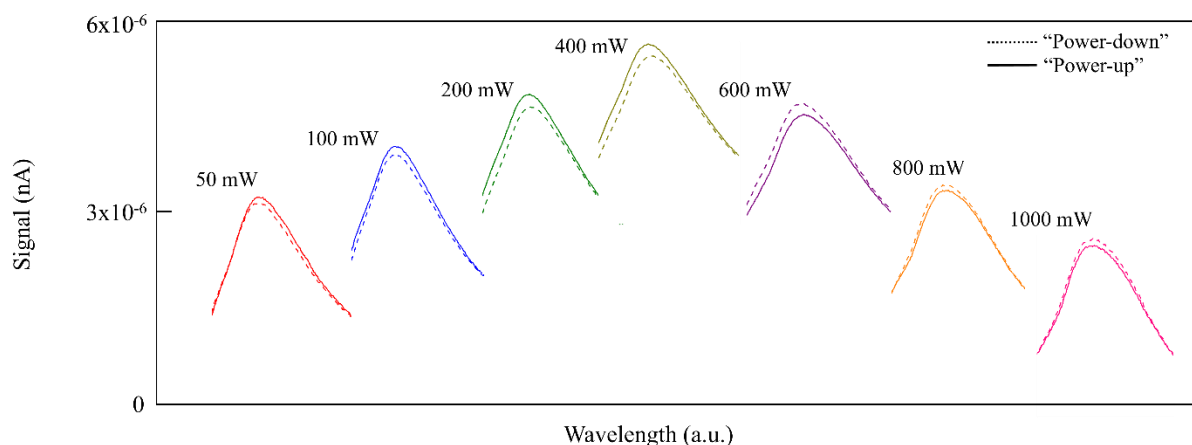


Figure 6.7: Plot of the signal as a function of the excitation power for “power-up” (solid lines) and “power-down” (dashed lines) approaches of chemically passivated InAs nanosheets.

For a more thorough inspection of the passivation effect, the peak intensity is plotted as a function of the excitation for both approaches (similar to Fig. 6.6a for pristine samples). The results are shown in Fig. 6.8a, where it can be deduced that the “power-up” and “power-down” curves follow the same trend, accentuating the strong influence of surface passivation on the “memory effect”. It is noted that some slight discrepancies in the specific values of the intensity are presented between the two methods. Moreover, for excitation powers above 400 mW the intensity of the PL signal is reduced. The explanation for this could be laser heating that intrinsically increases ambient temperatures and reduces the intensity of the PL signal. Even though the critical value is higher than the case of pristine structures (200 mW), temperature-related phenomena which affect surface-related processes have an impact on the intensity of the emission despite the presence of the chemical passivation. Hence, the stability of the sulphur treatment is not ideal.

Additionally, Gaussian fitting was performed in the peak with the highest intensity (400 mW excitation power). The results, presented at Fig. 6.8b, show that the emission

peak is centred at 3020 nm (spectrum A) and is attributed to two individual transitions, one with higher intensity at 2983 nm (spectrum B) and a weaker peak at 3370 nm (spectrum C). It is noted that the former which presents the highest contribution to the overall peak corresponds to an emission energy of 415 meV and is suspected to derive from ZB band-edge emission.^[237] This peak is similar to spectrum C of Fig. 6.6b for the pristine samples. Furthermore, the peak at the highest wavelength (spectrum C) corresponds to an emission energy of 367 meV. Similar peaks have been observed in the past for epitaxially grown InAs structures and have been attributed to impurities that were located roughly 35 meV above the valence band level.^[299-300] The peak at the lowest wavelength in the case of pristine samples is entirely suppressed after surface passivation, further supporting the hypothesis that it stems from surface state-related emission.

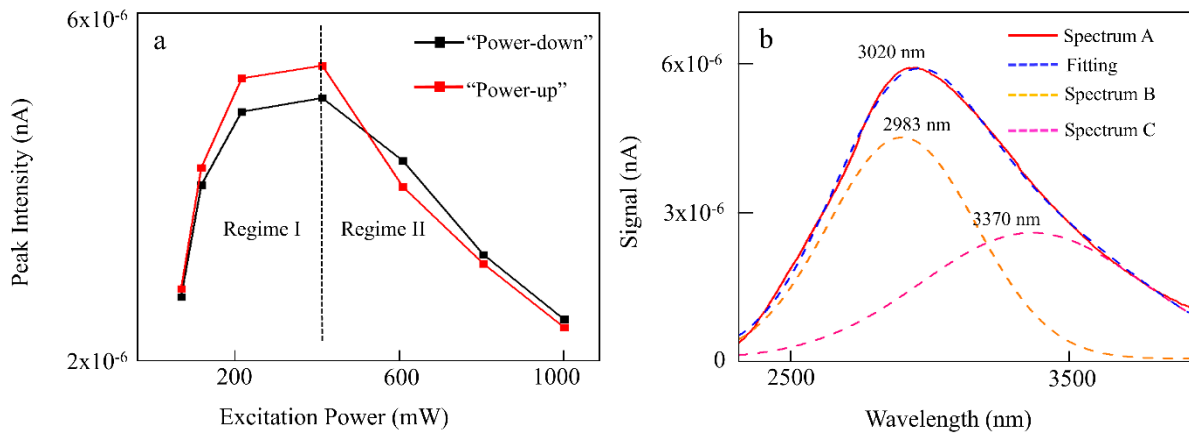


Figure 6.8: a) Plot of the peak intensity as a function of the excitation power for both “power-up” (red) and “power-down” (black) approaches in chemically passivated InAs nanosheets. b) Fitting of the peak with the maximum intensity at 400 mW excitation power of chemically passivated samples. Two transitions contribute to the overall signal.

6.3.4) Physically passivated InAs nanosheet samples

Even though the aforementioned passivation via sulphur treatment is effective for neutralizing surface states, as seen by the elimination of the carrier trapping, it can be observed that thermal instability is still present as indicated by laser heating. In addition, residual impact of “memory effect” is observed signifying that albeit effective sulphur treatment does not fully suppress this phenomenon. The above created the need for another alternative. A widely used method for surface passivation is the configuration of core/shell, acting as a means of physical passivation. It is well known from studies in NWs that core/shell architecture, where the main structure is surrounded by layers has a 3-fold role of surface passivation, carrier confinement in the core and protection of the core from oxidation, while improving thermal stability of the core.^[170-171] It is noted, however, that it is possible for crystal defects such as dislocations to be observed at the core/shell interface owing to strain induced by the different material platforms. Hence, it is important to consider the design of the core/shell architecture using the optimum material combinations for the aimed nanostructures.

Similar to NWs, a shell comprised of layers of a different material platform can also be grown surrounding the active material of the nanosheet, which in this case is InAs. The shell that was grown in this particular scenario was InGaAs, which was achieved by the introduction of Ga in the reactor, after the termination of the InAs nanosheet growth and prior to terminating the entire procedure. InGaAs is a ternary alloy with a bandgap ranging from 0.35 eV (InAs) and 1.42 eV (GaAs) at room temperature. Due to InAs being one of the binary compounds synthesizing the ternary alloy, this material has been exploited in the past for the realization of InAs/InGaAs heterostructures.^[301-303] For instance, reports have shown that vertical metal-oxide-semiconductor FETs

(MOSFETs) can be achieved from InAs/InGaAs core/shell NWs.^[301-302] To the best of our knowledge this material combination has not been employed for the realization of InAs/InGaAs core/shell nanosheets in the past. However, considering the good results on the same platform when adopted for NWs, it is anticipated that further works can enable its wider-scale employment for nanosheets especially with respect to the promising potential of the structures.

In the case of the InAs nanosheet samples, physical passivation was acquired via growing an InGaAs shell surrounding them. The identical power-dependent methods as in the previous cases were performed in order to assess the impact of the InGaAs shell on the optical behaviour of the structures. “Power-up” results that were initially conducted revealed very robust emission peaks, whose intensity is increasing with arising excitation power. The peaks are depicted as solid lines in Fig. 6.9. The “power-down” approach produces similar results, shown by the dashed lines in Fig. 6.9. Interestingly, laser heating effect that caused weakening of the peak of chemically passivated samples after the threshold of 400 mW excitation power, is not exhibited in core/shell nanosheets. Moreover, the intensity of the signal exhibits a twofold increase when compared to the chemically passivated samples and threefold increase when compared to pristine InAs nanosheets.

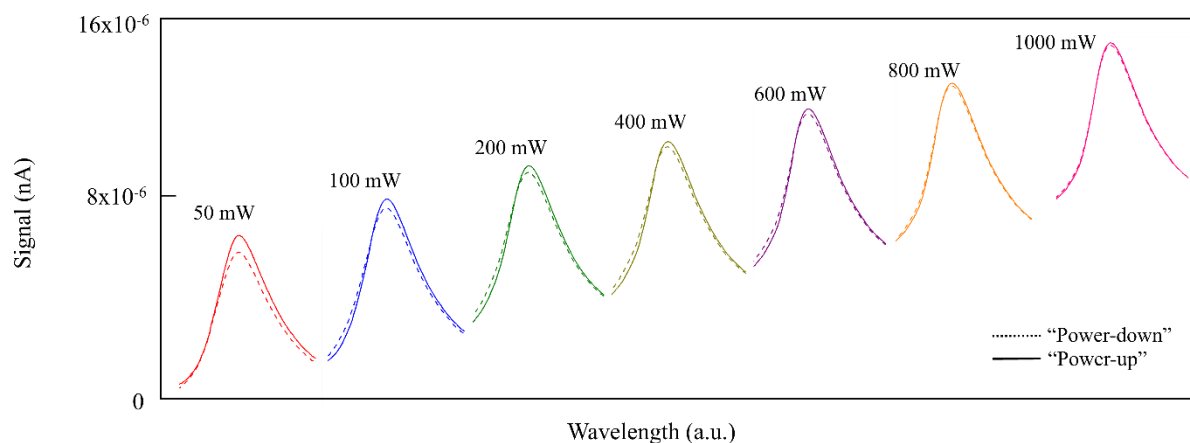


Figure 6.9: Plot of the signal as a function of the excitation power for “power-up” (solid lines) and “power-down” (dashed lines) approaches of InAs/InGaAs core/shell nanosheets, with the shell acting as a means of physical passivation.

For a complete evaluation of the effect of the physical passivation on the optical behaviour of the structures, the intensity of the signal as a function of the excitation power was plotted for both the “power-up” and the “power-down” approach (Fig. 6.10a). The results convey that the intensities are very close and follow the same trend in both procedures. In addition, the intensities in the case of the “power-up” approach are always slightly higher. This is in stark contrast to the previous cases of pristine and chemically passivated samples where the trends of the intensities of the signal were significantly differentiated between the two approaches. This is suggestive of good stability and shows potential for functionality of these structures. It is pointed out that the peak that presented the highest intensity in this case was acquired for 1000 mW. This indicates that laser heating did not occur in the current samples, unlike the previous cases. It could be attributed to the fact that the InGaAs shell protected the core from laser heating, thus InAs-related emission did not exhibit any quenching as a result of the increasing power of excitation. Moreover, the peak that presented the highest intensity was processed via Gaussian fitting (Fig. 6.10b). It can be distinctly

observed that the overall peak located at 3110 nm (spectrum A) derives from the contributions of two individual transitions, similar to the case of the chemically passivated nanosheet. In this case the first transition that has the highest contribution is exhibited at 3095 nm (spectrum B), at slightly higher wavelength when compared to the chemically passivated samples and the pristine samples, where the dominant peak was presented at 2983 nm and 2838 nm, respectively. This peak corresponds to an emission energy of 400.6 meV and is stemming from ZB band-edge emission.^[237] It is noted that this value is different to the one of the chemically passivated sample or pristine InAs nanosheets, which were 415 meV and 437 meV, respectively. These differences could be attributed to state filling effect. In pristine nanosheets or chemically passivated where the passivation is not so stable, there is a high concentration of carriers that accumulate as they are being trapped by the surface states and carrier depletion in the channel occurs, as described earlier. This means that it is possible for the Fermi level to shift into the conduction band, rendering the transitions below this level impossible, causing a blueshift of the peak.^[304] The second peak is located at 3377 nm and is weaker and broader. It is almost similar to the spectrum C in the case of chemically passivated samples, which was centred at 3370 nm and is possibly deriving from impurities that were located roughly 35 meV above the valence band level.^[299-300]

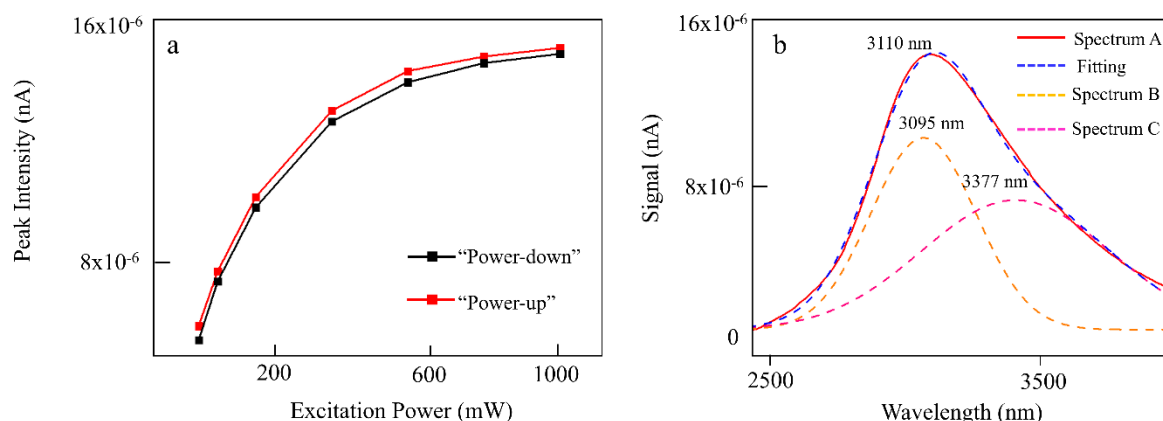


Figure 6.10: Plot of the peak intensity as a function of the excitation power for both “power-up” (red) and “power-down” (black) approaches in core/shell InGaAs/InAs nanosheets. f) Fitting of the peak with the maximum intensity of core/shell nanosheets. The signal is comprised of two individual peaks.

6.4) Temperature-dependent photoluminescence measurements

Following the interesting findings of the power-dependent analysis and interpretation for the realized configurations, we measured the temperature-dependent results. Initially, the relevant spectra for pristine InAs nanosheets are presented (Fig. 6.11a). It is underlined that the excitation power was the one that produced the signal with the highest intensity in order to compensate for the anticipated rapid reduction of the PL signal with increasing temperature. So, in this case it is 200 mW. A robust peak is distinguished at 10 K. As expected, the intensity of the signal quenches fast with elevating temperatures. After 125 K, emission is fully suppressed. It is noted that laser heating that was estimated to reduce PL intensity as seen earlier could play a role in this premature suppression of the peak. Nevertheless, the fact that the peak can be observed up to 125 K, which is far above the cryogenic limit, is promising for the potential of the nanosheets as light emitters.

Similar spectra were recorded for the sulphur-treated samples. The power of excitation used was 400 mW, as it was the value that led to the strongest signal obtained. The results are illustrated in Figs. 6.11b-c. Specifically, it is presented that the intensity of the peak is quickly limited and is reducing fast above 100 K (Fig. 6.11b). The remaining spectra are presented in a separate graph, for facilitation of the readers (Fig. 6.11c). It can be seen that despite the weakening of the signal, emission is sustained up to 225 K. Moreover, the results for the physically passivated samples are presented. Initially, the power of excitation was set at 140 mW, as it produced a signal with similar intensity as in the case of sulphur-treated structures. Similar to chemically passivated nanosheets, increasing temperature caused fast decay of the peak intensity (Fig. 6.11d). However, in this case there was room to increase the excitation power, as the initially chosen one was not the optimal but it was the one that produced a signal comparable to the sulphur-treated nanosheets. Consequently, after 150 K, the power was increased. Specifically, after 200 K, the power reached 600 mW, which allowed us to acquire spectra with more noticeable peaks and observe RT emission deriving from the samples (Fig. 6.11e). It is reminded that as shown earlier in the power-dependent measurements, the shell protected the samples for laser heating effect and provided them with stable passivation, which could account for the improved temperature-dependent results. Nevertheless, further works and studies should follow in order to fully elucidate the underlying phenomena and evaluate the potential of these structures in light-emitting applications.

Finally, for a direct comparison of the results, the intensity of the signal as a function of the temperature was obtained for all three configurations and is presented in Fig. 6.11f. In the graph, it is corroborated that the intensity of the peak for pristine InAs samples remains at a comparatively low level throughout the measurements and is

entirely suppressed after 125 K. On the contrary, sulphur treatment has led to an augmented initial intensity at 10 K, which is however rapidly diminished with increasing temperatures. Nevertheless, the peak remains noticeable at 225 K. Regarding the physically passivated InAs samples, it is significant to observe that while no RT signal was noticed at low excitation powers for core/shell nanosheets, at powers above 400 mW the peak was maintained up to 300 K. This could not be valid for sulphur-treated and pristine structures as above this excitation power the intensity of the signal was reduced potentially due to laser heating. The dashed, blue lines in Fig. 6.11f correspond to the temperatures where the excitation power for core/shell samples was increased to combat the suppression of the signal.

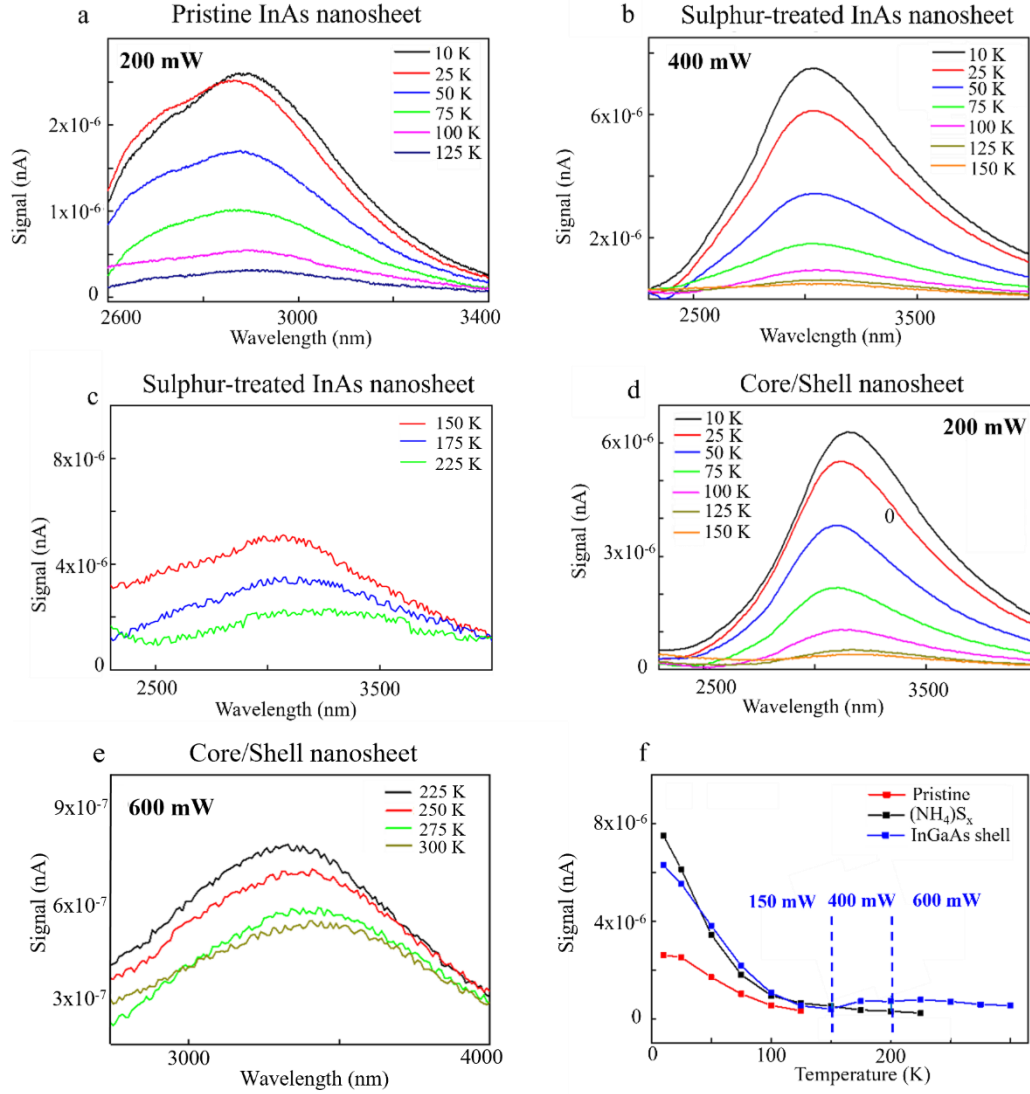


Figure 6.11: a) Temperature-dependent PL on pristine samples. b) Temperature-dependent PL measurements on chemically treated samples, within the range of 10 K-150 K. c) Temperature-dependent PL on chemically treated samples, within the range of 150 K-225 K. d) Temperature-dependent PL on core/shell nanosheet from 10 K until 150 K. e) Temperature-dependent PL of core/shell samples from 225 K until RT using power of 600 m. f) Plot of the maximum intensity of peaks as a function of the temperature for all the realized samples.

Before proceeding to the description of the rest of the experiments, we consider it important to demonstrate a comparison among the three types of 2D InAs nanosheets

that we examined with respect to their optical properties. This is significant due to the wide variations in terms of optical response as a result of different surface state configurations. The summary of the comparison is encapsulated in Table 4 below. The three types we inspected were pristine, chemically passivated (via $(\text{NH}_4)\text{S}_x$ treatment) and InAs/InGaAs core/shell nanosheets. The most prominent difference is the direct result of surface passivation which is the response during the “power-up” approach. While pristine nanosheets did not produce noticeable signals during this procedure as a result of carrier trapping at the rich surface states, after passivation this phenomenon was eliminated. Therefore, robust peaks appear for both chemically passivated and core/shell structures. The above observation also leads to the major difference of the optically investigated samples, which is related to the existence of “memory effect” for the pristine nanosheets as opposed to the passivated.

The third difference is related to the wavelength of the emission. It can be seen that while the emission peak with the maximum intensity was located at 2870 nm for the pristine nanosheets, this peak appeared at 3020 nm for the chemically passivated and 3110 nm for the core/shell nanosheets. It is reminded that this observation is attributed to state filling effect in pristine nanosheets and existing but less dominant state filling effect in chemically passivated nanosheets. Since the sulphur passivation is not as stable, there are carriers that accumulate at the surface as they are trapped by the rich surface states. The same is the case for pristine structures. This leads to carrier depletion in the channel that causes Fermi level shifting into the conduction band, prohibiting transitions at low energies (high wavelengths).^[256] Besides, the intensity of the signal is increased as a function of the stability of the passivation as anticipated. The maximum intensity of the signal for pristine nanosheets is 3.6×10^{-6} nA. It is noted that this value is observed at 200 mW during the “power-down” approach. For the

chemically passivated structures the maximum intensity is 6.2×10^{-6} nA, as a result of surface passivation improving thermal stability, while for the optimum core/shell nanosheets the intensity reaches 1.4×10^{-5} nA.

The thermal stability is also varying. This is suggested by the existence and impact of laser heating effect. Specifically, pristine InAs nanosheets exhibit laser heating effect after 200 mW, leading to the power for the signal with the maximum intensity being 200 mW. The corresponding value for chemically passivated structures is 400 mW, while for the core/shell nanosheets no laser heating is observed leading to the maximum intensity being obtained at the maximum power applied, which in this case is 1000 mW.

InAs Nanosheet type	“Power-up” signal	Memory Effect	Wavelength for max signal (nm)	Max Intensity (nA)	Laser Heating Effect	Power for max signal (mW)
Pristine	No	Yes	2870	3.6×10^{-6}	Yes (after 200 mW)	200 mW
Sulphur-treated	Yes	No	3020	6.2×10^{-6}	Yes (after 400 mW)	400 mW
Core/Shell (InAs/InGaAs)	Yes	No	3110	1.4×10^{-5}	No	1000 mW

Table 4: Encapsulation of the basic comparison merits among the three different types of InAs nanosheets that were examined.

6.5) Comparison of our work with previous works on InAs nanosheets

Following the optical analysis of the InAs nanosheets that we investigated, it is important to highlight the importance of our experiments by presenting a brief comparison among the current samples and previously reported works on InAs nanosheets. It is reminded that III-V semiconductor nanosheets have attracted attention because of the combination of the III-V optically active features, including

high carrier mobility and direct bandgap, with the advantageous characteristics of nanosheets such as their free-standing nature and their two-dimensionality. It is noted that as a result of the last two properties mentioned, several devices have been fabricated based on nanosheet structures, including optoelectronic memory applications^[305-307] and hybrid superconductor-semiconductor applications for use in topological networks.^[308-310] In addition, the fabrication of gate-all-around FET based on InGaAs nanosheets has been reported.^[311] Regarding the particular category of III-V nanosheets, InAs is a beneficial alloy due to its inherent properties namely the high electron mobility and narrow bandgap, which were discussed earlier in the current chapter. High-purity InAs nanosheets have been reported.^[200,208-209] The studies on their crystallinity and material quality have shown that one good route for their fabrication, ensuring high quality is their growth directly from 1D NWs, which can be tuned by altering the growth parameters, as is the case for the nanosheets that we optically investigated.^[200]

Free-standing InAs nanosheets grown via MBE have been used for the fabrication of FETs in the past.^[312] The study of magnetotransport measurements on the devices revealed that strong spin-orbit interaction is present as indicated by the short spin-orbit length. Their results suggested that such structures can be used for spintronic devices.^[312] Moreover, time-resolved PL measurements on both 1D InAs NWs and 2D InAs nanosheets have shown that the latter have a much higher lifetime, which increases with elevating temperatures.^[200]

It is noted that the use of nanosheets for optoelectronic memory units has been reported in previous works using materials other than III-V, so the prominent role of surface traps and their exploitation for “memory effect” in such structures has been established.^[305-307] Nevertheless, despite the important works cited above, to the best

of our knowledge, there have been no reports of PL studies with respect to the existence of “memory effect” in InAs or other III-V nanosheets, which further accentuates the importance of the work presented above.

6.6) Optical Memory Unit Based on pristine InAs nanosheets

Following the analysis of the vibrant optical properties of InAs nanosheets, we will focus on the performance of fabricated FETs based on the pristine samples. We consider that this work can be regarded as a continuous research project directly linked to the results that we acquired via the PL measurements on the same InAs nanosheets that were described earlier. Ergo, we believe that it is important to include those results in the current section of the thesis.

The fabrication of the devices was achieved via the following procedure. A small piece of InAs nanosheet on Si(111) was cleaned with oxygen plasma to eliminate contamination by dirt and to promote the oxide layer formation on the surface of the structure. This ensures the NPR that was wanted. Then the nanosheets were released via ultrasonication of the sample, immersed with small amount of IPA in a beaker for roughly 1 min. Moreover, a pipet was used to transfer the IPA solution with released InAs nanosheets onto a clean SOI substrate, whilst the natural evaporation of IPA followed. The SOI substrate was fabricated with an Au/Ni gate via the following method. Initially, a piece of 285 nm SiO₂ on P⁺-Si(001) substrate was spin-coated with photoresist and heated for 1 min on a hot plate at 180°C. An area of 1x3 μm was optically exposed via Karl Suss MJB3 Mask Aligner. Then the SOI substrate was dipped into BOE solution for 2.5 mins in order for the SiO₂ to be removed from the exposed area. After cleaning and drying with a N₂ gun, the substrate was thermally evaporated with Ni/Au in an analogy of 10 nm/100 nm. Then the lift-off process took

place with MIBK solution, cleaning and drying. The SOI was then ready to accommodate the transferred nanosheets. The Ni/Au layer was deposited by thermal evaporation. EBL Elinox was conducted for the patterned electrodes on the SOI with gate, which was then followed by the lift-off in acetone. A final EBL was required to connect the InAs nanosheets to the contacts.

As mentioned earlier, the reason of this particular choice for our device fabrication is the “memory effect” that renders the structures promising for optoelectronic memory compounds. Due to the nature of the InAs material, InAs-based devices have demonstrated negative photoresponse (NPR) and positive photoresponse (PPR) under different experimental methods and fabrication procedures. In the former regime, the current is decreased after light illumination, while the opposite is the case in the second regime. The carrier trapping in the oxide layer or photon gating layer can cause NPR,^[293,313-314] while on the other hand reports have shown that there is a light intensity threshold for NPR to PPR transition with proper oxidation layer removal.^[315] Moreover, NPR to PPR transition can be wavelength-dependent over 1060 nm wavelength of the incident light.^[293] Based on the above, photoexcitation scattering centres can be charged under minimum light intensity, which leads to a non-negligible lowering of the current in the devices. Opposite to this, under high light intensity the carrier density is enhanced leading to PPR. Hence, we can deduce that InAs nanosheets demand low channel current under two different scenarios. In one scenario, the devices require low channel current with no light illumination, while a notable PPR is necessary to burden power consumption. In the second scenario, in order to obtain stable NPR, the low channel also needs to remain at adequately low levels. In both situations the demand for low channel current is an important prerequisite. Hence, considering that the channel current, which is the drain-source

current is proportional to the drain-source voltage, it can be inferred that in order to minimize the power consumption of the devices, NPR driven by low V_{DS} is desired.

The mechanism of NPR is schematically presented in Fig. 6.12a. For 2D materials, the area of the InAs/surface oxide and InAs/SOI interfaces is much larger when compared to 1D materials, such as NWs. When the light source is provided, photoexcitation causes more electron-hole pairs within the alloy (Fig. 6.12a). These hot carriers have different potential of being trapped by surface states or trapping centres at the interfaces that were mentioned, as illustrated in Fig. 6.12b. The trapped electrons create an internal electric field. The energy barrier of these electrons is released slowly via thermalization or rapidly via the influence of external electrostatic field. During the time that electrons are trapped, the electron density in the InAs channel is much lower which causes a drastic decrease in the channel current, as is typical in NPR. It is noted that if the trapped centres are rare or if low energy photons are used as light source, PPR becomes dominant in the excitation mechanism. Hence, O_2 plasma is used to increase trapping state on the nanosheet surface. The light source that is chosen is blue at 405 nm.

Besides, I-V sweeps were conducted to corroborate the gate controllability and expose the basic electronic characteristics of the FETs. V_{DS} was swept from -1 mV to 1 mV and the gate voltage took the values of 0, 50 V or -50 V. The results suggest a gate-controlled ratio of I_{DS} of 10^4 , as shown in Fig. 6.12c that encapsulates the I_{DS} - V_{DS} curve. The I_{DS} - V_{GS} curve is presented in Fig. 6.12d and suggests fast increase of I_{DS} at $V_{GS}=-13$ V. The mobility of the FETs can be calculated by employing the following two equations:

$$\mu = \frac{\partial I_{ds}}{\partial V_{gs}} \frac{L^2}{C_{ox} V_{ds}} \quad (1)$$

$$C_{ox} = \frac{\epsilon_0 \epsilon_r W L}{d} \quad (2)$$

The typical length for the channel (L) is 4 μm and the typical width (W) is 1 μm . The thickness of the dielectric layer is 285 nm. The differential part of equation 1 can be obtained by the differential plots of Fig. 6.12d. C_{ox} is the back-gate capacitance. Fig. 6.12e shows an example of the differential plot, where the peak transconductance is $g_m = 5.868 \times 10^{-9} \Omega^{-1}$, ϵ_0 is the permittivity of the vacuum and ϵ_r is the relative permittivity of SiO_2 . Based on the described variables and the calculations, the peak mobility of the InAs FETs is $1936.87 \text{ cm}^2 \text{V}^{-1} \text{s}^{-1}$ at 290 K, with $V_{DS} = 1 \text{ mV}$ and $V_g = -17.5 \text{ V}$. The high value of the mobility reveals the high quality of the InAs nanosheets.

Moreover, the gate sweep from -50 V to 50 V and vice versa is presented in Fig. 6.12f. The V_{DS} is kept at 1 mV and the gate sweep speed at 10 V/s. The hysteresis loop that is formed and the n-type trend are shown as a result of the internal electrostatic field that originates from the electron trapping at the InAs/oxide and InAs/SOI interfaces. The gate hysteresis is dependent on the InAs/ SiO_2 interface and the sweeping rate of the gate voltage. Specifically, it has been indicated that slow sweep rates allow for neutral charging of the surface states, which causes higher transconductance values.^[316] The high gate sweep in this case leads to hysteresis voltage of 37.5 V, defined by the width between the two highest mobility points of the sweeps (Fig. 6.12f). Even though these results may not accurately reflect the intrinsic values as they are strongly dependent on the measurement configurations, the high mobility that was calculated demonstrates the promising potential of InAs nanosheets for low channel current when compared to the dark current under the influence of a low V_{DS} . Stability can also be inferred via measurements of I_{DS} of the nanosheets under continuous gate voltage for 1000 sec, as provided in Fig. 6.12g. Different gate voltages allow for more controllability of the channel current.

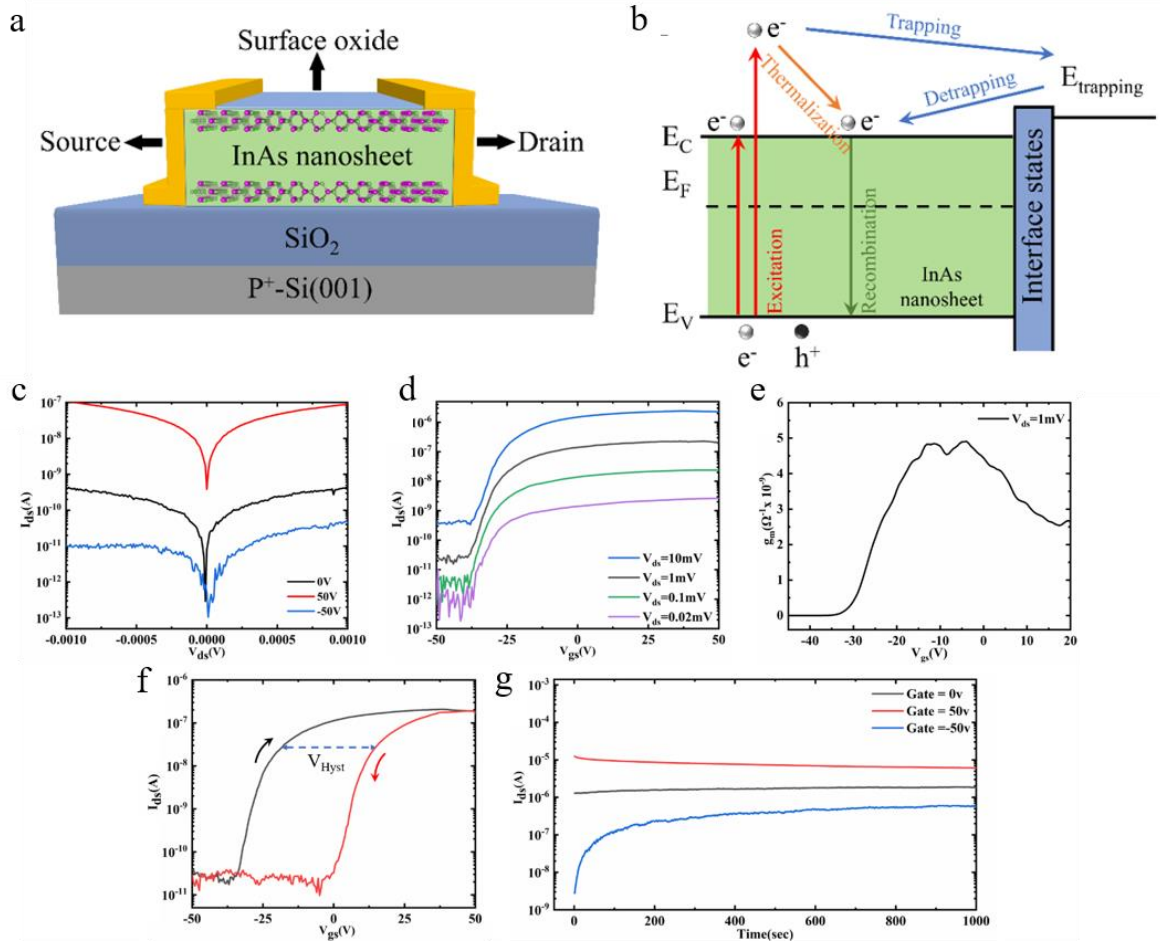


Figure 6.12: a) Schematic representation of structure layout of InAs nanosheet on SIO substrate. b) The mechanism of NPR of InAs nanosheet. Grey ball indicates electrons, black ball indicates holes. c) Transfer curve of drain-source voltage sweep versus drain-source current, where drain-source voltage V_{ds} sweeps from -1mV to 1mV with different gate voltage $V_g = 0V, -50V$ and $50V$. d) The drain-source behaviour under sweep of gate voltage from -50V to 50V, with different V_{ds} . e) The differential of up sweep in Fig. 6.12d when $V_{ds}=1mV$, showing the transconductance from Gate voltage -50V to 50V. f) Transfer curve of gate voltage sweep from -50V to 50V and vice versa with $V_{ds}=1mV$. Gate hysteresis is indicated by joining the inception points of peak mobility points of up sweep and down sweep. g) The channel current stability with applying continuous gate voltage $V_g = 0V, -50V$ and $50V$.

The hysteresis effect that is conspicuously presented in the I-V curves above and the stability of the electrical characteristics of the FETs show the potential of InAs nanosheets as the foundation of electronic devices with respect to their gate-tuneable electron-doping capability. The electrically modulated trends that are exhibited in the structures are inspected as the next step to their thorough characterization. To establish the same level of trapped electrons within the FETs, an erase pulse of $V_G = -50$ V was applied for 1 s before the conduction of each set of measurements. This eradicates the trapped electrons at the device interfaces. The negative gate voltage causes an external electric field promoting the de-trapping of electrons in the surface centres. Different V_{BG} of -10 V, 0 V and 10 V are applied, leading to the values of the base channel current varying at $V_{DS} = -1$ V. The results are shown in Fig. 6.13a.

Moreover, programmed gate pulses are applied with ascending order (20 V-50 V) for 1 s, with a time interval of 45 s between each set of pulses. It can be concluded that the I_{DS} adopts a step-like form, while the application of higher pulse voltage leads to a distinct decline. This is originating from the free carrier trapping as a result of the electric field, in the reverse process of the de-trapping mechanism. However, the density of carriers that can be trapped following this scenario is small when compared to the light excitation. With a base-gate voltage of 10 V, the first pulse of 20 V does not formulate step-like characteristics. This suggests that the base-gate voltage contributes to trapping of electrons. Further decline in the I_{DS} demands for stronger positive voltage, as observed in Fig. 6.13a for the remaining pulses. On the contrary, a negative base-gate voltage of -10 V leads to noise and instability of the step-like features. This phenomenon can stem from the fact that I_{DS} approaches the intrinsic dark current and is difficult to distinguish one from the other. Under the adequate conditions, the programming is stable for V_{BG} of 0 V or 10 V. A repeated procedure of

erase and stepping of electrical programming can be demonstrated in Fig. 6.13b for three periods. The erasing pulses, V_{DS} and the programming pulses are similar to the ones used for the production of Fig. 6.13a. The electrical programming shows a high level of reproducible behaviour in the absence of external impacts such as light. The above are highly promising for optical memory units, with the potential of reprogramming and erasing. Eventually, as shown in Fig. 6.13c, the binary flash memory features are depicted under V_{BG} of 10 V, with erase pulses with a voltage of -50 V and programming pulses with a voltage of 30 V.

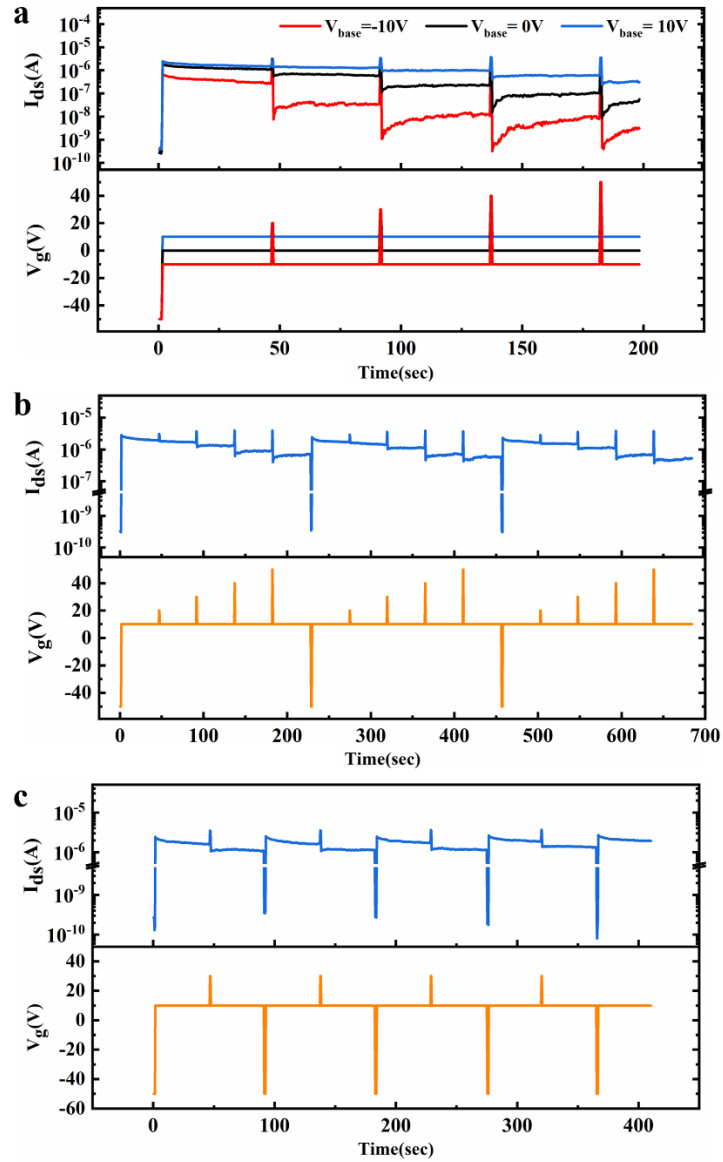


Figure 6.13: a) Graph of V_g (lower panel) and I_{DS} (upper panel) under V_{DS} of -1 V, with programming pulses of ascending voltage being applied every 45 seconds. The step-like behaviour of the I_{DS} is conspicuously shown. b) Graph of V_g (lower panel) and I_{DS} (upper panel) following a repeated procedure of erase and step of electrical programming, with the conditions being identical to the ones of Fig. 6.13a. c) Graph of V_g (lower panel) and I_{DS} (upper panel) under base-gate voltage of 10 V, erase pulses at -50 V and programming pulses at 30 V.

Apart from the aforementioned electrical programming of the pulses, the optical features of the InAs nanosheet-based FETs were further investigated. During the first steps, a -50 V pulse was applied for 1 second to erase the trapped electrons at the interfaces of the devices before each measurement. As a result of this pulse, the channel current is lowered to a minimum level. After this, it returns to the default level after the application of the erasing pulse. The different power of the laser source which is 405 nm wavelength exposes the device for 3 seconds. In Fig. 6.14a, the drain-source current is measured under different laser powers for 1000 seconds. While it can be seen that some decay is presented over time, the current is low and gradually obtains the value of 1 nA with increasing laser power of 63 mW, without significant fluctuations. The V_{DS} is fixed at 1 mV. After the carriers are trapped, the current level remains low for a relatively long period of time, which is indicative of the capacity of the device for data storage.

For the next stage of the experiment and to examine photodetection, the device with the best conductivity was chosen. In order to ensure reproducibility of the channel current and guarantee that it can be reset to the default level, the repeated binary test was carried out by a loop, an erase and light exposure. This is conspicuously shown in Fig. 6.14b, where a repeated period of 100 seconds was set and the blue light with a power of 63 mW was applied at 50 seconds of the period, while V_{DS} was fixed at 1 mV. After every erasing pulse, the channel current is reset to a level of 10^{-7} A and after every light exposure it is decreased to roughly 2×10^{-8} A. Furthermore, the mobility of InAs and the low resistance of the device allow for a high channel current even at the low level of drain-source voltage that was selected for the experiments. Hence, V_{DS} was varied in order to find a lower limit for the FET photoresponse, which would be energetically preferential as it would signify low power consumption and consequent

energy saving. In order to achieve ultra-low photoresponse, it needed to remain low and present a decrease after light exposure. In Figs. 6.14c, the binary tests were conducted under various V_{DS} of 10 mV, 0.1 mV and 0.02 mV, from top to bottom panel, respectively. The channel current ratio before and after exposure was 5 for every V_{DS} employed. The photoresponse at the lowest V_{DS} of 0.02 mV that was chosen shows a current level difference when compared to the default current level. It is reminded that similar to the initial electrical sweeps, the driving voltage obtained low values with good results, potentially as a result of the combination of InAs intrinsic high carrier mobility, 2D nature of the structure and high material quality. Eventually, in order to corroborate a representative comparison, the power of the devices before and after light exposure are shown in Fig. 6.14d, under the influence of different V_{DS} . It can be inferred that at the lowest V_{DS} used, the power of the devices after exposure is ultra-low at 10^{-5} nW, which demonstrates the potential of the devices for achieving ultra-low power consumption from an optoelectronic memory unit.

It is noted that the driving voltages of the aforementioned mechanism were chosen to be conducted with at ultra-low values reaching 0.02 mV, while the driving voltage of Fig. 6.12 is merely 1 mV. The equipment in our facilities allows for the reduction of drain-source voltage down to less than 0.001 mV, which facilitates the experiments in terms of demonstrating the capacity of the structures to be used for the realization of ultra-low power consumption memory cells. We believe that the intrinsic high carrier mobility of InAs along with the high material quality with only occasional defects which reduces scattering contributed to the low value of the voltage that was used for the experimental procedure. The frame of reduction of the V_{DS} that was provided to us as a result of the good material properties and high carrier mobility allowed for a ratio of the channel current post and prior exposure to take a value of 5. The aforementioned

features led to the channel current being much higher compared to the dark current even at the low programming voltages that were employed and display the potential of the structures for implementation in device applications.

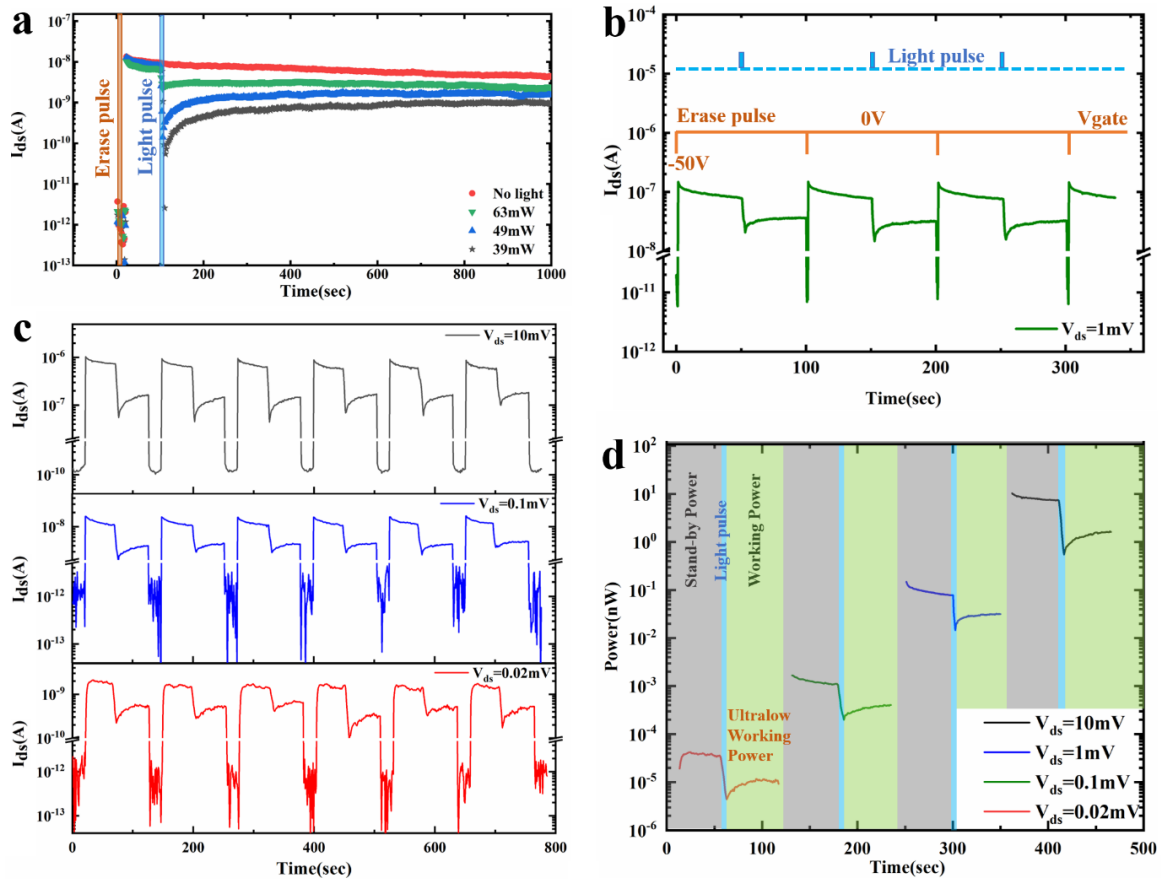


Figure 6.14: a) The channel current stability after applying one second erase voltage pulse of -50V and different power of blue light with wavelength of 405 nm . b) A binary NPR loop includes one second erase voltage pulse of -50V and light exposure of blue light with wavelength of 405 nm and 63mW , under $V_{ds}=1\text{mV}$. c-e) Similar loops of binary NPR to the one shown in Fig.6b, under $V_{ds}=10\text{mV}$, 0.1 mV and 0.02mV . f) The power of stand-by stage and detection/working stage of each binary NPR shown in Figs. 6b-e, showing the lowest working power of 10^{-5} nW when $V_{ds}=0.02\text{mV}$.

6.7) Summary and Conclusions

In chapter 6 of the current thesis, we focused on the optical response of InAs nanosheets and the analysis of the results that followed. For the thorough inspection of the optical properties of the examined structures, “power-up” and “power-down” approaches were employed, as described earlier.

Pristine InAs nanosheets, which have a high density of surface states, presented suppressed optical emission during the initial “power-up” method. On the contrary, the subsequent “power-down” measurements led to robust peaks from the same samples. This phenomenon has been attributed to the fact that after the “power-up” approach, the overwhelming majority of surface states have trapped carriers and are occupied, which allows for the new excitation beam to eventually lead to radiative recombination of the photoinduced carriers in the nanosheet channel. This is indicative of the “memory effect” and can be exploited for optoelectronic memory applications. The examination of chemically passivated and physically passivated (core/shell) nanosheets exposed that the neutralization of surface states caused the appearance of strong peaks during both “power-down” and “power-up” approaches, due to the elimination of the carrier trapping, thus surface charging, phenomenon. It is reminded that while laser heating was observed in the pristine and sulphur-passivated nanosheets, no such observation was made for the core/shell nanosheets which indicates the suitability of physical passivation in light-emitting applications.

In addition, pristine InAs nanosheets were employed for the fabrication of an optoelectronic memory unit in an FET configuration. The device showed NPR, while the application of programmed gate pulse showed that higher pulse voltage led to a decline of the I_{DS} as a result of carrier trapping and de-trapping mechanism induced

by the electric field. The I_{DS} under positive base-gate voltage adopted a step-like form, while negative base-gate voltage led to instability of these features as in the latter case, I_{DS} approached the intrinsic dark current of the device. Furthermore, the application of erasing and programming pulses exposed that the electrical programming of the device had a highly reproducible nature, which revealed potential of reprogramming and erasing that are key functions in optoelectronic memory units.

Importantly, using the device with the best conductivity, a binary test was conducted via an erase and light exposure for a repeated period of 100 seconds. After every erasing pulse, the channel current was reset to 10^{-7} A and after every light exposure it was decreased to 2×10^{-8} A. Moreover, V_{DS} was modified to find the lower critical value for the device photoresponse. It was proven that the lowest V_{DS} that was chosen caused an ultra-low power after light exposure. The reduction of the current after light exposure along with the reduced power at the lowest V_{DS} indicate the capability of such devices for ultra-low power consumption.

The subject of the fabricated optoelectronic memory unit based on pristine InAs nanosheets ends the experimental section of the current thesis. In the following section, we will summarize the results that were obtained from our research, conduct discussion on the potential of the nanoscale structures and comment on possible challenges. Finally, we will briefly introduce relevant research plans and works that are programmed to be carried out in the near future.

Chapter 7: Discussion and Conclusion

7.1) Summary of the presented results

In the work described in the current thesis, the importance of III-V low-dimensional structures was accentuated, while the prominent role as building blocks for optoelectronic and electrical devices and circuit components was displayed. Via employing the beneficial MBE technique via adopting the VLS growth mode, the synthesis and exploration of NWs and NWQDs was achieved, with an in-depth characterization of their morphological, structural and optical properties following.

AlGaAs NWs were developed via the self-catalysed growth mode, which included the complete elimination of Au and thus the metal-related contamination that affect the structure compatibility with Si photonic applications. The droplet that initiated the growth was composed of an Al/Ga alloy in the majority of the cases. The majority of the NWs were perpendicularly oriented on the Si (111) substrates, with two frequent variations being presented: namely kinked and branched NWs. Through the careful TEM analysis, the elemental composition along the NW axis was found to be highly non-uniform, with Al being concentrated more often at the bottom regions, while the segment in the vicinity of the tip was Ga-rich, most likely attributed to the low diffusivity of Al when compared to Ga. For the same reason, Al adatoms are more likely to adhere to the sidewall facets causing a lateral VS expansion of the structures rather than reach the droplet and contribute to VLS growth. Consequently, the NW core bears a much higher Ga content, while the accumulation of Al at the sidewalls of the NWs causes the spontaneous formation of an Al-rich, AlGaAs shell, with two distinct features being observed. First, there are severe alloy fluctuations in the shell manifesting themselves as phase separation. This characteristic can be exploited for

the formation of QWs, quantum rings or QDs in the AlGaAs shell, which provides us with a type of self-assembled non-classical light emitters. The second feature of the shell is its varying thickness, which is reduced from bottom to top. Importantly, whilst the crystallinity is predominantly ZB and no dislocations are observed (as an intrinsic advantage of NW structures), there are severe twin defects and occasional thin WZ insertions of roughly 6 MLs. The NWs are revealed to be optically active, with a fully tuneable emission wavelength with the Al content of the structures. The range of the NW emission capability ranges from the red to the near-infrared region of the spectrum (700-850 nm).

As mentioned earlier, one frequently encountered morphological variation of the AlGaAs NWs is the formation of 3-D branched structures. These NWs present increased scientific interest owing to their large surface area and prolonged carrier path, which renders them ideal candidates for energy harvesting and energy storage applications, such as Li ion batteries, solar cells and supercapacitors. For that reason, they were studied separately and the results are demonstrated in a different chapter. Initially, SEM images exposed that the branching events were conspicuously increased at the Al-richest sample that was grown (40% nominal Al content). A statistical analysis that followed showed that the percentage of NWs that develop branches was limited to 15% or below for the Al-deficient samples, whilst it was significantly higher at 60% or more for the NWs with 40% nominal Al composition. For that reason, the detailed TEM analysis was conducted on Al-rich structures with more pronounced branching events. The ADF images that were acquired showed that the branches were orthogonal to the NW trunk axis, while the crystallinity of the branch and the trunk was identical. This signifies that crystal planes continue with the same phase or twinning from the NW trunk to the branch. The above are corroborated by

the identical FFT patterns of the two NW parts, establishing the epitaxial nature of the growth.

Based on the above, the growth mechanism was formulated and supported by ab initio calculations using VASP. The basis of the growth is the formation of the Al-rich, AlGaAs shell which exhibits a rough surface. This leads to the realization of concavities, where it is preferential for Ga adatoms to accumulate. The accumulated Ga atoms amalgamate as droplets inducing the VLS growth of the NW branches. A more thorough examination of the branches also depicted an intriguing finding. It can be seen that there are Ga-rich stripes along the branch axis and perpendicular to it with the latter presenting a periodic arrangement. This causes the formation of Ga-rich elemental boxes in the intersection of the stripes, causing the appearance of an intricate checked pattern of compositional distribution. The axial stripes are suspected to originate from the different polarity and crystallinity of the NW branch, with Ga being accumulated at one type of ZB-polar facets. On the other hand, the perpendicular stripes are stemming from the constant rotation of the samples within the growth chamber. The above are important for the design and analysis of such complex and versatile structures, while showing the promising role of the elemental boxes as quantum light emitters.

Despite the exceptional properties and potential of 1D and 3D NW structures, the functionality can be further expanded by embedding 0D QDs along their axis. Hence, single GaAs QDs were axially grown in each AlGaAs NW. To accomplish this, the Al supply was interrupted for several seconds in order for the GaAs segment to grow, before restoring it to enable the formation of the AlGaAs NW top region. The morphology of the NWQDs was similar to the one of the NW samples. Nonetheless, significant changes were observed via TEM and PL inspection. First, TEM confirmed

the formation of the dot via DF imaging and EDX scanning. The width of the dot reached 4.9 nm and the diameter was relatively large at 140 nm. The axial embedding of the dot led to important modifications in the PL response of the structures. PL spectra exhibited peaks located at 787 nm which corresponded to GaAs-related emission. The peaks attributed to the dot were spatially localized in the centre of the NWs and exhibited a narrow linewidth of 490 μeV . It is also significant to mention that increasing temperature led to a rapid quenching of the dot peaks, which were fully suppressed after 40 K. Moreover, polarization-dependent measurements showed that whilst the AlGaAs NW-related peaks had a small degree of polarization, which was anticipated from the intrinsic NW properties, the dot-related peaks were more strongly polarized, with a degree of 70% at 60° off the NW axis. The above are good properties for entangled photon generation.

Finally, the optical investigation of a different structure and material platform followed. Specifically, 2D InAs nanosheets were probed by macro-PL measurements. Initially, pristine structures were examined, where a vibrant property was noticed. Power-dependent measurements revealed suppression of PL emission with increasing power of excitation attributed to the high density of surface states. However, after this procedure a second set of measurements with decreasing power of excitation caused the appearance of robust peaks corresponding to InAs ZB band edge emission. This is attributed to the “memory effect” where after the saturation of the surface state by trapped electrons, strong PL peaks appear owing to the recombination of photogenerated electron-hole pairs. This renders the structures promising as optoelectronic memory units. Besides, two types of surface passivation were applied, namely chemical passivation and core/shell passivation. In both cases, the “memory effect” was drastically reduced and peaks with high intensity were

generated. In particular, the physical, core/shell passivation exhibited a high degree of stability with RT emission in the mid-infrared regime having been accomplished. The efficient passivation renders the 2D nanosheets good candidates for light-emitting applications in the fruitful yet demanding mid-infrared range. Eventually, the fabrication of an InAs nanosheet-based FET via using the pristine structures enabled us to formulate an optoelectronic memory unit that exhibited NPR at low driving V_{DS} . The results were strongly suggestive of reproducible properties and ultra-low power consumption.

7.2) Discussion of the results

As mentioned in the introduction, the objective of the research project was the investigation of nanostructures monolithically integrated on Si (111) substrates, grown via MBE with the aim to demonstrate their optical properties and assess the morphological and structural findings, as well as show the potential of nanoscale structures for implementation in devices.

Regarding the growth of AlGaAs, the most important difference compared to previous works was the self-catalysed approach. The realization of standing, optically active NWs with interesting structural properties, stemming from Ga droplets displays the suitability of the self-catalysed VLS growth for developing ternary III-III-V NWs. It is reminded that although important works have been reported on the topic of AlGaAs NWs and AlGaAs/GaAs NWQDs, the aforementioned structures were grown via the Au-assisted method, which entails disadvantages. Most notably fast diffusion of Au can cause contamination and intermixing in the sample, while adhesion of Au on the Si substrate renders the structures incompatible with CMOS technology applications. On the contrary, this risk is eliminated via employing Ga droplets as catalysts, which

are easily consumed after growth under a high group V flux. In addition, the growth of these structures on Si facilitates their integration with CMOS technology applications, considering that Si is the prevailing platform in the field of optoelectronics. It is also noted that the (111) orientation of the substrates plays a role in their device implementation. For example, (111)-oriented Si is its resistance to higher temperatures, due to its crystallography, which makes it a good option for functionalities at higher temperatures. The low refractive index makes it reliable as a substrate for the rest of the materials that will be supplied. Typically, (100) orientation has been favoured in CMOS applications. Nevertheless, the aforementioned advantages along with the high carrier surface mobility have rendered (111)-oriented Si wafers a preferable option for CMOS microsystems. For instance, field emission devices based on (111) Si surfaces has been achieved with good results reported.^[317] Regarding the optical response of the NWs, tuneable emission in the red and near-infrared regions was observed, which is promising for light-emitting applications.

One of the interesting aspects of the self-catalysed AlGaAs NWs that we synthesized is the high Ga flux and the temperature that was chosen, which allowed for lateral growth of a self-formed shell, with rough surfaces. The existence of the concavities allowed for Ga accumulation and amalgamation as droplets, which drove the self-formation of AlGaAs branches, perpendicularly on the NW trunks. It is reminded that the branched NWs did not refer to different samples but rather morphological variations in the same 1D AlGaAs NW samples. Hence, the optical results of 1D AlGaAs NWs reflect the response of branched NWs as well. Even though the percentage of AlGaAs branches was pronounced at 40% Al content, which did not produce optical signal potentially due to direct-to-indirect transition of the bandgap, interesting and novel observations were made regarding the structure of the branches.

Specifically, the bright stripes of Ga accumulation both axial and perpendicular to the branch axis exhibit the intriguing formation of the checked pattern, while Ga-rich boxes at the intersections of the checked pattern have the potential to be harvested as novel light-emitters in the future, as shown in earlier works for other phase separations.^[109]

Besides, the self-catalysed growth of AlGaAs/GaAs NWQDs for the first time was reported. The structures did not present significant morphological differences when compared to bare AlGaAs NWs. This means that the basic features, such as the compositional inhomogeneity and the self-formed Al-rich AlGaAs shell are still presented in this case, with a brief interruption of Al supply for 7 seconds allowing for the GaAs segment to be grown. The optical study of the NWQDs demonstrates the centrally localized GaAs peak, which is comprised of an exciton and biexciton transition and exhibits a high degree of polarization. These properties reveal the QD-nature of the GaAs segment and are indicative of strong carrier confinement in this region. It is noted that such structures are ideal candidates for single photon emission and for generation of indistinguishable photons, which are crucial for quantum information processing applications. Another good indication which is suggestive of such a functionality in our samples is the narrow linewidth of 490 μeV , which is comparable or better than previous results reported in ternary NWQDs. Here, it can be underlined that SKQDs exhibit lower linewidth, as in the case of ternary NWQDs some unintentional intermixing frequently occurs. Nevertheless, the acceptably narrow linewidth along with the previous optical features indicate the potential of our structures for single photon emission and generation of polarized light.

Eventually, InAs nanosheets were grown by our collaborators using solid-source MBE growth. The inspection of the samples at UCL via SEM showed similar results to the ones reported earlier by our collaborators.^[200] The focal point of our research was

the optical investigation of these nanosheets, which is something that has not been investigated so far for such III-V-based structures. The “memory effect” that was observed shows the potential of the pristine InAs nanosheets for optically controllable memory after light irradiation and the suitability for reading and writing optical data. On the other hand, the two methods of passivation that were applied reveal that such a functionality is not possible in these cases, which confirms that the driving force of the “memory effect” is carrier trapping at the rich surface states. However, the passivated samples exhibit good optical properties with the most pronounced being the ability to emit mid-infrared light at elevated temperatures. The fabrication of the memory cell based on an FET configuration is something that has been conducted earlier for other types of nanosheets, such as In_2Se_3 ^[321] and black phosphorus.^[322] However, the advantage in the current work is that such a functionality was based on high-mobility III-V nanosheets which allows for channel current driven by ultra-low V_{DS} signifying low power consumption in the operating mode (10^{-5} nW, in this case), while optical memory was indicated by the ability to read and write optical information.

However, apart from the significance of the presented results it is interesting to shed light on the challenges that we met and potential solutions in future works. This will be the topic of discussion in the following section.

7.3) Discussion of the challenges and future works

Despite the importance of the employed material platforms, there have been problems emerging while fabricating them or while studying their properties and potential. Some of these challenges were addressed, while the emergence of others provided us with important information that will help us formulate our plans for future works.

First, regarding AlGaAs NWs, as typical examples of III-III-V structures, they are particularly challenging with respect to the control of the compositional distribution along the NW axis. This is a phenomenon that is evident in the TEM inspection of the AlGaAs NWs that was conducted in chapter 3. This is also the reason why reports on III-III-V ternary NWs are considerably less when compared to III-V-V alloys. Group III elements have a high solubility in group III droplets, signifying that even minor changes or distortions in the elemental fluxes disrupt the stability and chemical balance of the droplet seeds, hence rendering the growth extremely sensitive. The short diffusion length of Al causing its adhesion on the sidewall facets, which is a very important feature of AlGaAs NWs, further intricates the compositional distribution. It is however noted that increased Al presence could improve the distribution, as demonstrated earlier for InGaP NWs.^[251] Nevertheless, this should be carefully controlled as increase of Al percentage above 40% would cause a direct-to-indirect transition of the bandgap which would render the samples optically inactive, as in our case where no signal could be traced from samples with 40% Al composition. For that reason, modifications in the growth temperature and more specifically increase of this parameter seems a more preferable route, which has shown to be effective in modifying composition and distribution characteristics in other III-III-V material platforms.^[242]

The improvement of this challenge can also contribute to widening the frame of practical applications for the NW structures. It has been mentioned in the introduction that III-V NWs can be employed for laser fabrication. More specifically, the combination of GaAs/AlGaAs in core/shell architecture has been established as a platform suitable for laser implementation.^[48-49, 318] For example, continuous wave lasing was reported for GaAs/AlGaAs core/shell NWs grown monolithically on Si

substrates.^[318] It is important to remind that Si is suitable as a substrate for device implementation, which allows for the monolithic growth of III-V structures without the need to be transferred on a different substrate. However, no such functionality has been achieved so far in AlGaAs NWs. Potential improvement of the compositional distribution, which has an impact on the optical properties, such as broadening of the linewidth and decreased intensity of the peak could allow for examination of lasing from AlGaAs core NWs.

Another challenge that was met was that the optically active NW samples (10%-30% Al content) did not exhibit pronounced branching events, although some branches were clearly noticed, as described in chapter 4. On the other hand, 40% Al content caused a radical increase in the branching events which allowed us to thoroughly inspect their morphology. However, the latter were optically inactive, signifying that the optical response of the branches and the effect of the checked pattern and Ga-rich boxes could not be investigated. However, considering that such phase separation has given rise to the spontaneous formation of QD-like structures in AlGaAs shells along the (112) direction, it is anticipated that such a function can be acquired in the AlGaAs NW samples. It is important to mention that such alloy segregation was the case based on the VLS growth model of the branches, signifying that adopting other techniques may alter this phenomenon. However, in our case, one potential method that could be employed would be to increase the accumulated Ga droplets at the concavities of the shell, which could lead to more branching events. This could be achieved via adequately modifying the Ga flux, while ensuring that the axial growth of NWs will not be interrupted. The increase of branching events would allow for an analysis of the optical signal deriving from the Al-deficient samples that

are direct-bandgap structures and observe potential quantum confinement-related phenomena driven by the checked pattern of the bright stripes in the branches.

Regarding the growth of GaAs QD, the main challenge was to keep the interfaces abrupt and reduce unintentional intermixing. The supply of Al was terminated for 7 seconds to grow the dot and then reintroduced to form the top NW in order for the dot to be fully embedded. By adopting a sufficiently high Ga flux, the interfaces were abrupt as demonstrated by the small intermixing that was achieved in the QD region. The Al counts do not reach zero. Nevertheless, this is mainly attributed to contributions from the Al-rich shell surrounding the dot, while the percentage of intermixing is small enough to be considered acceptable. Besides, the good results and optical properties of the NWQD exhibits the suitability of the structures for the applications described earlier. The linewidth is considered acceptably low at 490 μeV . However, there could be room for further improvement upon reducing the non-uniformity of the elemental distribution, which as mentioned earlier could be influenced by the growth parameters such as the temperature and the group III flux. Despite this fact, the narrow linewidth, localized peaks and polarized emission are good indications for generation of indistinguishable photons. One of the plans for future work is the recording of the second order correlation function at zero time delay in order to obtain an insight on the possibility of two photons being emitted simultaneously, as will be discussed in the final paragraph of this section.

It is clarified that the branching and morphological complexities of the NWs did not pose an obstacle to the success of the NWQD synthesis, as the dot is axially embedded, which means that its formation is depending on the alteration of the elemental supplies rather than the additional NW components. The nucleation of the branches was a result of the high Ga flux that was used which has a twofold role; first,

it promotes amalgamation of a higher number of accumulated Ga atoms at the concavities of the shell and second, it increases the roughness of the shell. Moreover, the duration of the growth was long signifying that this provided adequate time for the self-formed shell to be developed. Based on the above, we can see that the growth of branches and the morphological complexity resulted from the growth conditions which allowed us to inspect this interesting variation, while the formation of the dot axially in the NW is a consequence of the termination of Al supply, which allowed for the deposition of merely GaAs layer for the given duration.

Besides, challenges can be met in the case of InAs nanosheets that were optically investigated. The first challenge was the interpretation of the irregular findings regarding the peaks during the “power-up” and “power-down” methods, which was overcome by a thorough systematic study of the trends that were similar in several rounds of measurements. Owing to the temperature that was used for the growth, the nanosheets were fully formed from 1D InAs NWs, which ensures a high density as viewed in chapter 6, along with a high material quality with few defects. The difficulty in the optical investigation however, despite the good quality, also relied on the suppression of the peak at high temperatures, which signified that measurements should be recorded in a small time frame so as not to distort the results. Another difficulty is the control of the thermal stability of the passivation, as it could be possible that S-In or S-As bonds can degrade over time. However, it is interesting to notice that after conducting the same measurements with a two-week delay, the results obtained were the same, suggesting good stability of the passivation. Importantly, the sample should be kept as protected as possible from ambient air to reduce degrading oxidation of the surface. The pristine structures were employed for FET fabrication that displayed the potential for reading and writing optical information driven by ultra-

low V_{DS} thus being promising for ultra-low power consumption. On the other hand, chemically passivated and core/shell nanosheets showed potential to emit light up to elevated temperatures (225 K and room temperature, respectively). It is interesting to highlight that the investigation for the optical properties of such passivated structures is far from being fully understood. However, optical devices such as nanosheet lasers have been fabricated in the past with good results. For instance, CdSSe nanosheet heterostructures exhibited lasing at 526 and 623 nm, achieved by a side-to-side CdS dominant central region and CdSe edges, which formed a natural cavity for the lasing to be achieved.^[319] In addition, GaSe nanosheets were used as broadband saturable absorbers with good results, showing potential for laser generation.^[320] Nevertheless, further works are needed to circumvent the obstacle of the effective cavity and structural complexity of the structures.

Interestingly, a topic for discussion is the possibility to growth pure WZ AlGaAs in NW configuration. It has been inferred that the WZ insertions affect the wavelength of the emission and is a contributing factor for a blueshift of the PL peak when compared to the anticipated value. It is also known from the recent work of Leandro et al.,^[252] that WZ AlGaAs has a narrower bandgap energy when compared to ZB. This is also in agreement with the results of previous reports on theoretical computations and simulations which demonstrate that despite the fact that usually WZ III-V alloys have a larger bandgap when compared to their ZB counterparts, the case for AIAs is the opposite, where the bandgap energy is reduced from 3.144 eV (ZB) to 2.671 (WZ). For these reasons, exploring the properties of WZ AlGaAs and optically probing the structures is one of the plans for our research project in the future. For instance, AlGaAs can be grown as shell surrounding WZ NW cores, such as Ge. Hybrid III-V/IV core/shell NWs have been grown in our lab earlier, with the III-V core and IV shell

presenting the same crystal structure due to the epitaxial nature of the growth. Ergo, the realization of WZ AlGaAs could be accomplished by following this configuration with a WZ material chosen as the NW core component.

Moreover, as shown earlier, embedding of single GaAs dots in AlGaAs NWs has been proven an important asset for the optical properties of the structures, as the GaAs-related peak exhibits good features such as the narrow linewidth, spatial localization and exciton/biexciton transitions. The aforementioned improvements related to the homogeneity of the AlGaAs NWs can ameliorate even further the response, due to the accentuated abruptness of the dot/NW interfaces. Experiments, on the second-order correlation function are planned in order to explore the possibility of employing the promising structures that we realized in single photon generation applications. Moreover, the potential embedding of multiple QDs on the NW axis can be exploited for laser fabrication, which is one of the plans for our future work.

We hope that the content of the current thesis and the results that were presented exhibit the excellent properties and promising potential of the realized structures and employed material platforms aiming to their wider implementation in Si nanophotonics.

Chapter 8: Bibliography

- 1) R. S. Wagner, W. C. Ellis, Vapour-Liquid-Solid mechanism of single crystal growth, Appl. Phys. Lett., **1964**, 4, 89
- 2) Y. Zhang, J. Wu, M. Aagesen, J. Holm, S. Hatch, M. Tang, S. Huo, H. Liu, Self-Catalyzed Ternary Core-Shell GaAsP Nanowire Arrays Grown on Patterned Si Substrates by Molecular Beam Epitaxy, Nano Lett., **2014**, 14(8), 4542-4547
- 3) S. Ambrosini, M. Fanetti, V. Grillo, A. Franciosi, S. Rubini, Self-catalyzed GaAs nanowire growth on Si-treated GaAs (100) substrates, Journal of Applied Physics, **2011**, 109, 094306
- 4) B. Mandl, A. W. Dey, J. Stangl, M. Cantoro, L. E. Wernersson, G. Bauer, L. Samuelson, K. Deppert, C. Thelander, Self-seeded position-controlled InAs nanowire growth on Si: A growth parameter study, Journal of Crystal Growth, **2011**, 334(1), 51-56
- 5) V. G. Dubrovskii, Theory of VLS Growth of Compound Semiconductors, Semiconductors and Semimetals, Chapter 1, Elsevier Inc, **2015**, 93
- 6) A. Li, J. Zou, X. Han, Growth of III-V semiconductor nanowires and their heterostructures, Sci China Mater, **2016**, 59(1), 51–91
- 7) T. Martensson, C. P. T. Svensson, B. A. Wacaster, M. W. Larsson, W. Seifert, K. Deppert, A. Gustafsson, L. R. Wallenberg, L. Samuelson, Epitaxial III-V Nanowires on Silicon, Nano Lett., **2004**, 4(10), 1987-1990
- 8) H. J. Joyce, J. Wong-Leung, Q. Gao, H. H. Tan, C. Jagadish, Phase Perfection in Zinc Blende and Wurtzite III-V Nanowires Using Basic Growth Parameters, Nano Lett., **2010**, 10(3), 908-915
- 9) X. Ren, H. Huang, V. G. Dubrovskii, N. V. Sibirev, M. V. Nazarenko, A. D. Bolshakov, X. Ye, Q. Wang, Y. Huang, X. Zhang, J. Guo, X. Liu, Experimental

- and theoretical investigations on the phase purity of GaAs zincblende nanowires, *Semicond. Sci. Technol.*, **2011**, 26, 014034
- 10) C. Zhou, K. Zheng, Z.-M. Liao, P.-P. Chen, W. Lu, J. Zou, Phase purification of GaAs nanowires by prolonging the growth duration in MBE, *J. Mater. Chem. C*, **2017**, 5, 5257-5262
 - 11) H. Zeng, X. Yu, H. Aruni Fonseka, J. A. Gott, M. Tang, Y. Zhang, G. Boras, J. Xu, A. M. Sanchez, H. Liu, Hybrid III-V/IV Nanowires: High-Quality Ge Shell Epitaxy on GaAs Cores, *Nano Lett.* **2018**, 18(10), 6397-6403
 - 12) S. Conesa-Boj, S. Dunand, E. Russo-Averchi, M. Heiss, D. Ruffer, N. Wyrsh, C. Ballif, A. Fontcuberta i Morral, Hybrid axial and radial Si-GaAs heterostructures in nanowires, *Nanoscale*, **2013**, 5, 9633-9639
 - 13) B. Hua, J. Motohisa, Y. Kobayashi, S. Hara, T. Fukui, Single GaAs/GaAsP Coaxial Core/Shell Nanowire Lasers, *Nano Lett.* **2009**, 9(1), 112-116
 - 14) W. Z. Xu, F. F. Ren, D. Jevtics, A. Hurtado, L. Li, Q. Gao, J. Ye, F. Wang, B. Guilhabert, L. Fu, H. Lu, R. Zhang, H. H. Tan, M. D. Dawson, C. Jagadish, Vertically emitting Indium Phosphide Nanowire Lasers, *Nano Lett.* 2018, 18(6), 3414-3420
 - 15) D. Saxena, S. Mokkapati, P. Parkinson, N. Jiang, Q. Gao, H. H. Tan, C. Jagadish, Optically pumped room-temperature GaAs nanowire lasers, *Nat. Photonics* **2013**, 7, 963-968
 - 16) T. Stettner, T. Kostenbader, D. Ruhstorfer, J. Bissinger, H. Riedl, M. Kaniber, G. Koblmüller, J. J. Finley, Direct Coupling of Coherent Emission from Site-Selectively Grown III-V Nanowire Lasers into Proximal Silicon Waveguides, *ACS Photonics* **2017**, 4(10), 2537-2543

- 17) B. Mayer, L. Janker, B. Loitsch, J. Treu, T. Kostenbader, S. Lichtmannecker, T. Reichert, S. Morkötter, M. Kaniber, G. Abstreiter, C. Gies, G. Koblmüller, J. J. Finley, Monolithically Integrated High- β Nanowire Lasers on Silicon, *Nano Lett.* **2016**, 16(1), 152-156
- 18) H. P. T. Nguyen, M. Djavid, S. Y. Woo, X. Liu, A. T. Connie, S. Sadaf, Q. Wang, G. A. Botton, I. Shih, Z. Mi, Engineering the Carrier Dynamics of InGaN Nanowire White Light-Emitting Diodes by Distributed p-AlGaN Electron Blocking Layers, *Scientific Reports* **2015**, 5, 7744
- 19) G. T. Wang, Q. Li, J. J. Wierer, D. D. Joleske, J. J. Fiegel, Top-down fabrication and characterization of axial and radial III-nitride nanowire LEDs, *Phys. Status Solidi A* **2014**, 211, 4, 748-751
- 20) A. T. M. G. Sarwar, B. J. May, J. I. Deitz, T. J. Grassman, D. W. McComb, R. C. Myers, Tunnel junction enhanced nanowire ultraviolet light emitting diodes, *Appl. Phys. Lett.* **2015**, 107, 101103
- 21) C. P. T. Svensson, T. Mårtensson, J. Trägårdh, C. Larsson, M. Rask, D. Hessman, L. Samuelson, J. Ohlsson, Monolithic GaAs/InGaP nanowire light emitting diodes on silicon, *Nanotechnology* **2008**, 19(30), 305201
- 22) S. Zhao, A. T. Connie, M. H. T. Dastjerdi, X. H. Kong, Q. Wang, M. Djavid, S. Sadaf, X. D. Liu, I. Shih, H. Guo, Z. Mi, Aluminium nitride nanowire light emitting diodes: Breaking the fundamental bottleneck of deep ultraviolet light sources, *Scientific Reports* **2015**, 5, 8332
- 23) N. Huang, C. Lin, M. L. Povinelli, Limiting efficiencies of tandem solar cells consisting of III-V nanowire arrays on silicon, *J. Appl. Phys.* **2012**, 112, 064321
- 24) R. R. LaPierre, Numerical model of current-voltage characteristics and efficiency of GaAs nanowire solar cells, *J. Appl. Phys.* **2011**, 109, 034311

- 25) E. C. Garnett, M. L. Brongersma, Y. Cui, M. D. McGehee, Nanowire Solar Cells, *Annu. Rev. Mater. Res.* **2011**, 41, 269-95
- 26) P. Yu, J. Wu, S. Liu, J. Xiong, C. Jagadish, Z. M. Wang, Design and Fabrication of Silicon Nanowires Towards Efficient Solar Cells, *NanoToday* **2016**, 11(6), 704-737
- 27) Z. Zhong, Z. Li, Q. Gao, Z. Li, K. Peng, L. Li, S. Mokkaapati, K. Vora, J. Wu, G. Zhang, Z. Wang, L. Fu, H. H. Tan, C. Jagadish, Efficiency enhancement of axial junction InP single nanowire solar cells by dielectric coating, *Nano Energy* **2016**, 28, 106-114
- 28) X. Dai, S. Zhang, Z. Wang, G. Adamo, H. Liu, Y. Huang, C. Couteau, C. Soci, GaAs/AlGaAs Nanowire Photodetector, *Nano Lett.* **2014**, 14(5), 2688-2693
- 29) H. Park, J. H. Kim, R. Beresford, J. Xu, Effects of electrical contacts on the photoconductive gain of nanowire photodetectors, *Appl. Phys. Lett.* **2011**, 99, 143110
- 30) F. Gonzalez-Posada, R. Songmuang, M. den Hertog, E. Monroy, Environmental sensitivity of n-i-n and undoped single GaN nanowire photodetectors, *Appl. Phys. Lett.* **2013**, 102, 213113
- 31) R. R. LaPierre, M. Robson, K. M. Azizur-Rahman, P. Kuyanov, A review of III-V nanowire infrared photodetectors and sensors, *J. Phys. D: Appl. Phys.* **2017**, 50(12), 123001
- 32) H. W. Shin, S. J. Lee, D. G. Kim, M.-H. Bae, J. Heo, K. J. Choi, W. J. Choi, J.-w. Choe, J. C. Shin, Short-wavelength infrared photodetector on Si employing strain-induced growth of very tall InAs nanowire arrays, *Scientific Reports* **2015**, 5, 10764

- 33) N. Hang, F. Wang, J. J. Hou, S. P. Yip, H. Lin, F. Xiu, M. Fang, Z. Yang, X. Shi, G. Dong, T. F. Hung, J. C. Ho, Tunable Electronic Transport Properties of Metal-Cluster-Decorated III-V Nanowire Transistors, *Adv. Mater.* **2013**, 25(32), 4445-4451
- 34) C. Thelander, L. E. Fröberg Froberg, C. Rehnstedt, L. Samuelson, L.-E. Wernersson, Vertical Enhancement-Mode InAs Nanowire Field-Effect Transistor With 50-nm Wrap Gate, *IEEE Electron Device Letters*, **2008**, 29(3), 206-208
- 35) K. Takase, Y. Ashikawa, G. Zhang, K. Tateno, S. Sasaki, Highly gate-tuneable Rashba spin-orbit interaction in a gate all-around InAs nanowire metal oxide-semiconductor field-effect transistor, *Scientific Reports* **2017**, 7, 930
- 36) S. A. Dayeh, D. P. R. Aplin, X. Zhou, P. Yu, P. K. L. Yu, E. T. Yu, D. Wang, High electron mobility InAs nanowire field-effect transistors, *Small* **2017**, 1613-68293(2), 326-332
- 37) C. Thelander, M. T. Bjork, M. W. Larsson, A. E. Hansen, L. R. Wallenberg, L. Samuelson, Electron transport in InAs nanowires and heterostructure nanowire devices, *Solid State Commun.* **2004**, 0038-1098131(9-10), 573-579
- 38) M. H. Huang, S. Mao, H. Feick, H. Yan, Y. Wu, H. Kind, E. Weber, R. Russo, P. Yang, Room-Temperature Ultraviolet Nanowire Nanolasers, *Science*, **2001**, 292(5523), 1897-1899
- 39) M. A. Zimmler, F. Capasso, S. Müller, C. Ronning, Optically pumped nanowire lasers: invited review, *Semicond. Sci. Technol.*, **2010**, 25(2), 024001
- 40) A. V. Maslov, C. Z. Ning, Reflection of guided modes in a semiconductor nanowire laser, *Appl. Phys. Lett.*, **2003**, 83, 1237

- 41) Q. Y. Tong, U. Gösele, Semiconductor wafer bonding, science and technology, John Wiley & Sons, **1999**, 204
- 42) B. Mandl, J. Stang, E. Hilner, A. A. Zakharov, K. Hillerich, A. W. Dey, L. Samuelson, G. Bauer, K. Deppert, A. Mikkelsen, Growth mechanism of Self-Catalyzed Group III-V Nanowires, Nano Lett., **2010**, 10(11), 4443-4449
- 43) S. Plissard, K. A. Dick, G. Larrieu, S. Godey, A. Addad, X. Wallart, P. Caroff, Gold-free growth of GaAs nanowires on silicon: arrays and polytypism, Nanotechnology **2010**, 21, 385602
- 44) G. Boras, X. Yu, H. Liu, III-V ternary nanowires on Si substrates: growth, characterization and device applications, J. Semicond. **2019**, 40, 101301
- 45) J. Treu, T. Stettner, M. Watzinger, S. Morkötter, M. Döblinger, S. Matich, K. Saller, M. Bichler, G. Abstreiter, J. J. Finley, J. Stangl, G. Koblmüller, Lattice-Matched InGaAs-InAlAs Core-Shell Nanowires with Improved Luminescence and Photoresponse Properties, Nano Lett. **2015**, 15(5), 3533-3540
- 46) J. C. Shin, A. Lee, P. K. Mohseni, D. Y. Kim, L. Yu, J. H. Kim, H. J. Kim, W. J. Choi, D. Wasserman, K. J. Choi, X. Li, Wafer-Scale Production of Uniform InAs_yP_{1-y} Nanowire Array on Silicon for Heterogeneous Integration, ACS Nano **2013**, 7(6), 5463-5471
- 47) J. Wu, Y. Li, J. Kubota, K. Domen, M. Aagesen, T. Ward, A. Sanchez, R. Beanland, Y. Zhang, M. Tang, S. Hatch, A. Seeds, H. Liu, Wafer-Scale Fabrication of Self-Catalyzed 1.7 eV GaAsP Core-Shell Nanowire Photocathode on Silicon Substrates, Nano Lett. **2014**, 14(4), 2013-2018
- 48) D. Saxena, N. Jiang, X. Yuan, S. Mokkapati, Y. Guo, H. H. Tan, C. Jagadish, Design and Room-Temperature Operation of GaAs/AlGaAs Multiple Quantum Well Nanowire Lasers, Nano Lett. **2016**, 16(8), 5080-5086

- 49) T. Stettner, P. Zimmermann, B. Loitsch, M. Döblinger, A. Regler, B. Mayer, J. Winnerl, S. Matich, H. Riedl, M. Kaniber, G. Abstreiter, G. Koblmüller, J. J. Finley, Coaxial GaAs-AlGaAs core-multishell nanowire lasers with epitaxial gain control, *Appl. Phys. Lett.* **2016**, 108, 011108
- 50) K. Tomioka, J. Motohisa, S. Hara, K. Hiruma, T. Fukui, GaAs/AlGaAs Core Multishell Nanowire-Based Light-Emitting Diodes on Si, *Nano Lett.* **2010**, 10(5), 1639-1644
- 51) A. Berg, S. Yazdi, A. Nowzari, K. Storm, V. Jain, N. Vainorius, L. Samuelson, J. B. Wagner, M. T. Borgström, Radial Nanowire Light-Emitting Diodes in the $(\text{Al}_x\text{Ga}_{1-x})_y\text{In}_{1-y}\text{P}$ Material System, *Nano Lett.*, **2016**, 16(1), 656-662
- 52) J. Huh, D.-C. Kim, A. M. Munshi, D. L. Dheeraj, D. Jang, G.-T. Kim, B.-O. Fimland, H. Weman, Low frequency noise in single GaAsSb nanowires with self-induced compositional gradients, *Nanotechnology* **2016**, 27, 385703
- 53) M. Sharma, E. Ahmad, D. Dev, J. Li, C. L. Reynolds Jr, Y. Liu, S. Iyer, Improved performance of GaAsSb/AlGaAs nanowire ensemble Schottky barrier based photodetector via in situ annealing, *Nanotechnology* **2018**, 30, 034005
- 54) K. Tomioka, M. Yoshimura, T. Fukui, A III-V nanowire channel on silicon for high-performance vertical transistors, *Nature* **2012**, 488, 189-192
- 55) J. J. Hou, N. Han, F. Wang, F. Xiu, S. Yip, A. T. Hui, T. Hung, J. C. Ho, Synthesis and Characterizations of Ternary InGaAs Nanowires by a Two-Step Growth Method for High-Performance Electronic Devices, *ACS Nano* **2012**, 6(4), 3624-3630
- 56) H. Shu, X. Yang, P. Liang, D. Cao, X. Chen, Impact of Surface Point Defects on Electronic Properties and p-Type Doping of GaAs Nanowires, *J. Phys. Chem. C* **2016**, 120(38), 22088-22095

- 57) D. Gupta, N. I. Goktas, A. Rao, R. LaPierre, O. Rubel, Stacking defects in GaP nanowires: Electronic structure and optical properties, *J. Appl. Phys.* **2019**, 126, 084306
- 58) C. Haller, J.-F. Carlin, G. Jacopin, W. Liu, D. Martin, R. Butté, N. Grandjean, GaN surface as the source of non-radiative defects in InGaN/GaN quantum wells, *Appl. Phys. Lett.* **2018**, 113, 111106
- 59) D. Rudolph, K. Schweickert, S. Morkötter, L. Hanschke, S. Hertenberger, M. Bichler, G. Koblmüller, G. Abstreiter, J. J. Finley, Probing the trapping and thermal activation dynamics of excitons at single twin defects in GaAs-AlGaAs core-shell nanowires, *New J. Phys.* **2013**, 15, 113032
- 60) M. J. L. Sourribes, I. Isakov, M. Panfilova, H. Liu, P. A. Warburton, Mobility Enhancement by Sb-mediated Minimisation of Stacking Fault Density in InAs Nanowires Grown on Silicon, *Nano Lett.* **2014**, 14(3), 1643-1650
- 61) S. G. Ghalamestani, M. Ek, B. Ganjipour, C. Thelander, J. Johansson, P. Caroff, K. A. Dick, Demonstration of Defect-Free and Composition Tunable $\text{Ga}_x\text{In}_{1-x}\text{Sb}$ Nanowires, *Nano Lett.* **2012**, 12(9), 4914-4919
- 62) H. Zhou, M. Pozuelo, R. F. Hicks, S. Kodambaka, Self-catalyzed vapor-liquid-solid growth of $\text{InP}_{1-x}\text{Sb}_x$ nanostructures, *J. Cryst. Growth* **2011**, 319(1), 25-30
- 63) H. B. Russell, A. N. Andriotis, M. Menon, J. B. Jasinski, A. Martinez-Garcia, M. K. Sunkara, Direct Band Gap Gallium Antimony Phosphide ($\text{GaSb}_x\text{P}_{1-x}$) Alloys, *Scientific Reports* **2016**, 6, 20822
- 64) L. Gagliano, M. Kruijsse, J. D. D. Schefold, A. Belabbes, M. A. Verheijen, S. Meuret, S. Koelling, A. Polman, F. Bechstedt, J. E. M. Haverkort, E. P. A. M. Bakkers, Efficient Green Emission from Wurtzite $\text{Al}_x\text{In}_{1-x}\text{P}$ Nanowires, *Nano Lett.* **2018**, 18(6), 3543-3549

- 65) D. C. Unitt, A. J. Bennett, P. Atkinson, K. Cooper, P. See, D. Gevaux, M. B. Ward, R. M. Stevenson, D. A. Ritchie, A. J. Shields, Quantum dots as single-photon sources for quantum information processing, *J. Opt. B: Quantum and Semiclass. Opt.* **2005**, 7, S129
- 66) B.-C. Ren, F.-G. Deng, Hyper-parallel photonic quantum computation with coupled quantum dots, *Scientific Reports* **2015**, 4, 4623
- 67) K. Takemoto, Y. Nambu, T. Miyazawa, Y. Sakuma, T. Yamamoto, S. Yorozu, Y. Arakawa, Quantum key distribution over 120 km using ultrahigh purity single-photon source and superconducting single-photon detectors, *Scientific Reports* **2015**, 5, 14383
- 68) T. Heindel, C. A. Kessler, M. Rau, C. Schneider, M. Fürst, F. Hargart, W.-M. Schulz, M. Eichfelder, R. Roßbach, S. Nauerth, M. Lermer, H. Weier, M. Jetter, M. Kamp, S. Reitzenstein, S. Höfling, P. Michler, H. Weinfurter, A. Forchel, Quantum key distribution using quantum dot single-photon emitting diodes in the red and near infrared spectral range, *New J. Phys.* **2012**, 14, 083001
- 69) Z. Othaman, L. K. Boo, S. Sakrani, R. Muhammad, The Stransi-Krastanov three dimensional island growth perdition of finite size model (part I), *J. Fiz. UTM.* **2008**, 3, 78-83
- 70) C. Dietrich, A. Fiore, M. G. Thompson, M. Kamp, S. Hofling, GaAs integrated quantum photonics: Towards compact and multi-functional quantum photonic integrated circuits, *Laser Photonics Rev.* **2016**, 10(6), 870-894
- 71) Y. Kim, K. Y. Ban, C. Honsberg, Multi-stacked InAs/GaAs quantum dots grown with different growth modes for quantum dot solar cells, *Appl. Phys. Lett.* **2015**, 106, 222104

- 72) D. Das, D. P. Panda, B. Tongbram, J. Saha, V. Deviprasad, H. Rawool, S. M. Singh, V. Chavan, S. Chakrabarti, Improved near infrared energy harvesting through heterogeneously coupled Sk on SML quantum dot heterostructure, *Solar Energy Materials and Solar Cells* **2018**, 185, 549-557
- 73) D. Bimberg, G. Fiol, M. Kuntz, C. Meuer, M. Lämmlin, N. N. Ledentsov, A. R. Kovsh, High speed nanophotonic devices based on quantum dots, *Phys. Status Solidi (a)* **2006**, 203(14), 3523-3532
- 74) L. Mancini, F. Moyon, J. Houard, I. Blum, W. Lefebvre, F. Vurpillot, A. Das, E. Monroy, L. Rigutti, Multi-excitonic emission from Stranski-Krastanov GaN/AlN quantum dots inside a nanoscale tip, *Appl. Phys. Lett.* **2017**, 111, 243102
- 75) H. S. Oh, S. M. Kim, H. H. Lee, J. H. Baek, J. S. Kwak, Realization of the 700 nm Emitting Spectrum Using GaInP Quantum Dots in the AlGaIn P-Based Light Emitting Diodes, *J. Electrochem. Soc.* **2010**, 157(9), 863-865
- 76) L. Francaviglia, Y. Fontana, A. Fontcuberta i Morral, Quantum Dots in Nanowires, Semiconductors and Semimetals, Chapter V, Elsevier Inc. **2016**, 94
- 77) A. Tribu, G. Sallen, T. Aichele, R. Andre, J. P. Poizat, C. Bougerol, S. Tatarenko, K. Kheng, A High-Temperature Single-Photon Source from Nanowire Quantum Dots, *Nano Lett.* **2008**, 8(12), 4326-4329
- 78) J. Claudon, J. Bleuse, N. S. Malik, M. Bazin, P. Jaffrenou, N. Gregersen, C. Sauvan, P. Lalanne, J. M. Gerard, A highly efficient single-photon source based on a quantum dot in a photonic nanowire, *Nat. Photonics* **2010**, 4, 174-177
- 79) M. J. Holmes, K. Choi, S. Kako, M. Arita, Y. Arakawa, Room-Temperature Triggered Single Photon Emission from a III-Nitride Site-Controlled Nanowire Quantum dot, *Nano Lett.* **2014**, 14(2), 982-986

- 80) S. Bounouar, M. Elouneg-Jamroz, M. den Hertog, C. Morchutt, E. Bellet-Amalric, R. Andre, C. Bougerol, Y. Genuist, J.-Ph. Poizat, S. Tatarenko, K. Kheng, Ultrafast Room Temperature Single-Photon Source from Nanowire Quantum Dots, *Nano Lett.* **2012**, 12(6), 2977-2981
- 81) P. Yu, Z. Li, T. Wu, Y.-T. Wang, X. Tong, C.-F. Li, Z. Wang, S.-H. Wei, Y. Zhang, H. Liu, L. Fu, Y. Zhang, J. Wu, H. H. Tan, C. Jagadish, Z. M. Wang, Nanowire Quantum Dot Surface Engineering for High Temperature Single Photon Emission, *ACS Nano*, **2019**, 13(11), 13492-13500
- 82) M. R. Philip, D. D. Choudhary, M. Djavid, K. Q. Le, J. Piao, H. P. T. Nguyen, High efficiency green/yellow and red InGaN/AlGaIn nanowire light-emitting diodes grown by molecular beam epitaxy, *Journal of Science: Advanced Materials and Devices 2* **2017**, 2(2), 150-155
- 83) E. D. Minot, F. Kelkensberg, M. van Kouwen, J. A. van Dam, L. P. Kouwenhoven, V. Zwiller, M. T. Borgstrom, O. Wunnicke, M. A. Verheijen, E. P. A. M. Bakkers, Single Quantum Dot Nanowire LEDs, *Nano Lett.* **2007**, 7(2), 367-371
- 84) H. P. T. Nguyen, K. Cui, S. Zhang, S. Fatholouloumi, Z. Mi, Full-color InGaIn/GaIn dot-in-a-wire light emitting diodes on silicon, *Nanotechnology* **2011**, 22(44), 445202
- 85) M. T. Bjork, C. Thelander, A. E. Hansen, L. E. Jensen, M. W. Larsson, L. R. Wallenberg, L. Samuelson, Few-Electron Quantum Dots in Nanowires, *Nano Lett.* **2004**, 4(9), 1621-1625
- 86) A. Fuhrer, L. E. Froberg, J. N. Pedersen, M. W. Larsson, A. Wacker, M.-E. Pistol, L. Samuelson, Few Electron Double Quantum Dots in InAs/InP Nanowire Heterostructures, *Nano Lett.* **2007**, 7(2), 243-246

- 87) J. Tatebayashi, S. Kako, J. Ho, Y. Ota, S. Iwamoto, Y. Arakawa, Room-temperature lasing in a single nanowire with quantum dots, *Nat. Photonics* **2015**, 9, 501-505
- 88) J. Wu, A. Ramsay, A. Sanchez, Y. Zhang, D. Kim, F. Brossard, X. Hu, M. Benamara, M. E. Ware, Y. I. Mazur, G. J. Salamo, M. Aagesen, Z. Wang, H. Liu, Defect-Free Self-Catalyzed GaAs/GaAsP Nanowire Quantum Dots Grown on Si Substrate, *Nano Lett.* **2016**, 16(1), 504-511
- 89) J. Johansson, K. A. Dick, P. Caroff, M. E. Messing, J. Bolinsson, K. Deppert, L. Samuelson, Diameter Dependence of the Wurtzite-Zinc Blende Transition in InAs Nanowires, *J. Phys. Chem. C*, **2010**, 114(9), 3837-3842
- 90) C. Wilhelm, A. Larrue, X. Dai, D. Migas, C. Soci, Anisotropic photonic properties of III-V nanowires in the zinc-blende and wurtzite phase, *Nanoscale*, **2012**, 4, 1446-1454
- 91) K. Ikejiri, Y. Kitauchi, K. Tomioka, J. Motohisa, T. Fukui, Zinc Blende and Wurtzite Crystal Phase Mixing and Transition in Indium Phosphide Nanowires, *Nano Lett.*, **2011**, 11(10), 4314-4318
- 92) C. Thelander, P. Caroff, S. Plissard, A. W. Dey, K. A. Dick, Effects of Crystal Phase Mixing on the Electrical Properties of InAs Nanowires, *Nano Lett.*, **2011**, 11(6), 2424-2429
- 93) M. D. Schroer, J. R. Petta, Correlating the Nanostructure and Electronic Properties of InAs Nanowires, *Nano Lett.*, **2010**, 10(5), 1618-1622
- 94) S. A. Dayeh, D. Susac, K. L. Kavanagh, E. T. Yu, D. Wang, Structural and Room-Temperature Transport Properties of Zinc Blende and Wurtzite InAs Nanowires, *Adv. Funct. Mater.*, **2009**, 19(13), 2102-2108

- 95) M. Heiss, S. Conesa-Boj, J. Ren, H.-H. Tseng, A. Gali, A. Rudolph, E. Uccelli, F. Peiro, J. R. Morante, D. Schuh, E. Reiger, E. Kaxiras, J. Arbiol, A. Fontcuberta i Morral, Direct correlation of crystal structure and optical properties in wurtzite/zinc-blende GaAs nanowire heterostructures, *Phys. Rev. B*, **2011**, 83, 045303
- 96) P. Kusch, E. Grelich, C. Somaschini, E. Luna, M. Ramsteiner, L. Geelhaar, H. Riechert, S. Reich, Type-II band alignment of zinc-blende and wurtzite segments in GaAs nanowires: A combined photoluminescence and resonant Raman scattering study, *Phys. Rev. B*, **2014**, 89, 045310
- 97) D. Spirkoska, J. Arbiol, A. Gustafsson, S. Conesa-Boj, F. Glas, I. Zardo, M. Heigoldt, M. H. Gass, A. L. Bleloch, S. Estrade, M. Kaniber, J. Rossler, F. Peiro, J. R. Morante, G. Abstreiter, L. Samuelson, A. Fontcuberta i Morral, Structural and optical properties of high quality zinc-blende/wurtzite GaAs nanowire heterostructures, *Phys. Rev. B*, **2010**, 80, 245325
- 98) L. Zhang, J.-W. Luo, A. Zunger, N. Akopian, V. Zwiller, J.-C. Harmand, Wide InP Nanowires with Wurtzite/Zincblende Superlattice Segments Are Type-II whereas Narrower Nanowires Become Type-I: An Atomistic Pseudopotential Calculation, *Nano Lett.*, **2010**, 10(10), 4055-4060
- 99) P. Kusch, S. Breuer, M. Ramsteiner, L. Geelhaar, H. Riechert, S. Reich, Band gap of wurtzite GaAs: A resonant Raman study, *Phys. Rev. B*, **2012**, 86, 075317
- 100) F. Bechstedt, A. Belabbes, Structure, energetics and electronic states of III-V compound polytypes, *J. Phys. Condens. Matter.*, **2013**, 25(27), 273201
- 101) N. Jeon, D. Ruhstorfer, M. Döblinger, S. Matich, B. Loitsch, G. Koblmüller, L. Lauhon, Connecting Composition-Driven Faceting with Facet-Driven

- Composition Modulation in GaAs-AlGaAs Core-Shell Nanowires, *Nano Lett.* **2018**, 18(8), 5179-5185
- 102) M. Hjort, S. Kratzer, S. Lehman, S. J. Patel, K. A. Dick, C. J. Palmstrom, R. Timm, A. Mikkelsen, Crystal Structure Induced Preferential Surface Alloying of Sb on Wurtzite/Zinc Blende GaAs Nanowires, *Nano Lett.* 2017, 17(6), 3634-3640
- 103) M. Galicka, R. Buczko, P. Kacman, Segregation of Impurities in GaAs and InAs Nanowires, *J. Phys. Chem. C* **2013**, 117(39), 20361-20370
- 104) M. Galicka, R. Buczko, P. Kacman, Structure-Dependent Ferromagnetism in Mn-Doped III-V Nanowires, *Nano Lett.* **2011**, 11(8), 3319-3323
- 105) J. Johansson, E. D. Leschchenko, Zinc blende and wurtzite crystal structure formation in gold catalyzed InGaAs nanowires, *J. Cryst. Growth* **2019**, 509, 118-123
- 106) V. G. Dubrovskii, N. V. Sibirev, Effect of nucleation on the crystalline structure of nanowhiskers, *Tech. Phys. Lett.* **2009**, 35(4), 380-383
- 107) F. Glas, J.-C. Harmand, G. Patriarche, Why Does Wurtzite Form in Nanowires of III-V Zinc Blende Semiconductors?, *Phys. Rev. Lett.* **2007**, 99, 146101
- 108) Mårtensson, E. K.; Lehmann, S.; Dick, K. A.; Johansson, J. Simulation of GaAs Nanowire Growth and Crystal Structure. *Nano Lett.* **2019**, 19(2), 1197-1203
- 109) M. Heiss, Y. Fontana, A. Gustafsson, G. Wüst, C. Magen, D. D. O'Regan, J. W. Luo, B. Ketterer, S. Conesa-Boj, A. V. Kuhlmann, J. Houel, E. Russo-Averchi, J. R. Morante, M. Cantoni, N. Marzari, J. Arbiol, A. Zunger, R. J. Warburton, A. Fontcuberta i Morral, Self-assembled quantum dots in a nanowire system for quantum photonics, *Nature Materials* **2013**, 12, 439-444

- 110) G. Boras, X. Yu, H. A. Fonseka, D. Zhang, H. Zeng, A. M. Sanchez, H. Liu, Checked Patterned Elemental Distribution in AlGaAs Nanowire Branches via Vapor-Liquid-Solid Growth, *Nanoscale* **2020**, 12, 15711-15720
- 111) J. A. Gott, R. Beanland, H. A. Fonseka, J. J. P. Peters, Y. Zhang, H. Liu, A. M. Sanchez, Defect Dynamics in Self-Catalyzed III-V Semiconductor Nanowires, *Nano Lett.* **2019**, 19(7), 4574-4580
- 112) B. Mayer, D. Rudolph, J. Schnell, S. Morkötter, J. Winnerl, J. Treu, K. Müller, G. Bracher, G. Abstreiter, G. Koblmüller, J. J. Finley, Lasing from individual GaAs-AlGaAs core-shell nanowires up to room temperature, *Nat. Commun.*, **2013**, 4, 2931
- 113) J. Ho, J. Tatebayashi, S. Sergent, C. F. Fong, Y. Ota, S. Iwamoto, Y. Arakawa, A Nanowire-Based Plasmonic Quantum Dot Laser, *Nano Lett.* **2016**, 16(4), 2845-2850
- 114) D. Ren, L. Ahtapodov, J. S. Nilsen, J. Yang, A. Gustafsson, J. Huh, G. J. Conibeer, A. T. J. van Helvoort, B.-O. Fimland, H. Weman, Single-Mode Near-Infrared Lasing in a GaAsSb-Based Nanowire Superlattice at Room Temperature, *Nano Lett.*, **2018**, 18(4), 2304-2310
- 115) R. Chen, T.-T. D. Tran, K. Wei Ng, W. S. Ko, L. C. Chuang, F. G. Sedgwick, C. Chang-Hasnain, Nanolasers grown on silicon, *Nat. Photonics*, **2011**, 5, 170-175
- 116) Y. Zhang, H. Liu, Nanowires for high-efficiency, low-cost solar photovoltaics, *Crystals*, **2019**, 9(2), 87
- 117) M. J. Bierman, S. Jin, Potential applications of hierarchical branching nanowires in solar energy conversion, *Energy Environ. Sci.*, **2009**, 2, 1050-1059

- 118) Y. Zhang, A. M. Sanchez, M. Aagesen, S. Huo, H. A. Fonseka, J. A. Gott, D. Kim, X. Yu, X. Chen, J. Xu, T. Li, H. Zeng, G. Boras, H. Liu, Growth and Fabrication of High-Quality Single Nanowire Devices with Radial p-i-n Junctions, *Small*, **2019**, 15(3), 1803684
- 119) J. V. Holm, H. I. Jorgensen, P. Krogstrup, J. Nygard, H. Liu, M. Aagesen, Surface-passivated GaAsP single-nanowire solar cells exceeding 10% efficiency grown on silicon, *Nat. Commun.*, **2013**, 4, 1498
- 120) J. Huh, H. Yun, D.-C. Kim, A. M. Munshi, D. L. Dheeraj, H. Kauko, A. T. J. van Helvoort, S. Lee, B.-O. Fimland, H. Weman, Rectifying Single GaAsSb Nanowire Devices Based on Self-Induced Compositional Gradients, *Nano Lett.*, **2015**, 15(6), 3709-3715
- 121) M. D. Thompson, A. Alhodaib, A. P. Craig, A. Robson, A. Aziz, A. Krier, J. Svensson, L.-E. Wernersson, A. M. Sanchez, A. R. J. Marshall, Low Leakage-Current InAsSb Nanowire Photodetectors on Silicon, *Nano Lett.*, **2016**, 16(1), 182-187
- 122) J. J. Hou, F. Wang, N. Han, H. Zhu, K. Fok, W. Lam, S. Yip, T. Hung, J. E.-Y. Lee, J. C. Ho, Diameter dependence of electron mobility in InGaAs nanowires, *Appl. Phys. Lett.*, **2013**, 102, 093112
- 123) J. J. Hou, F. Wang, N. Han, F. Xiu, S. Yip, M. Fang, H. Lin, T. F. Hung, J. C. Ho, Stoichiometric Effect on Electrical, Optical and Structural Properties of Composition Tunable $\text{In}_x\text{Ga}_{1-x}\text{As}$ Nanowires, *ACS Nano*, **2012**, 6(10), 9320-9325
- 124) J. L. O' Brien, Optical Quantum Computing, *Science*, **2007**, 318, 5856, 1567-1570

- 125) P. Grünwald, Effective second-order correlation function and single-photon detection, *New J. Phys.*, **2019**, 21, 093003
- 126) M. Anderson, T. Müller, J. Skiba-Szymanska, A. B. Krysa, J. Huwer, R. M. Stevenson, J. Heffernan, D. A. Ritchie, A. J. Shields, Coherence in single photon emission from droplet epitaxy and Stranski-Krastanov quantum dots in the telecom C-band, *Appl. Phys. Lett.*, **2021**, 118, 014003
- 127) M. Arita, F. Le Roux, M. J. Holmes, S. Kako, Y. Arakawa, Ultraclean Single Photon Emission from a GaN Quantum Dot, *Nano Lett.*, 2017, 17(5), 2902-2907
- 128) S. Deshpande, T. Frost, A. Hazari, P. Bhattacharya, Electrically pumped single-photon emission at room temperature from a single InGaN/GaN quantum dot, *Appl. Phys. Lett.*, **2014**, 105, 141109
- 129) S. Kako, C. Santori, K. Hoshino, S. Götzinger, Y. Yamamoto, Y. Arakawa, A gallium nitride single-photon source operating at 200 K, *Nat. Mater.*, **2006**, 5, 887-892
- 130) B. Loitsch, J. Winnerl, G. Grimaldi, J. Wierzbowski, D. Rudolph, S. Morkötter, M. Döblinger, G. Abstreiter, G. Koblmüller, J. J. Finley, Crystal Phase Quantum Dots in the Ultrathin Core of GaAs-AlGaAs Core-Shell Nanowires, *Nano Lett.*, **2015**, 15(11), 7544-7551
- 131) L. Leandro, C. P. Gunnarsson, R. R. Reznik, K. D. Jons, I. V. Shtrom, A. I. Khrebtov, T. Kasama, V. Zwiller, G. E. Cirlin, N. Akopian, Nanowire Quantum Dots Tuned to Atomic Resonances, *Nano Lett.*, **2018**, 18(11), 7217-7221
- 132) M. Munsch, J. Claudon, J. Bleuse, N. S. Malik, E. Dupuy, J. M. Gerard, Y. Chen, N. Gregersen, J. Mork, Linearly Polarized Single-Mode Spontaneous Emission in a Photonic Nanowire, *Phys. Rev. Lett.* **2012**, 108, 077405

- 133) N. Dhindsa, S. S. Saini, Top-down fabricated tapered GaAs nanowires with sacrificial etching of the mask, *Nanotechnology* **2017**, 28(23), 235301
- 134) R. Lin, S. V. Galan, H. Sun, Y. Hu, M. S. Alias, B. Janjua, T. K. Ng, B. S. Ooi, X. Li, Tapering-induced enhancement of light extraction efficiency of nanowire deep ultraviolet LED by theoretical simulations, *Photonics Res.*, **2018**, 6(5), 457-462
- 135) N. Gregersen, T. R. Nielsen, J. Claudon, J.-M. Gerard, J. Mork, Controlling the emission profile of a nanowire with a conical taper, *Optics Lett.*, **2008**, 33(15), 1693-1695
- 136) J. Bleuse, J. Claudon, M. Creasey, N. S. Malik, J. M. Gerard, I. Maksymov, J. P. Hugonin, P. Lalanne, Inhibition enhancement and control of Spontaneous Emission in Photonic Nanowires, *Phys. Rev. Lett.* **2011**, 106, 103601
- 137) I. Yeo, P. L. de Assis, A. Gioppe, E. Dupont-Ferrier, P. Verlot, N. S. Malik, E. Dupuy, J. Claudon, J. M. Gerard, A. Auffieues, G. Nogues, S. Seidelin, J. P. Poizat, O. Arcizet, M. Richard, Strain mediated coupling in a quantum dot-mechanical oscillator hybrid system, *Nat. Nanotechnol.* **2014**, 9(2), 106-110
- 138) A. Bengoechea-Encabo, F. Barbagini, S. Fernandez-Garrido, J. Grandal, J. Ristic, M. A. Sanchez-Garcia, E. Calleja, U. Jahn, E. Luna, A. Trampert, Understanding the selective area growth of GaN nanocolumns by MBE using Tinanomasks, *Journal of Crystal Growth* **2011**, 325(1), 89-92
- 139) X. Ji, X. Yang, W. Du, H. Pan, T. Yang, Selective-Area MOCVD Growth and Carrier-Transport-Type Control of InAs(Sb)/GaSb Core-Shell Nanowires, *Nano Lett.* **2016**, 16(12), 7580-7587
- 140) P. Aseev, A. Fursina, F. Boekhout, F. Krizek, J. E. Sestoft, F. Borsoi, S. Heedt, G. Wang, L. Binci, S. Marti-Sanchez, T. Swoboda, R. Koops, E. Uccelli, J.

- Arbiol, P. Krogstrup, L. P. Kouwenhoven, P. Caroff, Selectivity Map for Molecular Beam Epitaxy of Advanced III-V Quantum Nanowire Networks, *Nano Lett.* **2019**, 19(1), 218-227
- 141) K. Tomioka, T. Tanaka, S. Hara, K. Hiruma, T. Fukui, III-V Nanowires on Si Substrate: Selective-Area Growth and Device Applications, *IEEE J. Sel. Top Quantum Electron* **2011**, 17(4), 1112
- 142) K. Yamano, K. Kishino, Selective area growth of InGa_N-based nanocolumn LED crystals on AlN/Si substrates useful for integrated μ -LED fabrication, *Appl. Phys. Lett.*, **2018**, 112, 091105
- 143) X. Liu, B. H. Le, S. Y. Woo, S. Zhao, A. Pofelski, G. A. Botton, Z. Mi, Selective area epitaxy of AlGa_N nanowire arrays across nearly the entire compositional range for deep ultraviolet photonics, *Optics Express* **2017**, 25(24), 30494-30502
- 144) H. Kim, W.-J. Lee, A. C. Farrell, A. Balgarkashi, D. L. Huffaker, Telecom-Wavelength Bottom-up Nanobeam Lasers on Silicon-on-Insulator, *Nano Lett.*, **2017**, 17(9), 5244-5250
- 145) H. Kim, A. C. Farrell, P. Senanayake, W.-J. Lee, D. L. Huffaker, Monolithically Integrated InGaAs Nanowires on 3D Structured Silicon-on-Insulator as a New Platform for Full Optical Links, *Nano Lett.*, **2016**, 16(3), 1833-1839
- 146) W.-J. Lee, H. Kim, J.-B. You, D. L. Huffaker, Ultracompact bottom-up photonic crystal lasers on silicon-on-insulator, *Sci. Rep.*, **2017**, 7, 9543
- 147) G. Otnes, M. Heurlin, X. Zeng, M. T. Borgstrom, In_xGa_{1-x}P Nanowire Growth Dynamics Strongly Affected by Doping Using Diethylzinc, *Nano Lett.*, **2017**, 17(2), 702-707

- 148) J. Treu, M. Speckbacher, K. Saller, S. Morkötter, M. Döblinger, X. Xu, H. Riedl, G. Abstreiter, J. J. Finley, G. Koblmüller, Widely tunable alloy composition and crystal structure in catalyst-free InGaAs nanowire arrays grown by selective area molecular beam epitaxy, *Appl. Phys. Lett.*, **2016**, 108, 053110
- 149) Y. Zhang, J. Wu, M. Aagesen, H. Liu, III-V nanowires and nanowire optoelectronic devices, *J. Phys. D.* **2015**, 48, 463001
- 150) K. Sarkar, M. Palit, P. Banerji, S. Chattopadhyay, N. N. Halder, P. Biswas, B. Nagabhusan, S. Chowdhury, Silver catalyzed growth of $\text{In}_x\text{Ga}_{1-x}\text{As}$ nanowires on Si(001) by metal-organic chemical vapor deposition, *CrystEngComm*, **2015**, 17, 8519-8528
- 151) J. Sun, M. Peng, Y. Zhang, L. Zhang, R. Peng, C. Miao, D. Liu, M. Han, R. Feng, Y. Ma, Y. Dai, L. He, C. Shan, A. Pan, W. Hu, Z. Yang, Ultrahigh Hole Mobility of Sn-Catalyzed GaSb Nanowires for High Speed Infrared Photodetectors, *Nano Lett.*, **2019**, 19(9), 5920-5929
- 152) A. C. Ford, J. C. Ho, Z. Fan, O. Ergen, V. Altoe, S. Aloni, H. Razavi, A. Javey, Synthesis, contact printing and device characterization of Ni-catalyzed, crystalline InAs nanowires, *Nano Res.*, **2008**, 1, 32-39
- 153) S. T. Boles, C. V. Thompson, E. A. Fitzgerald, Influence of indium and phosphine on Au-catalyzed InP nanowire growth on Si substrates, *J. Cryst. Growth*, **2009**, 311, 1446-1450
- 154) V. G. Dubrovskii, M. A. Timofeeva, A. Kelrich, D. Ritter, Growth and morphological modeling of InP nanowires obtained by Au-catalyzed selective area MOMBE, *J. Cryst. Growth*, **2015**, 413, 25-30

- 155) Z. H. Wu, X. Y. Mei, D. Kim, M. Blumin, H. E. Ruda, Growth of Au-catalyzed ordered GaAs nanowire arrays by molecular-beam epitaxy, *Appl. Phys. Lett.*, **2002**, 81, 5177
- 156) N. Jiang, J. Wong-Leung, H. J. Joyce, Q. Gao, H. H. Tan, C. Jagadish, Understanding the True Shape of Au-catalyzed GaAs Nanowires, *Nano Lett.*, **2014**, 14(10), 5865-5872
- 157) C. B. Maliakkal, D. Jacobsson, M. Tornberg, A. R. Persson, J. Johansson, R. Wallenberg, K. A. Dick, In situ analysis of catalyst composition during gold catalyzed GaAs nanowire growth, *Nat. Commun.*, **2019**, 10, 4577
- 158) U. P. Gomes, D. Ercolani, V. Zannier, F. Beltram, L. Sorba, Controlling the diameter distribution and density of InAs nanowires grown by Au-assisted methods, *Semicond. Sci. Technol.*, **2015**, 30, 115012
- 159) C. G. Nunez, A. F. Brana, N. Lopez, B. J. Garcia, A Novel Growth Method To Improve the Quality of GaAs Nanowires Grown by Ga-Assisted Chemical Beam Epitaxy, *Nano Lett.* **2018**, 18(6), 3608-3615
- 160) X. Yu, L. Li, H. Wang, J. Xiao, C. Shen, D. Pan, J. Zhao, Two-step fabrication of self-catalyzed Ga-based semiconductor nanowires on Si by molecular-beam epitaxy, *Nanoscale* **2016**, 8(20), 10615-10621
- 161) U. P. Gomes, D. Ercolani, V. Zannier, J. David, M. Gemmi, F. Beltram, L. Sorba, Nucleation and growth mechanism of self-catalyzed InAs nanowires on silicon, *Nanotechnology* **2016**, 27(25), 255601
- 162) B. Li, X. Yan, X. Zhang, X. Ren, Self-catalyzed Growth of InAs Nanowires on InP Substrate, *Nanoscale Research Letters* **2017**, 12:34

- 163) C. Colombo, D. Spirkoska, M. Frimmer, G. Abstreiter, A. Fontcuberta I Morral, Ga-assisted catalyst-free growth mechanism of GaAs nanowires by molecular beam epitaxy, *Phys. Rev. B* **2008**, 77, 155326
- 164) Y. Zhang, M. Aagesen, J. V. Holm, H. I. Jorgensen, J. Wu, H. Liu, Self-Catalyzed GaAsP Nanowires Grown on Silicon Substrates by Solid-Source Molecular Beam Epitaxy, *Nano Lett.*, **2013**, 13(8), 3897-3902
- 165) E. A. Anyebe, M. K. Rajpalke, T. D. Veal, C. J. Jin, Z. M. Wang, Q. D. Zhuang, Surfactant effect of antimony addition to the morphology of self-catalyzed InAs_{1-x}Sb_x nanowires, *Nano Res.*, **2015**, 8, 1309-1319
- 166) J. Tatebayashi, A. Lin, P. S. Wong, R. F. Hick, D. L. Huffaker, Visible light emission from self-catalyzed GaInP/GaP core-shell double heterostructure nanowires on silicon, *J. Appl. Phys.*, **2010**, 108, 034315
- 167) M. E. Reimer, G. Bulgarini, N. Akopian, M. Hocevar, M. B. Bavinck, M. A. Verheijen, E. P. A. M. Bakkers, L. P. Kouwenhoven, V. Zwiller, Bright single-photon sources in bottom-up tailored nanowires, *Nat. Communications* **2012**, 3, 737
- 168) D. Dalacu, K. Mnaymneh, J. Lapointe, X. Wu, P. J. Poole, G. Bulgarini, V. Zwiller, M. E. Reimer, Ultraclean emission from InAsP Quantum Dots in Defect-Free Wurtzite InP Nanowires, *Nano Lett.* **2012**, 12(11), 5919-5923
- 169) J. Tatebayashi, Y. Ota, S. Ishida, M. Nishioka, S. Iwamoto, Y. Arakawa, Site-controlled formation of InAs/GaAs quantum-dot-in-nanowires for single photon emitters, *Appl. Phys. Lett.* **2012**, 100, 263101
- 170) B. Ohlsson, M. Bjork, A. Persson, C. Thealander, L. Wallenberg, M. Magnusson, K. Deppert, L. Samuelson, Growth and characterization of GaAs

- and InAs nano-whiskers and InAs/GaAs heterostructures, Phys. E **2002**, 1386-947713 (2-4), 1126-1130
- 171) M. T. Bjork, B. J. Ohlsson, T. Sass, A. I. Persson, C. Thelander, M. H. Magnusson, K. Deppert, L. R. Wallenberg, L. Samuelson, One dimensional heterostructures in semiconductor nanowhiskers, Appl. Phys. Lett. **2002**, 80(6), 1058-1060
- 172) M. T. Borgstrom, V. Zwiller, E. Muller, A. Imamoglu, Optically Bright Quantum Dots in Single Nanowires, Nano Lett. **2005**, 5(7), 1439-1443
- 173) R. R. Reznik, I. V. Shtrom, Y. B. Samsonenko, A. I. Khrebtov, I. P. Soshnikov, G. E. Cirlin, The dependence of the wavelength on MBE growth parameters of GaAs quantum dot in AlGaAs NWs on Si (111) substrate, J. Phys.: Conf. Ser. **2017**, 929, 012047
- 174) A. I. Persson, M. T. Bjork, S. Jeppesen, J. B. Wagner, L. R. Wallenberg, L. Samuelson, InAs_{1-x}P_x Nanowires for Device Engineering, Nano Lett. **2006**, 6(3), 403-407
- 175) J. Trägårdh, A. I. Persson, J. B. Wagner, D. Hessman, L. Samuelson, Measurements of the band gap of wurtzite InAs_{1-x}P_x nanowires using photocurrent spectroscopy, J. Appl. Phys. **2007**, 101(12), 123701
- 176) J. H. van der Merwe, Misfit dislocations in epitaxy, Metall. Mater. Trans. A **2002**, 33(8), 2475
- 177) K. L. Kavanagh, Misfit dislocations in nanowire heterostructures, Semicond. Sci. Technol. **2010**, 25, 024006
- 178) N. Li, T. Y. Tam. U. Gosele, Transition region width of nanowire hetero- and pn-junctions grown using vapor-liquid-solid processes, Appl. Phys. A. **2008**, 0947-839690(4), 591-596

- 179) K. A. Dick, J. Bolinsson, B. M. Borg, J. Johansson, Controlling the Abruptness of Axial Heterojunctions in III-V Nanowires: Beyond the Reservoir Effect, Nano Lett. **2012**, 12(6), 3200-3206
- 180) M. de la Mata, C. Magen, P. Caroff, J. Arbiol, Atomic Scale Strain Relaxation in Axial Semiconductor III-V Nanowire Heterostructures, Nano Lett. **2014**, 14(11), 6614-6620
- 181) C. Himwas, S. Collin, P. Rale, N. Chauvin, G. Patriarche, F. Oehler, F. H. Julien, L. Travers, J. C. Harmand, M. Tchernycheva, In situ passivation of GaAsP nanowires, Nanotechnology **2017**, 28, 495707
- 182) M. J. Tambe, S. K. Lim, M. J. Smith, L. F. Allard, S. Gradecak, Realization of defect-free epitaxial core/shell GaAs/AlGaAs nanowire heterostructures, Appl. Phys. Lett. **2008**, 93, 151917
- 183) J. Grönqvist, N. Søndergaard, F. Boxberg, T. Guhr, S. Åberg, H. Q. Xu, Strain in semiconductor core-shell nanowires, J. Appl. Phys. **2009**, 106, 053508
- 184) D. Ferrand, J. Cibert, Strain in crystalline core-shell nanowires, Eur. Phys. J.: Appl. Phys. **2014**, 67(3), 30403
- 185) L. Gagliano, M. Albani, M. A. Verheijen, E. P. A. M. Bakkers, L. Miglio, Twofold origin of strain-induced bending in core-shell nanowires: the GaP/InGaP case, Nanotechnology **2018**, 29, 315703
- 186) R. B. Lewis, P. Corfdir, H. Küpers, T. Flissikowski, O. Brandt, L. Geelhaar, Nanowires Bending over Backward from Strain Partitioning in Asymmetric Core-Shell Heterostructures, Nano Lett. **2018**, 18(4), 2343-2350
- 187) K. L. Kavanagh, I. Saveliev, M. Blumin, G. Swadener, H. E. Ruda, Faster radial strain relaxation in InAs-GaAs core-shell heterowires. Appl. Phys. Lett. **2012**, 111, 044301

- 188) J. Y. Lao, J. G. Wen, Z. F. Ren, Hierarchical ZnO Nanostructures, *Nano Lett.* **2002**, 2(11), 1287-1291
- 189) S. R. Das, C. Akatay, A. Mohammad, M. R. Khan, K. Maeda, R. S. Deacon, K. Ishibashi, Y. P. Chen, T. D. Sands, M. A. Alam, D. B. Janes, Electrodeposition of InSb branched nanowires: Controlled growth with structurally tailored properties, *J. Appl. Phys.* **2014**, 116, 083506
- 190) K. A. Dick, K. Deppert, T. Mårtensson, W. Seifert, L. Samuelson, Growth of GaP nanotree structures by sequential seeding of 1D nanowires, *J. Cryst. Growth* **2004**, 272, 131-137
- 191) G. Zha, M. Li, Y. Yu, L. Wang, J. Xu, X. Shang, H. Ni, Z. Niu, Strain-driven synthesis of self-catalyzed branched GaAs nanowires, *Appl. Phys. Lett.* **2013**, 102(16), 163115
- 192) M. Tornberg, K. A. Dick, S. Lehmann, Branched InAs nanowire growth by droplet confinement, *Appl. Phys. Lett.* **2018**, 113, 123104
- 193) C. Cheng, H. J. Fan, Branched nanowires: Synthesis and energy applications, *Nano Today* **2012**, 7, 327-343
- 194) S. Kim, S. Park, H. Ko, B. Y. Jeong, C. Lee, Enhanced near-UV emission from self-catalytic brush-like GaN nanowires, *Matter. Lett.* **2014**, 116, 314-317
- 195) X. Liu, Y. Lin, S. Zhou, S. Sheehan, D. Wang, Complex Nanostructures: Synthesis and Energetic Applications, *Energies*, **2010**, 3(3), 285-300
- 196) L. Tsakalakos, J. Balch, J. Fronheiser, B. A. Korevaar, O. Sulima, J. Rand, Silicon nanowire solar cells, *Appl. Phys. Lett.*, **2007**, 91, 233117
- 197) T. Haggren, V. Khayrudinov, V. Dhaka, H. Jiang, A. Shah, M. Kim, H. Lipsanen, III-V nanowires on black silicon and low-temperature growth of self-catalyzed rectangular InAs NWs, *Sci. Rep.*, **2018**, 8, 6410

- 198) M. Dahl, L. Namazi, R. R. Zamani, K. A. Dick, Sb Incorporation in Wurtzite and Zinc Blende $\text{InAs}_{1-x}\text{Sb}_x$ Branches on InAs Template Nanowires, *Small* **2018**, 14, 1703785
- 199) Y. Yu, M. Fi, J. F. He, Y. M. He, Y. J. Wei, Y. He, G. W. Zha, X. J. Shang, J. Wang, L. J. Wang, G. W. Wang, H. Q. Ni, C. Y. Lu, Z. C. Niu, Single InAs Quantum Dot Grown at the Junction of Branched Gold-Free GaAs Nanowire, *Nano Lett.* **2013**, 13(4), 1399-1404
- 200) D. Pan, J.-Y. Wang, W. Zhang, L. Zhu, X. Su, F. Fan, Y. Fu, S. Huang, D. Wei, L. Zhang, M. Sui, A. Yartsev, H. Xu, J. Zhao, Dimension Engineering of High-Quality InAs Nanostructures on a Wafer Scale, *Nano Lett.* **2019**, 19(3), 1632-1642
- 201) T.-W. Kim, Y. Gao, O. Acton, H.-L. Yip, H. Ma, H. Chen, A. K.-Y. Jen, Graphene oxide nanosheets based organic field effect transistors for nonvolatile memory applications, *Appl. Phys. Lett.* **2010**, 97, 023310
- 202) L. Liang, K. Li, C. Xiao, S. Fan, J. Liu, W. Zhang, W. Xu, W. Tong, J. Liao, Y. Zhou, B. Ye, Y. Xie, Vacancy Associates-Rich Ultrathin Nanosheets for High Performance and Flexible Nonvolatile Memory Device, *J. Am. Chem. Soc.* **2015**, 137(8), 3102-3108
- 203) S. Arab, C.-Y. Chi, T. Shi, Y. Wang, D. P. Dapkus, H. E. Jackson, L. M. Smith, S. B. Cronin, Effects of Surface Passivation on Twin-Free GaAs Nanosheets, *ACS Nano* **2015**, 9(2), 1336-1340
- 204) C.-Y. Chi, C.-C. Chang, S. Hu, T.-W. Yeh, S. B. Cronin, P. D. Dapkus, Twin-Free GaAs Nanosheets by Selective Area Growth: Implications for Defect-Free Nanostructures, *Nano Lett.* **2013**, 13(6), 2506-2515

- 205) S. Arab, P. D. Anderson, C.-Y. Chi, P. D. Dapkus, M. L. Povinelli, S. B. Cronin, Observation of Asymmetric Nanoscale Optical Cavity in GaAs Nanosheets, *ACS Photonics* **2015**, 2(8), 1124-1128
- 206) D. Pan, D. X. Fan, N. Kang, J. H. Zhi, X. Z. Yu, H. Q. Xu, J. H. Zhao, Free-Standing Two-Dimensional Single-Crystalline InSb Nanosheets, *Nano Lett.* **2016**, 16(2), 834-841
- 207) S. Tong, D. Pan, X. Wang, Z. Yu, Y. Xu, D. Wei, Unsaturated linear magnetoresistance effect in high-quality free-standing InSb single-crystal nanosheets, *J. Phys. D: Appl. Phys.* **2020**, 53, 18LT04
- 208) Q. Sun, H. Gao, X. Zhang, X. Yao, S. Xu, K. Zheng, P. Chen, W. Lu, J. Zou, High-quality epitaxial wurtzite structured InAs nanosheets grown in MBE, *Nanoscale* **2020**
- 209) Q. Sun, H. Gao, X. Yao, K. Zheng, P. Chen, W. Lu, J. Zou, Au-catalysed free-standing wurtzite structured InAs nanosheets grown by molecular beam epitaxy, *Nano Res.* **2019**, 12, 2718-2722
- 210) Y. T. Lee, J. Lee, J. Hyunsu, J. A. Lim, Y. Yi, W. K. Choi, D. K. Hwang, S. Im, Nonvolatile Charge Injection Memory Based on Black Phosphorous 2D Nanosheets for Charge Trapping and Active Channel Layers, *Adv. Funct. Mater.* **2016**, 26(31), 5701-5707
- 211) G. Ding, K. Zeng, K. Zhou, Z. Li, Y. Zhou, Y. Zhai, L. Zhou, X. Chen, S.-T. Han, Configurable multi-state non-volatile memory behaviors in Ti_3C_2 nanosheets, *Nanoscale* **2019**, 11, 7102-7110
- 212) F. Panciera, Z. Baraissov, G. Patriarche, V. G. Dubrovskii, L. Travers, U. Mirsaidov, J.-C. Harmand, Phase Selection in Self-Catalyzed GaAs Nanowires, *Nano Lett.*, **2020**, 20(3), 1669-1675

- 213) F. Matteini, V. G. Dubrovskii, D. Ruffer, G. Tütüncüoğlu, Y. Fontana, A. Fontcuberta i Morral, Tailoring the diameter and density of self-catalyzed GaAs nanowires on silicon, *Nanotechnology*, **2015**, 26(10), 105603
- 214) E. Uccelli, J. Arbiol, C. Magen, P. Krogstrup, E. Russo-Averchi, M. Heiss, G. Mugny, F. Morier-Genoud, J. Nygard, J. R. Morante, A. Fontcuberta i Morral, Three-Dimensional Multiple-Order Twinning of self-catalyzed GaAs Nanowires on Si Substrates, *Nano Lett.*, **2011**, 11(9), 3827-3832
- 215) V. G. Dubrovskii, W. Kim, V. Piazza, L. Güniat, A. Fontcuberta i Morral, Simultaneous Selective Area Growth of Wurtzite and Zincblende Self-Catalyzed GaAs Nanowires on Silicon, *Nano Lett.*, **2021**, 21(7), 3139-3145
- 216) Y. Kang, H. Li, J. Tang, H. Jia, X. Hou, X. Li, X. Chu, K. Li, F. Lin, X. Wang, Z. Wei, Structural and optical properties of Be-doped high-quality self-catalyzed GaAs nanowires, *Optics Mater. Express*, 2021, 11(8), 2422-2431
- 217) H. S. Im, C. Su Jung, K. Park, D. Myung Jang, Y. Rok Lim, J. Park, Band Gap Tuning of Twinned GaAsP Ternary Nanowires, *J. Phys. Chem. C*, **2014**, 118(8), 4546-4552
- 218) Y. Zhang, M. Aage, J. V. Holm, J. I. Jorgensen, J. Wu, H. Liu, Self-Catalyzed GaAsP Nanowires Grown on Silicon Substrates via Solid-Source Molecular Beam Epitaxy, *Nano Lett.*, **2013**, 13(8), 3897-3902
- 219) Z. H. Wu, M. Sun, X. Y. Mei, H. E. Ruda, Growth and Photoluminescence Characteristics of AlGaAs Nanowires, *Appl. Phys. Lett.* **2004**, 85(4), 657-659
- 220) C. Chen, S. Shehata, C. Fradin, R. LaPierre, C. Couteau, G. Weihs, Self-Directed Growth of AlGaAs Core-Shell Nanowires for Visible Light Applications, *Nano Lett.* **2007**, 7(9), 2584-2589

- 221) S. K. Lim, M. J. Tambe, M. M. Brewster, S. Gradečak, Controlled Growth of Ternary Alloy Nanowires Using Metalorganic Chemical Vapor Deposition, *Nano Lett.* **2008**, 8(5), 1386
- 222) A. Li, D. Ercolani, L. Lugani, L. Nasi, F. Rossi, G. Salviati, F. Beltram, L. Sorba, Synthesis of AlAs and AlAs-GaAs Core-Shell Nanowires, *Cryst. Growth & Des.* **2011**, 11(9), 4053-4058
- 223) V. G. Dubrovskii, I. V. Shtrom, R. R. Reznik, Y. B. Samsonenko, A. I. Khrebtov, I. P. Soshnikov, S. Rouvimov, N. Akopian, T. Kasama, G. E. Cirlin, Origin of Spontaneous Core-Shell AlGaAs Nanowires Grown by Molecular Beam Epitaxy, *Cryst. Growth & Des.* **2016**, 16(12), 7251-7255
- 224) L. V. Titova, T. B. Hoang, H. E. Jackson, L. M. Smith, J. M. Yarrison-Rice, Y. Kim, H. J. Joyce, H. H. Tan, C. Jagadish, Temperature dependence of photoluminescence from single core-shell GaAs-AlGaAs nanowires, *Appl. Phys. Lett.* **2006**, 89, 173126
- 225) T. B. Hoang, L. V. Titova, J. M. Yarrison-Rice, H. E. Jackson, A. O. Govorov, Y. Kim, H. J. Joyce, H. H. Tan, C. Jagadish, L. M. Smith, Resonant Excitation and Imaging of Non-equilibrium Exciton Spins in Single Core-Shell GaAs-AlGaAs Nanowires, *Nano Lett.* **2007**, 7(3), 588-595
- 226) P. Krogstrup, S. Curiotto, E. Johnson, M. Aagesen, J. Nygård, D. Chatain, Impact of Liquid Phase Shape on the Structure of III-V Nanowires, *Phys. Rev. Lett.* **2011**, 106, 125505
- 227) Y. Zhang, A. V. Velichko, H. A. Fonseka, P. Parkinson, J. A. Gott, G. Davis, M. Aagesen, A. M. Sanchez, D. Mowbray, H. Liu, Defect-Free Axially Stacked GaAs/GaAsP Nanowire Quantum Dots with Strong Carrier Confinement, *Nano Lett.*, **2021**, 21(13), 5722-5729

- 228) G. E. Cirlin, R. R. Reznik, I. V. Shtrom, A. I. Khrebtov, I. P. Soshnikov, S. A. Kukushkin, L. Leandro, T. Kasama, N. Akopian, AlGaAs and AlGaAs/GaAs/AlGaAs nanowires grown by molecular beam epitaxy on silicon substrates, *J. Phys. D: Appl. Phys.*, **2017**, 50, 484003
- 229) Y. Zhang, H. A. Fonseka, M. Agesen, J. A. Gott, A. M. Sanchez, J. Wu, D. Kim, P. Jurczak, S. Huo, H. Liu, Growth of Pure Zinc-Blende GaAs(P) Core-Shell Nanowires with Highly Regular Morphology, *Nano Lett.* **2013**, 13(8), 3897-3902
- 230) O. D. D. Couto Jr, D. Sercombe, J. Puebla, L. Otubo, I. J. Luxmoore, M. Sich, T. J. Elliott, E. A. Checkhovich, L. R. Wilson, M. S. Skolnick, H. Y. Liu, A. I. Tartakovskii, Effect of a GaAsP Shell on the Optical Properties of Self-Catalyzed GaAs Nanowires Grown on Silicon, *Nano Lett.* **2012**, 12(10), 5269-5274
- 231) P. Jurczak, Y. Zhang, J. Wu, A. M. Sanchez, M. Agesen, H. Liu, Ten-Fold Enhancement of InAs Nanowire Photoluminescence Emission with an InP Passivation Layer, *Nano Lett.* **2017**, 17(6), 3629-3633
- 232) T. Dursap, M. Vettori, C. Botella, P. Regreny, N. Blanchard, M. Gendry, N. Chauvin, M. Bugnet, A. Danescu, J. Penuelas, Wurtzite phase control for self-assisted GaAs nanowires grown by molecular beam epitaxy, *Nanotechnology*, **2021**, 32, 155602
- 233) M. De Luca, S. Rubini, M. Felici, A. Meaney, P. C. M. Christianen, F. Martelli, A. Polimeni, Addressing the Fundamental Electronic Properties of Wurtzite GaAs Nanowires by High-Field Magneto-Photoluminescence Spectroscopy, *Nano Lett.*, **2017**, 17(11), 6540-6547
- 234) G. E. Cirlin, R. R. Reznik, I. V. Shtrom, A. I. Khrebtov, Y. B. Samsonenko, S.

- A. Kukushkin, T. Kasama, N. Akopian, L. Leandro, Hybrid GaAs/AlGaAs Nanowire-Quantum dot System for Single Photon Sources, *Semiconductors*, **2018**, 52(4), 462-464
- 235) G. Boras, X. Yu, H. A. Fonseka, G. Davis, A. V. Velichko, J. A. Gott, H. Zeng, S. Wu, P. Parkinson, X. Xu, D. Mowbray A. M. Sanchez, H. Liu, Self-Catalyzed AlGaAs Nanowires and AlGaAs/GaAs Quantum Dots on Si Substrates, *J. Phys. Chem. C*, 2021, 125(26), 14338-14347
- 236)** R. R. Reznik, K. M. Morozov, I. L. Krestnikov, K. P. Kotlyar, I. P. Soshnikov, L. Leandro, N. Akopian, G. E. Cirlin, Directional Radiation from GaAs quantum dots in AlGaAs nanowires, *Tech. Phys. Lett.*, **2021**
- 237) M. B. Rota, A. S. Ameruddin, H. A. Fonseka, Q. Gao, F. Mura, A. Polimeni, A. Miriametro, H. H. Tan, C. Jagadish, M. Capizzi, Bandgap Energy of Wurtzite InAs Nanowires, *Nano Lett.* **2016**, 16(8), 5197-5203
- 238) J. R. Arthur, Molecular Beam Epitaxy, *Surface Science* **2002**, 500(1-3), 189-217
- 239) Y. Zhang, Thesis: “Developing Self-Catalyzed GaAsP Nanowires on Silicon Substrates for High-Efficient Solar Cells”, Experimental Growth Section
- 240) H. Xing, D. S. Green, H. Yu, T. Mates, P. Kozodoy, S. Keller, S. P. Den Baars, U. K. Mishra, Memory Effect and Redistribution of Mg into Sequentially Regrown GaN Layer by Metalorganic Chemical Vapor Deposition, *Jpn. J. Appl. Phys.* **2003**, 42(1), 50-53
- 241) M. Mittal, S. Sardar, A. Jana, *Handbook of Nanomaterials for Sensing Applications*, Chapter 7, Elsevier Inc., **2021**

- 242) S. G. Ghalamestani, M. Ek, M. Ghasemi, P. Caroff, J. Johansson, K. A. Dick, Morphology and composition controlled $\text{Ga}_x\text{In}_{1-x}\text{Sb}$ nanowires: understanding ternary antimonide growth, *Nanoscale* **2014**, 6, 1086-1092
- 243) P. Gutowski, I. Sankowska, T. Slupinski, D. Pierscinska, K. Pierscinski, A. Kuzmich, K. Golaszewska-Malec, M. Bugajski, Optimization of MBE Growth Conditions of $\text{In}_{0.52}\text{Al}_{0.48}\text{As}$ Waveguide Layers for InGaAs/InAlAs/InP Quantum Cascade Lasers, *Materials*, **2019**, 12, 1621
- 244) D. Scarpellini, A. Fedorov, C. Somaschini, C. Frigeri, M. Bollani, S. Bietti, R. Nöetzel, S. Sanguinetti, Ga crystallization dynamics during annealing of self-assisted GaAs nanowires, *Nanotechnology*, **2017**, 28, 045605
- 245) D. Rudolph, S. Hertenberger, S. Bolte, W. Paosangthong, D. Spirkoska, M. Döblinger, M. Bichler, J. J. Finley, G. Abstreiter, G. Koblmüller, Direct Observation of a Noncatalytic Growth Regime for GaAs Nanowires, *Nano Lett.*, **2011**, 11, 3848–3854
- 246) S. Bonnamy, A. Oberlin, *Materials Science and Engineering of Carbon: Characterization*, Chapter 4, **2016**, Elsevier Inc
- 247) H. Detz, M. Kriz, D. MacFarland, S. Lancaster, T. Zederbauer, M. Capriotti, A. M. Andrews, W. Schrenk, G. Strasser, Nucleation of Ga droplets on Si and SiO_x surfaces, *Nanotechnology* **2015**, 26, 315601
- 248) C. Zhou, X. T. Zhang, K. Zheng, P. P. Chen, W. Lu, J. Zou, Self-Assembly Growth of In-Rich InGaAs Core-Shell Structured Nanowires with Remarkable Near-Infrared Photoresponsivity, *Nano Lett.* **2017**, 17(12), 7824-7830
- 249) Y. Liao, *Practical Electron Microscopy and Database*, **2006**, www.globalsino.com/EM/

- 250) B. Loitsch, N. Jeon, M. Döblinger, J. Winnerl, E. Parzinger, S. Matich, U. Wurstbauer, H. Riedl, G. Abstreiter, J. J. Finley, L. J. Lauhon, G. Koblmüller, Suppression of alloy fluctuations in GaAs-AlGaAs core-shell nanowires, Appl. Phys. Lett. **2016**, 109, 093105
- 251) A. Berg, F. Lenrick, N. Vainorius, J. P. Beech, L. R. Wallenberg, M. T. Borgstrom, Growth parameter design for homogeneous material composition in ternary $Ga_{1-x}In_xP$ nanowires, Nanotechnology **2015**, 26, 435601
- 252) L. Leandro, R. Reznik, J. D. Clement, J. Repan, M. Reynolds, E. V. Ubyivovk, I. V. Shtrom, G. Cirlin, N. Akopian, Wurtzite AlGaAs Nanowires, Sci. Rep. **2020**, 10, 735
- 253) P. Corfdir, B. Van Hattem, E. Uccelli, A. Fontcuberta i Morral, R. T. Phillips, Charge carrier generation, relaxation and recombination in polytypic GaAs nanowires studied by photoluminescence excitation spectroscopy, Appl. Phys. Lett. **2013**, 103, 133109
- 254) S. Arab, M. Yao, C. Zhou, P. D. Dapkus, S. B. Cronin, Doping concentration dependence of the photoluminescence spectra of n-type GaAs nanowires, Appl. Phys. Lett. **2016**, 108, 182106
- 255) J. Valente, T. Godde, Y. Zhang, D. J. Mowbray, H. Liu, Light-Emitting GaAs Nanowires on a Flexible Substrate, Nano Lett. **2018**, 18(7), 4206-4213
- 256) O. Demichel, M. Heiss, J. Bleuse, H. Mariette, A. Fontcuberta i Morral, Impact of surfaces on the optical properties of GaAs nanowires, Appl. Phys. Lett. **2010**, 97, 201907
- 257) L. Francaviglia, G. Tütüncüoglu, F. Matteini, A. Fontcuberta i Morral, Tuning adatom mobility and nanoscale segregation by twin formation and polytypism, Nanotechnology **2009**, 30, 054006

- 258) T. Matsuda, K. Takada, K. Yano, R. Tsutsumi, K. Yoshikawa, S. Shimomura, Y. Shimizu, K. Nagashima, T. Yanagida, F. Ishikawa, Controlling Bi Provoked Nanostructure Formation in GaAs/GaAsBi Core-Shell Nanowires, Nano Lett. **2009**, 19(12), 8510-8518
- 259) C. Yan, X. Li, K. Zhou, A. Pan, P. Werner, S. L. Mensah, A. T. Vogel, V. Schmidt, Heteroepitaxial Growth of GaSb Nanotrees with an Ultra-Low Reflectivity in a Broad Spectral Range, Nano Lett. **2012**, 12(4), 1799-1805
- 260) D. Spirkoska, G. Abstreiter, A. Fontuberta i Morral, GaAs nanowires and related prismatic heterostructures, Semicond. Sci. Technol. **2009**, 24(11), 113001
- 261) J. Lähnemann, M. O. Hill, J. Herranz, O. Marquardt, G. Gao, A. Al Hassan, A. Davtyan, S. O. Hruszkewycz, M. V. Holt, C. Huang, I. Calvo-Almazan, U. Jahn, U. Pietsch, L. J. Lauhon, L. Geelhaar, Correlated Nanoscale Analysis of the Emission from Wurtzite versus Zincblende (In,Ga)As/GaAs Nanowire Core-Shell Quantum Wells, Nano Lett. **2019**, 19(7), 4448-4457
- 262) D. J. Chadi, Atomic and electronic structures of (111), (211) and (311) surfaces of GaAs, J. Vac. Sci. Technol. B: Microelectron. Process. Phenom. **1985**, 3, 1167
- 263) J. Guo, H. Hang, Y. Ding, Z. Ji, M. Liu, X. Ren, X. Zhang, Y. Huang, Growth of zinc blende GaAs/AlGaAs heterostructure nanowires on Si substrate by using AlGaAs buffer layers, J. Cryst. Growth **2012**, 359, 30-34
- 264) Y. Zhang, A. M. Sanchez, J. Wu, M. Aagesen, J. V. Holm, R. Beanland, T. Ward, H. Liu, Polarity-Driven Quasi-3-Fold Composition Symmetry of Self-Catalyzed III-V-V Ternary Core-Shell Nanowires, Nano Lett. **2015**, 15(5), 3128-3133

- 265) C. Zheng, J. Wong-Leung, Q. Gao, H. H. Tan, C. Jagadish, J. Etheridge, Polarity-Driven 3-Fold Symmetry of GaAs/AlGaAs Core Multishell Nanowires, Nano Lett. **2013**, 13(8), 3742-3748
- 266) S. Adachi, GaAs and Related Materials: Bulk Semiconducting and Superlattice Properties, World Scientific **1994**
- 267) N. Erhard, S. Zenger, S. Morkötter, D. Rudoph, M. Weiss, H. J. Krenner, H. Karl, G. Abstreiter, J. J. Finley, G. Koblmüller, A. W. Holleitner, Ultrafast Photodetection in the Quantum Wells of Single AlGaAs/GaAs-Based Nanowires, Nano Lett. **2015**, 15(10), 6869-6874
- 268) A. Graf, D. Sonnenberg, V. Paulava, A. Schliwa, C. Heyn, W. Hansen, Excitonic states in GaAs quantum dots fabricated by local droplet etching, Phys. Rev. B **2014**, 89, 115314
- 269) D. Gammon, E. S. Snow, B. V. Shanabrook, D. S. Katzer, D. Park, Homogeneous Linewidths in the Optical Spectrum of a Single Gallium Arsenide Quantum Dot, Science **1996**, 273, 87-90
- 270) T. Huber, A. Predojevic, M. Khoshnegar, D. Dalacu, P. J. Poole, H. Majedi, G. Weihs, Polarization Entangled Photons from Quantum Dots Embedded in Nanowires, Nano Lett. **2014**, 14(12), 7107-7114
- 271) A. Trellakis, T. Zibold, T. Andlauer, S. Birner, R. K. Smith, R. Morschl, P. Vogl, The 3D nanometer device project nextnano: Concepts, methods, results, J. Comput. Electron., **2006**, 5, 285-289
- 272) S. Birner, S. Hackenbuchner, M. Sabathil, G. Zandler, J. A. Majewski, T. Andlauer, T. Zibold, R. Morschl, A. Trellakis, P. Vogl, Modeling of Semiconductor Nanostructures with nextnano, Acta Phys. Polonica A, **2006**, 110(2)

- 273) A. S. Baimuratov, I. D. Rukhlenko, R. E. Noskov, P. Ginzburg, Y. K. Gun'ko, A. V. Baranov, A. V. Fedorov, Giant Optical Activity of Quantum Dots, Rods and Disks with Screw Dislocations, *Sci. Rep.*, **2015**, 5, 14712
- 274) V. N. Kats, V. P. Kocheresko, A. V. Platonov, T. V. Chizhova, G. E. Cirlin, A. D. Bouravleuv, Y. B. Samsonenko, I. P. Soshnikov, E. V. Ubyivovk, J. Bleuse, Optical study of GaAs quantum dots embedded into AlGaAs nanowires. *Semicond. Sci. Technol.*, **2012**, 27, 015009
- 275) V. P. Kochereshko, V. N. Kats, A. V. Platonov, G. E. Cirlin, A. D. Bouravleuv, Y. B. Samsonenko, L. Besombes, H. Mariette, GaAs single quantum dot embedded into AlGaAs nanowire, *AIP Conference Proceedings*, **2013**, 1566, 482
- 276) A. V. Platonov, V. P. Kochereshko, V. N. Kats, G. E. Cirlin, A. D. Buravleuv, Y. B. Samsonenko, L. Besombes, H. Mariette, Optical properties of individual GaAs quantum dots embedded into AlGaAs nanowires, *J. Synch. Investig.*, **2013**, 7, 622-625
- 277) L. Leandro, J. Hastrup, R. Reznik, G. Cirlin, N. Akopian, Resonant excitation of nanowire quantum dots, *npj Quantum Information*, **2020**, 6, 93
- 278) H. A. Fonseka, A. V. Velichko, Y. Zhang, J. A. Gott, G. D. Davis, R. Beanland, H. Liu, D. J. Mowbray, A. M. Sanchez, Self-Formed Quantum Wires and Dots in GaAsP-GaAsP Core-Shell Nanowires, *Nano Lett.* **2019**, 19(6), 4158-4165
- 279) X. Y. Gong, T. Yamaguchi, H. Kan, T. Makino, K. Ohshimo, M. Aoyama, M. Kumagawa, N. L. Rowell, R. Rinfret, R. Sulphur passivation of InAs(Sb), *Appl. Surf. Sci.* **1997**, 113-114, 388-392
- 280) C. Zhao, T. K. Ng, A. Prabaswara, M. Conroy, S. Jahangir, T. Frost, J. O'Connell, J. D. Holmes, P. J. Parbrook, P. Bhattacharya, B. S. Ooi, An

- enhanced surface passivation effect in InGaN/GaN disk-in-nanowire light emitting diodes for mitigating Shockley-Read-Hall recombination, *Nanoscale* **2015**, 7, 16658-16665
- 281) B. Li, S. Li, Y. Sun, S. Li, G. Chen, X. Wang, Enhanced luminescence properties of InAs nanowires via organic and inorganic sulfide passivation, *Nanotechnology* **2019**, 30, 445704
- 282) G. W. Holloway, C. M. Haapamaki, P. Kuyanov, R. R. LaPierre, J. Baugh, Electrical characterization of chemical and dielectric passivation of InAs nanowires, *Semicond. Sci. Technol.* **2016**, 31, 114004
- 283) M. H. Sun, H. J. Joyce, Q. Gao, H. H. Tan, C. Jagadish, C. Z. Ning, Removal of surface states and recovery of band-edge emission in InAs nanowires through surface passivation, *Nano Lett.* **2012**, 12(7), 3378-3384
- 284) . Treu, M. Bormann, H. Schmeiduch, M. Döblinger, S. Morkötter, S. Matich, P. Wiecha, K. Saller, B. Mayer, M. Bichler, M. C. Amann, Enhanced Luminescence Properties of InAs-InAsP Core-Shell Nanowires, *Nano Lett.* **2013**, 13(12), 6070-6077
- 285) Y. Kanai, R. S. Deacon, S. Takahashi, A. Oiwa, K. Yoshida, K. Shibata, K. Hirakawa, Y. Tokura, S. Tarucha, Electrically tuned spin-orbit interaction in an InAs self-assembled quantum dot, *Nature Nanotechnology* **2011**, 6, 511-516
- 286) D. Kim, S. G. Carter, A. Greilich, A. S. Bracker, D. Gammon, Ultrafast optical control of entanglement between two quantum-dot spins, *Nature Physics* **2011**, 7, 223-229
- 287) K. De Greve, L. Yu, P. L. McMahon, J. S. Pelc, C. M. Natarajan, N. Y. Kim, E. Abe, S. Maier, C. Schneider, M. Kamp, S. Höfling, R. H. Hadfield, A. Forchel, M. M. Fejer, Y. Yamamoto, Quantum-dot spin-photon entanglement via

- frequency downconversion to telecom wavelength, *Nature* **2012**, 491, 421-425
- 288) A. C. Ford, J. C. Ho, Y.-L. Chueh, Y.-C. Fan, J. Guo, J. Bokor, A. Javey, Diameter-Dependent Electron Mobility of InAs Nanowires, *Nano Lett.* **2009**, 9(1), 360-365
- 289) K. A. Dick, C. Thelander, L. Samuelson, P. Caroff, Crystal Phase Engineering in Single InAs Nanowires, *Nano Lett.* **2010**, 10(9), 3494-3499
- 290) S. Nadj-Perge, S. M. Frolov, E. P. A. M. Bakkers, L. P. Kouwenhoven, Spin-orbit qubit in semiconductor nanowire, *Nature* **2010**, 468, 1084-1087
- 291) C. Thelander, H. A. Nilsson, L. E. Jensen, L. Samuelson, Nanowire Single-Electron Memory, *Nano Lett.* **2005**, 5(4), 635-638
- 292) Y. Yang, X. Peng, H.-S. Kim, T. Kim, S. Jeon, H. K. Kang, W. Choi, J. Song, Y.-J. Doh, D. Yu, Hot Carrier Trapping Induced Negative Photoconductance in InAs Nanowires toward Novel Nonvolatile Memory, *Nano Lett.* **2015**, 15(9), 5875-5882
- 293) X. Zhang, Z. Li, X. Yao, H. Huang, D. Wei, C. Zhou, Z. Tang, X. Yuan, P. Chen, W. Hu, J. Zou, W. Lu, L. Fu, Light-Induced Positive and Negative Photoconductances of InAs Nanowires toward Rewritable Nonvolatile Memory, *ACS Appl. Electron. Mater.* **2019**, 1(9), 1825-1831
- 294) D. Lynall, S. V. Nair, D. Gutstein, A. Shik, I. G. Savelyev, M. Blumin, H. E. Ruda, Surface State Dynamics Transport in InAs Nanowires, *Nano Lett.* **2018**, 18(2), 1387-1395
- 295) M. H. Sun, E. S. P. Leong, A. H. Chin, C. Z. Ning, G. E. Cirlin, Y. B. Samsonenko, V. G. Dubrovskii, L. Chuang, C. Chang-Hasnain, Photoluminescence Properties of InAs Nanowires Grown on GaAs and Si Substrates, *Nanotechnology* **2010**, 21, 335705

- 296) Y. Lacroix, C. A. Tran, S. P. Watkins, M. L. W. Thewalt, Low-temperature photoluminescence of epitaxial InAs, J. Appl. Phys. **1996**, 80, 6416
- 297) S. Ichikawa, N. Sanada, N. Utsumi, Y. Fukuda, Surface structures and electronic states of clean and (NH₄)₂S_x-treated InAs(111)A and (111)B, J. Appl. Phys. **1998**, 84, 3658
- 298) L. O. Olsson, C. B. M. Andersson, M. C. Hakansson, J. Kanski, L. Ilver, U. O. Karlsson, Charge Accumulation at InAs surfaces, Phys Rev. Lett. **1996**, 76, 3626
- 299) P. Gladkov, D. Nohavica, Z. Sourek, A. P. Litvinchuk, M. N Iliev, Growth and characterization of InAs layers obtained by liquid phase epitaxy from Bi solvents, Semicond. Sci. Technol. **2006**, 21(4), 544
- 300) R. D. Grober, H. D. Drew, J.-I. Chyi, S. Kalem, H. Morkoc, Infrared photoluminescence of InAs epilayers grown on GaAs and Si substrates, J. Appl. Phys. **1989**, 65, 4079
- 301) O.-P. Kilpi, J. Svensson, J. Wu, A. R. Persson, R. Wallenberg, E. Lind, L.-E. Wernersson, Vertical InAs/InGaAs Heterostructure Metal-Oxide-Semiconductor Field-Effect Transistors on Si, Nano Lett., **2017**, 17(10), 6006-6010
- 302) O.-P. Kilpi, J. Svensson, L.-E. Wernersson, Sub-100-nm gate-length scaling of vertical InAs/InGaAs nanowire MOSFETs on Si, IEEE International Electron Devices Meeting, **2017**, 17.3.1-17.3.4
- 303) P. K. Mohseni, A. Benham, J. D. Wood, C. D. English, J. W. Lyding, E. Pop, X. Li, In_xGa_{1-x}As Nanowire Growth on Graphene: van der Waals Epitaxy Induced Phase Segregation, Nano Lett., **2013**, 13(3), 1153-1161

- 304) Y. Yan, Z.-M. Liao, Y.-Q. Bie, H.-C. Wu, Y.-B. Zhou, X.-W. Fu, D.-P. Yu, Luminescence blue-shift of CdSe nanowires beyond the quantum confinement regime, *Appl. Phys. Lett.* **2011**, 99, 103103
- 305) H. S. Lee, S.-W. Min, M. K. Park, Y.T. Lee, P. J. Jeon, J. H. Kim, S. Ryu, S. Im, MoS₂ Nanosheets for Top-Gate Nonvolatile Memory Transistor Channel, *Small*, **2012**, 8(20), 3111-3115
- 306) L. Liang, K. Li, C. Xiao, S. Fan, J. Liu, W. Zhang, W. Xu, W. Tong, J. Liao, Y. Zhou, B. Ye, Y. Xie, Vacancy Associates-Rich Ultrathin Nanosheets for High Performance and Flexible Nonvolatile Memory Device, *J. Am. Chem. Soc.*, **2015**, 137(8), 3102-3108
- 307) T.-W. Kim, Y. Gao, O. Acton, H.-L. Yip, H. Ma, H. Chen, A. K.-Y. Jen, Graphene oxide nanosheets based organic field effect transistor for nonvolatile memory applications. *Appl. Phys. Lett.*, **2010**, 97, 023310

- 308) A. Das, Y. Ronen, Y. Most, Y. Oreg, M. Heiblum, H. Shtrikman, Zero-bias peaks and splitting in an Al-InAs nanowire topological superconductor as a signature of Majorana fermions, *Nature Physics* **2012**, 8, 887-895
- 309) J. Shabani, M. Kjaergaard, H. J. Suominen, Y. Kim, F. Nichele, K. Pakrouski, T. Stankevic, R. M. Lutchyn, P. Krogstrup, R. Feudenhans'l, S. Kraemer, C. Nayak, M. Troyer, C. M. Marcus, C. J. Palmstrøm. Two-dimensional epitaxial superconductor-semiconductor heterostructures: A platform for topological superconducting networks, *Phys. Rev. B*, **2016**, 93, 155402
- 310) H. J. Suominen, M. Kjaergaard, A. R. Hamilton, J. Shabani, C. J. Palmstrøm, C. M. Marcus, F. Nichele, Zero-Energy Modes from Coalescing Andreev States in a Two-Dimensional Semiconductor-Superconductor Hybrid Platform, *Phys. Rev. Lett.*, **2017**, 119, 176805
- 311) S. Lee, C.-W. Cheng, X. Sun, C. D'Emic, H. Miyazoe, M. M. Frank, M. Lofaro, J. Bruley, P. Hashemi, J. A. Ott, T. Ando, W. Spratt, G. M. Cohen, C. Lavoie, R. Bruce, J. Patel, H. Schmid, L. Czornomaz, V. Narayanan, R. T. Mo, E. Leobandung, High Performance InGaAs Gate-All-Around Nanosheet FET on Si Using Template Assisted Selective Epitaxy, *IEEE IEDM San Francisco CA*, **2018**, 39.5.1-39.5.4
- 312) F. Fan, Y. Chen, D. Pan, J. Zhao, H. Q. Xu, Measurements of spin-orbit interaction in epitaxially grown InAs nanosheets, *Appl. Phys. Lett.*, **2020**, 117, 1
- 313) N. Guo, W. Hu, L. Liao, S. Yip, J. C. Ho, J. Miao, Z. Zhang, J. Zou, T. Jiang, S. Wu, X. Chen, W. Lu, Nanowires: Anomalous and Highly Efficient InAs

- Nanowire Phototransistors Based on Majority Carrier Transport at Room Temperature, *Adv. Mater.* **2014**, 26, 8203
- 314) J. A. Webber-Alexander, C. K. Groschner, A. A. Sagade, G. Tainter, M. F. Gonzalez-Zalba, R. Di Pietro, J. Wong-Leung, H. H. Tan, C. Jagadish, S. Hofmann, H. J. Joyce, Engineering the Photoresponse of InAs Nanowires, *ACS Appl. Mater. Interfaces* **2017**, 9(50), 43993-44000
- 315) A. Konar, J. Mathew, K. Nayak, M. Bajaj, R. K. Pandey, S. Dhara, K. V. R. M. Murali, M. M. Deshmukh, Carrier Transport in High Mobility InAs Nanowire Junctionless Transistors, *Nano Lett.* **2015**, 15(3), 1684-1690
- 316) S. A. Dayeh, C. Soci, P. K. L. Yu, E. T. Yu, D. Wang, Influence of surface states on the extraction of transport parameters from InAs nanowire field effect transistors, *Appl. Phys. Lett.* **2007**, 90, 162112
- 317) M. Bachmann, A. Pahlke, C. Axt, B. Hinze, W. Hansch, CMOS field emission devices based on {111} silicon surfaces, *J. Vac. Sci. Technol. B*, **2014**, 32, 02B105
- 318) B. Mayer, L. Janker, D. Rudolph, B. Loitsch, T. Kostenbader, G. Abstreiter, G. Koblmüller, J. J. Finley, Continuous wave lasing from individual GaAs-AlGaAs core-shell nanowires, *Appl. Phys. Lett.*, **2016**, 108, 071107
- 319) F. Fan, Z. Liu, L. Yin, P. L. Nichols, H. Ning, S. Turkdogan, C. Z. Ning, Simultaneous two-color lasing in a single CdSSe heterostructure nanosheet, *Semicond. Sci. Technol.*, **2013**, 28(6), 065005
- 320) B. Shi, G. He, K. Yang, B. Zhang, J. He, Few-layer GaSe nanosheet-based broadband saturable absorber for passively Q-switched solid-state bulk laser, *Appl. Optics*, **2020**, 59(28), 8834-8838
- 321) Q. Li, C. Yuan, T. Yu, Q. Wang, J. Li, Nonvolatile charge memory with optical

controllability in two-terminal pristine α -In₂Se₃ nanosheets, J. Phys. D: Appl. Phys., **2020**, 53(7), 075108

- 322) M. Gu, B. Zhang, B. Liu, Q. Che, Z. Zhao, Y. Chen, Solution-processable black phosphorus nanosheets covalently modified with polyacrylonitrile for nonvolatile resistive random access memory, J. Mater. Chem. C, **2020**, 8, 1231-1238